Development of functional materials based on boron clusters for energy storage and conversion

By

Litwin Jacob

Supervised by prof. Piotr Kaszyński

A Dissertation submitted for the partial fulfillment of

the degree of Doctor of Philosophy

in Chemistry

Organic Material Research Group

Centre of Molecular and Macromolecular Studies of

Polish Academy of Sciences

Henryka Sienkiewicza 112, 90-001 Łódź, Poland

September 2023

DECLARATION

The work presented in this Dissertation entitled "***Development of functional materials based on boron clusters for energy storage and conversion***" has been carried out by me under the guidance of **Prof. Piotr Kaszyński** at the Centre of Molecular and Macromolecular Studies of Polish Academy of Sciences, Łódź, Poland. This work has not been submitted in part or in full for a degree, a diploma, or a fellowship to any other university or institute. Whenever contributions of others are involved, every effort is made to indicate this clearly, with due acknowledgment of collaborative research and discussions. This Dissertation is a bonafide record of original work done by me and all sources listed within have been detailed in the bibliography.

Date:04/9/2023 Litwin Jacob

Place: Łódź, Poland

ACKNOWLEDGMENT

In accomplishing my PhD dissertation, I would like to express my sincere gratitude to the European Space Agency (ESA) and the Foundation for Polish Science (FNP) for their financial support. I would also like to acknowledge ESA's support during my visit to the European Space Research and Technology Center (ESTEC) in the Netherlands.

My Dissertation could not have been possible without the help of many people. First of all, I would like to thank my supervisor, Prof. Piotr Kaszyński for providing me the opportunity to work in his research group. His knowledge, expertise, and profound understanding in my area of research greatly aided my research, and he was always encouraging and supportive. I am extremely grateful to him for transforming me into a skilled and confident scientist.

I cannot forget my colleagues for being a great bunch of people. Due to the constant assistance, I received from Dr. Agnieszka Bodzioch and Dr. Rafał Jakubowski in and out of the laboratory, I never encountered the difficulties associated with being a foreigner in Poland. I sincerely value their assistance and thank them for being such a tremendous help. I also thank Dr. Shivakumar I. Kilingaru, Dr. Martin Cigl, Dr. Maria Koyioni, Dr. Georgia Zissimou, Dr. Hemant Kumar Singh, Dr. Szymon Kapuściński, Dr. Paulina Bartos, Ms. Dominika pomikło, Ms. Edyta Rzeszotarska, Ms. Bindushree Anand, Ms. Mahshid Teimouri, and Ms. Patrycja Szamweber for making the past 5 years much more enjoyable and keeping me active throughout the whole process. I would like to thank Dr. Jannick Guschlbauer for teaching me the fundamentals of electrochemical impedance measurements. I would also like to thank Prof. Kevin Shaughnessy for offering courses on transition metal-catalyzed reactions and mechanisms. I also want to express my gratitude to the director, professors, technical staff, and other members of CBMM for helping me in various matters.

It is my honor to thank Prof. Matthias Lehmann of the University of Wurzburg, Prof. Piotr Guga, and Dr. Simon Duttwyler for agreeing to be members of my PhD review committee. Special thanks to Prof. Piotr Guga for his continued support.

I express my deep sense of gratitude to my collaborators from various institutions. I am grateful to Dr. Damian Pociecha from the University of Warsaw for teaching me how to conduct powder XRD measurements and always assisting me with them. I am thankful to Dr. Leszek Niedzicki of the Technical University of Warsaw for helping me with battery research. I would also like to thank Prof. Wiktor Piecek and Dr. Eva Oton of the Military University of Technology in Warsaw for teaching sample alignment techniques and polymerization. I am really thankful to Dr. Anna Pietrzak of the Łódź University of Technology, for always helping with single crystal XRD measurements. I would like to express my gratitude to Dr. Malgorzata Hołynska for serving as my program officer and contact at ESA, arranging my visit to ESTEC, and providing assistance and support throughout the various phases of the project. Also, I would like to thank Engr. Geraldine Palissat for her generosity, support, and assistance during my time at ESTEC.

I am indebted to Prof. Sandeep Kumar, Dr. Ashwath Narayana Gowda, and Dr. Yuvaraj Aralapura for training and teaching me the fundamentals of scientific research during my stay at the Raman Research Institute in Bangalore, India, prior to beginning my PhD. In addition, I would like to thank all my teachers and friends who have contributed to my success in various ways.

I would also like to express my gratitude to my family for their endless encouragement and support. I have a deep sense of appreciation for my parents and brother for always having faith in me and believing in me. Unfortunately, my father, who had always wanted to see me earn a PhD, passed away during my PhD studies. There are no sufficient words to describe the amount of support and encouragement I received from my dear wife Dayana during my PhD journey, and I

am so grateful to have such a wonderful life partner. I would like to conclude by expressing gratitude to God for the blessings He has bestowed upon my life.

TABLE OF CONTENTS

Page

Introduction …….....1

1 Batteries, energy storage, and space exploration 1

2 Boron clusters 3

3 Application of boron clusters in contemporary technologies 6

3.1 Biomedical application of boron clusters 7

3.2 Significance of boron clusters in material science 8

3.3 Boron clusters in liquid crystals 10

3.3.1 Liquid crystals 10

3.3.2 Liquid crystals derived from boron clusters 14

4 References …….....16

Goals and objectives 27

PART A

Development of functional materials based on 1,10-disubstituted [closo-$B_{10}H_{10}$]$^{2-}$ anion derivatives

Chapter A1: *Chemistry of the 1,10-disubstituted derivatives of the closo-decaborate anion ([closo-$B_{10}H_{10}$]$^{2-}$)* 2

1.1 Introduction 2

1.2 Preparation and reactivity of the 1,10-homodisubstituted derivatives of the [*closo*-$B_{10}H_{10}$]$^{2-}$ anion 7

1.2.1 Derivatives with the Boron-Carbon bond 7

1.2.2 Derivatives with the Boron-Oxygen bond 11

1.2.3 Derivatives with the Boron-Nitrogen bond 13

1.2.4 Derivatives with the Boron-Sulfur bond 18

1.2.5 Derivatives with the Boron-Halogen bond 20

1.3 Preparation of 1,10-heterodisubstituted derivatives 21

1.4 Self-organizing materials based on the [*closo*-$B_{10}H_{10}]^{2-}$ anion 30

1.4.1 Zwitterionic quadrupolar liquid crystals 30

1.4.2 Ionic liquid crystals 31

1.5 Photoactive materials derived from [*closo*-$B_{10}H_{10}]^{2-}$ anion 33

1.6 Metal complexes based on the [*closo*-$B_{10}H_{10}]^{2-}$ anion 34

1.7 Summary and outlook 35

1.8 References 36

Chapter A2: *Synthesis, structural analysis, and functional group interconversion in the [closo-*$B_{10}H_8$*-1,10-*$X_2]^{2-}$ *(X = CN,* $[OCRNMe_2]^+$*, OCOR, and* $[OH_2]^+$*) derivatives.* (L. Jacob, E. Rzeszotarska, A. Pietrzak, V. G. Young Jr., P. Kaszyński. *Eur. J. Inorg. Chem.*, **2020**, *32*, 3083–3093, DOI: 10.1002/ejic.202000456) 42

2.1 Introduction 42

2.2 Published text.....44

Chapter A3: *Tunable intermolecular charge transfer in ionic liquid crystalline derivatives of the [closo-*$B_{10}H_{10}]^{2-}$ *anion.* (L. Jacob, E. Rzeszotarska, M. Koyioni, R. Jakubowski, D. Pociecha, A. Pietrzak, P. Kaszyński. *Chem. Mater.*, **2022**, *34*, 6476–6491, DOI: 10.1021/acs.chemmater.2c01-165) 55

3.1 Introduction 55

3.2 Published text 58

3.3 Additional information 74

3.3.1 Additional synthetic details 74

3.3.2 DSC measurements 76

3.3.3 Powder XRD data 79

PART B

Development of new efficient electrolytes based on [closo-$CB_{11}H_{12}$]$^-$ for Li-ion battery applications

Chapter B1: *Electrolytes for Li-ion batteries* 2

1.1 Introduction 2

1.2 Li-ion batteries 3

1.3 Electrolytes for Li-ion batteries 5

1.3.1 Solid polymer electrolytes 6

1.3.2 Liquid crystalline electrolytes 8

1.3.3 Liquid crystalline polymer electrolytes 11

1.4 Boron clusters in solid-state electrolytes 12

1.4.1 Electrolytes based on boron clusters 13

1.5 Principles of electrochemical impedance spectroscopy 15

1.6 References 17

Chapter B2: *Liquid crystalline electrolytes derived from the 1,12-disubstituted [closo-$CB_{11}H_{12}$]$^-$ anion.* (J. Guschlbauer, L. Niedzicki, L. Jacob, E. Rzeszotarska, D. Pociecha, P. Kaszyński, *J. Mol. Liq.*, **2023**, 121525, DOI: 10.1016/j.molliq.2023.121525) 37

2.1 Introduction 37

2.2 Published text 39

Chapter B3: *Liquid crystalline electrolytes containing Li^+ salt of a [closo-$CB_{11}H_{12}$]$^-$ derivative: Synthesis, characterization, and anisotropic Li-ion transport* 47

3.1 Introduction 47

3.2 Results and discussion 49

3.3 Summary and conclusions 56

3.4 Experimental section 57

3.5 Acknowledgements 68

3.6 References 68

Chapter B4: *Liquid crystalline polymer electrolytes based on [closo-1-$CB_{11}H_{12}$]$^-$ for Li-ion battery applications* 73

4.1 Introduction 73

4.2 Results and discussion 75

4.3 Summary and conclusions 86

4.4 Experimental section 87

4.5 Acknowledgements 93

4.6 References 94

Declaratory statement from co-authors of the published results 1–9

INTRODUCTION

The technological advancements of the 21st century had a profound impact on all aspects of human life on Earth. The modern world has been shaped by technological innovations in transportation, communication, health care, security, the energy sector, and space exploration. This has made life on Earth easier, and at the moment, everyone enjoys the benefits of these technologies. In today's world, which is all about speed and efficiency, there is always a quest for novel technologies. As a consequence, it is important to develop new materials that can be used in both current and future technologies.

1. Batteries, energy storage, and space exploration

Innovative energy technologies that provide reliable and sustainable energy storage and conversion play a significant role in current technological advancements. Uninterrupted power supply is necessary for the proper operation of many modern devices, and it is critically important in achieving the goals of space missions of the European Space Agency (ESA). To ensure a continuous power supply, the basic energy technology used in space exploration combines a primary energy source (photovoltaics or radioisotope-based electric generator) and an energy storage system (batteries) [1].

Several types of batteries, including primary, secondary, and nuclear batteries, are utilized in space exploration, and their use varies depending on the mission requirements [2]. For instance, nuclear batteries are used in interplanetary missions, where the availability of sunlight is limited. Commonly used rechargeable batteries in space exploration include Ag-Zn batteries (characteristics: high specific energy, compact size, super discharge performance, and stable voltage), Ni-Cd batteries (characteristics: require low maintenance and are suitable for short-

duration missions), and Ni-H_2 systems (characteristics: long cycle life and a calendar life >15 years in GEO operation) [2-4]. The operation of these batteries in space frequently faces challenges, such as temperature and gravity fluctuations, the presence of high-energy particles, radiation environments, and hard ultraviolet light [5]. Despite the fact that some of these batteries have been successfully employed in numerous missions, such as earth observation missions, telecommunication satellite missions, astronomy missions, interplanetary missions, etc., the majority of conventional batteries suffer from their large size, low energy density, poor performance at extreme temperatures, electrolyte leakage, capacity loss, corrosion of the battery components, and short lifespan [4-8]. A study on the satellite failures between 2000 and 2016 carried out in 2019 revealed that battery defects caused more failures than thrusters [9].

With the increasing demand for a reliable energy technology in space research, Li-ion batteries (LIBs) have received considerable interest due to their high energy density, lightweight, and increased life span [10-11]. In 2001, Li-ion batteries were used for the first time in ESA's Proba-1 [12], a technology demonstration satellite and currently, they are emerging as the primary energy source for spacecrafts, launch vehicles, interplanetary missions, and the space station [13-15]. LIBs have several advantages over the conventional batteries in space applications due to their developed technology, lightweight (a 50% weight reduction over Ni–H_2 is possible with less volume required), and much lower thermal dissipation. Most of the currently available LIBs operate in the temperature range of 25 to 60 °C. Therefore, they are not suitable for the outer space missions that require battery operation at extreme temperature ranges (such as in Mercury, Mars or Venus missions). Most LIBs are susceptible to irreversible electrode/electrolyte reactions and a variety of electrolyte-related safety issues (including leakage, volatility, flammability, and decomposition) above 80 °C, which eventually lead to battery failure [16]. The stability and

performance of the LIBs under extreme temperatures largely depend on the type of electrolyte employed. To overcome the current technical challenges, it is critical to develop new materials for use in advanced energy storage and conversion systems.

This Dissertation focuses on addressing some of these issues by using anionic boron clusters as the key structural element for photoactive and ion conductive ionic liquid crystals (ILCs). The Dissertation comprised of two parts. The first part of the Dissertation (Part A) is concerned with the [*closo*-$B_{10}H_{10}$]$^{2-}$ anion and photoactive ILCs derived from it. Part B is focused on the [*closo*-1-$CB_{11}H_{12}$]$^{-}$ anion as the key structural element of Li-ion conductive ILCs for battery applications. Boron clusters and their applications are reviewed in the sections below.

2. Boron clusters

The capacity of boron to create bonds and structures has resulted in an intriguing class of compounds known as boron hydrides. Boron has a ground state valence shell electronic configuration $2s^2 2p^1$. Unlike carbon, which forms chains and rings through covalent bonds with other atoms, boron having only three electrons in its valance shell chooses to form a cluster pattern by covalently bonding to itself. The most ubiquitous structure is the icosahedral B_{12} unit present in all three polymorphs of elemental boron, which demonstrates the unique bonding characteristics of the boron atom [17].

closo-Boranes, such as [*closo*-B_6H_6]$^{2-}$, [*closo*-$B_{10}H_{10}$]$^{2-}$, [*closo*-$B_{12}H_{12}$]$^{2-}$ etc., are fascinating class of compounds that are tri-dimensional frameworks of covalently bonded boron hydrides with characteristic non-classical bonding [18]. Its distinctive properties include the skeleton structure with three-center two-electron bonds, electron delocalization in the σ-framework, and excellent chemical, electrochemical, and thermal stability [19]. Huckel's aromaticity rules are used to explain the stability of these compounds. Therefore, boron clusters

are excellent prospects for the development of a variety of cutting-edge functional materials with unique properties.

In 1912, Alfred Stock and his co-workers successfully synthesized and characterized the first boron hydrides [20]. Subsequently, this research helped to comprehend a revolutionary bonding principle and herald a new era of structural chemistry. The simplest boron hydride is borane BH_3. The boron center in this derivative has only six valence electrons, which violates the octet rule. The diborane B_2H_6 is yet another derivative that does not satisfy the octet rule. A total of 12 valence electrons are involved in bonding in this derivative: six from the two boron atoms and six from the hydrogen atoms. Only four hydrogen atoms make typical covalent bonds with the boron atoms in this derivative, while the remaining two hydrogen atoms are shared by the two boron atoms through B–H–B bridges (Figure 1) [21]. Later, Lipscomb and co-workers described this B–H–B bridge (B–B–B bridge in the case of *closo*-boranes) as a three-center two-electron (3c2e) bond, which connects three atoms through a pair of delocalized electrons [22]. This represents the basic concept of bonding in all polyhedral boron hydrides, including the 10- and 12-vertex boron clusters (structures **A-E** and **F-J**, respectively) shown in Figure 2.

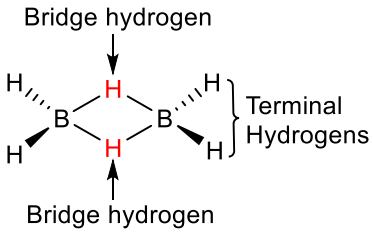

Figure 1. The structure of B_2H_6 with bridging B–H–B bonds and terminal B–H bonds.

Allard's (1932) and also Pauling and Weinbaum's (1934) research on metal hexaborides unveiled the first closed boron polyhedra with the generic formula MB_6 [23-24]. Longuet-Higgins and Roberts used the MO theory to investigate the existence of this closed network of highly stable

electronic arrangements in hexaborides [25]. In addition, their research on the B_{12} icosahedron revealed that the prototypical borane [*closo*-$B_{12}H_{12}]^{2-}$ (**F**, Figure 2) and other boranes with the general structural formula $(BH)_n$ would only be stable as dianions $(BH)_n^{2-}$. Hawthorne and Pitochelli subsequently synthesized the *closo*-dodecaborate anion **F** and analyzed it using X-ray diffraction, which reaffirmed the earlier conclusion regarding its structure [26]. Further research revealed the [*closo*-$B_{10}H_{10}]^{2-}$ anion (**A**, Figure 2) as well as other deltahedral boranes, [*closo*-$B_{11}H_{11}]^{2-}$, [*closo*-$B_9H_9]^{2-}$, [*closo*-$B_8H_8]^{2-}$, [*closo*-$B_7H_7]^{2-}$, and [*closo*-$B_6H_6]^{2-}$ [27].

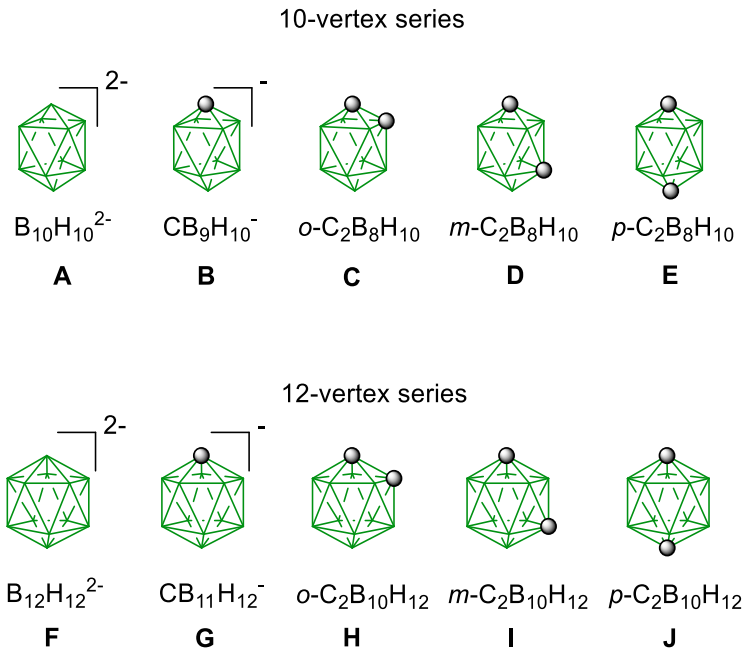

Figure 2. Structures of 10- and 12-vertex *closo*-boranes. The circles in the structure represent a CH vertex, and all other vertices are BH groups.

Prefixes, including *closo*-, *nido*-, and *arachno*- are used to describe the structural motifs of stable boranes [27]. The *closo*- represents the covalent network of polyhedral boranes that is closed. *Nido*- and *arachno*- boron clusters have one and two missing vertices of the closed network, respectively, and therefore have an additional pair of bridging hydrogen atoms (in the former) or two pairs (in the latter) [28]. Later on, Wade's rule established a common relationship between the

members of these three types of boron clusters and their number of skeleton electrons. According to this rule, there should be n+1 MOs in *closo*-borane, n+2 MOs in *nido*-borane, and n+3 MOs in *arachno*-borane [29].

Current research focuses primarily on boron clusters with 10 or 12 vertices, which are also of interest to investigation in this Dissertation. In addition to [*closo*-$B_{10}H_{10}]^{2-}$ (**A**) and [*closo*-$B_{12}H_{12}]^{2-}$ (**F**), several 10- and 12-vertex boron clusters exist with heteroatoms present in their closed skeletal structure (Figure 2). Carboranes and metallaboranes are only two such subclasses, although there are many others [30]. The 12-vertex carborane [*closo*-1-$CB_{11}H_{12}]^{-}$ (**G**) is obtained by replacing a "BH" vertex in the prototypical borane **F** with a "CH^{+}" group. Similarly, other neutral carborane derivatives are known, such as [*closo*-$C_2B_{10}H_{12}$], in which two "BH" vertices in **F** are replaced by two "CH^{+}" groups. This derivate exists in three distinct isomeric forms: 1,2-carborane (**H**), 1,7-carborane (**I**), and 1,12-carborane (**J**). Commonly encountered 10-vertex carborane derivatives include [*closo*-1-$CB_9H_{10}]^{-}$ (**B**) and the three isomers of [*closo*-$C_2B_8H_{10}$] (**C**, **D**, and **E**).

3. Application of boron clusters in contemporary technologies

Due to the unique properties of the *closo*-boron clusters, their chemistry is notably distinct from that of their organic counterparts. Boron clusters did not receive the attention they deserved as true building blocks for functional materials for a long time due to the lack of understanding of their chemistry and encountered functionalization challenges. Over the last few decades, scientists have made significant advances in understanding the fundamental chemistry of boron clusters and in synthesis of their derivatives. Consequently, this paved the way for the development of a number of fascinating new materials with properties that can be tuned for specific applications. Some of the applications of boron clusters in contemporary technologies are discussed below.

3.1 Biomedical application of boron clusters

Boron neutron capture therapy (BNCT) for the treatment of tumors is one of the most significant applications of boron clusters in the medical field [31]. In this technique, the ^{10}B isotope of boron with a high neutron cross section of 3840 barns (it is a measure of the ability to absorb thermal neutrons) uptaken by the neoplastic cell captures a thermal neutron and undergoes radioactive decay to produce an alpha particle, ^{7}Li nucleus and a gamma photon, thereby providing a localized lethal dose for selective destruction of the malignant cells. For successful BNCT applications, there must be high selectivity and sufficient concentration of boron in the targeted cell, which continues to remain a challenge. The introduction of boron clusters with a high concentration of the ^{10}B isotope as a boron carrier compound significantly improved BNCT. In a recent study, magnetic nanocomposites containing carborane cages were found to provide a high ^{10}B isotope concentration in tumor cells [31b]. Carbohydrates, nucleic acids, proteins and amino acids conjugated with boron clusters are among new boron carrier molecules investigated for BNCT treatment [32].

Recently, boron clusters were utilized in developing of carrier molecules for transport of hydrophilic cargo molecules, such as cationic and neutral peptides, amino acids, neurotransmitters, vitamins, antibiotics, and drugs across liposomal membranes [33]. Boron clusters have additional medical applications in biosensors, targeted drug delivery, the treatment of cancer and HIV, and the investigation of protein-biomolecular interactions [34]. The amphiphilicity, lipophilicity, or hydrophilicity of different boron clusters, as well as their capacity for non-covalent interactions, such as ionic interactions and dihydrogen bond formation, made it possible to design drugs with tunable interactions with biological targets. Additionally, the chemical stability of the boron

clusters makes them biologically stable and minimizes the toxicity. Their resistance to high ionizing radiation is important for the development of radiopharmaceutical agents [35].

3.2 Significance of boron clusters in material science

Boron clusters are being explored in several areas of material science. They are characterized by aromaticity of their three-dimensional σ-framework and this property is being explored, for example, in the development of luminescent materials with tunable photophysical properties [36]. Multiple studies demonstrated that the incorporation of 12-vertex neutral carboranes into π-conjugated systems significantly increased emission intensity and its quantum yield. Such derivatives, particularly *meta*- and *para*-carborane were found to be suitable for the use in organic light-emitting diodes [37] and light-emitting polymeric materials [38]. Due to its shape, *ortho*-carborane hinders π-staking which limit aggregation-induced quenching [39]. By incorporation of a sterically bulky monocarborate anion [*closo*-1-$CB_{11}H_{12}$]$^-$ onto a bidentate ligand platform, high-performance phosphorescent materials have been synthesized recently [40]. The availability of various carborane clusters enables the emission properties to be tailored to meet specific requirements.

Carboranes have been used in the development of polymers with improved thermal and electrochemical stability. Carborane-based polymers, such as phenylene ether carboranylene ketone (PECK), have demonstrated high thermal stability with minimal mass loss even at temperatures as high as 1000 °C [41]. Also, incorporation of carborane into the structure of conducting organic polymers (COPs) enhanced their thermal stability and resistance to overoxidation [42-43]. Such materials are potential substitutes for conventional metal and inorganic semiconductors.

Boron clusters, particularly 12-vertex carboranes, are used in the development of thermally stable coordination polymers and metal-organic frameworks (MOFs). The empty space within MOFs can accommodate guest molecules and counterions. Zn(II) and Co(II)-based MOFs containing the *para*-carborane derivative have demonstrated gas-absorption properties [44-45], and such molecules are important in zeolite applications.

Nanoscience is another significant field of study involving boron clusters. Nanoparticles composed of boron clusters have been found to have a wide range of applications, including those in the medical field. When used in BNTC, magnetic nanocomposites containing carborane cages were found to provide high boron concentration in tumor cells, which is key for a successful BNTC [33b]. Carboranes are also used to develop molecular architectures, such as rods [46] and boxes [47] for nanomachines and molecular electronics. The development of nanomachines is of high interest because they could perform tasks at the molecular level in a similar manner as conventional machines in the macro scale. Several nano vehicles, such as nonocars, nanoinchworms, and nanocaterpillars have been demonstrated, in which *para*-carborane serves as the wheels [48-49]. These nanovehicles are propelled by a photochemical process at 365 nm wavelength. In this spectral region, *para*-carborane does not absorb light and has no quenching effect on the photochemical process. Consequently, *para*-carborane replaced fullerenes previously used in nanovehicles, which operate on the same principle.

Boron clusters and their derivatives are promising candidates for nonlinear optical applications (NLOs). When interacting with an external electromagnetic field, NLO-active materials generate a field with a modified pulse and frequency. These materials are crucial for contemporary technological applications involving data storage and retrieval, optical switching and limiting, image processing, and optical communication. Theoretical investigations on several

derivatives of boron clusters revealed large nonlinear optical responses, with hyperpolarizabilities ranging from 8.6 to 1226 × 10^{-30} cm^5 esu^{-1} [50]. Their high hyperpolarizability tends to be associated with the degree to which the HOMO of the polyhedral boron hydrides mixes with the π system of the substituent.

Other applications of boron clusters involve advanced catalysts, coordination chemistry for the development of dianionic ligands and ligand substituents by the utilization of a σ-bound cluster via its C vertex, and covalently bound spectator substituents to enhance the stability of radicals [51].

3.3 Boron clusters in liquid crystals

Boron clusters are of particular interest for the synthesis of liquid crystals due to their three-dimensional geometry, effective charge delocalization, high polarizability, and chemical and thermal stabilities. Several boron clusters, such as [*closo*-$B_{10}H_{10}]^{2-}$, [*closo*-1-$CB_9H_{10}]^-$, and [*closo*-$C_2B_{10}H_{12}$], were substituted with organic groups in such a way to form rod-like molecules exhibiting liquid crystal-like behavior. Such a combination resulted in several classes of unique quadrupolar and ionic liquid crystals that are suitable for application in NLO materials, molecular electronics, and photovoltaics.

3.3.1 Liquid crystals

An intriguing observation made by the Austrian botanist Friedrich Reinitzer in 1888 regarding the melting of cholesteryl benzoate led to Otto Lehmann's investigation of this phenomenon and the discovery of liquid crystallinity [52-54]. Liquid crystals (LCs) are soft, functional materials that exist in a distinct phase of matter between the solid and liquid states (Figure 3). This thermodynamically stable intermediate phase, also known as the "fourth state of matter", possesses anisotropy of its properties found in the solid, and fluidity characteristic of a

liquid [52-57]. Due to these reasons, a LC phase is commonly referred to as a mesophase and the molecules capable of forming a mesophase are known as mesogens.

The most fascinating aspect of LCs is their ability to form self-organized anisotropic structures that combine order and mobility. Because of the ability of LCs to align in different directions, to switch orientations, and to change properties in response to external stimuli, such as an electric field, heat, mechanical force, and so on, they are appealing components of modern technologies [58-62].

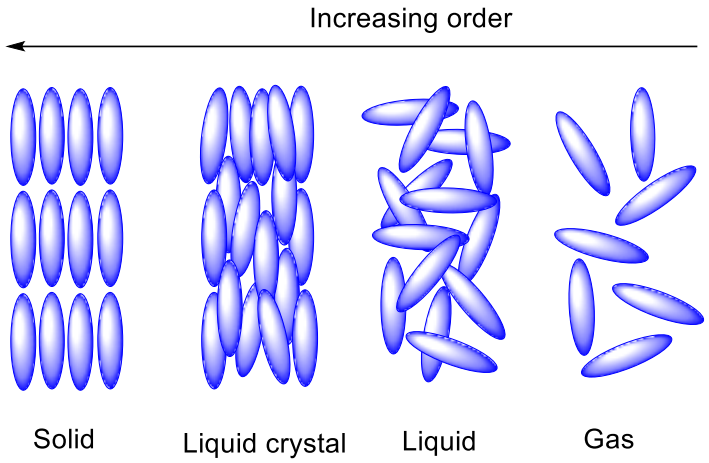

Figure 3. Schematic diagrams of molecular order present in different states of matter.

Depending on how the mesophases are obtained, LCs are typically classified as either thermotropic or lyotropic [52-54]. The thermotropic liquid crystalline phase is formed by heating of a mesogen to a specific temperature. Thermotropic LCs are further classified as disc-like, rod-like, and bent-core based on the geometry of the LC molecule. The formation of lyotropic liquid-crystalline phases is attained by preparing solutions of LCs in solvents of appropriate concentration. On the basis of their constituents, LCs may be organic, ionic, or organometallic. Thermotropic ionic LCs necessitate special consideration in the context of my research on anionic boron clusters [63-64]. Ionic liquid crystals (ILC) are ion pairs composed of an anion and a cation, and they

combine the properties of both ionic liquids (ionic conductivity, wide electrochemical window, high thermal stability, low vapor pressure, etc.) and liquid crystals (dynamic molecular order, self-assembling ability, birefringence, anisotropic physical properties, etc.).

Thermotropic LC phases are referred to as enantiotropic, when they show a LC phase on both heating and cooling temperature scans. Liquid crystals (LCs) with a monotropic phase, on the other hand, exhibit the liquid crystal phase only when cooled from the isotropic liquid phase [53]. The general molecular design of a thermotropic liquid crystal consist of a central rigid core and at least one flexible chain surrounding the rigid core [54]. Formation of the mesophase is also influenced by the shape, geometry, the extent of non-covalent interactions, nano-segregation, self-assembly, and self-organization.

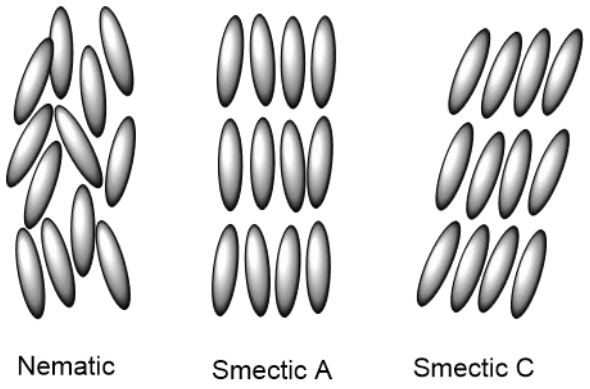

Figure 4. Schematic diagrams of commonly observed phases in road like liquid crystals.

LC phases are designated as nematic (N), smectic (Sm), columnar (Col), B phase (B stands for a banana phase formed by a bow-shaped or bent-core mesogen), etc. based on the type of arrangement of molecules in the mesophase [52-54]. Based on the strength of non-covalent interactions, such as van der Waals forces, hydrogen bonding, hydrophobic interactions, dipolar interactions, and charge transfer interactions, liquid crystals are able to self-organize and self-assemble into different phases. Typically, molecules with a rod-like shape and a bent core

molecular architecture exhibit smectic and nematic phases (Figure 4). In addition, bent-core molecules display columnar phases, which are characteristic of disc-shaped molecules. Disc-shaped molecules rarely exhibit nematic phases (discotic nematic, N_D).

In this research, the rod-like LCs are of particular interest. As the name suggests, they have the shape of a rod and are composed of one or two aromatic rings connected directly or via a linker, and alkyl chains at the terminal positions of the rigid core (Figure 5). The properties of LC are determined by the number of rings, the presence of lateral substituents in the rings, the type and nature of linking groups, the length and nature of alkyl chains, the presence of polar groups, etc.

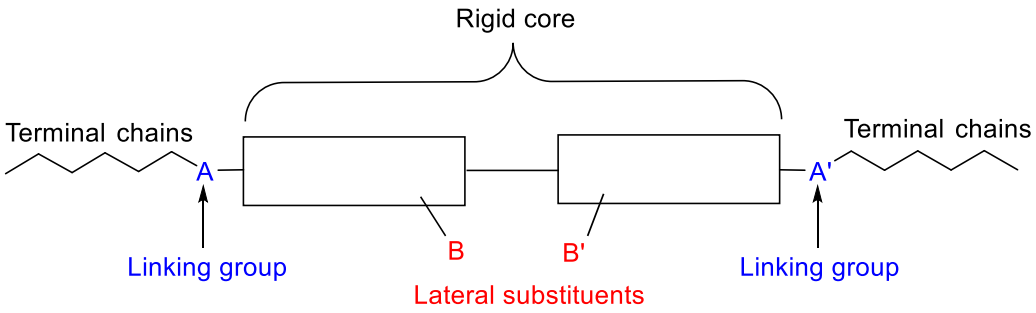

Figure 5. General schematic of rod-like liquid crystal molecules.

The nematic phase is the least ordered mesophase, as only orientational order without positional order is present. In the smectic phase, in addition to the long-range orientational order, molecules also possess some short-range positional order. In this phase, molecules self-organize to form a layered structure with well-defined boundaries between them. Based on the molecular arrangement within the layers of the smectic phase, they are further classified as SmA, SmC, SmF, SmI, SmB_{hex}, etc. SmA and SmC are the least ordered smectic phases and there is no positional correlation between the molecules within the layer or between the layers. Molecules, when arranged in layers with their long molecular axis perpendicular to the layer plane, form the orthogonal SmA phase. The SmC phase is a tilted analogue of the SmA phase, with a similar

arrangement of molecules and a tilt of their long molecular axis with respect to the layer plane. Similarly, molecules in the SmF and SmI phases also have a tilted orientation, but in addition they have a hexagonal arrangement within the layers. SmB_{hex} has an orthogonal orientation similar to that of the SmA phase, but with an additional hexagonal order within the layers [52-53, 56].

3.3.2 Liquid crystals derived from boron clusters

The availability of several boron clusters, such as [*closo*-$B_{10}H_{10}]^{2-}$ (**A**), [*closo*-1-$CB_9H_{10}]^-$ (**B**), [*closo*-1,10-$C_2B_8H_{10}$] (**E**), [*closo*-1-$CB_{11}H_{12}]^-$ (**G**), and [*closo*-1,12-$C_2B_{10}H_{12}$] (**J**, Figure 2) with varying electronic properties enabled the development of liquid crystals with intriguing properties (Figure 6) [65].

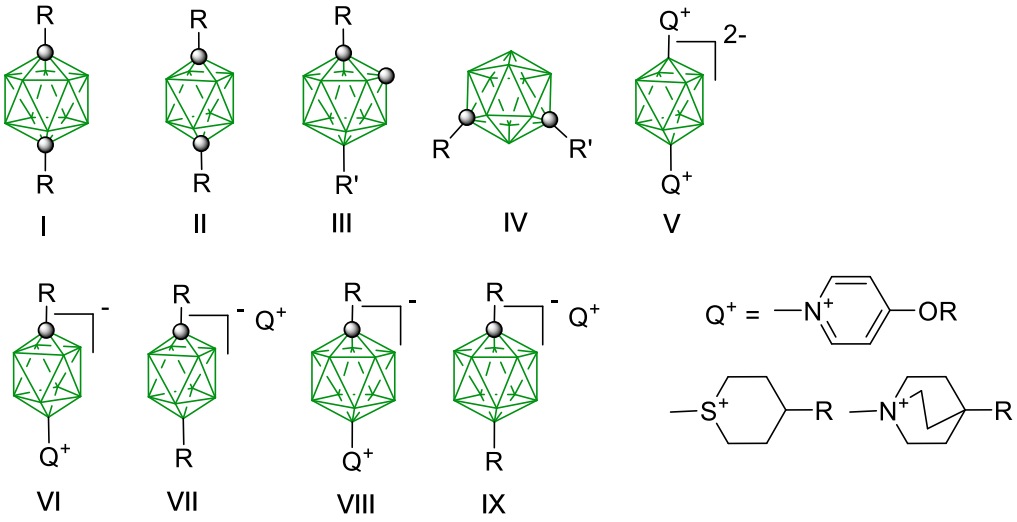

Figure 6. Representation of general structures of classes of liquid crystals derived from boron *closo*-clusters. Q^+ represents an onium fragment, such as quinuclidinium, pyridinium, or sulphonium, and R represents any suitable organic fragment.

When neutral *para*-carboranes, [*closo*-1,12-$C_2B_{10}H_{12}$] (**J**) and [*closo*-1,10-$C_2B_8H_{10}$] (**E**) were used as structural elements in liquid crystalline materials (type **I** and **II**), they were found to have a detrimental effect on the smectic phase stability in favor of the nematic phase, when

compared to their organic analogues benzene, cyclohexane, and bicyclo[2.2.2]octane [66]. 1,12-Disubstituted derivatives of *ortho*-carborane also formed liquid crystalline materials (type **III)** with a moderate dipole moment [67]. *meta*-Carborane (**I**) was used in the synthesis of liquid crystalline molecules with bent-core molecular architecture (type **IV**) [68].

closo-Decaborate anion [*closo*-$B_{10}H_{10}]^{2-}$ (**A**) was investigated in the context of the formation of highly quadrupolar zwitterionic liquid crystals (type **V**). Several 1,10-disubstituted pyridinium and sulfonium derivatives were synthesized, and the effect of lateral polar interactions between the negatively charged boron cluster and the positively charged pyridinium groups on their LC phase stability was investigated [69]. Also, a study conducted on a homologous series of 1,10-disubstituted 4-alkoxypyridinium zwitterions of the anion **A** demonstrated the effect of this strong lateral polar interaction in the formation of a new type of lamellar phases, which are not typical for calamitic molecules [70]. These quadrupolar materials are of particular interest as NLO materials.

Carboranes [*closo*-1-$CB_9H_{10}]^-$ (**B**) and [*closo*-1-$CB_{11}H_{12}]^-$ (**G**) have been extensively studied in the context of the development of polar and ionic liquid crystals. Several zwitterionic liquid crystals (type **VI** and **VIII**) were prepared by proper disubstitution of the monocarboranes with an onium fragment (quinuclidinium, pyridinium or sulphonium) in the antipodal boron atom and an organic fragment linked to the apical carbon atom through –COO– or $–CH_2CH_2–$ groups [71-75]. These derivatives are suitable for use in the electro-optics and liquid crystal display industries due to their high longitudinal dipole moments. Some of these compounds were discovered to be efficient positive $\Delta\varepsilon$ additives to nematic hosts. Appropriately disubstituted monocarborane derivatives with at least three rings in their structure and a positive counter ion (*N*-alkyl-4-alkoxypyridinium) resulted in ionic liquid crystals (type **VII** and **IX**) [72,76-78]. Such derivatives are examples of materials with anion-driven mesogenicity. Li^+ salts of these

monocarborane derivatives are being studied in the context of electrolytes for Li-ion battery applications, and this will be discussed in detail in Part B of this Dissertation.

Despite possessing a variety of attractive characteristics, including the D_{4d} molecular symmetry and a high-lying HOMO [72], the [*closo*-$B_{10}H_{10}]^{2-}$ anion (**A**) did not receive enough attention as a component in functional materials because of the challenges with its functionalization. Several 1,10-disubstituted dinitrogen, pyridinyl, and acetonitrile derivatives of the cluster have already demonstrated its capacity for efficient interaction with π-substituents [79-81]. Due to this feature, it is possible to adjust the electronic properties of the cluster derivatives so that they conform to the requirements of specific applications. It is expected that 1,10-difunctional derivatives of the [*closo*-$B_{10}H_{10}]^{2-}$ anion will find numerous fascinating applications in areas, such as molecular electronics, semiconductors, NLO materials, and photovoltaics. As a result, it is essential to further develop the chemistry of the [*closo*-$B_{10}H_{10}]^{2-}$ anion, and the first part of this Dissertation (Part A) is devoted entirely to the functionalization of the [*closo*-$B_{10}H_{10}]^{2-}$ anion in order to facilitate the development of novel ionic functional materials.

4. References

1. (a) A. D. Pathak, S. Saha, V. K. Bharti, M. M. Gaikwad, C. S. Sharma, A review on battery technology for space application, *J. Energy Storage*, **2023**, *61*, 106792; (b) Energy storage technologies for future space science missions, NASA solar system exploration. https://solarsystem.nasa.gov/resources/295/energy-storage-technologies-for-future-space-science-missions/; (c) NASA technology roadmaps (archive), NASA **2015**.
2. G. Halpert, H. Frank, S. Surampudi, Batteries and fuel cells in space, *Electrochem. Soc. Interface*, **1999**, *8*, 25–30.

3. A. J. Salkind, A. P. Karpinski, J. R. Serenyi, Secondary batteries – zinc systems | Zinc–Silver, Encyclopedia of Electrochemical Power Sources, **2009**, 513–523.
4. G. Halpert, The design and application of nickel-cadmium batteries in space, *J. Power Sources*, **1985**, *15*, 119–140.
5. A. F. Hepp, P. N. Kumta, O. I. Velikokhatnyi, M. K. Datta, Batteries for aeronautics and space exploration: Recent developments and future prospects, *Lithium-Sulfur Batteries*, **2022**, 531–595.
6. G. Halpert, H. Frank, S. Surampudi, Batteries and fuel cells in space, *The Electrochem. Soc. Interface*, **1999**, *8*, 25–32.
7. T. Jiang, W. Chen, Nickel hydrogen gas batteries: From aerospace to grid-scale energy storage applications. *Curr. Opin. Electrochem.*, **2021**, *30*, 100859.
8. W. Chen, Y. Jin, J. Zhao, N. Liu, Y. Cui, Nickel-hydrogen batteries for large-scale energy storage, *Proc. Natl. Acad. Sci. U. S. A.*, **2018**, *115*, 11694–11699.
9. S. A. Jacklin, Small-satellite mission failure rates. In NASA STI program, issue march **2019**. https://ntrs.nasa.gov/citations/20190002705.
10. C. Bubulinca, N. E. Kazantseva, V. Pechancova, N. Joseph, H. Fei, M. Venher, A. Ivanichenko, P. Saha, Development of all-solid-state Li-ion batteries: From key technical areas to commercial use, *Batteries*, **2023**, *9*,157–182.
11. C. A. Vincent, Lithium batteries: A 50-year perspective, *Solid State Ion.*, **2000**, *134*, 159–167.
12. Proba lithium-ion battery, European Space Agency, **2002**. https://www.esa.int/ESA_Multimedia/Images/2002/10/Proba_lithium-ion_battery.
13. R. Bugga, M. Smart, J. Whitacre, W. West, Lithium ion batteries for space applications, IEEE aerospace conference, MT, USA, **2007**, 1–7.

14. Spacewalkers complete multi-year station battery upgrades, NASA, **2021**. https://www.nasa.gov/feature/spacewalkers-completemulti-year-effort-to-upgrade-space-station-batteries.
15. S. Russell, M. Elder, A. Williams, J. Dembeck, The extravehicular maneuvering unit's new long-life battery and lithium ion battery charger, Presented at AIAA SPACE 2010 conference & exposition, at Anaheim, California USA, **2010**. https://doi.org/10.2514/6.
16. J. B. Goodenough, K. S. Park, The Li-ion rechargeable battery: A perspective, *J. Am. Chem. Soc.*, **2013**, *135*, 1167–1176.
17. A. F. Wells, Structural inorganic chemistry, ch. 24, Oxford University Press, **1979**.
18. W. N. Lipscomb, Boron hydrides. New York: Benjamin;**1963**.
19. (a) R. N. Grimes, Boron clusters come of age, *J. Chem. Educ.*, **2004**, *81*, 658–672; (b). J. Poater, C. Viñas, I. Bennour, S. Escayola, M. Sola, F. Teixidor, Too persistent to give up: Aromaticity in boron clusters survives radical structural changes, *J. Am. Chem. Soc.*, **2020**, *142*, 9396–9407; (c) J. Aihara, Three-dimensional aromaticity of polyhedral boranes, *J. Am. Chem. Soc.*, **1978,** *100*, 3339–3342; (d) R. B. King, Three-dimensional aromaticity in polyhedral boranes and related molecules, *Chem. Rev.*, **2001**, *101*, 1119–1152; (d) J. Poater, M. Sola, C. Viñas, F. Teixidor, π Aromaticity and three-dimensional aromaticity: Two sides of the same coin?, *Angew. Chem. Int. Ed.*, **2014**, *53*, 12191–12195; *Angew. Chem.*, **2014**, *126*, 12387–12391.
20. (a) A. Stock, C. Massanez, Boron hydrides, *Chem. Ber.*, **1912**, *45*, 3539; (b) A. Stock, Hydrides of boron and silicon, Cornell University Press, Ithaca, New York, **1933**.
21. (a) W. Dilthey, *Z. Angew. Chem.*, **1921**, *34*, 596–599; (b) S. M. Blinder, Second edition of introduction to quantum mechanics, Academic Press, **2021**.

22. W. H. Eberhardt, B. Crawford, W. N. Lipscomb, The valance structure of the boron hydrides, *J. Chem. Phys.*, **1954**, *22*, 989–1001.

23. G. Allard, X-ray study of some borides, *Bull. Soc. Chim. Fr.*, **1932**, *51*, 1213–1215.

24. L. Pauling, S. Weinbaum, The structure of calcium boride CaB_6, *Z. Kristallogr.*, **1934**, *87*, 181–182.

25. H. C. Longuet-Higgins, M. D. V. Roberts, The electronic structure of an icosahedron of boron atoms, *Proc. R. Soc. (London)*, **1955**, *230*, 110–119.

26. (a) J. L. Hoard, S. Geller, R. E. Hughes, On the structure of the elementary boron, *J. Am. Chem. Soc.*, **1951**, *73*, 1892–1893; (b) W. N. Lipscomb, M. F. Hawthorn, A. R. Pitochelli, Probable structure of the $[B_{10}H_{10}]^{2-}$ ion, *J. Am. Chem. Soc.*, **1959**, *81*, 5833–5834; (c) M. F. Hawthorn, A. R. Pitochelli, The reactions of bis-acetonitrile decaborane with amines, *J. Am. Chem. Soc.*, **1959**, *81*, 5519-5519.

27. (a) W. N. Lipscomb, Boron hydride chemistry, Academic Press (New York), **1975**; (b) R. E. Dickerson, W. N. Lipscomb, Semitopological approach to boron-hydride structures, *J. Chem. Phys.*, **1957**, *27*, 212–217; (c) E. D. Jemmis, M. M. Balakrishnarajan, P. D. Pancharatna, Electronic requirements for macropolyhedral boranes, *Chem. Rev.*, **2002**, *102*, 93–144; (d) E. D. Jemmis, P. V. R. Schleyer, Aromaticity in three dimensions. 4. Influence of orbital compatibility on the geometry and stability of capped annulene rings with six interstitial electrons, *J. Am. Chem. Soc.*, **1982**, *104*, 4781–4788; (e) Z. X. Wang, P. V. R. Schleyer, A "sea urchin" family of boranes and carboranes: The $6m + 2n$ electron rule, *J. Am. Chem. Soc.*, **2003**, *125*, 10484–10485.

28. R. E. Williams, Carboranes and boranes; Polyhedra and polyhedral fragments, *Inorg, Chem.*, **1971**, *10*, 210–214.

29. K. Wade, The structural significance of the number of skeletal bonding electron-pairs in carboranes, the higher boranes and borane anions, and various transition-metal carbonyl cluster compounds, *J. Chem. Soc. D,* **1971**, *15*, 792–793.

30. (a) Grimes, N. Russel, Carboranes, Academic Press, **2016**; (b) J. D. Kennedy, The polyhedral metallaboranes, *Prog. inorg. chem.*, **2009**, *34*, 211–425.

31. (a) A. H. Soloway, H. D. Hatanaka, M. A. Davis, Penetration of brain and brain tumor. VII. Tumor-binding sulfhydryl boron compounds, *J. Med. Chem.,* **1967**, *10,* 714; (b) Z. Yinghuai, L. Yongxiang, Z. Y. Zhun, L. Jia, J. A. Maguire, N. S. Hosmane, Boron drug delivery via encapsulated magnetic nanocomposites: a new approach for BNCT in cancer treatment, *J. Nanomater.*, **2010**, *2010*, 1–8; ($_{C}$). M. F. Hawthorne, A. Maderna, Applications of radiolabeled boron clusters to the diagnosis and treatment of cancer. *Chem. Rev.,* **1999**, *99*, 3421–3434; (d) N. S. Hosmane, ed. Boron science: New technologies and applications, CRC press, **2011**; (e) Y. Zhu, Frontiers in boron-based medicinal chemistry, World Scientific publishing company, **2023**.

32. (a) A. F. Armstrong, J. F. Valliant, The bioinorganic and medicinal chemistry of carboranes: From new drug discovery to molecular imaging and therapy, *Dalton Trans.,* **2007**, *38*, 4240–4251; (b) V. Bregadze, I. Sivaev, S. Glazun, Polyhedral boron compounds as potential diagnostic and therapeutic antitumor agents, *Anticancer Agents Med. Chem.*, **2006**, *6*, 75–109; (c) A. G. Beck Sickinger, D. P. Becker, O. Chepurna, B. Das, S. Flieger, E. Hey Hawkins, N. Hosmane, S. S. Jalisatgi, H. Nakamura, R. Patil, M. D. G. H. Vicente, New boron delivery agents, *Cancer Biother. Radiopharm.*, **2022**, *38*, 160–172; (d) Z. J. Lesnikowski, New opportunities in boron chemistry for medical applications, Boron Sciences: New Technologies and Applications; CRC Press: Boca Raton, FL, USA, **2011**, 3–19.

33. (a) A. Barba Bon, G. Salluce, I. Lostalé Seijo, K. I. Assaf, A. Hennig, J. Montenegro, W. M. Nau, Boron clusters as broadband membrane carriers, *Nature*, **2022**, *603*, 637–642; (b) E. A. Qian, A. L. Wixtrom, J. C. Axtell, A. Saebi, D. Jung, P. Rehak, Y. Han, E. H. Moully, D. Mosallaei, S. Chow, atomically precise organomimetic cluster nanomolecules assembled via perfluoroaryl-thiol SNAr chemistry, *Nat. Chem.*, **2017**, *9*, 333–340.

34. (a) B. C. Das, N. K. Nandwana, S. Das, V. Nandwana, M. A. Shareef, Y. Das, M. Saito, L. M. Weiss, F. Almaguel, N. S. Hosmane, T. Evans, Boron chemicals in drug discovery and development: Synthesis and medicinal perspective, *Molecules*, **2022**, *27*, 2615-2651; (b) P. Rezácová, J. Pokorná, J. Brynda, M. Kozisek, P. Cigler, M. Lepsik, J. Fanfrlik, J. Rezác, K. Grantz Šašková, I. Sieglová, J. Plesek, Design of HIV protease inhibitors based on inorganic polyhedral metallacarboranes, *J. Med. Chem.*, **2009**, *52*, 7132–7141; (c) N. S. Hosmane, Boron science: new technologies and applications, CRC Press, **2011**.

35. Z. J. Lesnikowski, Challenges and opportunities for the application of boron clusters in drug design, *J. Med. Chem.*, **2016**, *59*, 7738–7758.

36. (a) S. Mukherjee, P. Thilagar, Boron clusters in luminescent materials, *Chem. Commun.*, **2016**, *52*, 1070–1093; (b) B. P. Dash, R. Satapathy, J. A. Maguire, N. S. Hosmane, Polyhedral boron clusters in materials science, *New J. Chem.*, **2011**, *35*, 1955–1972; (c) R. Núñez, M. Tarrés, A. Ferrer-Ugalde, F. Fabrizi de Biani, F. Teixidor, Electrochemistry and photoluminescence of icosahedral carboranes, boranes, metallacarboranes, and their derivatives, *Chem. Rev.*, **2016**, *116*, 14307–14378.

37. B. P. Dash, R. Satapathy, E. R. Gaillard, K. M. Norton, J. A. Maguire, N. Chug, N. S. Hosmane, Enhanced π-conjugation and emission via icosahedral carboranes: Synthetic and spectroscopic investigation, *Inorg. Chem.*, **2011**, *50*, 5485–5493.

38. K. Kokado, Y. Tokoro, Y. Chujo, Luminescent *m*-carborane-based π-conjugated polymer, *Macromolecules*, **2009**, *42*, 2925–2930.

39. B. P. Dash, R. Satapathy, E. R. Gaillard, J. A. Maguire, N. S. Hosmane, Synthesis and properties of carborane-appended C_3-symmetrical extended π systems, *J. Am. Chem. Soc.*, **2010**, *132*, 6578–6587.

40. Y. Shen, X. Kong, F. Yang, H. D. Bian, G. Cheng, T. R. Cook, Y. Zhang, Deep blue phosphorescence from platinum complexes featuring cyclometalated *N*-pyridyl carbazole ligands with monocarborane clusters ($CB_{11}H_{12}^-$), *Inorg. Chem.*, **2022**, *61*, 16707–16717.

41. A. M. Fox, K, Wade, Model compounds and monomers for phenylene ether carboranylene ketone (PECK) polymer synthesis: Preparation and characterization of boron-arylated ortho-carboranes bearing carboxyphenyl, phenoxyphenyl or benzoylphenyl substituents, *J. Mater, Chem*., **2002**, *12*, 1301–1306.

42. C. Masalles, S. Borros, C. Viñas, F. Teixidor, Are low-coordinating anions of interest as doping agents in organic conducting polymers?, *Adv. Mater.*, **2000**, *12*, 1199–1202.

43. (a) C. Masalles, J. Llop, C. Viñas, F. Teixidor, Extraordinary overoxidation resistance increase in self-doped polypyrroles by using non-conventional low charge-density anions, *Adv. Mater.*, **2002**, *14*, 826–829.

44. O. K. Farha, A. M. Spokoyny, K. L. Mulfort, M. F. Hawthorne, C. A. Mirkin, J. T. Hupp, Synthesis and hydrogen sorption properties of carborane based metal-organic framework materials, *J. Am. Chem. Soc.*, **2007**, *129*, 12680–12681.

45. Y. S. Bae, A. M. Spokoyny, O. K. Farha, R. Q. Snurr, J. T. Hupp, C. A. Mirkin, Carborane-based metal-organic frameworks as highly selective sorbents for CO_2 over methane, *Chem. Commun*., **2008**, *35*, 4135–4137.

46. J. Muller, K. Base, T. F. Magnera, J. Michl, Rigid-rod oligo-*p*-carboranes for molecular tinkertoys. An inorganic Langmuir-Blodgett film with a functionalized outer surface, *J. Am. Chem. Soc.*, **1992**, *114*, 9721–9722.
47. W. Jiang, D. E. Harwell, M. D. Mortimer, C. B. Knobler, M. F. Hawthorne, Palladium-catalyzed coupling of ethynylated *p*-carborane derivatives: Synthesis and structural characterization of modular ethynylated *p*-carborane molecules, *Inorg. Chem.*, **1996**, *35*, 4355–4389.
48. T. Sasaki, J. M. Tour, Synthesis of a new photoactive nanovehicle: A nanoworm, *Org. Lett.*, **2008**, *10*, 897–900.
49. J. F. Morin, T. Sasaki, Y. Shirai, J. M. Guerrero, J. M. Tour, Synthetic routes toward carborane-wheeled nanocars, *J. Org. Chem.*, **2007**, *72*, 9481–9490.
50. D. G. Allis, J. T. Spencer, Polyhedral-based nonlinear optical materials: part 1. Theoretical investigation of some new high nonlinear optical response compounds involving carboranes and charged aromatic donors and acceptors, *J. Organomet. Chem.*, **2000**, *614*, 309–313.
51. S. P. Fisher, A. W. Tomich, S. O. Lovera, J. F. Kleinsasser, J. Guo, M. J. Asay, H. M. Nelson, V. Lavallo, Nonclassical applications of *closo*-carborane anions: From main group chemistry and catalysis to energy storage, *Chem. Rev.*, **2019**, *119*, 8262–8290.
52. (a) P. J. Collings, J. S. Patel, Handbook of liquid crystal research, **1997**; (b) J. W. Goodby, P. J. Collings, T. Kato, C. Tschierske, H. Gleeson, P. Raynes, V. Vill, Chemical structure and mesogenic properties, Handbook of liquid crystals, John Wiley & Sons, **2014**.
53. E. Priestly, Introduction to liquid crystals, Springer Science & Business Media, **2012**.
54. S. Kumar, Chemistry of discotic liquid crystals: From monomers to polymers, CRC press, **2016**.

55. H. K. Bisoyi, Q. Li, Liquid crystals: versatile self-organized smart soft materials, *Chem. Rev.*, **2021**, *122*, 4887–4926.

56. I. C. Khoo, Liquid crystals, John Wiley & Sons, **2022**.

57. P. G. De Gennes, J. Prost, The physics of liquid crystals, (No.83), Oxford University Press, **1993**.

58. (a) M. Schadt, Liquid crystal materials and liquid crystal displays, *Annu. rev. mater. sci.*, **1997**, *27*, 305–379; (b) B. Bahadur, Liquid crystal displays, *Mol. Cryst.*, **1984**, *109*, 3–93; (c) E. Lueder, P. Knoll, S. H. Lee, Liquid crystal displays: Addressing schemes and electro-optical effects, John Wiley & Sons, **2022**.

59. (a) G. Meier, E. Sackmann, J. G. Grabmaier, Applications of liquid crystals, Springer Science & Business Media, **2012**; (b) J. P. Lagerwall, G. Scalia, A new era for liquid crystal research: Applications of liquid crystals in soft matter nano-, bio-, and microtechnology, *Curr. Appl. Phys.*, **2012,** *12*, 1387–1412.

60. T. Kato, J. Uchida, T. Ichikawa, T. Sakamoto, Functional liquid crystals towards the next generation of materials, *Angew. Chem. Int. Ed.*, **2018**, *57*, 4355–4371.

61. S. J. Woltman, G. D. Jay, G. P. Crawford, Liquid-crystal materials find a new order in biomedical applications, *Nat. mater.*, **2007**, *6*, 929–938.

62. M. Kumar, S. Kumar, Liquid crystals in photovoltaics: A new generation of organic photovoltaics, *Polym. J.*, **2017**, *49*, 85–111.

63. (a) K. Binnemans, Ionic liquid crystals, *Chem. Rev.* **2005**, *105*, 4148–4204; (b) K. V. Axenov, S. Laschat, Thermotropic ionic liquid crystals, *Materials*, **2011**, *4*, 206–259.

64. (a) N. Kapernaum, A. Lange, M. Ebert, M. A. Grunwald, C. Haege, S. Marino, A. Zens, A. Taubert, F. Giesselmann, S. Laschat, Current topics in ionic liquid crystals, *ChemPlusChem*,

2022, *87*, 202100397, (b) K. Goossens, K. Lava, C. W. Bielawski, K. Binnemans, Ionic liquid crystals: Versatile materials, *Chem. Rev.*, **2016**, *116*, 4643–4807.

65. P. Kaszyński, *closo*-Boranes as structural elements for liquid crystals, *Boron Science: New Technologies and Applications*, **2016**, 319–353.
66. B. Ringstrand, J. Vroman, D. Jensen, A. Januszko, P. Kaszyński, J. Dziaduszek, W. Drzewinski, Comparative studies of three- and four-ring mesogenic esters containing *p*-carborane, bicyclo[2.2.2]octane, cyclohexane, and benzene, *Liq. Cryst.*, **2005**, *32*, 1061–1070.
67. A. Jankowiak, P. Kaszyński, Practical synthesis of 1,12-difunctionalized *o*-carborane for the investigation of polar liquid crystals, *Inorg. Chem.*, **2014**, *53*, 8762–8769.
68. D. Pociecha, K. Ohta, A. Januszko, P. Kaszyński, Y. Endo, Symmetric bent-core mesogens with *m*-carborane and adamantane as the central units, *J. Mater. Chem.*, **2008**, *18*, 2978–2982.
69. A. Jankowiak, A. Baliński, J. E. Harvey, K. Mason, A. Januszko, P. Kaszyński, V. G. Young, A. Persoons, [*closo*-$B_{10}H_{10}$]$^{2-}$ as a structural element for quadrupolar liquid crystals: A new class of liquid crystalline NLO chromophores, *J. Mater. Chem. C*, **2013**, *1*, 1144–1159.
70. M. O. Ali, D. Pociecha, J. Wojciechowski, I. Novozhilova, A. C. Friedli, P. Kaszyński, Highly quadrupolar derivatives of the [*closo*-$B_{10}H_{10}$]$^{2-}$ anion: investigation of liquid crystalline polymorphism in an homologous series of 1,10-bis(4-alkoxypyridinium) zwitterions, *J. Organomet. Chem.*, **2018**, *865*, 226–233.
71. R. Jakubowski, J. Pecyna, M. O. Ali, A. Pietrzak, A. C. Friedli, P. Kaszyński, Polar derivatives of [*closo*-1-CB_9H_{10}]$^-$ and [*closo*-1-$CB_{11}H_{12}$]$^-$ anions as high $\Delta\varepsilon$ additives to a nematic host: A comparison of the CH_2CH_2 and COO linking groups, *Dalton Trans.*, **2021**, *50*, 3671–3681.
72. B. Ringstrand, P. Kaszyński, Functionalization of the [*closo*-1-CB_9H_{10}]$^-$ anion for the construction of new classes of liquid crystals, *Acc. Chem. Res.*, **2013**, *46*, 214–225.

73. B. Ringstrand, P. Kaszyński, High Δε nematic liquid crystals: Fluxional zwitterions of the [*closo*-1-CB_9H_{10}]$^-$ cluster, *J. Mater. Chem.*, **2011**, *21*, 90–95.

74. J. Pecyna, P. Kaszyński, B. Ringstrand, M. Bremer, Investigation of high Δε derivatives of the [*closo*-1-CB_9H_{10}]$^-$ anion for liquid crystal display applications, *J. Mater. Chem. C*, **2014**, *2*, 2956–2964.

75. J. Pecyna, R. Żurawiński, P. Kaszyński, D. Pociecha, P. Zagórski, S. Pakhomov, Polar liquid crystals derived from sulfonium zwitterions of the [*closo*-1-$CB_{11}H_{12}$]$^-$ anion, *Eur. J. Inorg. Chem.*, **2016**, *18*, 2923–2931.

76. B. Ringstrand, H. Monobe, P. Kaszyński, Anion-driven mesogenicity: Ionic liquid crystals based on the [*closo*-1-CB_9H_{10}]$^-$ cluster, *J. Mater. Chem.*, **2009**, *19*, 4805–4812.

77. B. Ringstrand, A. Jankowiak, L. E. Johnson, P. Kaszyński, D. Pociecha, E. Gorecka, Anion-driven mesogenicity: A comparative study of ionic liquid crystals based on the [*closo*-1-CB_9H_{10}]$^-$ and [*closo*-1-$CB_{11}H_{12}$]$^-$ clusters, *J. Mater. Chem.*, **2012**, *22*, 4874–4880.

78. R. Jakubowski, A. Pietrzak, A. C. Friedli, P. Kaszyński, C(1)-Phenethyl derivatives of [*closo*-1-$CB_{11}H_{12}$]$^-$ and [*closo*-1-CB_9H_{10}]$^-$ anions: Difunctional building blocks for molecular materials, *Eur. J. Chem.*, **2020**, *26*, 17481–17494.

79. P. Kaszyński, *closo*-Boranes as π structural elements for advanced anisotropic materials, Vol. 798, ACS symposium series, Washington, D. C. **2001.**

80. S. Pakhomov, P. Kaszyński, V. G. Young Jr., 10-Vertex *closo*-boranes as potential π linkers for electronic materials, *Inorg. Chem.*, **2000**, *39*, 2243–2245.

81. P. Kaszyński, S. Pakhomov, V. G. Young Jr., Investigation of electronic interaction between *closo*-boranes and triple-bonded substituents, *Collect. Czech. Chem. Commun.*, **2002**, *67*, 1061–1083.

GOALS AND OBJECTIVES

The overall goal of this PhD Dissertation was to develop self-organizing molecular materials based on boron clusters specifically designed for modern technological needs in energy storage and conversion. This Dissertation is divided into two parts, namely Part A and Part B, each focusing on separate aspects of this program.

The 1,10-difunctional derivatives of the [*closo*-$B_{10}H_{10}$]$^{2-}$ anion are attractive for the synthesis of self-organizing rod-like materials with controlled electronic properties, photophysical behavior, and the degree of intramolecular electronic interactions. Part A of the Dissertation investigated the fundamental chemistry of the 1,10-difunctionalized derivatives of the *closo*-decaborate anion [*closo*-$B_{10}H_{10}$]$^{2-}$ in order to facilitate the development of new ionic functional materials. The main objective was to investigate the bis-phenyliodonium zwitterion [*closo*-$B_{10}H_8$-1,10-$(IPh)_2$] as a convenient precursor for the efficient synthesis of the known dicarboxylic acid derivative [*closo*-$B_{10}H_8$-1,10-$(COOH)_2$]$^{2-}$ and the unknown dihydroxy derivative [*closo*-$B_{10}H_8$-1,10-$(OH)_2$]$^{2-}$ and their utilization as building blocks for the design of novel ionic liquid crystal materials with tunable intermolecular charge transfer. Tunability of the intermolecular charge in ILCs was achieved by modifying the energies of the HOMO of the anion and the LUMO of the cation by judicious choice of the substituents. Nanosegregation of the charged and aliphatic apolar regions in the ordered phase of ILCs can facilitate charge transport, and they are suitable for use in photovoltaics.

Boron clusters are advantageous for use as lithium salts in electrolytes due to their improved performance. Part B of the Dissertation focused on a project funded by the European Space Agency (ESA) for the development of electrolytes for use in lithium-ion battery applications in space

exploration. The main goal of the project was to obtain a parallelly aligned liquid crystalline solid polymer electrolyte based on a [*closo*-1-$CB_{11}H_{12}$]$^-$ anion derivative with enhanced ion mobility through the formation of ion conducting channels and planes and to test its performance in a CR2032 type coin cell battery. In order to achieve this, a new LC electrolyte system was investigated, in which the anion of the Li^+ salt is a 1,12-disubstituted [*closo*-$CB_{11}H_{12}$]$^-$ derivative that is structurally similar to the molecules of the LC host, exhibiting smectic C and nematic phases. This project involved several stages of development, including extensive synthesis and characterization of the liquid crystalline electrolyte samples, parallel alignment of the electrolyte samples using different surface treatment methods, photopolymerization of the parallelly aligned liquid crystalline electrolytes to generate the solid polymer electrolyte films, and finally cell assembly and battery testing.

PART A

Development of novel functional materials based on 1,10-disubstituted [*closo*-$B_{10}H_{10}]^{2-}$ anion derivatives

Part A of the Dissertation is dedicated to the fundamental chemistry of the *closo*-decaborate anion ([*closo*-$B_{10}H_{10}]^{2-}$) and its utilization in the design of novel ionic functional materials with tunable photophysical behavior. Since the [*closo*-$B_{10}H_{10}]^{2-}$ anion is the main focus of this part of the Dissertation, it begins with a review (Chapter A1) which discusses recent developments in the synthesis of 1,10-disubstituted derivates of the anion in the context of application in material science. Chapter A2 deals with the synthesis, structural analysis, and functional group interconversions of [*closo*-$B_{10}H_{10}]^{2-}$ derivatives. The synthesis and photophysical properties of a series of photoactive ionic liquid crystalline derivatives based on the [*closo*-$B_{10}H_{10}]^{2-}$ anion are described in Chapter A3.

CHAPTER A1

Chemistry of the 1,10-disubstituted derivatives of the *closo*-decaborate anion ([*closo*-$B_{10}H_{10}$]$^{2-}$)

1.1 Introduction

The unique properties of the boron clusters [1-4] make them attractive structural elements for the development of functional materials with properties that could be used in modern technological applications, such as NLO materials [5-9], π linkers in molecular electronics [10], and photovoltaics [11]. Among them, the *closo*-decaborate anion, [*closo*-$B_{10}H_{10}$]$^{2-}$ (**A**, Figure 1) is exceptional [1,2] and over the last six decades since its first synthesis [12] by Hawthrone and Pitochelli in 1959, derivatives of the anion **A** have been the subject of many investigations and revealed many unique properties of the cluster. It has the D_{4d} molecular symmetry and exhibits 3D σ-aromaticity [2-4,13,14]. The structure of the bicapped square antiprism with 5-coordinated apical and 6-coordinated equatorial boron atoms contains three-center two-electron bonds [15]. The two negative charges in the cluster are fully delocalized through its three-dimensional σ framework, which makes the cluster nucleophilic. As a consequence, the exo-polyhedral hydrogen atoms can be replaced by various electrophilic substituents. The high laying HOMO (Figure 1) [5], orbital symmetry, and its energy level make the anion **A** interactive with the apical π-substituents [5,10,16]. Therefore, the 1,10-disubstituted derivatives of the anion **A** are attractive for the synthesis of functional materials with controlled electronic properties, photophysical behavior, the degree of intramolecular electronic interactions, and charge transfer.

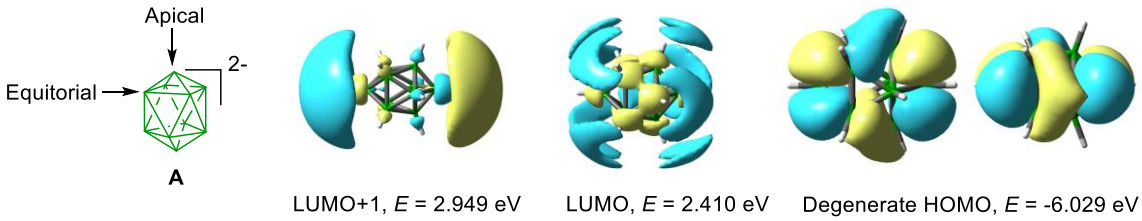

Figure 1. Structure of the *closo*-decaborate anion with selected MO contours and energies obtained at the CAM-B3LYP/def2TZVP//B3LYP/def2TZVP level of theory in CH_2Cl_2 dielectric medium.

Until recently, 1,10-difunctionalization of anion **A** was poorly developed, while materials containing this structural element potentially offer several new properties. Access to derivatives of the [*closo*-$B_{10}H_{10}$]$^{2-}$ anion (**A**) with apical substituents is difficult because most substitution reactions take place almost exclusively at the equatorial position leading to [*closo*-$B_{10}H_9$-2-X]$^{2-}$ derivatives [1,2,17]. The mechanism of the substitution reaction (electrophilic, radical, or electrophile-induced nucleophilic substitution) and electron density distribution within the cluster determine the formation of the substitution product, whether it is equatorially or apically substituted. Due to this reason, the introduction of the first substituent can lead to a mixture of isomeric products.

During the 1960s, work by Knoth gave access to the dinitrogen derivative [*closo*-$B_{10}H_8$-1,10-$(N_2)_2$] (**I**), which was the first practical precursor to 1,10-difunctional derivatives of the [*closo*-$B_{10}H_{10}$]$^{2-}$ cluster (Scheme 1) [18,19]. This dinitrogen derivative **I** was prepared in 15-25% yield by treating anion **A** with excess of nitrous acid followed by the reduction of the resulting intermediate with $NaBH_4$ in methanol or with zinc and hydrochloric acid. This method has the drawback of forming an explosive intermediate and a low overall yield of 15-25% due to the formation of undesired and unstable equatorial isomers. Similar to other derivatives of the anion **A**, derivative **I** was also found to exhibit hydrolytic and oxidative stability unusual for a boron hydride derivative.

It is a colorless, crystalline solid, stable towards air, water, dilute acid and base, and is not oxidized by alcoholic silver nitrate. It sublimes readily at 100 °C *in vacuo* and is soluble in common organic solvents, including benzene. It begins to decompose at about 125 °C in a sealed tube [18]. N_2 groups in **I** were efficiently replaced by variety of nucleophiles, such as NH_3, pyridines, and CO to yield the corresponding 1,10-disubstituted products with the general structure **1** [9,18,19].

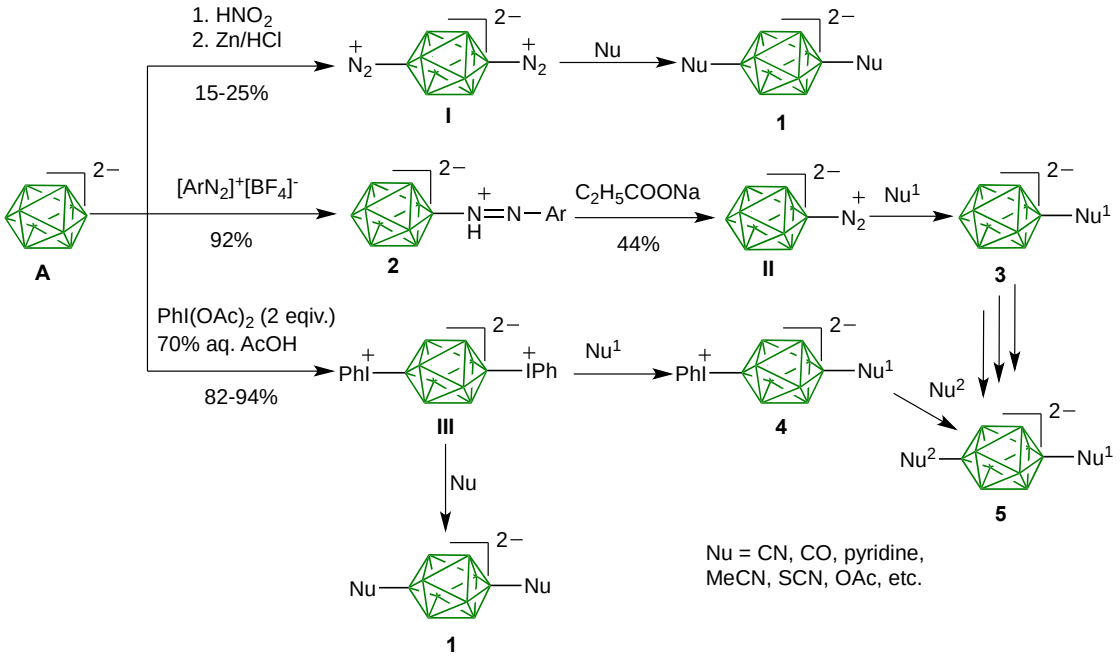

Scheme 1. General methods for the synthesis of 1,10-disubstituted derivatives of the [*closo*-$B_{10}H_{10}]^{2-}$ anion.

In 1965, Hawthorne *et al.* reported a facile azo coupling reaction between anion **A** and aryl diazonium cation to form the apically substituted azo-dye [*closo*-$B_{10}H_9$-1-NH=N-Ar]$^-$ (**2**, Scheme 1) [20,21]. Thus, a reaction of aryldiazonium tetrafluoroborates or hexafluorophosphates with anion **A** in acetonitrile solutions gave the corresponding apically substituted azobenzene derivatives **2** up to 92% yield (Scheme 1). These derivatives were found to be highly colored dyes.

Intramolecular charge transfer in azobenzene dyes was investigated and solvent and substituent effects were determined. Azo-dye **2** was easily converted to the monodinitrogen derivative [*closo*-$B_{10}H_9$-1-N_2]$^-$ (**II**) by treating it with sodium propionate in acetonitrile, which served as a general intermediate for the mono- and heterodisubstituted derivatives (general structures **3** and **5** respectively, in Scheme 1) of anion **A** by sequential introduction of the substituents at the apical positions.

For the next few decades, not much progress has been made in the chemistry of the apically substituted derivatives of the anion **A** and it has remained unexplored, mainly due to the difficulties with introducing of functional groups at the apical positions, demanding reaction conditions, and low yields.

A recent discovery by Kaszyński *et al*. has solved this long-standing problem and provided a convenient and general method for the regioselective functionalization of the anion **A** exclusively at the apical position through the bis-phenyliodonium zwitterion [*closo*-$B_{10}H_8$-1,10-$(IPh)_2$] (**III**, Scheme 1) [22]. The zwitterion **III** was synthesized by reacting a solution of [*closo*-$B_{10}H_{10}]^{2-}$ 2$[NH_4]^+$ (**A[NH₄]**) with solid $PhI(OAc)_2$ in 70% aqueous acetic acid. Analysis of the reaction mixture revealed that $[PhI]^+$ electrophile is fully selective for the apical position of the anion **A** and **III** was obtained in 82-90% yield as the sole product. Derivative **III** appeared to be stable and did not show any decomposition under ambient conditions over several months. Similarly, mono-phenyliodonium derivative **IV** was obtained in 60-65% yield by reacting $PhI(OAc)_2$ with a solution of **A[NH₄]** in 30% aqueous acetic acid [23]. Here, the selectivity for the mono-phenyliodination of **A** was achieved by controlling the concentration of acetic acid, which in turn affected the solubility of the derivative **IV** formed in the reaction medium: it precipitates before being reacted with another equivalent of $[PhI]^+$.

In contrast to the formation of monodinitrogen intermediate **II**, the electrophilic phenyliodine species, such as $PhI(OAc)_2$, was found to be the most selective electrophile exclusively giving the apically substituted product, and consequently, high yields of **III**. The main difference between the two methods lies in selectivity of the electrophilic substitution of the anion and also in the mechanism of the replacement of the leaving group in the intermediate. Thus, the substitution of the N_2 group in **I** involves heterolysis of the N–B bond and formation of highly reactive boronium ylide **6**, which is trapped with a nucleophile. Consequently, this mechanism is an analogous to that of S_N1 reaction. In contrast, the substitution of the nucleophile in phenyliodonium zwitterion **IV** proceeds through the heterolysis of the I–B bond and formation of boronium ylide **6,** formation of the 10-I-3 intermediate **7**, or by the formation of 9-I-2 intermediate **8**. depending on the reaction conditions and nature of the nucleophile (Figure 2) [22]. Charge nucleophiles, such as CN^- and AcO^-, and weak nucleophiles, such as MeCN and thiane, react with **IV**, the reactions proceed through the formation of 10-I-3 intermediate and boronium ylide, respectively, to yield the corresponding substituted product **3**. Phenyliodonium zwitterion **IV** efficiently undergoes SET from the Grignard reagent, resulting in the iodo derivative **9**.

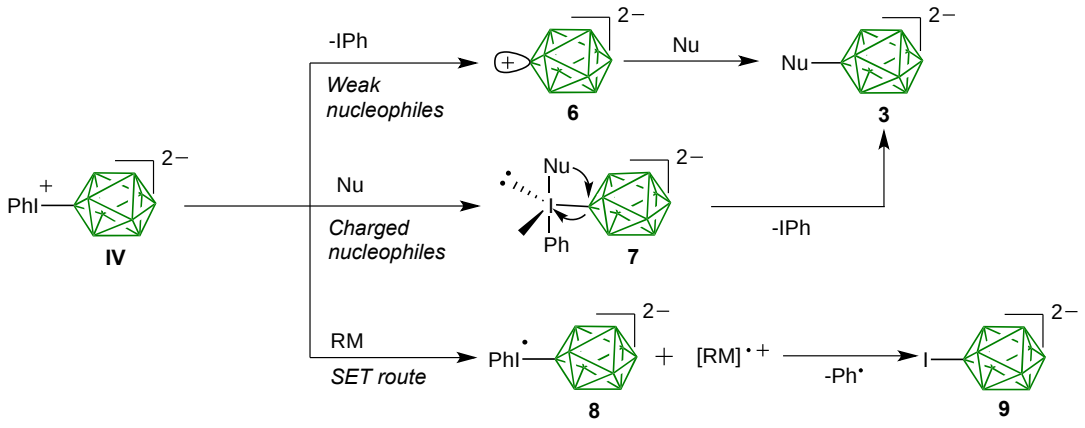

Figure 2. Possible pathways for phenyliodonium group replacement with nucleophiles in **IV**.

The reactions of zwitterions **I** and **III** with various nucleophiles provided pyridinium [9,24], sulfonium [24], carbonyl [18,25], nitrile [26], and other derivatives [21,23,27,28]. These derivatives gave unprecedented access to functionalized *closo*-borate and new classes of materials, such as liquid crystals [9,24,27], photonic materials [28], and metal complexes [29].

So far, reviews on the chemistry of anion **A** summarized various synthetic methods for obtaining the parent anion, its properties, salts and complexes, and the exo-polyhedral substitution of various atoms and groups on the boron cluster [1,30,31]. This review exclusively concentrates on the progress made in the chemistry of the 1,10-disubstituted derivatives of the anion **A** and their properties.

1.2 Preparation and reactivity of 1,10-disubstituted functional group derivatives

1.2.1 Derivatives with the Boron-Carbon bond

Until now, several derivatives of the anion **A** with a carbon atom substituted at the apical positions have been prepared and 1,10-dicarbonyl derivative [*closo*-$B_{10}H_8$-l,10-$(CO)_2$] (**10**) is among the first such derivatives. Initially, this derivative was obtained in 55-75% yield by the S_N-1-type displacement of the N_2 groups in [*closo*-$B_{10}H_8$-1,10-$(N_2)_2$] (**I**) by carbon monoxide under 140 °C and 1000 atm pressure (Scheme 2) [18,19]. This derivative is a formal anhydride of the diacid [*closo*-$B_{10}H_8$-1,10-$(COOH)_2]^{2-}$ (**11**), a potentially useful building block for a variety of materials. In water, the carbonyls in **10** are found to be in equilibrium with the carboxyl group. Also, reactions of **10** with amines and alcohols gave the corresponding amides (**12**) and esters (**13**) respectively (Scheme 2) [18].

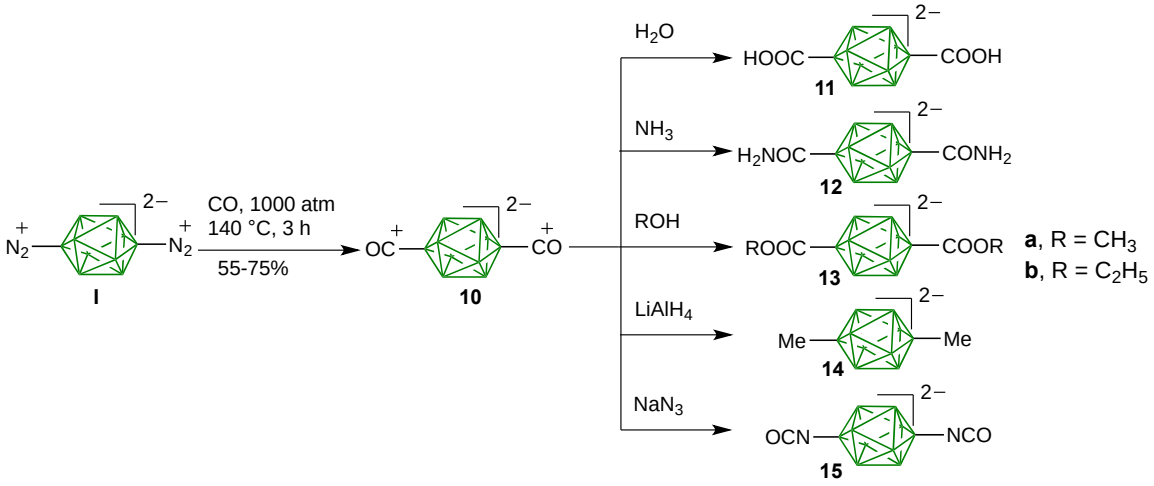

Scheme 2. Synthesis of [*closo*-$B_{10}H_8$-l,10-$(CO)_2$] (**10**) from [*closo*-$B_{10}H_8$-1,10-$(N_2)_2$] (**I**) and its reactions [18].

Interestingly, reduction of **10** using $LiAlH_4$ resulted in the 1,10-dimethyl derivative **14** (Scheme 2). Isocyanate derivative **15** was obtained by treating derivative **10** with NaN_3. Unfortunately, accessibility of the 1,10-dicarbonyl derivative **10** using this method is limited by high-pressure conditions (1000 atm) for its synthesis and low overall yields of 10-15%.

A recent work has solved this long-standing problem and provided a convenient access to the 1,10-dicarbonyl derivative **10** and the diacid **11** using the readily available dinitrile derivative [*closo*-$B_{10}H_8$-1,10-$(CN)_2$]$^{2-}$ (**16**, Scheme 3) [25]. An initial attempt to prepare the diacid **11** through the hydrolysis of dinitrile **16** was not successful due to the high electron density on the CN group and its low electrophilicity [26]. However, *N*-methylation of **16** with CF_3SO_3Me occurred smoothly and the resulting bis-zwitterion [*closo*-$B_{10}H_8$-1,10-$(CNMe)_2$] (**17**) was easily hydrolyzed in a two-step process to give the diacid **11** in a 30% overall yield [25], which is almost a double of the previous method [18]. Zwitterionic acid anhydride **10** was obtained, when a solution of diacid **11** was passed through an ion-exchange resin followed by evaporation of the solution to

dryness. The resulting acid anhydride **10** in a reaction with NaOEt in EtOH gave the known diethyl ester **13b** in 62% overall yield. However, this ester was found to be hydrolytically unstable.

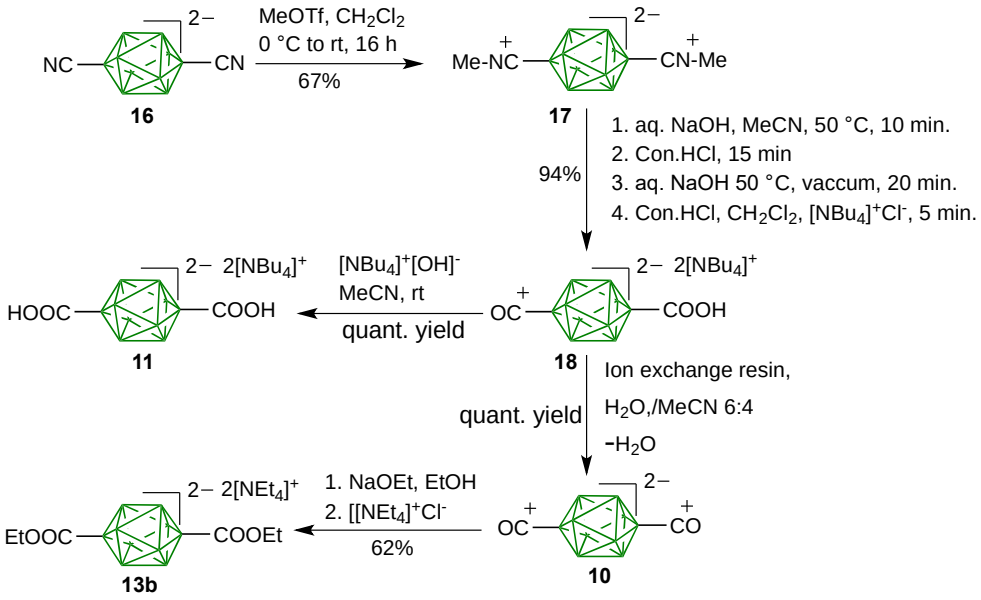

Scheme 3. Synthesis of acid **11** and carbonyl derivative **10** from [*closo*-$B_{10}H_8$-1,10-$(CN)_2$]$^{2-}$ (**16**) [25].

Furthermore, the addition of methylamine to zwitterion **17** cleanly gave the bis-ylide **19** in 76% yield (Scheme 4). Crystal structures for several of these derivatives were obtained using single-crystal XRD [25].

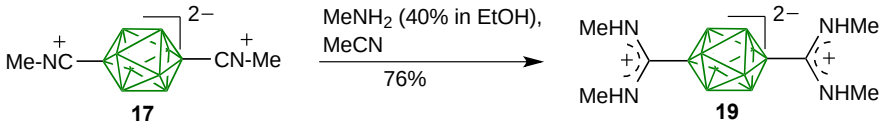

Scheme 4. Reaction of [*closo*-$B_{10}H_8$-1,10-$(CNMe)_2$] (**17**) with methylamine [25].

The dinitrile derivative [*closo*-$B_{10}H_8$-1,10-$(CN)_2$]$^{2-}$ (**16**) was efficiently synthesized in 62–67% yield by the reaction of the bis-phenyliodonium derivative **III** with $[NEt_4]^+CN^-$ in MeCN (Scheme 5) [26]. The solubility of the [*closo*-$B_{10}H_8$-1,10-$(CN)_2$]$^{2-}$ $2[NEt_4]^+$ (**16[NEt$_4$]**) salt in

organic solvents was improved by exchanging the $[NEt_4]^+$ cation for $[NBu_4]^+$ using Dowex exchange resin.

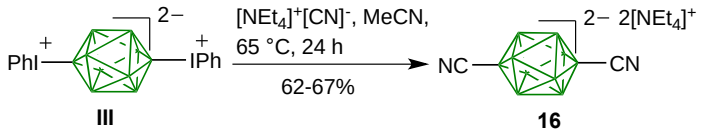

Scheme 5. Synthesis of the $[closo\text{-}B_{10}H_8\text{-}1,10\text{-}(CN)_2]^{2-}$ derivative (**16**) [26].

Dinitrile **16** was surprisingly resistant to hydrolysis and found to be unaffected on most classical reaction conditions. Stronger reducing reagents such as $LiAlH_4$, $NaBH_4$-$BF_3{\cdot}Et_2O$, and $LiAlH_4$–$BF_3{\cdot}Et_2O$ gave partial conversion of the dinitrile to a complex mixture of products. The inertness of the C≡N groups in **16** was ascribed to the extensive delocalization of the negative charge from the $\{closo\text{-}B_{10}\}^{2-}$ cluster. The availability of high negative charge density on the C≡N bond has been explored in the context of metal complexes (see section 1.6: Metal complexes based on $[closo\text{-}B_{10}H_{10}]^{2-}$ anion). Single-crystal XRD analysis of $[closo\text{-}B_{10}H_8\text{-}1,10\text{-}(CN)_2]^{2-}$ $2[NPr_4]^+$ (**16[NPr$_4$]**) provided more insight into the molecular structure of this derivative [26].

Derivatives of the anion **A** with aryl substituents at the apical positions were obtained by the Pd(0)-catalyzed cross-coupling reactions of $[closo\text{-}B_{10}H_8\text{-}1,10\text{-}I_2]^{2-}$ (**20**) and $[closo\text{-}B_{10}H_9\text{-}1\text{-}I]^{2-}$ (**9**). Thus, a reaction of **20** with 4-$MeOC_6H_4MgBr$ in the presence of 2 mol% PEPPSI-IPr catalyst gave the 1,10-diaryl derivatives $[closo\text{-}B_{10}H_8\text{-}1,10\text{-}(C_6H_4OR)_2]^{2-}$ (**21**) in 60-75% yield (Scheme 6) [26]. Similarly, monoaryl derivative **22** was also synthesized in 75-88% yield from the iodo derivative **9** [26,27]. These aryl derivatives were explored in the context of ionic liquid crystalline derivatives (see section 1.4: Self-organizing materials based on the $[closo\text{-}B_{10}H_{10}]^{2-}$ anion).

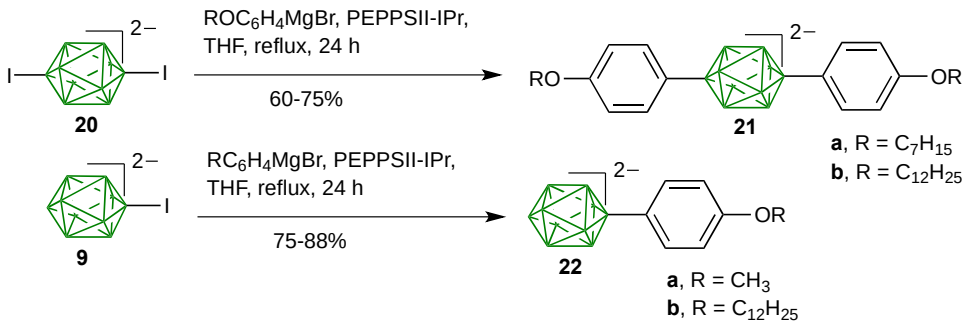

Scheme 6. Synthesis of the aryl derivatives of anion **A** [27].

1.2.2 Derivatives with the Boron-Oxygen bond

Monosubstituted hydroxy derivative [*closo*-$B_{10}H_9$-1-OH]$^{2-}$ (**23**) was obtained by heating an aqueous solution of [*closo*-$B_{10}H_9$-1-N_2]$^{-}$ (**II**) and NaOH. However, some amounts of $[B(OH)_4]^-$ were also formed as a product of cage degradation. This was overcome by carrying out the reaction in a mild alkaline aqueous solution of NaF, and triphenylbenzylphosphonium salt of the hydroxy derivative **23** was isolated in 83% yield (Scheme 7) [32].

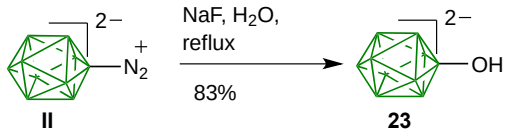

Scheme 7. Synthesis of the monohydroxy derivative [*closo*-$B_{10}H_9$-1-OH]$^{2-}$ (**23**) [32].

Apical dihydroxy derivative [*closo*-$B_{10}H_8$-1,10-$(OH)_2$]$^{2-}$ (**26**) remained unknown until a recent work demonstrated a convenient and efficient preparation of this derivative starting with bis-phenyliodonium zwitterion [*closo*-$B_{10}H_8$-1,10-$(IPh)_2$] (**III**, Scheme 8) [26]. Thus, thermolysis of **III** in DMF gave the bis-DMF adduct [*closo*-$B_{10}H_8$-1,10-$(OCHNMe_2)_2$] (**24a**) isolated in 72–80% yield, which upon hydrolysis with aqueous $[NBu_4]^+[OH]^-$ in MeCN yielded the formate ester [*closo*-$B_{10}H_8$-1,10-$(OCHO)_2$]$^{2-}$ (**25a**) instead of the expected dihydroxy derivative. Further experiments revealed the inertness of **25a** to solutions of KOH in MeOH/H_2O. Finally, treatment

of **25a** with diluted HCl in MeOH gave the dihydroxy derivative obtained in the protonated form [*closo*-$B_{10}H_8$-1,10-$(OH_2)_2$] (**26-2H**) in 68–72% yield (Scheme 8). The solid-state structure of derivatives **24a**, **25a**, and **26-2H** were determined by single-crystal X-ray analysis. Analysis of the experimental C=O vibrational frequencies showed a markedly lower force constant in **25a** than in the hydrocarbon analogs, which was well reproduced with DFT calculations [26]. This indicates an effective electronic interaction between the cluster and the substituents, which in turn lowers the bond order.

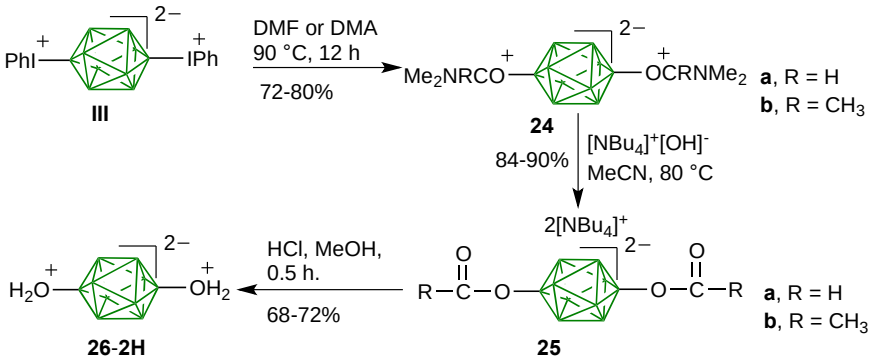

Scheme 8. Synthesis of the bis-oxonium derivative [*closo*-$B_{10}H_8$-1,10-$(OH_2)_2$] (**26-2H**) [26].

Similarly, [*closo*-$B_{10}H_8$-1,10-$(OH_2)_2$] (**26-2H**) was synthesized in comparable yields from the DMA adduct [*closo*-$B_{10}H_8$-1,10-$(OCMeNMe_2)_2$] (**24b**), which was obtained by the thermolysis of **III** in $MeCONMe_2$ (DMA, Scheme 8) [25]. Dihydroxy derivative **26** was found to be prone to oxidation and was unstable in most organic solvents. Only the solid-state of the protonated form **26-2H** was found to be stable. Its synthetic utility was demonstrated by a successful acylation reaction with C_6H_5COCl in THF in the presence of excess NaH under argon atmosphere (Scheme 9). Despite sensitivity of esters to acid, the $[NBu_4]^+$ cation in [*closo*-$B_{10}H_8$-1,10-$(OCOC_6H_5)_2]^{2-}$ $2[NBu_4]^+$ (**27a[NBu4]**) was successfully exchanged for $[NEt_4]^+$ cation using Dowex exchange resin [26].

Ester derivatives [*closo*-$B_{10}H_8$-1,10-$(OCOC_{11}H_{23})_2$]$^{2-}$ (**27b**) and [*closo*-$B_{10}H_8$-1,10-$(OCOC_6H_4OC_{12}H_{25})_2$]$^{2-}$ (**27c**) were also synthesized using the same esterification method described above (Scheme 9) [27]. All ester derivatives were found to be unstable towards acidic conditions including silica gel. Therefore, pure derivatives were obtained in about 70% and 60% yields respectively using column chromatography on basic alumina. Derivatives **27b** and **27c** were investigated as ionic liquid crystals (see section 1.4.2: Ionic liquid crystals of [*closo*-$B_{10}H_{10}$]$^{2-}$).

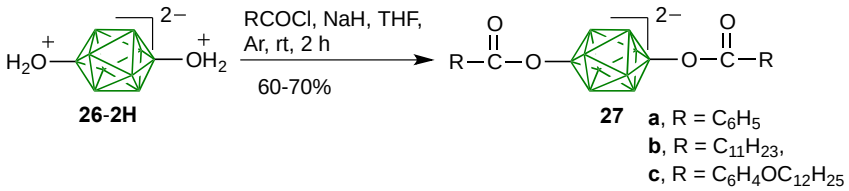

Scheme 9. Synthesis of ester derivatives from bis-oxonium derivative **26-2H** [26,27].

1.2.3 Derivatives with the Boron-Nitrogen bond

Several new compounds with the boron-nitrogen bond were synthesized from the dinitrogen derivative **I**. A variety of nucleophiles, such as ammonia, pyridine, acetonitrile, and 4-alkoxypyridine, readily displaced the dinitrogen groups in **I** to give the corresponding [*closo*-$B_{10}H_8$-l,10-$(Nu)_2$] species (structures **28**, **29**, **30**, and **31**, respectively, in Scheme 10) [18,19]. Derivative **28** on alkylative cyclization with tribromide $C_5H_{11}C(C_2H_4Br)_3$ resulted in the diquinuclidinium derivative **32** obtained in 25% yield. N–protonated diacetamide **33** was obtained by evaporating a solution of **30** in aqueous acetonitrile. Dinitrogen derivative **I**, when treated with NaN_3, gave the monosubstituted product **34**. Hydrazinium derivative **35** was obtained by refluxing a solution of **I** in 98% hydrazine.

1,10-Disubstituted 4-alkoxypyridinium (**31**) and pentylquinuclidinium (**32**) derivatives (Scheme 10) were explored in the context of liquid crystals and their thermal and physical

properties were investigated (see section 1.4.1: Zwitterionic quadrupolar liquid crystals of [*closo*-$B_{10}H_{10}]^{2-}$) [9]. Hydrolytic and thermal instability have been observed for these bis-onium derivatives. Also, these 1,10-disubstituted bis-onium derivatives were found to be configurationally unstable above 200 °C, and they rearrange into other isomers [9].

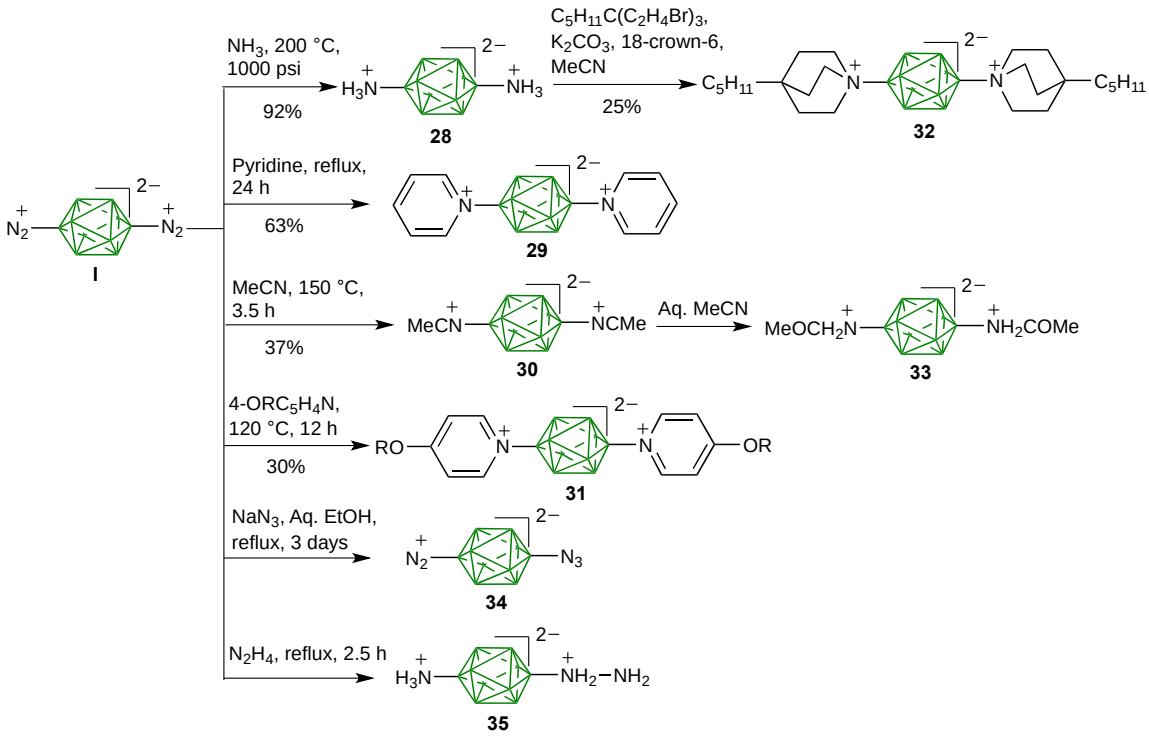

Scheme 10. Synthesis of derivatives with the boron-nitrogen bond from the dinitrogen derivative [*closo*-$B_{10}H_8$-1,10-$(N_2)_2$] (**I**) [9,18,19].

Azobenzene [*closo*-$B_{10}H_9$-1-NH=N-Ar]$^-$ (**2**) on reduction with basic zinc dust, basic hydrosulfite, or tin in acidic methanol gave the corresponding ammonium derivative [*closo*-$B_{10}H_9$-1-$NH_3]^-$ (**36**). Alkylative cyclization of **36** with tribromide $C_5H_{11}C(C_2H_4Br)_3$ provided the quinuclidinium derivative **37** in 90% yield [9]. Further reactions of the ammonium derivative **36** with a second equivalent of aryldiazonium ion resulted in the azo-dye [*closo*-$B_{10}H_9$-1-(NH_3)-10-N=NAr]$^-$ (**38**) isolated in 32% yield (Scheme 11) [20]. However, this reaction was slower compared

to the reaction of aryldiazonium ion with anion **A**, because the ammonium group in **36** renders the anion less reactive towards the electrophilic attack. Derivative **38** was isolated as an ether-soluble solid protonated both on the azo and amino groups, or as a mono anion, with only the azo group being protonated. 1,10-Diammonium derivative [*closo*-$B_{10}H_8$-1,10-$(NH_3)_2$] (**28**) was obtained in 48% yield by reduction of **38** with tin in 30:70 hydrochloric acid-methanol solvent (Scheme 11).

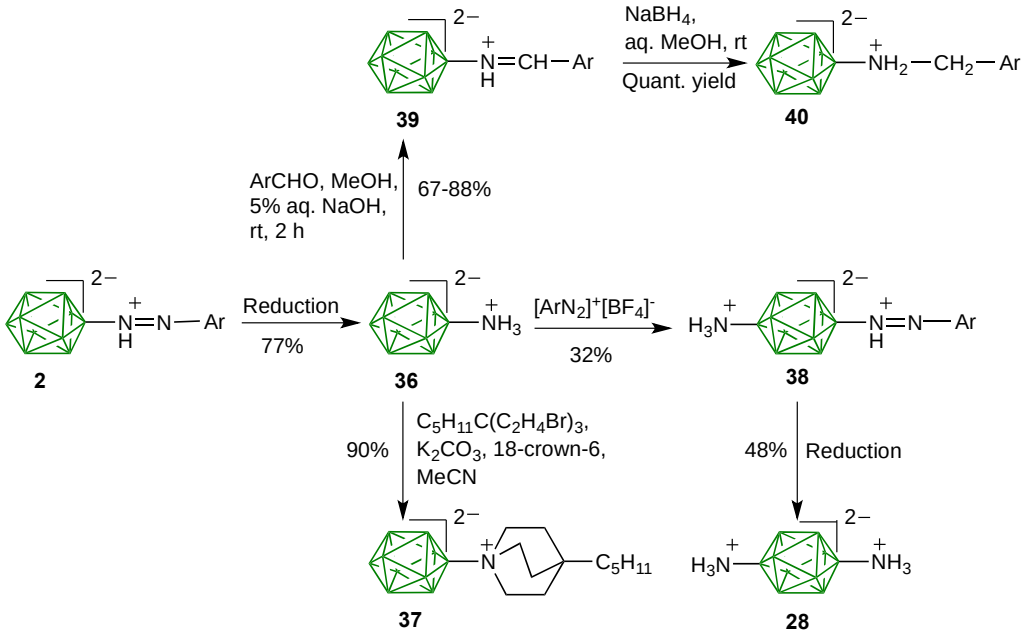

Scheme 11. Synthesis of new derivatives from azobenzene derivative [*closo*-$B_{10}H_9$-1-NH=N-Ar]$^-$ (**2**) [9,20,33].

Also, ammonium derivative **36**, on reaction with benzaldehydes ArCHO (Ar = Ph, 2-C_6H_4OMe, 4-$C_6H_4NHCOMe$), gave the corresponding Schiff bases (**39**) in 67-88% yield. Reduction of **39** with $NaBH_4$ resulted in the corresponding benzylamino derivatives (**40**) in quantitative yields (Scheme11) [33]. Derivatives **39** and **40** are important for the use in medicine [33].

A recent work demonstrated a new potential and efficient method for the synthesis of ammonium derivative **28** by basic hydrolysis of the acetamidinium zwitterion [*closo*-$B_{10}H_8$-1,10-(acetamidinium)$_2$] (**41**, Scheme 12) [34]. Acetamidinium zwitterion was obtained in 61% yield by treating [*closo*-$B_{10}H_8$-1,10-(IPh)$_2$] (**III**) with acetamidine in MeCN at 80 ^oC.

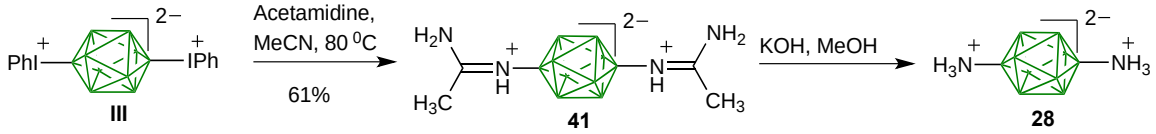

Scheme 12. Synthesis of the [*closo*-$B_{10}H_8$-1,10-$(NH_3)_2$] (**28**) [34].

Mongeot and co-workers synthesized several bulky tertiary amine derivatives from [*closo*-$B_{10}H_9$-1-N_2]$^-$ (**II**) in a two-step process (Scheme 13) [35]. Initially, derivative **II** on reaction with primary and secondary ammines resulted in the corresponding ammonium derivatives **42** and **43**, respectively. The subsequent reactions of **42** and **43** with alkyl halides resulted in the tertiary ammine derivatives **44** and **45**.

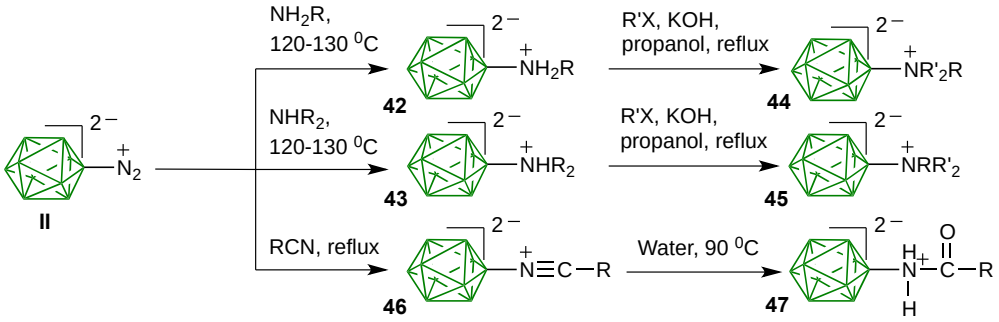

Scheme 13. Synthesis of the hydrophobic monoanions of [*closo*-$B_{10}H_{10}$]$^{2-}$ (**A**) from [*closo*-$B_{10}H_9$-1-N_2]$^-$ (**II**) [35].

They also reported the nitrile derivatives [*closo*-$B_{10}H_9$-1-NCR]$^-$ (**46**) {R = CH_3, $(C_6H_5)_2CH$} formed from a solution of derivative **II** in alkyl nitrile under reflux. These nitrile derivatives were

found to be thermally stable, however they easily hydrolyzed to [*closo*-$B_{10}H_9$-1-NH_2COR]$^-$ (**47**) in hot water (Scheme 13).

When a solution of [*closo*-$B_{10}H_{10}$]$^{2-}$ anion (**A**) in aqueous MeCN was treated with aliphatic and aromatic nitro compounds (RNO_2, where R = Et, *n*-Pr, *i*-Pr, *t*-Bu, Ph), a mixture of nitration products was formed (Scheme 14) [36]. The 1,10-disubstituted nitro derivative [*closo*-$B_{10}H_8$-1,10-$(NO_2)_2$]$^{2-}$ (**48**) was successfully isolated from the crude mixture in yields up to 7% by ion exchange chromatography on diethylaminoethyl (DEAE) cellulose support. The NMR spectrum for this derivative exhibits the characteristic pattern for 1,10-disubstituted *closo*-decaborane cluster with a strong downfield shift of the apical boron atoms at +17.3 ppm. The X-ray crystal structure was determined for this molecule. The IR and Raman spectra showed strong NO stretching vibration at 1384 and 1425 cm^{-1}.

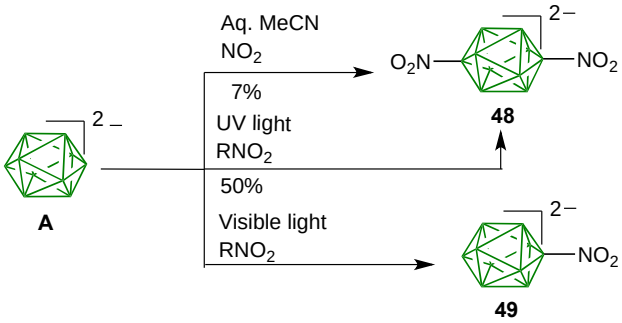

Scheme 14. Synthesis of nitro derivatives of the anion **A** [36,37].

A more selective way was found to obtain the nitro derivative of the anion **A**, which involved a radical mechanism [37]. In this method, irradiation of a solution of the [*closo*-$B_{10}H_{10}$]$^{2-}$ 2[PPh_4]$^+$ (**A[PPh_4]**) salt in nitroalkane (RNO_2, where R = Et, *n*-Pr, *i*-Pr, *t*-Bu) led to the formation of substituted derivatives and the degree of substitution depended on the radiation energy (Scheme 14). Thus, under irradiation with the visible light, the reaction gave mainly the monosubstituted product [*closo*-$B_{10}H_9$-1-NO_2]$^{2-}$ (**49**), while under irradiation with UV light, the reaction gave the

disubstituted derivative **48** isolated in approximately 50% yield. The structures of these anions were determined by X-ray crystallography [37].

1.2.4 Derivatives with the Boron-Sulfur bond

Several derivatives of the anion **A** with the boron-sulfur bonds are also known. Dimethylsulfonium derivatives [*closo*-$B_{10}H_9$-1-SMe_2]$^-$ (**50**) and [*closo*-$B_{10}H_8$-1,10-$(SMe_2)_2$] (**51**) were obtained in good yields, when hydrogen chloride was passed through a solution of anion **A** in dimethyl sulfoxide at 40-60 °C (Scheme 15) [38]. Pure dimethylsulfonium derivative **50** was isolated in 77% by separation from its equatorial isomer by recrystallization from water. Although apical substitution predominates during the synthesis of the derivative **51**, its pure form was isolated only in 56% yield by column chromatography of a crude mixture containing its 1,6-isomer. When excess dimethyl sulfoxide was used as a solvent, the ratio of these products varied with reaction time. The preferential formation of **51** in 65% yield occurs when acetic acid was used as the solvent regardless of stoichiometry or reaction time. Both derivatives **50** and **51** were found to be chemically stable towards moderate acidic and basic conditions, and neither of the zwitterions was oxidized by silver nitrate. Heating **51** at 230 °C for 45 minutes resulted in its partial rearrangement to [*closo*-$B_{10}H_8$-2,7(8)-$(SMe_2)_2$] (2.8% yield).

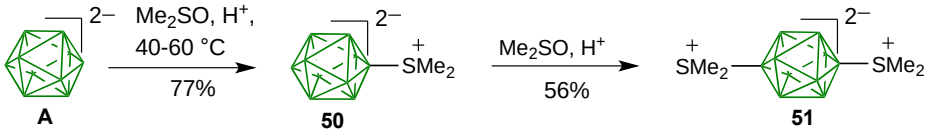

Scheme 15. Synthesis of dimethylsulfonium derivatives of the anion **A** [38].

When anion **A** was treated with equimolar amounts of $Pb(SCN)_2$ in CH_2Cl_2, a mixture of equatorially and apically monosubstituted thiocyanate (**52**) derivatives in the ratio 60:40 was obtained. Separation of the pure isomers was accomplished using an ion-exchange chromatography

on diethylaminoethyl cellulose support. The almost exclusive formation of apically disubstituted thiocyanate derivative (**53**) was observed with two equivalents of $Pb(SCN)_2$ (Scheme 16) [39].

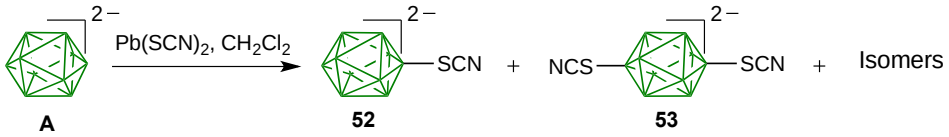

Scheme 16. Synthesis of the thiocyanate derivatives of anion **A** [39].

Another derivative to be mentioned in this section is the thiol derivative [*closo*-$B_{10}H_9$-1-SH]$^{2-}$ (**55**), which was obtained by basic hydrolysis of [*closo*-$B_{10}H_9$-1-SCH=NMe_2]$^-$ (**54**) formed by heating of [*closo*-$B_{10}H_9$-1-N_2]$^-$ (**II**) with *N*,*N*-dimethylthioformamide (Scheme 17) [40]. Thus, refluxing of a solution of derivative **54** in aqueous acetone with excess $[NMe_4]^+[OH]^-$ or aqueous CsOH for several hours gave **55** in 15% yield after fractional crystallization from hot water. S-alkylation of **55** using Me_3SI under hydrolytic condition resulted in S-methylated derivative [*closo*-$B_{10}H_9$-1-$S(CH_3)_2$]$^-$ (**50**) in 32% yield. Alkylative cyclization of **54** with dibromide derivative $C_5H_{11}CH(C_2H_4Br)_2$ under hydrolytic conditions in the presence of $[NMe_4]^+[OH]^- \cdot 5H_2O$ gave the thianium derivative **56** in 53% yield.

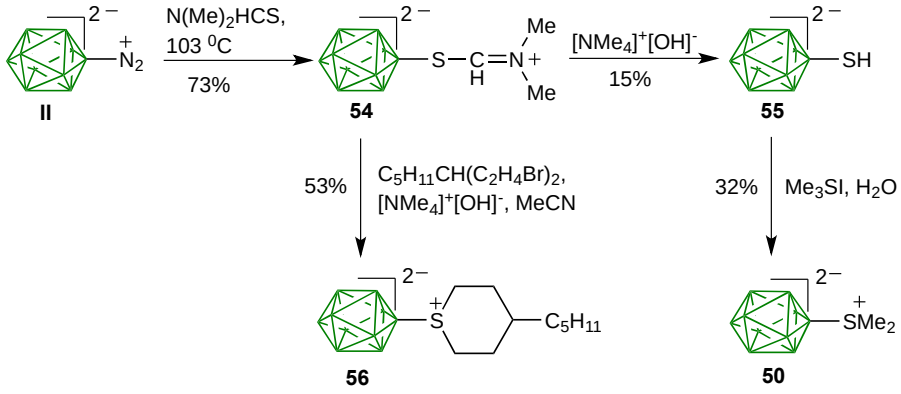

Scheme 17. Synthesis of derivatives with the boron-sulfur bond from [*closo*-$B_{10}H_9$-1-N_2]$^-$ (**II**) [9, 40].

Bis-thianium derivative [*closo*-$B_{10}H_8$-1,10-(SC_5H_4-C_5H_{11})$_2$] (**57**) was obtained in 18% yield by the thermolysis of [*closo*-$B_{10}H_8$-1,10-(N_2)$_2$] (**I**) in 4-pentylthiane (Scheme 18) [9].

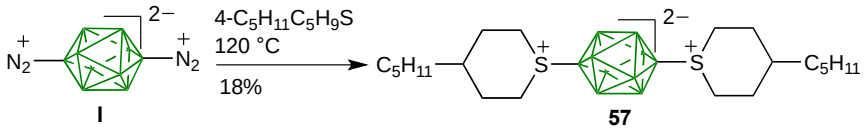

I 57

Scheme 18. Synthesis of bis-thianium derivative **57** from [*closo*-$B_{10}H_8$-1,10-(N_2)$_2$] (**I**) [9].

1.2.5 Derivatives with Boron-Halogen bond

Halogenation was one of the first attempted reactions of the [*closo*-$B_{10}H_{10}$]$^{2-}$ anion (**A**) and several halogenated derivatives have been synthesized and investigated. Most of the halogenation reactions resulted in a mixture of derivatives with different substitution levels preferably at the equatorial positions, which was separated fully or partially by tedious electrophoresis or ion-exchange chromatography [41].

Isomerically pure apically substituted iodo derivatives [*closo*-$B_{10}H_9$-1-I]$^{2-}$ (**9**) and [*closo*-$B_{10}H_8$-1,10-I_2]$^{2-}$ (**20**) were obtained in 90-95% yield by treating the corresponding phenyliodonium zwitterions [*closo*-$B_{10}H_9$-1-IPh]$^-$ (**IV**) and [*closo*-$B_{10}H_8$-1,10-(IPh)$_2$] (**III**) with *n*-BuLi in THF (Scheme 19) [23]. The solid-state structure for the [*closo*-$B_{10}H_8$-1,10-I_2]$^{2-}$ 2[NPr_4]$^+$ (**20[NPr_4]**) was determined by X-ray diffraction analysis. Iodo derivatives **9** and **20** were found to be useful synthetic precursors and they were used in Pd(0)-catalyzed cross-coupling reactions [23,27] to make new functional materials of the anion **A** (see Scheme 6).

Although iodo derivatives appear to be the only useful halogenated precursors for the 1,10-disubstituted derivatives of the anion **A** through the Pd(0)-catalyzed cross-coupling reactions, derivatives of the anion **A** substituted with fluorine, chlorine, and bromine are also known [41]. Fluorination of anion **A** resulted in a mixture of products and 1,10-disubstituted fluoro derivative

[*closo*-$B_{10}H_8$-1,10-F_2]$^{2-}$ was isolated in a low yield (3% yield). The crystal structure of [*closo*-$B_{10}H_8$-1,10-F_2]$^{2-}$ 2[Ph_4P]$^+$·3CH_2Cl_2 was determined [41a]. Chlorination and bromination of the [*closo*-$B_{10}H_{10}$]$^{2-}$ gave a complex mixture of products with different substitution level [*closo*-$B_{10}H_{10-x}Cl_x$]$^{2-}$ (x = 1-10) and [*closo*-$B_{10}H_{10-x}Br_x$]$^{2-}$ (x = 1-6). Iodination of the anion **A** resulted in a complex mixture of iodo derivatives due to the inability to control the degree of cage iodination combined with the stereochemistry of the anion [41b-41c].

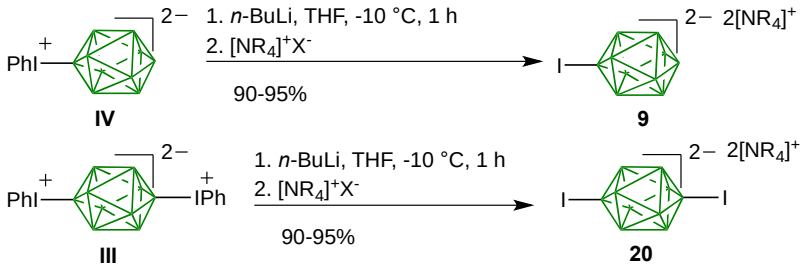

Scheme 19. Synthesis and reactions of iodo derviavtives of [*closo*-$B_{10}H_{10}$]$^{2-}$ anion [23].

1.3 Preparation of 1,10-heterodisubstituted derivatives

Heterodisubstitution at the apical positions of the [*closo*-$B_{10}H_{10}$]$^{2-}$ anion (**A**) provides more options to effectively tune the electronic properties of its derivatives. Such derivatives are expected to exhibit photophysical properties that are relevant to modern technological applications. Recent development in the *closo*-decaborate anion chemistry has provided access to a variety of such derivatives, which are unsymmetrically substituted at the apical positions via a multistep synthesis process.

Dinitrogen derivative [*closo*-$B_{10}H_8$-1-SMe_2-10-N_2] (**58**) was one of the first such derivatives synthesized. It was obtained in 30% yield by reaction of [*closo*-$B_{10}H_9$-1-SMe_2]$^-$ (**50**) with nitrous acid, followed by the reduction of the precipitated explosive intermediate with $NaBH_4$

in methanol [38]. An improved yield of 64% for the dinitrogen derivative **58** was obtained by replacing HCl with AcOH in the reaction (Scheme 20).

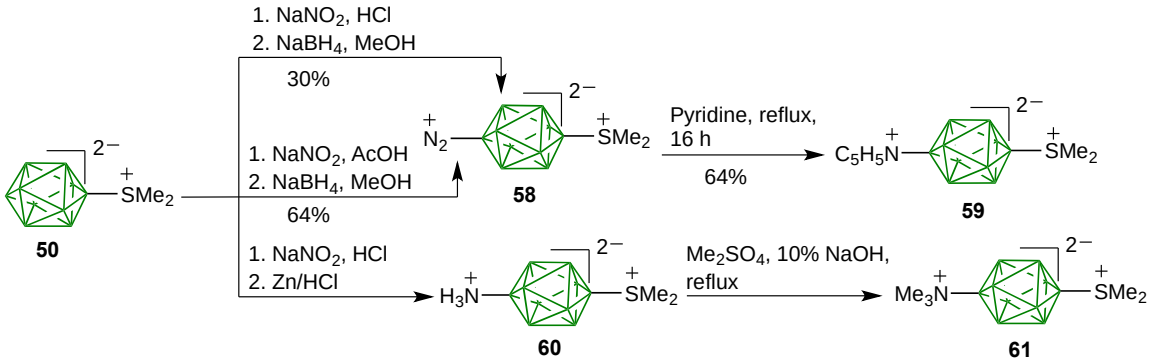

Scheme 20. Synthesis of heterodisubstituted derivatives of the [*closo*-$B_{10}H_{10}]^{2-}$ anion from [*closo*-$B_{10}H_9$-1-$SMe_2]^-$ (**50**) [38]

Derivative **58** was also obtained by treating [*closo*-$B_{10}H_9$-1-$SMe_2]^-$ with aryldiazonium salts in acetonitrile followed by treatment with sodium propionate in acetonitrile [38]. The dinitrogen in **58** was subjected to a displacement reaction to obtain derivatives such as [*closo*-$B_{10}H_8$-1-SMe_2-10-NC_5H_5] (**59**) in good yields [38]. Another derivative to be mentioned here is the ammonium derivative [*closo*-$B_{10}H_8$-1-SMe_2-10-NH_3] (**60**), which was obtained by the reduction of [*closo*-$B_{10}H_8$-1-SMe_2-10-NO] with Zn and HCl [38]. Derivative **60** on refluxing with dimethyl sulfate in the presence of 10% NaOH solution resulted in [*closo*-$B_{10}H_8$-1-SMe_2-10-NMe_3] (**61**, Scheme 20) [38].

The above two strategies for the selective preparation of apically substituted dinitrogen derivative were used for making other heterodisubstituted derivatives of the anion **A** by a sequential introduction of the substituents. In such an approach, thianium derivative **56** was diazotized to provide [*closo*-$B_{10}H_8$-1-(SC_5H_4-C_5H_{11})-10-N_2] (**62**) in 40-55% yield, which was thermolyzed with

4-alkoxypyridines at 120 °C giving heterodisubstituted derivatives [*closo*-$B_{10}H_8$-1-(SC_5H_4-C_5H_{11})-10-(NC_5H_4OR)] (**63a-63e**, Scheme 21) [9].

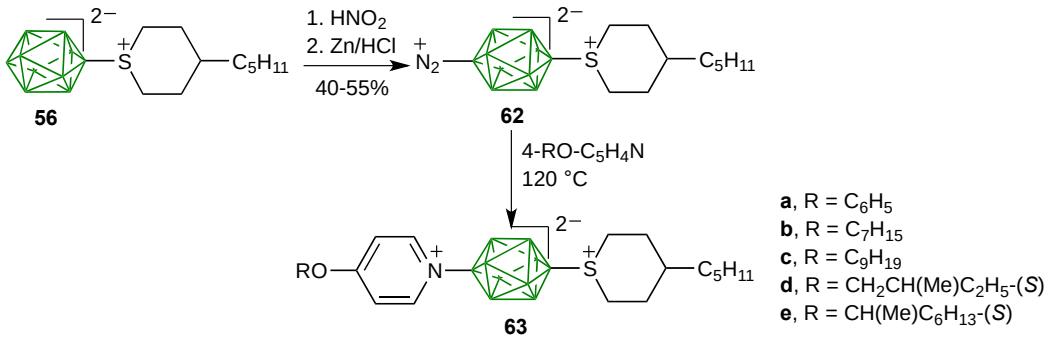

Scheme 21. Synthesis of the heterodisubstituted derivative [*closo*-$B_{10}H_8$-1-(SC_5H_4-C_5H_{11})-10-(NC_5H_4OR)] (**63**) [9]

In a similar way, quinuclidinium derivative **37** was diazotized to give the corresponding dinitrogen derivative **64** in 40% yield. Thermolysis of **64** with 4-alkoxypyridines at 120 °C resulted in pyridinium derivatives **65a-65e** (Scheme 22) [9].

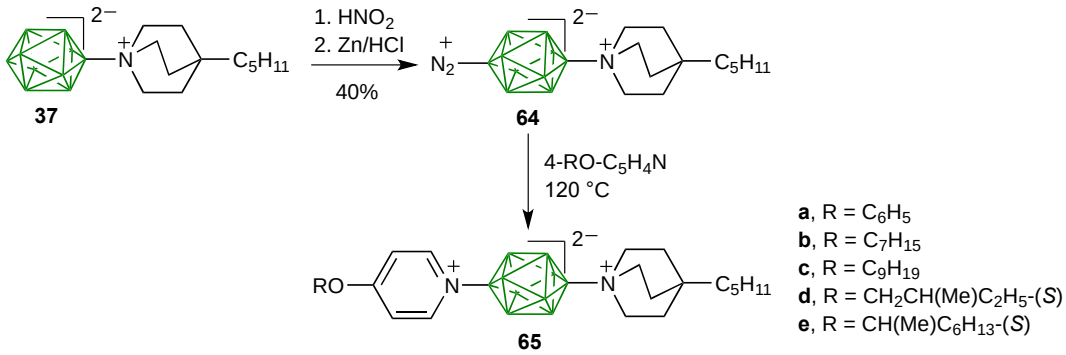

Scheme 22. Synthesis of heterodisubstituted derivatives from quinuclidine ring derivative **37** [9].

Recent work on *closo*-decaborate anion chemistry have explored the phenyliodonium zwitterion method to obtain several apically heterodisubstituted derivatives with the general formula [*closo*-$B_{10}H_8$-1-X-10-Y]$^{2-}$ (Scheme 23). Synthesis of the derivative [*closo*-$B_{10}H_8$-1-

($C_6H_4OC_{12}H_{25}$)-10-($OCOC_{11}H_{23}$)]$^{2-}$ (**70**) was achieved in a multistep sequence of reactions starting from [*closo*-$B_{10}H_9$-1-IPh]$^-$ (**IV**) [27]. Derivative **22b** (synthesis in Scheme 6) was selectively substituted at the B(10) position using $PhI(OAc)_2$ and the resulting unstable iodonium intermediate [*closo*-$B_{10}H_8$-1-($C_6H_4OC_{12}H_{25}$)-10-IPh]$^-$ (**66**) was thermolyzed in dry DMF to obtain adduct [*closo*-$B_{10}H_8$-1-($C_6H_4OC_{12}H_{25}$)-10-($OCHNMe_2$)]$^-$ (**67**). The latter was isolated by column chromatography in 35-43% yield based on the derivative **22b**. Subsequent treatment of the DMF adduct **67** with $[Bu_4N]^+[OH]^-$ gave [*closo*-$B_{10}H_8$-1-($C_6H_4OC_{12}H_{25}$)-10-OCHO]$^{2-}$ (**68**) in 93% yield, which upon treatment with aqueous HCl provided an unstable oxonium intermediate [*closo*-$B_{10}H_8$-1-($C_6H_4OC_{12}H_{25}$)-10-OH_2]$^{2-}$ (**69**). Acylation of **69** with $C_{11}H_{23}COCl$ in the presence of NaH in THF resulted in the ester **70** in 34-40% yield. Compound **70** was investigated as ionic liquid crystalline derivatives (see section 1.4.2: Ionic liquid crystals of [*closo*-$B_{10}H_{10}$]$^{2-}$).

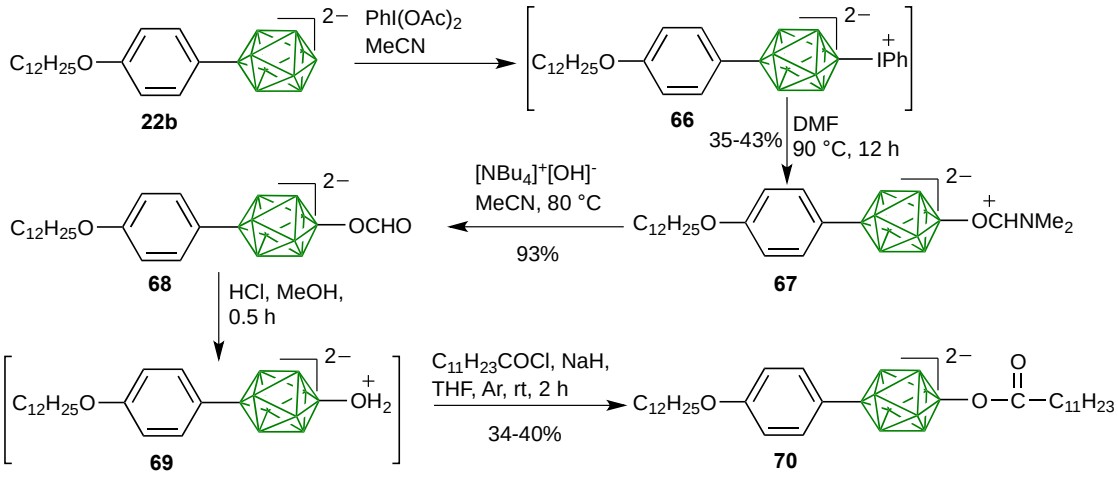

Scheme 23. Synthesis of heterodisubstituted derivative [*closo*-$B_{10}H_8$-1-($C_6H_4OC_{12}H_{25}$)-10-($OCOC_{11}H_{23}$)]$^{2-}$ (**70**) [27].

Synthetic utility of the phenyliodonium derivatives of the anion **A** has also been explored in preparation of several new heterodisubstituted photonic materials (Scheme 24) [28]. Thus, reaction of [*closo*-$B_{10}H_9$-1-IPh]$^-$ $[NBu_4]^+$ (**IV[NBu$_4$]**) with $[NBu_4]^+[CN]^-$ at 55 °C in MeCN gave

the mono substituted derivative [*closo*-$B_{10}H_9$-1-CN]$^{2-}$ 2[NBu_4]$^+$ (**71a**) in 60–55% yield. The subsequent reaction of this derivative with $PhI(OAc)_2$ in a MeCN solution resulted in [*closo*-$B_{10}H_8$-1-CN-10-IPh]$^-$ [NBu_4]$^+$ (**72a**) and this derivative was reacted with excess pyridine to provide the expected pyridinium derivative [*closo*-$B_{10}H_8$-1-CN-10-NC_5H_5]$^-$ [NBu_4]$^+$ (**73a**). In a similar way, **IV[NBu$_4$]** was reacted with [NBu_4]$^+N_3^-$ and the azide [*closo*-$B_{10}H_9$-1-N_3]$^{2-}$ 2[NBu_4]$^+$ (**71b**) was isolated by column chromatography in 95% yield. Azide **71b** was subsequently converted to phenyliodonium [*closo*-$B_{10}H_8$-1-N_3-10-IPh]$^-$ [NBu_4]$^+$ (**72b**) and reacted with pyridine to obtain [*closo*-$B_{10}H_8$-1-N_3-10-NC_5H_5]$^-$ [NBu_4]$^+$ (**73b**) in 55% yield for the two-step process. Iodo derivative [*closo*-$B_{10}H_8$-1-I-10-NC_5H_5]$^-$ [NBu_4]$^+$ (**73c**) was obtained in 49% overall yield by reacting [*closo*-$B_{10}H_8$-1-I-10-IPh]$^-$ [NBu_4]$^+$ (**72c**) with pyridine. Derivative **72c** was conveniently synthesized by treating [*closo*-$B_{10}H_9$-1-IPh]$^-$ [NBu_4]$^+$ (**IV[NBu$_4$]**) with *n*-BuLi followed by treating the resulting [*closo*-$B_{10}H_9$-1-I]$^{2-}$ 2[NBu_4]$^+$ (**9[NBu$_4$]**) with $PhI(OAc)_2$.

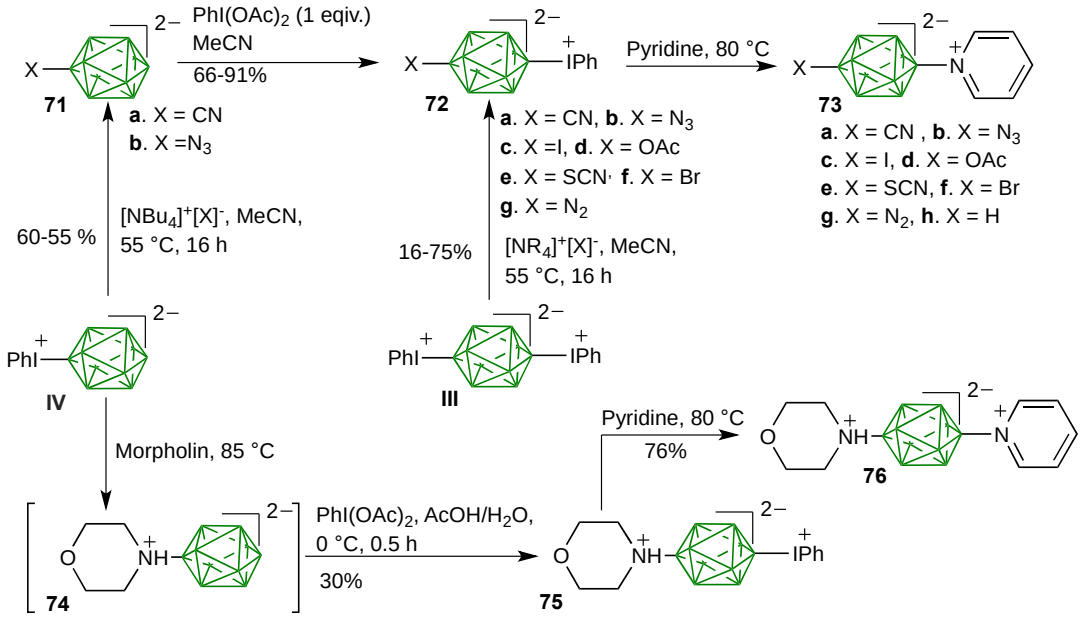

Scheme 24. Synthesis of the heterodisubstituted photonic materials of the [*closo*-$B_{10}H_{10}$]$^{2-}$ anion from phenyliodonium zwitterions [28].

Alternatively, heterodisubstituted derivatives were synthesized efficiently from the phenyliodonium zwitterion **III** (Scheme 24) [28]. Reaction of the zwitterion **III** with $[AcO]^-$ gave monosubstituted product [*closo*-$B_{10}H_8$-1-OAc-10-IPh]$^-$ $[NEt_4]^+$ (**72d**) with high selectivity, which was reacted with excess pyridine to yield the desired product [*closo*-$B_{10}H_8$-1-OAc-10-NC_5H_5]$^-$ $[NEt_4]^+$ (**73d**) in 74% yield. A similar reaction of **III** with 1.5 equivalents of $[NEt_4]^+$ $[SCN]^-$ in MeCN at 60 °C resulted in a mixture of products, from which [*closo*-$B_{10}H_8$-1-SCN-10-IPh]$^-$ $[NEt_4]^+$ (**72e**) was isolated by column chromatography in 16% yield. Subsequent thermolysis of **72e** in pyridine solution gave [*closo*-$B_{10}H_8$-1-SCN-10-NC_5H_5]$^-$ $[NEt_4]^+$ (**73e**) in 78% yield. Bromo derivative [*closo*-$B_{10}H_8$-1-Br-10-NC_5H_5]$^-$ (**73f**) was obtained in 56% overall yield from derivative **III** in the same two-step sequence reaction with 75% yield for each [*closo*-$B_{10}H_8$-1-Br-10-IPh]$^-$ (**72f**) and [*closo*-$B_{10}H_8$-1-Br-10-NC_5H_5]$^-$ (**73f**). Derivatives [*closo*-$B_{10}H_8$-1-N_3-10-NC_5H_5]$^-$ $[NBu_4]^+$ (**73b**) and [*closo*-$B_{10}H_8$-1-Br-10-NC_5H_5]$^-$ $[NEt_4]^+$ (**73f**) were also obtained through a one-pot preparation method without purification of the intermediate monoiodonium derivatives [*closo*-$B_{10}H_8$-1-N_3-10-IPh]$^-$ $[NEt_4]^+$ (**72b**) and [*closo*-$B_{10}H_8$-1-Br-10-IPh]$^-$ $[NEt_4]^+$ (**72f**). The final products **73b** and **73f** were obtained in 64% and 68% overall yields respectively based on **III**. Derivative [*closo*-$B_{10}H_8$-1-CN-10-NC_5H_5]$^-$ $[NBu_4]^+$ (**73a**) was also obtained in this method and the product was isolated by column chromatography in 53% yield.

Reaction of **IV[NBu_4]** with neat morpholine at 85 °C followed by treating the resulted complex mixture of products with $PhI(OAc)_2$ in AcOH gave the bis-zwitterion [*closo*-$B_{10}H_8$-1-morpholinium-10-IPh] (**75**) in a 30% overall yield, after column chromatography (Scheme 24) [28]. The subsequent reaction of this derivative with neat pyridine gave the pyridinium derivative [*closo*-$B_{10}H_8$-1-morpholinium-10-NC_5H_5] (**76**) in the protonated form in 76% yield. The deprotonated form of the derivative was found to be unstable.

It was found that the presence of an onium substituent in the antipodal position facilitates substitution of the $[PhI]^+$ group in the derivatives of the anion **A**, and thiocyanate derivative [*closo*-$B_{10}H_8$-1-SCN-10-NC_5H_5]$^-$ $[Et_4N]^+$ (**73e**) was alternatively obtained in an improved yield of 55% by the reaction of [*closo*-$B_{10}H_8$-1-IPh-10-NC_5H_5] (**77**) with $[NEt_4]^+[SCN]^-$ in MeCN (Scheme 25) [28].

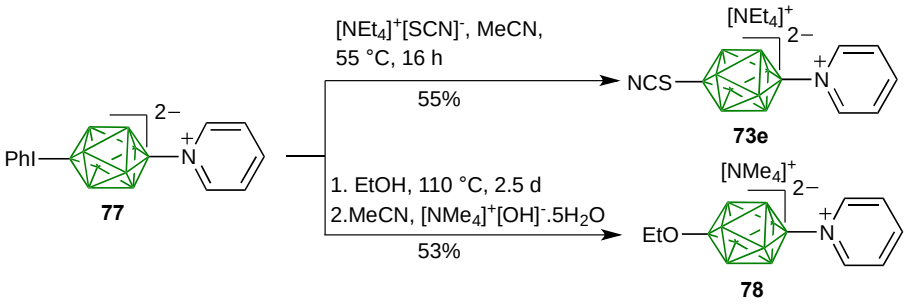

Scheme 25. Synthesis of hetero substituted derivative from [*closo*-$B_{10}H_8$-1-(IPh)-10-(NC_5H_5)] (**77**) [28].

Refluxing of derivative **77** in a solution of EtOH for several days progressed slowly towards a single product. But when the reaction mixture was heated to 110 °C in a pressure tube for 2 days, **77** was completely converted into the protonated product [*closo*-$B_{10}H_8$-1-OHEt-10-NC_5H_5] (**78-H**) isolated in 69% yield. Treatment of the product with $[NMe_4]^+$ $[OH]^-{\cdot}5H_2O$ in MeCN resulted in the non-protonated derivative [*closo*-$B_{10}H_8$-1-OEt-10-NC_5H_5]$^-$ (**78**) isolated in a 53% yield [28].

Selective nucleophilic substitution of derivative **III** with one equivalent of $[NBu_4]^+$ $[CN]^-$ in MeCN gave the mononitrile derivative [*closo*-$B_{10}H_8$-1-CN-10-IPh]$^-$ (**72a**) in 50-55% yield after column chromatography. **72a** when treated with 5.0 equivalents of an azine in minimum volume of MeCN at 80 °C gave the corresponding azine substituted derivatives (**79a**-**79g**) in 50-78% yield (Scheme 26) [42].

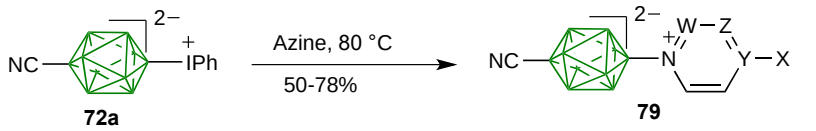

72a **79**

a, W = N, Y = Z = C
b, Z = N, Y = W= C
c, Y = N, W = Z = C
d, X = CN, Y = Z = W = C
e, X = CN, Y = W = Z = C
f, X = Me, Y = N, Z = W = C
g, X = $C_{12}H_{25}$, Y = N, Z = W = C

Scheme 26. Synthesis of azine substituted derivatives from [*closo*-$B_{10}H_8$-1-CN-10-IPh]$^-$ (**72a**) [42].

Mono substituted pyridazine, pyrazine, and 2,6-dimethylpyridine derivatives were also obtained in 25-60% yield by treating 5.0 equivalents of the corresponding azines with [*closo*-$B_{10}H_9$-1-IPh]$^-$ (**IV**) in MeCN at 80 ^oC (Scheme 27) [42].

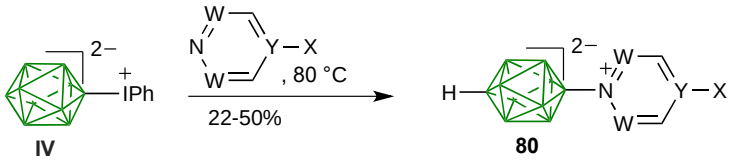

IV **80**

a. X = H, Y = C, W1 = N, W2 = CH
b. Y= N, W = C
c. X = H, Y = C, W = CCH_3

Scheme 27. Synthesis of azine substituted derivatives from [*closo*-$B_{10}H_9$-1-IPh]$^-$ (**IV**) [42].

The nitrilium zwitterion [*closo*-$B_{10}H_8$-1-CNMe-10-IPh] (**81**, Scheme 28) [24], was synthesized in 50-78% yield by the reaction of mononitrile **72a** with CF_3SO_3Me. This zwitterion was treated with aqueous NaOH in MeCN, followed by concentrated HCl, providing a mixture of monoacid derivative [*closo*-$B_{10}H_8$-1-COOH-10-IPh]$^-$ (**82**) and its formal anhydride [*closo*-$B_{10}H_8$-1-CO-10-IPh] (**83**). The crude reaction mixture was then treated with $NaHCO_3$ and passed through Dowex exchange resin, giving a 59% yield of pure **82** after precipitation with $[NEt_4]^+[OH]^-$. After collecting the pure **82**, a mixture of **82** and **83** was also obtained by extracting the filtrate. Derivative

82, when treated with dry pyridine resulted in a mixture of products from which 68% yield of pure **84** was collected after precipitation in CH_2Cl_2/Hexane, followed by recrystallization from MeCN/H_2O. Sodium salt **85** was obtained by passing a solution of **84** in MeCN through Dowex ion exchange resin and then treating it with aqueous NaOH [43].

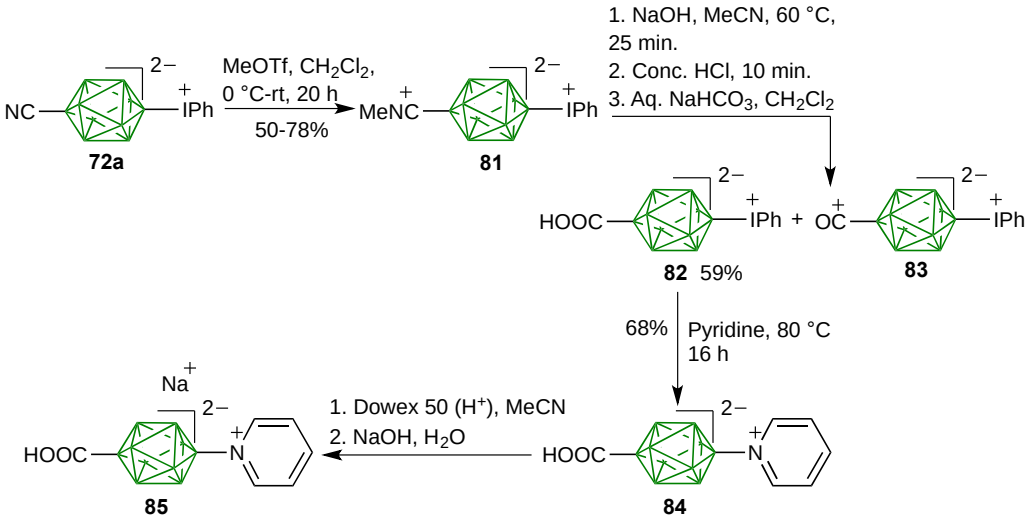

Scheme 28. Synthesis and reactivity of the [*closo*-$B_{10}H_8$-1-COOH-10-IPh]$^-$ (**82**) derivative [43].

Reaction of dicarbonyl derivative **10** with ethylene diamine $NH_2CH_2CH_2NH_2$ resulted in the corresponding zwitterionic diamide **86** in a quantitative yield (Scheme 29) [25]. Subsequent treatment of **86** with TMS polyphosphate resulted in the dehydrative cyclization of one of the amide groups and loss of amino group from the second amide to give the corresponding monocarbonyl derivatives **87** in 63% yield. Derivative **87** was smoothly converted to the corresponding monoacid derivative **88** in 75% yield, when treated with $[NBu_4]^+$ $[OH]^-$. Crystallization of **88** in ethanol gave the corresponding ethyl ester as the only product. Reaction of **10** with other ethylene diamine derivatives, such as $MeNHCH_2CH_2NHMe$ gave similar results.

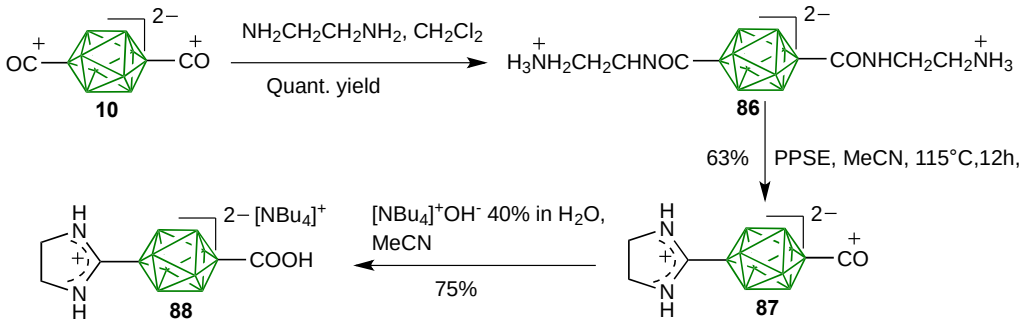

Scheme 29. Reaction of dicarbonyl derivative **10** with ethylenediamine [25].

1.4 Self-organizing materials based on the [*closo*-$B_{10}H_{10}$]$^{2-}$ anion

Liquid crystals (LC) are functional materials forming dynamic self-organized structures with anisotropy of their properties (see section 2.4.1 of the Introduction). Ionic liquid crystals (ILC) exhibit a combination of properties of ionic liquids and LC. One such property of interest in ILC is ion conduction, which is attractive for technological applications, for instance in electrolytes for batteries and photovoltaic cells [44,45]. Chemistry of the [*closo*-$B_{10}H_{10}$]$^{2-}$ anion (**A**), relevant to liquid crystals has developed significantly in the last couple of decades and several zwitterionic quadrupolar and ILC were synthesized [9,24,27]. The characteristic high thermal and oxidative stability of the ILC based on anion **A** have vast potential for applications.

1.4.1 Zwitterionic quadrupolar liquid crystals

Several zwitterionic quadrupolar liquid crystal derivatives of the *closo*-decaborate anion **A** substituted at the apical positions have been synthesized by the nucleophilic substitution either on the dinitrogen derivative **I** or phenyliodonium zwitterion **III** by onium fragments, such as 4-alkoxypyridinium (**31**) and 4-pentylthianium (**63**), (Figure 3) [9,24]. Investigation of the thermal behavior of the homologous series of pyridinium zwitterion **31[n]** revealed liquid crystalline and crystalline lamellar phases with increasing lamellar behavior for longer alkyl chains. [24].

Derivative **31[8]** exhibited only nematic (N) behavior. In addition to the N phase, crystalline lamellar phases (Lam_{cr}) were observed in higher homologs **31[10]** and **31[12]**, and the N phase was totally replaced by the Lam_{cr} phases in **31[16]** and **31[18]**. The stability of the crystalline and N phases for these compounds has been found to be largely dependent on the polar intermolecular interactions in the phase. Powder XRD investigation suggested sequential melting of the crystalline phase and revealed more about the interlayer spacing and its temperature dependency.

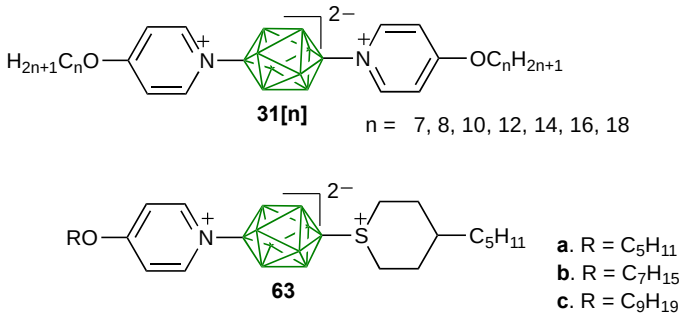

Figure 3. Zwitterionic quadrupolar liquid crystals based on [*closo*-$B_{10}H_{10}]^{2-}$ anion [9,24].

Heterodisubstituted liquid crystalline derivatives were also prepared by a sequential introduction of the onium fragments at the apical positions of the [*closo*-$B_{10}H_{10}]^{2-}$ cluster (Figure 3) [9]. In the heptyloxypyridinium substituted derivative **63b**, a broad-range enantiotropic nematic phase with a clearing temperature of 160 °C was observed. When the heptyloxy unit in derivative **63b** was extended by two carbon atoms to form **63c**, the phase transition temperature dropped by 6 K. The melting point of derivative **63a** with the pentyloxypyridinium moiety was 42 K higher compared to derivative **63b** with a negligible effect on the N-I transition.

1.4.2 Ionic liquid crystals

Recent advancements in the boron cluster chemistry led to the development of the first ILC derivatives of anion **A** with tunable intermolecular charge transfer (CT) absorption bands in the

UV-visible range (Figure 4) [27]. In the general molecular design for ILC (Figure 4), ions have mesogenicity inducing groups, which affect the level of the HOMO of the anion and the LUMO of the pyridinium cations. In total four different anions (**21b**, **27b**, **27c**, **70**) and five different pyridinium cations were investigated as liquid crystalline ion pairs obtained by $[Bu_4N]^+$ cation exchange.

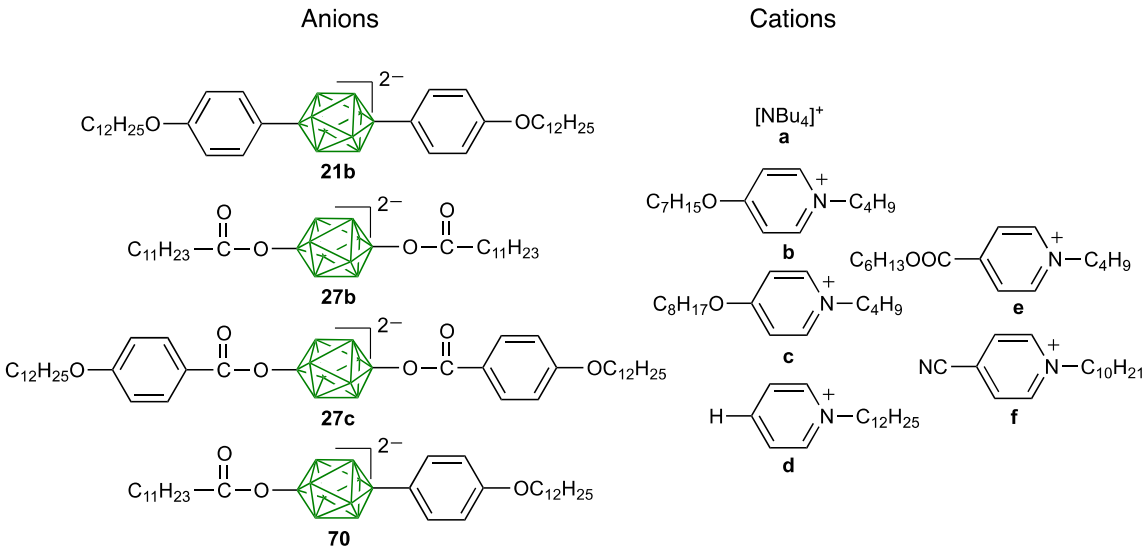

Figure 4. ILC derivatives based on [*closo*-$B_{10}H_{10}]^{2-}$ with tunable intermolecular charge transfer [27].

Investigations revealed a broad range smectic A (SmA) phase with high clearing temperatures (most of the compounds start decomposing above 200 °C) for all ion pairs. The melting temperature of the ion pairs in series **27b** was determined to be relatively low, increasing in the order **27b[b]** < **27b[e]** < **27b[c]** < **27b[f]** < **27b[d]** within the series. Ion pair **27b[b]** has been found to exist in a smectic phase at room temperature. Ion pairs of series **21b**, **27c**, and **70** with one or two benzene rings in the anion's core exhibited higher melting points, with the highest melting temperatures to the smectic phase observed in ion pairs of series **21[b]**.

Powder XRD and DSC analyses indicated that many ion pairs undergo a stepwise melting to the SmA phase, with the initial melting of the alkyl chains and then the ionic cores as two independent thermodynamic events. Analysis of the transition enthalpy to the SmA phases suggested that ion pairs, such as **27b[e]**, **70[d]**, and **21b[f]**, may exist as solids with molten alkyl chains at ambient temperature. The sheets of rigid arrangements of electroactive ions (due to the charge transfer between donor anion and acceptor cation) observed in the intermediate phase with melted alkyl chains are of general interest for organic semiconductors.

1.5 Photo active materials derived from [*closo*-$B_{10}H_{10}$]$^{2-}$ anion

Photonic materials and devices play a critically important role in modern technological applications. The unique properties of boron cluster derivatives make them excellent candidates for such applications and many cluster derivatives were synthesized and explored. Among them, anion **A** is exceptional and a recent work has demonstrated two series of heterodisubstituted photo active derivatives (**73a-73k** and **89a-89d**) based on the pyridinium derivative of anion **A** [*closo*-$B_{10}H_9$-1-NC_5H_5]$^-$, substituted either at the antipodal B(10) position with CN, OAc, N_3, I, Br, SCN, pyridine, OEt, and morpholine, or at the C(4) position of the pyridine ring with CN, COOEt, Me, and OMe groups (Figure 5) [28].

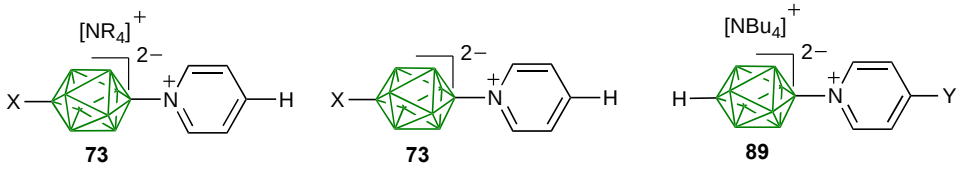

a. X = CN , **b**. X = N_3
c. X = I, **d**. X = OAc
e. X = SCN, **f**. X = Br
g. X = N_2, **h**. X = H
i. X = morpholinium

j. X = pyridinium
k. X = morpholinium

a. Y = CN, **b**. Y = COOEt
c. Y = Me, **d**. Y = OMe

Figure 5. Photoactive materials based on [*closo*-$B_{10}H_{10}$]$^{2-}$ anion [28].

Spectroscopic investigation supported with TD-DFT calculations revealed the tunability of the intramolecular (π, π*) CT absorption band for these derivatives in the UV-visible region, which results from the significant substituent and solvent effects. The substituents on the pyridine ring were found to affect the LUMO 2.4 times more strongly than substituents on the anion **A** impact the HOMO. Several derivatives were found to fluoresce weakly in MeCN solutions at substantially lower energies. Further studies revealed that most derivatives fluoresce in the solid state. Aggregation-induced emission was also investigated for two representative derivatives [28].

1.6 Metal complexes based on the [*closo*-$B_{10}H_{10}]^{2-}$ anion

The double negative charge associated with the [*closo*-$B_{10}H_{10}]^{2-}$ anion (**A)** make its derivatives suitable candidates for the preparation of metal complexes with low overall electric charge, and hence greater stability of the oxidized species. One such a derivative is the [*closo*-$B_{10}H_8$-1,10-$(CN)_2]^{2-}$ (**16**) with high electron density transferred from the cluster to the CN group as a result of the effective electronic communication between them [26]. Recently, a diiron complex [{(η^5-Cp)(dppe)Fe}$_2${μ_2-(NC-$B_{10}H_8$-CN)}] (**91**) was prepared in 76% yield by reacting [*closo*-$B_{10}H_8$-1,10-$(CN)_2]^{2-}$ $2[Et_4N]^+$ (**16[Et$_4$N]**) with 2 equivalents of (η^5-Cp)(dppe)FeCl (**90**) in CH_2Cl_2 (Scheme 30) [29].

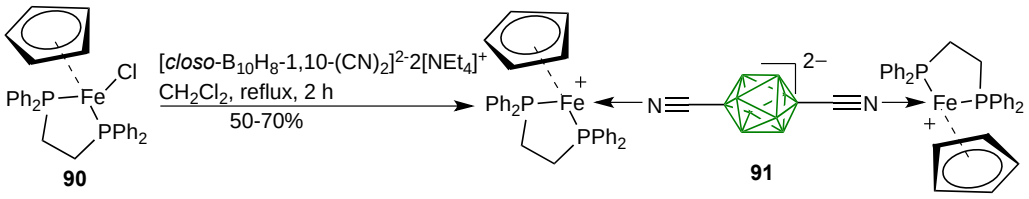

Scheme 30. Synthesis of the diiron complex of [*closo*-$B_{10}H_8$-1,10-$(CN)_2]^{2-}$ (**16**) [29].

Electronic communication between the Fe centers in the complex **91** was investigated and compared to that in the organic and carborane analogs. Despite significant differences in their

electronic structures, the [*closo*-$B_{10}H_{10}]^{2-}$ anion (**A**) and benzene derivatives demonstrated a remarkable similarity in their ability to mediate electronic communication between two terminal metal centers. This study also revealed that the anion **A** can more effectively communicate with the π-substituents than the analogous carboranes. The observed particularly high effectiveness of complex **91** was found to be associated with the strong electron-donating ability, effective metal-bridge MO mixing, and extensive delocalization of the charge within the borane cluster, but not all the way through to the other Fe center [29]. The σ-aromatic [*closo*-$B_{10}H_8$-1,10-diyl]$^{2-}$ bridge was also found to be a reasonably efficient transmitter of electron spin information between the Fe centers, although it is not as good as the 1,4-phenylene. All these studies showed the potential for applications of derivatives of anion **A** in metal complexes and opened the door for future applications, such as in the construction of molecular electronic systems and in the assembly of multifunctional MOFs.

1.7 Summary and outlook

In the recent decade, significant progress has been achieved in the chemistry of the [*closo*-$B_{10}H_{10}]^{2-}$ anion (**A**), providing easy access to new functional materials. Among all the available methods for apical functionalization of the anion **A**, the phenyliodonium zwitterion method was found to be the most efficient and versatile. The synthetic utility of several derivatives was explored in the context of developing photoactive materials, liquid crystals, and metal complexes, demonstrating a vast potential for such derivatives. Extensive studies on derivatives of anion **A** revealed several interesting properties that may find application, for instance, in solar cells, NLO materials, photovoltaics, and electrolytes. Therefore, the development of such functional materials is important and this offers a wide scope for future research.

1.8 References

1. B. Sivaev, A. V. Prikaznov, D. Naoufal, Fifty years of the *closo*-decaborate anion chemistry, *Collect. Czech. Chem. Commun.*, **2010,** *75*, 1149–1199.
2. K. Y. Zhizhin, A. P. Zhdanov, N. T. Kuznetsov, Derivatives of *closo*-decaborate anion $[B_{10}H_{10}]^{2-}$ with exo-polyhedral substituents, *Russ. J. Inorg. Chem.*, **2010**, *55*, 2089–2127.
3. J. Aihara, Three-dimensional aromaticity of polyhedral boranes, *J. Am. Chem. Soc*., **1978,** *100*, 3339–3342.
4. R. B. King, Three-dimensional aromaticity in polyhedral boranes and related molecules, *Chem. Rev*., **2001**, *101*, 1119–1152.
5. P. Kaszyński, *closo*-Boranes as π structural elements for advanced anisotropic materials, Vol. 798, ACS symposium series, Washington, D. C. **2001.**
6. A. Miniewicz, A. Samoc, M. Samoc, P. Kaszyński, Observation of second-harmonic generation in an oriented glassy nematic phase of a *closo*-decaborane derivative, *J. Appl. Phys.*, **2007**, *102*, 033108.
7. D. G. Allis, J. T. Spencer, Polyhedral-based nonlinear optical materials. 2.1 Theoretical investigation of some new high nonlinear optical response compounds involving polyhedral bridges with charged aromatic donors and acceptors, *Inorg. Chem.*, **2001**, *40*, 3373–3380.
8. A. Voge, D. Gabel, Boron derivatives for application in nonlinear optics in Boron Science: New Technologies and Applications (Ed.: N. S. Hosmane); CRS Press, New York, **2012**, 295–317.
9. A. Jankowiak, A. Baliński, J. E. Harvey, K. Mason, A. Januszko, P. Kaszyński, V. G. Young Jr., A. Persoons, [*closo*-$B_{10}H_{10}]^{2-}$ as a structural element for quadrupolar liquid

crystals: A new class of liquid crystalline NLO chromophores, *J. Mater. Chem. C*, **2013**, *1*, 1144–1159.

10. S. Pakhomov, P. Kaszyński, V. G. Young Jr., 10-vertex *closo*-boranes as potential π linkers for electronic materials, *Inorg. Chem.*, **2000**, *39*, 2243–2245.
11. R. Núñez, M. Tarrés, A. Ferrer-Ugalde, F. Fabrizi de Biani, F. Teixidor, Electrochemistry and photoluminescence of icosahedral carboranes, boranes, metallacarboranes, and their derivatives, *Chem. Rev.*, **2016**, *116*, 14307–14378.
12. M. F. Hawthorne**,** A. R. Pitochelli, The reactions of bis-acetonitrile decaborane with amines, *J. Am. Chem. Soc.*, **1959,** *81*, 5519–5519.
13. J. Poater, M. Sola, C. Viñas, F. Teixidor, π Aromaticity and three-dimensional aromaticity: Two sides of the same coin? *Angew. Chem. Int. Ed.* **2014**, *53*, 12191–12195; *Angew. Chem.*, **2014**, *126*, 12387–12391.
14. J. Poater, C. Viñas, I. Bennour, S. Escayola, M. Sola, F. Teixidor, Too persistent to give up: Aromaticity in boron clusters survives radical structural changes, *J. Am. Chem. Soc.*, **2020**, *142*, 9396–9407.
15. W. N. Lipscomb, Boron hydrides. New York: Benjamin; **1963**.
16. P. Kaszyński, S. Pakhomov, V. G. Young Jr., Investigations of electronic interactions between closo-boranes and triple-bonded substituents, *Collect. Czech. Chem. Commun.*, **2002**, *67*, 1061–1083.
17. K. Y. Zhizhin, V. N. Mustyatsa, E. A. Malinina, L. V. Goeva, N. T. Kuznetsov, The mechanism of acid-catalyzed nucleophilic substitution in decahydro-*closo*-decaborate $^{(2-)}$ anions, *Russ. J. Coord. Chem.*, **2001**, *27*, 619–621.

18. W. H. Knoth, J. C. Sauer, H. C. Miller, E. L. Muetterties, Diazonium and carbonyl derivatives of polyhedral boranes, *J. Am. Chem. Soc.*, **1964**, *86*, 115–116.
19. W. H. Knoth, Chemistry of boranes. XXVI. Inner diazonium salts 1,10-$B_{10}H_8(N_2)_2$, $B_{10}Cl_8(N_2)_2$, and $B_{10}I_8(N_2)_2$, *J. Am. Chem. Soc.*, **1966**, *88*, 935–939.
20. M.F. Hawthorne, F. P. Olsen, Reaction of $[B_{10}H_{10}]^{2-}$ with aryldiazonium salts, *J. Am. Chem. Soc.*, **1965**, *87*, 2366-2372.
21. R. N. Leyden, M. F. Hawthorne, Synthesis of diazonium derivatives of [*closo*-$B_{10}H_{10}]^{2-}$ from arylazo intermediates, *Inorg. Chem.*, **1975**, *14*, 2444–2446.
22. P. Kaszyński, B. Ringstrand, Functionalization of *closo*-borates via iodonium zwitterions, *Angew. Chem. Int. Ed.* **2015**, *54*, 6576–6581; *Angew. Chem.*, **2015**, *127*, 6676–6681.
23. E. Rzeszotarska, I. Novozhilova, P. Kaszyński, Convenient synthesis of [*closo*-$B_{10}H_9$-1-$I]^{2-}$ and [*closo*-$B_{10}H_8$-1,10-$I_2]^{2-}$ anions, *Inorg. Chem.*, **2017**, *56*, 14351–14356.
24. M. O. Ali, D. Pociecha, J. Wojciechowski, I. Novozhilova, A. C. Friedli, P. Kaszyński, Highly quadrupolar derivatives of the [*closo*-$B_{10}H_{10}]^{2-}$ anion: Investigation of liquid crystalline polymorphism in an homologous series of 1,10-bis(4-alkoxypyridinium) zwitterions, *J. Organomet. Chem.*, **2018**, *865*, 226–233.
25. S. Kapuściński, O. Hietsoi, A. Pietrzak, A. C. Friedli, P. Kaszyński, [*closo*-$B_{10}H_8$-1,10-$(COOH)_2]^{2-}$: A building block for functional materials?, *Chem. Commun.*, **2022**, *58*, 851–854.
26. L. Jacob, E. Rzeszotarska, A. Pietrzak, P. Kaszyński, Synthesis, structural analysis, and functional group interconversion in the [*closo*-$B_{10}H_8$-1,10-$X_2]^{2-}$ (X= CN, $[OCRNMe_2]^+$, OCOR, and $[OH_2]^+$) derivatives, *Eur. J. Inorg. Chem.*, **2020**, *32*, 3083–3093.

27. L. Jacob, E. Rzeszotarska, M. Koyioni, R. Jakubowski, D. Pociecha, A. Pietrzak, and P. Kaszyński, Tunable intermolecular charge transfer in ionic liquid crystalline derivatives of the [*closo*-$B_{10}H_{10}]^{2-}$ anion, *Chem. Mater.*, **2022,** *34***,** 14307–14378.

28. S. Kapuściński, M. B. Abdulmojeed, T. E. Schafer, A. Pietrzak, O. Hietsoi, A. C. Friedli, P. Kaszyński, Photonic materials derived from the [*closo*-$B_{10}H_{10}]^{2-}$ anion: Tuning photophysical properties in [*closo*-$B_{10}H_8$-1-X-10-(4-Y-$NC_5H_5]^-$, *Inorg. Chem. Front.*, **2021**, *8*, 1066–1082.

29. J. Guschlbauer, K. H. Shaughnessy, A. Pietrzak, M. C. Chung, M. B. Sponsler, P. Kaszyński, [*closo*-$B_{10}H_8$-1,10-$(CN)_2]^{2-}$ as a conduit of electronic effects: Comparative studies of Fe···Fe communication in [{(η^5-Cp)(dppe)Fe}$_2${μ_2-(NC-X-CN)}]$^{n+}$ (n = 0, 2), *Organometallics*, **2021**, *40*, 2504–2515.

30. N. Mahfouz, F. A. Ghaida, Z. El Hajj, M. Diab, S. Floquet, A. Mehdi, D. Naoufal, Recent achievements on functionalization within *closo*-decahydrodecaborate $[B_{10}H_{10}]^{2-}$ clusters, *ChemistrySelect*, **2022**, *7*, 202200770.

31. K. Y. Zhizhin, A. P. Zhdanov, N. T. Kuznetsov, Derivatives of *closo*-decaborate anion $[B_{10}H_{10}]^{2-}$ with exo-polyhedral substituents, *Russ. J. Inorg. Chem.*, **2010**, *55*, 2089–2127.

32. V. I. Bragin, I. B. Sivaev, V. I Bregadze, Synthesis of the 1-hydroxy-*closo*-decaborate anion [1-$B_{10}H_9OH]^{2-}$, *J. Organomet. Chem.*, **2005**, *690*, 2847–2849.

33. B. Sivaev, V. I. Bragin, V. I. Bregadze, N. A. Votinova, S. Sjöberg, Synthesis of Schiff bases and benzylamino derivatives containing [1-$B_{10}H_9NH_3]^-$ anion, *Russ. Chem. Bull.*, **2004**, *53*, 2092–2095.

34. O. Hietsoi, S. Kapuściński, A. C. Friedli, P. Kaszyński, [*closo*-$B_{10}H_8$-1,10-(NHC(=NH_2)Me)$_2$]: A rare zwitterionic amidinium derivative, *J. Mol. Struct.*, **2023**, 135324.

35. D. Naoufal, B. Gruner, B. Bennetot, H. Mongeot, Replacement of the nitrogen of [1-$N_2B_{10}H_9]^-$ by amines or nitriles, a route to hydrophobic monoanions, *Polyhedron*, **1999**, *18*, 931–939.

36. C. Nachtigal, W. Preetz, Preparation, "B NMR, vibrational spectra, and crystal structure of $[P(C_6H_5)_4]_2$ [1,10-$(O_2N)_2B_{10}H_8$], *Z. Anorg. Allg. Chem*., **1997**, *623*, 683–686.

37. A. S. Kubasov, E. Y. Matveev, E. S. Turyshev, I. N. Polyakova, K. Y. Zhizhin, N.T. Kuznetsov, Interaction of $[B_{10}H_{10}]^{2-}$ and $[B_{12}H_{12}]^{2-}$ with nitro compounds, *Dokl. Chem.*, **2017**, 477, 257–260.

38. W. H. Knoth, W. R. Hertler, E. L. Muetterties, Chemistry of boranes. XXIII. $[B_{10}H_9S(CH_3)_2]^-$ and $B_{10}H_8[S(CH_3)_2]_2$, *Inorg. Chem.*, **1965**. *4*, 280–287.

39. H. G. Srebny, W. Preetz, Preparation and characterization of thiocyanate derivatives of the hydroborate anions $B_{10}H_{10}^{2-}$ and $B_{12}H_{12}^{2-}$, *Z. Anorg. Allg. Chem*., **1984**, *513*. 1950.

40. M. Komura, H. Nakai, M. Shiro, Regioselective synthesis of [1-$B_{10}H_9(SH)]^{2-}$ and [2-$B_{10}H_9(SH)]^{2-}$ potential agents for boron–neutron capture therapy of brain tumours, *J. Am. Chem. Soc*., *Dalton Trans.*, **1987**, *8*, 1953–1956.

41. (a) S. V. Ivanov, S. M. Ivanova, S. M. Miller, O. P. Anderson, N. T. Kuznetsov, K. A. Solntsev, S. H. Strauss, Synthesis, spectroscopic characterization, and structure of [*closo*-1,10-$B_{10}H_8F_2]^{2-}$ and related fluorinated derivatives of $[B_{10}H_{10}]^{2-}$, *Collect. Czech. Chem. Commun.*, **1997**, *62*, 1310–1324; (b) K.G. Bührens, W. Preetz, Isolation of halohydroborates of type $[B_{10}H_{10}$-nXn$]^{2-}$, *Angew. Chem., Int. Ed. Engl.*, **1977**, *16*, 173–174; (c) W.H. Knoth, H. C. Miller, J. C. Sauer, J. H. Balthis, Y. T. Chia, E. L. Muetterties, Chemistry of boranes. IX. Halogenation of $B_{10}H_{10}^{-2}$ and $B_{12}H_{12}^{-2}$, *Inorg. Chem.*, **1964**, *3*,159-167.

42. M. B. Abdulmojeed, S. Kapuściński, O. Hietsoi, A. C. Friedli, P. Kaszyński, [*closo*-$B_{10}H_8$-1-CN-10-Azinium]$^-$ anions as photoactive ligands for metal complexes, unpublished results.
43. R. Jakubowski, S. Kapuściński, O. Hietsoi, A. C. Friedli, P. Kaszyński, [*closo*-$B_{10}H_8$-1-COOH-10-IPh]$^-$: A versatile intermediate for functional materials, unpublished results.
44. (a) N. Kapernaum, A. Lange, M. Ebert, M. A. Grunwald, C. Haege, S. Marino, A. Zens, A. Taubert, F. Giesselmann, S. Laschat, Current topics in ionic liquid crystals, *ChemPlusChem*, **2022**, *87*, 202100397; (b) K. Goossens, K. Lava, C. W. Bielawski, K. Binnemans, Ionic liquid crystals: Versatile materials, *Chem. Rev.*, **2016**, *116*, 4643–4807.
45. K. V. Axenov, S. Laschat, Thermotropic ionic liquid crystals, *Materials*, **2011**, *4*, 206–259.

CHAPTER A2

Synthesis, structural analysis, and functional group interconversion in the [*closo*-$B_{10}H_8$-1,10-X_2]$^{2-}$ (X = CN, [$OCRNMe_2$]$^+$, OCOR, and [OH_2]$^+$) derivatives.

(L. Jacob, E. Rzeszotarska, A. Pietrzak, V. G. Young Jr., P. Kaszyński, *Eur. J. Inorg. Chem.*, **2020**, *32*, 3083-3093, DOI: 10.1002/ejic.202000456)

2.1 Introduction

For making ionic liquid crystals, typical connections are –OCO– and –O– groups. Therefore, the investigations in this work primarily focused on the dinitrile derivative [*closo*-$B_{10}H_8$-1,10-$(CN)_2$]$^{2-}$ and DMF adduct [*closo*-$B_{10}H_8$-1,10-$(OCHNMe_2)_2$] as precursors to diacid [*closo*-$B_{10}H_8$-1,10-$(COOH)_2$]$^{2-}$ and dihydroxy derivative [*closo*-$B_{10}H_8$-1,10-$(OH)_2$]$^{2-}$. The dinitrile and DMF adduct were obtained by the nucleophilic substitution on [*closo*-$B_{10}H_8$-1,10-$(IPh)_2$] with CN^- and DMF, respectively. The dihydroxy derivative (in the protonated form) was obtained in a good yield through a series of functional group transformation of the DMF adduct. The diacid derivative could not be obtained due to the inertness of the CN groups in [*closo*-$B_{10}H_8$-1,10-$(CN)_2$]$^{2-}$ towards classical reaction conditions.

This work demonstrated the usefulness of [*closo*-$B_{10}H_8$-1,10-$(IPh)_2$], for the synthesis of 1,10-disubstituted derivatives such as [*closo*-$B_{10}H_8$-1,10-$(CN)_2$]$^{2-}$ and [*closo*-$B_{10}H_8$-1,10-$(OH)_2$]$^{2-}$. This work also involved a detailed structural and computational analyses of these newly synthesized derivatives. These studies revealed a significant delocalization of the negative charge density from the cluster to the substituents as a result of the high effectiveness of electronic interactions between them. This was evident from the lower bond order in [*closo*-$B_{10}H_8$-1,10-

$(CN)_2]^{2-}$ compared to the hydrocarbon analogues. The resistance to hydrolysis and reduction of the dinitrile derivative is associated with its low electrophilicity. The high electron density available in the dinitrile derivative makes it particularly interesting for the development of metal complexes. The synthetic utility of [*closo*-$B_{10}H_8$-1,10-$(OH)_2$]$^{2-}$ as a building block for the construction of self-organizing materials was demonstrated by the preparation of [*closo*-$B_{10}H_8$-1,10-$(OCOC_6H_5)_2$]$^{2-}$.

My role in this project was to synthesize and characterize all compounds and conduct hydrolysis studies. Ms. Edyta Rzeszotarska contributed to the project by synthesizing the dinitrile derivative. Dr. Anna Pietrzak and Dr. Victor G. Young Jr. conducted the single crystal X-ray analysis of the compounds. Prof. Piotr Kaszyński performed quantum mechanical calculations to validate experimental findings.

2.2 Published text

Check for updates

EurJIC
European Journal of Inorganic Chemistry

Full Paper
doi.org/10.1002/ejic.202000456

Chemistry Europe
European Chemical Societies Publishing

Boron Cluster Functionalization | *Very Important Paper* |

VIP

Synthesis, Structural Analysis, and Functional Group Interconversion in the [*closo*-$B_{10}H_8$-1,10-X_2]$^{2-}$ (X = CN, [OCRNMe$_2$]$^+$, OCOR, and [OH_2]$^+$) Derivatives

Litwin Jacob,[a] Edyta Rzeszotarska,[a] Anna Pietrzak,[b,c] Victor G. Young Jr.,[d] and Piotr Kaszyński*[a,c,e]

Abstract: Derivatives [*closo*-$B_{10}H_8$-1,10-$(CN)_2$]$^{2-}$ and [*closo*-$B_{10}H_8$-1,10-$(OCHNMe_2)_2$], efficiently obtained from [*closo*-$B_{10}H_8$-1,10-$(IPh)_2$] by nucleophilic substitution with CN^- and DMF, were envisioned as precursors to diacid [*closo*-$B_{10}H_8$-1,10-$(COOH)_2$]$^{2-}$ and to dihydroxy derivative [*closo*-$B_{10}H_8$-1,10-$(OH)_2$]$^{2-}$, respectively. Attempts at hydrolysis or reduction of the dinitrile gave no reaction or complex mixtures of products. In contrast, the DMF adduct was cleanly hydrolyzed to diformate [*closo*-$B_{10}H_8$-1,10-$(OCHO)_2$]$^{2-}$ and subsequently to protonated dihydroxy [*closo*-$B_{10}H_8$-1,10-$(OH_2)_2$]. The latter was O-acylated with PhCOCl. Crystal and molecular structures of five derivatives were established by single crystal XRD methods and compared to those for other [*closo*-$B_{10}H_8$-1,10-X_2]$^{2-}$ derivatives. Trends in molecular geometry in the series and also reactivity of the dinitrile and intermediates were corroborated and correlated with DFT results (B3LYP/TZVP) by analysis of bonding, charge distribution and vibrational frequencies.

Introduction

The [*closo*-$B_{10}H_{10}$]$^{2-}$ cluster[1] (**A**, Figure 1) is a 3D σ aromatic anion[2] with high lying HOMO and symmetry and energy level appropriate to interact with π substituents.[3] Therefore its 1,10-difunctional derivatives have been considered as NLO materials[3a,4] and π linkers[3b] in molecular electronics. With respect to its shape, the [*closo*-$B_{10}H_{10}$]$^{2-}$ anion and its diapical derivatives are attractive structural elements for designing self-organizing rod-like materials (liquid crystals) with controlled electronic and photophysical properties.[4b,5]

Access to derivatives of the [*closo*-$B_{10}H_{10}$]$^{2-}$ anion with apical substituents is difficult; most substitution reactions (electrophilic of dianion **A** and nucleophilic[6] of its protonated form, [*closo*-$B_{10}H_{11}$]$^-$) take place almost exclusively at the equatorial position leading to [*closo*-$B_{10}H_9$-2-X]$^{2-}$ derivatives.[1b] Bisdinitrogen derivative [*closo*-$B_{10}H_8$-1,10-$(N_2)_2$] (**1a**, Figure 1), albeit obtained in low yields,[7] was the first convenient precursor to other diapical derivatives. Through a formal displacement of N_2, **1a** reacts with a range of nucleophiles, such as NH_3,[7b] pyridines,[4b,5b,7b] CO[7b] and Me_2NCHS[5b] giving rise to 1,10-difunctional derivatives, which include protonated diamine **1b**, protected dimercaptan **1c**, and 1,10-dicarbonyl derivative **1d**. The latter is of particular interest, since it is a formal anhydride of 1,10-dicarboxylic acid **1e**,[7a] a potentially useful building block for a variety of materials. Unfortunately, accessibility of **1d** is limited by high-pressure conditions (1000 atm) for its synthesis.[7b] It should be mentioned, that a highly selective monodiazo coupling of anion **A** with ArN_2^+ gave access to monodinitrogen derivative [*closo*-$B_{10}H_9$-1-(N_2)]$^-$,[8] which undergoes similar reactions as the bisdinitrogen analogue **1a**.[4b,9]

Recently, we discovered a highly selective and high yield formation of the bis-phenyliodonium derivative [*closo*-$B_{10}H_8$-1,10-

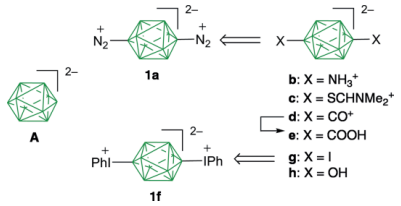

Figure 1. Structures of the [*closo*-$B_{10}H_{10}$]$^{2-}$ anion and some symmetrical 1,10-disubstituted derivatives.

[a] L. Jacob, E. Rzeszotarska, Prof. P. Kaszyński
Centre of Molecular and Macromolecular Studies, Polish Academy of Sciences,
Sienkiewicza 112, 90-363 Łódź, Poland
E-mail: piotrk@cbmm.lodz.pl
http://kaszynski-omrg.cbmm.lodz.pl/
[b] Dr. A. Pietrzak
Department of Chemistry, Łódź University of Technology,
Żeromskiego 116, 90-924 Łódź, Poland
[c] Dr. A. Pietrzak, Prof. P. Kaszyński
Department of Chemistry, Middle Tennessee State University,
Murfreesboro, TN, 37130, USA
[d] Dr. V. G. Young Jr.
Department of Chemistry, University of Minnesota,
Twin Cities, MN, 55455, USA
[e] Prof. P. Kaszyński
Faculty of Chemistry, University of Łódź,
Tamka 12, 91-403 Łódź, Poland
Supporting information and ORCID(s) from the author(s) for this article are available on the WWW under https://doi.org/10.1002/ejic.202000456.

© 2020 Wiley-VCH Verlag GmbH & Co. KGaA, Weinheim

$(IPh)_2$] (**1f**, Figure 1),[10] which undergoes nucleophilic substitution reactions through the 10-I-3 intermediate,[5a,10,11] or efficient dephenylation through the 9-I-2 intermediate[11] and formation of [*closo*-$B_{10}H_8$-1,10-I_2]$^{2-}$ (**1g**).[12] This demonstrates a great potential for **1f** as a more efficient and convenient intermediate than **1a** to 1,10-difunctionalized derivatives of **A**. In particular, we are interested in accessing diacid **1e** and hitherto unknown dihydroxy derivative **1h**, which are attractive building blocks for ionic liquid crystals with intermolecular charge transfer properties.

Herein we report our investigation on preparation of dicarboxylic acid **1e** and the dihydroxy derivative **1h** through substitution reactions of **1f** with the CN^- and DMF nucleophiles, respectively, and subsequent functional groups transformations. Synthetic work is accompanied by single crystal XRD analysis of several derivatives. Their reactivity and {*closo*-B_{10}} cage geometry are analyzed in terms of the substituent effect and are augmented with DFT calculations.

Results

Synthesis

The preparation of the dicarboxylic acid **1e** was envisioned through hydrolysis of the known[13] dinitrile **1i** using standard organic-type transformations[14] (Figure 2).

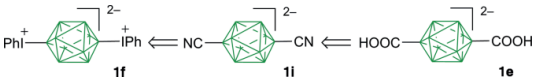

Figure 2. Retrosynthetic analysis of preparation of diacid **1e**.

Thus, a reaction of bis-phenyliodonium derivative **1f** with $[Et_4N]^+CN^-$ in MeCN gave the dinitrile [*closo*-$B_{10}H_8$-1,10-$(CN)_2$]$^{2-}$ $2[Et_4N]^+$ (**1i[Et$_4$N]**) isolated in 62–67 % yield. The reaction was conducted at 65 °C, since at higher temperatures the substitution reaction was complicated by formation of side products. To increase solubility of the salt in organic solvents, the $[Et_4N]^+$ cation was exchanged with the Dowex resin for $[Bu_4N]^+$ and, for obtaining single crystal XRD analysis (vide infra), for the $[Pr_4N]^+$ cation. Both salts, **1i[Bu$_4$N]** and **1i[Pr$_4$N]**, were obtained in nearly quantitative yields.

Dinitrile **1i** was surprisingly resistant to hydrolysis and none of over a dozen typical methods routinely used in similar transformations[14b] gave the desired dicarboxylic acid **1e**. Thus, reactions of **1i[Bu$_4$N]** with mineral acids (HCl and H_2SO_4 in H_2O, MeOH and AcOH) in temperatures up to 100 °C were ineffective and the starting **1i[Bu$_4$N]** was fully recovered. Similar difficulties were reported for hydrolysis of [*closo*-1-$CB_{11}H_{11}$-12-CN]$^-$ (**2**) which underwent smooth hydrolysis at 180 °C in HCl/H_2O/AcOH system in a microwave reactor.[15] Analogous reaction of dinitrile **1i** with aqueous H_2SO_4 in AcOH at 150 °C gave a complex mixture of products. This is consistent with the reported multiple acetoxylation of the [*closo*-$B_{10}H_{10}$]$^{2-}$ anion at the equatorial positions under similar conditions.[16] Dinitrile **1i** was unaffected by aqueous bases (NaOH or KOH).

Other reactions typically used to transform the nitrile group to other functionalities were ineffective. Thus, reactions with DIBAL[17] or with LDBIPA[18] in THF did not give the expected aldehyde and the starting **1i[Bu$_4$N]** was fully recovered. Stronger reducing reagents gave partial conversion of **1i** to a complex mixture of products. For instance, after reaction with $LiAlH_4$ in boiling THF, **1i[Bu$_4$N]** was recovered in 63 % from a complex reaction mixture, while in reduction with $NaBH_4$–BF_3·Et_2O[19] or $LiAlH_4$–BF_3·Et_2O only inseparable mixtures of products and starting **1i[Bu$_4$N]** were obtained. The observed resistance to hydrolysis and reduction of the C≡N groups in **1i** parallels that reported[15a,20] for the [*closo*-1-$CB_{11}H_{11}$-12-CN]$^-$ anion and is due to the extensive delocalization of the negative charge from the {*closo*-B_{10}} cluster (vide infra).

Transformation of bis-phenyliodonium derivative **1f** to [*closo*-$B_{10}H_8$-1,10-$(OH)_2$]$^{2-}$ (**1h**) was more successful, although equally surprising. Thus, thermolysis of **1f** in DMF solutions gave the bis-DMF adduct [*closo*-$B_{10}H_8$-1,10-$(OCHNMe_2)_2$] (**1j**) isolated in 72–80 % yield (Scheme 1). Attempts at hydrolysis of **1j** with aqueous solutions of HCl at ambient or elevated temperatures were unsuccessful and only unconsumed starting material was recovered. Treatment of **1j** with aqueous $[Bu_4N]^+OH^-$ in MeCN had, however, a different outcome and the hydrolysis product was isolated as the $[Bu_4N]^+$ salt. Detailed analysis demonstrated that the product was the formate diester **1k[Bu$_4$N]** obtained in 84–90 % yield, rather than the expected dihydroxy derivative **1h**. This surprising outcome results from nucleophilic displacement of the $-NMe_2$ substituent (after protonation) rather than the {*closo*-B_{10}}–O^- during the nucleophilic attack of the OH^- anion on the iminium carbon atom {*closo*-B_{10}}–$OCH{=}N^+Me_2$ in **1j**. This results is in sharp contrast to previous reports on smooth hydrolysis of analogous equatorial adducts of *N*-methylpyrrolidone (NMP)[9c] and DMF,[21] [*closo*-$B_{10}H_9$-2-NMP]$^-$ and [*closo*-$B_{10}H_9$-2-DMF]$^-$, which upon treatment with NaOH yielded [*closo*-$B_{10}H_9$-2-OH]$^{2-}$ in high yields. The observed difference in behavior of these equatorial derivatives is presumably due to the different negative charge distribution (different heteroatom basicity) and different degree of electronic interactions of the oxygen atom with the {*closo*-B_{10}} cluster.

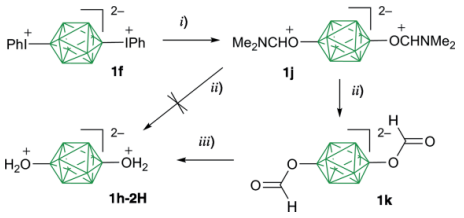

Scheme 1. Synthesis of **1h-2H**. Reagents and conditions: *i)* DMF, 90 °C, 12 h; *ii)* $[Bu_4N]^+OH^-$, MeCN, 80 °C, 2 h; (*iii)* HCl, MeOH, 0.5 h.

Further experiments demonstrated inertness of the diformate of **1k[Bu$_4$N]** to solutions of KOH in $MeOH/H_2O$, which again is in contrast to the reported smooth hydrolysis the analogous 2-formyloxy derivative.[16] Surprisingly, treatment of the diformate **1k[Bu$_4$N]** with diluted HCl in MeOH at ambient temperature resulted in fast cleavage of the ester functionality (Scheme 1). The desired product was isolated as protonated dihydroxy derivative [*closo*-$B_{10}H_8$-1,10-$(OH_2)_2$] (**1h-2H**) in 68–

© 2020 Wiley-VCH Verlag GmbH & Co. KGaA, Weinheim

72 % yield, after passing the solution through an ion exchange column and removing the solvent. Alternatively, crude reaction mixture was crystallized from water giving a mixture of **1h-2H** and $[Bu_4N]^+Cl^-$ in approximately 1:2 ratio and 58–68 % yield.

Brief investigations of other reactions of the diformate **1j**, such as palladium catalyzed arylation of formate esters[22] to form aryl esters or oxidation of the formate group with Tollens reagent or $PhI(OAc)_2$, demonstrated the formation of complex mixtures of products and were not pursued further.

Similar results were obtained, when DMF was replaced with $MeCONMe_2$ (DMA) in reactions with bis-phenyliodonium derivative **1f** (Scheme 2). The desired adduct, [*closo*-$B_{10}H_8$-1,10-$(OCMeNMe_2)_2$] (**1l**), was obtained in 64–67 % yield by column chromatography. Treatment of **1l** with $[Bu_4N]^+OH^-$ in MeCN smoothly led to the diacetate [*closo*-$B_{10}H_8$-1,10-$(OCOMe)_2]^{2-}$ $2[Bu_4N]^+$ (**1m[Bu$_4$N]**) isolated in 89–93 % yield.

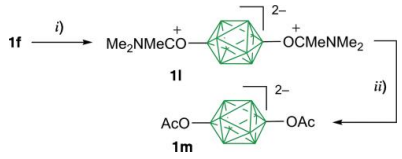

Scheme 2. Synthesis of diacetate **1m[Bu$_4$N]**. Reagents and conditions: *i)* DMA, 100 °C, 12 h; *ii)* $[Bu_4N]^+OH^-$, MeCN, 80 °C, 2 h.

Dianion **1h** and even its protonated form **1h-2H** are prone to oxidation and are unstable in most organic solvents. Only the solid-state form of **1h-2H** was found to be stable. For this reason, acylation of the dihydroxy derivative **1h** was conducted in strictly anaerobic atmosphere. Thus, a reaction of C_6H_5COCl with **1h-2H** in THF in the presence of excess NaH under argon atmosphere resulted in the formation of the corresponding dibenzoyloxy derivative [*closo*-$B_{10}H_8$-1,10-$(OCOPh)_2]^{2-}$ **1n** (Scheme 3). To increase solubility of the disodium salt **1h[Na]** formed in situ from **1h-2H** and NaH, stoichiometric amounts of $[Bu_4N]^+Br^-$ were added. Alternatively, the co-crystalline **1h-2H·[Bu$_4$N]Cl** (vide supra) was used. Pure product **1n[Bu$_4$N]** was isolated by column chromatography in about 40 % yield. The $[Bu_4N]^+$ cation was exchanged for $[Me_4N]^+$ by passing a solution of **1n[Bu$_4$N]** through an ion exchange column and treatment of its acidic form **1n[H$_3$O]** in H_2O either with $[Me_4N]^+Cl^-$ or $[Me_4N]^+OH^-{\cdot}5H_2O$. Pure salt **1n[Me$_4$N]** was isolated in both cases in about 70 % yield by filtration.

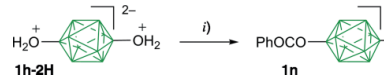

Scheme 3. Synthesis of diester **1n[Bu$_4$N]**. Reagents and conditions: *i)* NaH, $[Bu_4N]^+Br^-$, PhCOCl, THF, Ar, r.t., 2 h.

Crystal and Molecular Structures

Colorless orthorhombic crystals of **1i[Pr$_4$N]** and monoclinic crystals of **1k[Bu$_4$N]** were obtained by slow evaporation of $MeOH/H_2O$ and acetone/H_2O solutions, respectively, at ambient temperature. Similar approach to grow crystals of **1h-2H** from its aqueous solutions repeatedly gave only thin microcrystals unsuitable for conventional XRD analysis. Therefore, monoclinic co-crystals **1h-2H·[Bu$_4$N]Cl** were obtained by slow evaporation of $MeOH/H_2O$ solutions. Finally, monoclinic crystals of DMF adduct **1j** and triclinic crystals of bisphenyliodonium zwitterion **1f** were obtained by slow cooling of their MeCN solutions. Solid-state structures of these crystals were determined by low temperature single-crystal X-ray analysis. Results are shown in Table 1 and in Figure 3, Figure 4, Figure 5, and Figure 6, while detail of data collection and refinement are provided in the SI.

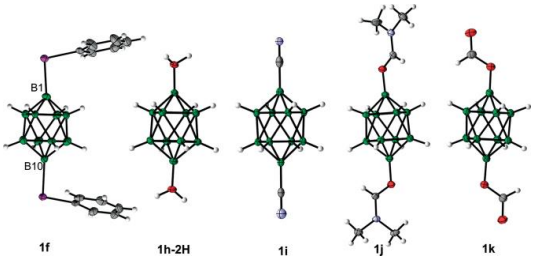

Figure 3. Atomic displacement ellipsoid representation for **1f**, **1h-2H**, **1i**, **1j** and **1k**. For geometrical dimensions see table 1 and the text. In **1f** only one symmetrically independent molecule is shown, while solvent MeCN molecule in **1j**, $[Bu_4N]Cl$ in **1h-2H**, and counterions in **1i** and **1k**, are omitted for clarity. Atomic displacement ellipsoid diagram drawn at 50 % probability and the numbering system according to the chemical structure.

Table 1. Selected interatomic distances and angles for **A** and derivatives **1**.[a]

X =	**A[Q]**[b] H	**1a**[c] N_2^+	**1f**[d] PhI^+	**1g**[e] I	**1h-2H**[f] H_2O^+	**1i[Pr$_4$N]** CN	**1j** $[OCHNMe_2]^+$	**1k[Bu$_4$N]** OCHO	**1o**[g] $C_5H_5N^+$	**1p**[h] Me_2S^+
X–B	–	1.499(2)	2.178(7)	2.180(5)	1.484(1)	1.566(13)	1.478(8)	1.469(2)	1.529(2)	1.866(2)
B(1)–B(2)$_{avrg}$	1.701(3)	1.668(2)	1.67(1)	1.686(4)	1.683(6)	1.702(2)	1.689(4)	1.689(2)	1.685(4)	1.682(4)
B(1)···B(2–5)[i]	1.100	1.006	1.029	1.059	1.056	1.088	1.059	1.069	1.056	1.049
B(2)–B(3) $_{avrg}$	1.835(9)	1.881(6)	1.87(1)	1.857(4)	1.854(10)	1.852(1)	1.855(7)	1.850(8)	1.857(2)	1.859(7)
B(2)–B(6) $_{avrg}$	1.813(6)	1.796(8)	1.81(1)	1.815(4)	1.810(11)	1.810(3)	1.811(7)	1.813(7)	1.812(6)	1.810(8)
B–B(1)–X	130.3(12)	127(1)	128(2)	128.9(2)	129(2)	129.7(2)	129(2)	129.2(9)	128.8(18)	128.6(13)
B(1)···B(10)	3.717	3.494	3.56(1)	3.628	3.620	3.682	3.623	3.648	3.620	3.602

[a] All distances are in Å and angles in degrees. Except for unique in each molecule distances B–X and the cage size B(1)···B(10), all parameters are average values and the esd refers to the distribution of individual values. [b] Q = 2,2′-bipyridinium, ref.[30] [c] Ref.[23] [d] Average values for 3 unique molecules. [e] Ref.[12] [f] Analyzed as a co-crystal with $2x[Bu_4N]^+Cl^-$. [g] Ref.[24] [h] Ref.[25] [i] The height of the square pyramid.

© 2020 Wiley-VCH Verlag GmbH & Co. KGaA, Weinheim

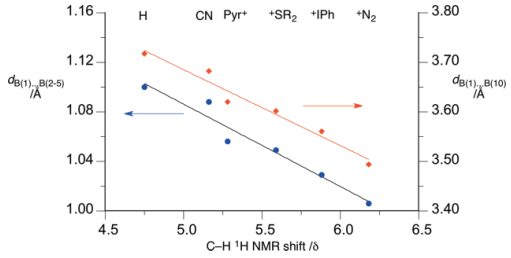

Figure 4. A correlation of geometrical parameters of the {*closo*-B_{10}} cage (pyramid height B(1)···B(2–5), blue dots, and length of the cage B(1)···B(10), red diamonds) with ^{1}H NMR chemical shifts of C(1)–H in [*closo*-1-CB_9H_9-10-X] derivatives. Best-fit lines: $d_{B(1)\cdots B(2\text{-}5)}$ = 1.42(4)–0.067(8) × $\delta_{C(1)H}$, r^2 = 0.951; $d_{B(1)\cdots B(10)}$ = 4.45(8)–0.15(1) × $\delta_{C(1)H}$, r^2 = 0.962.

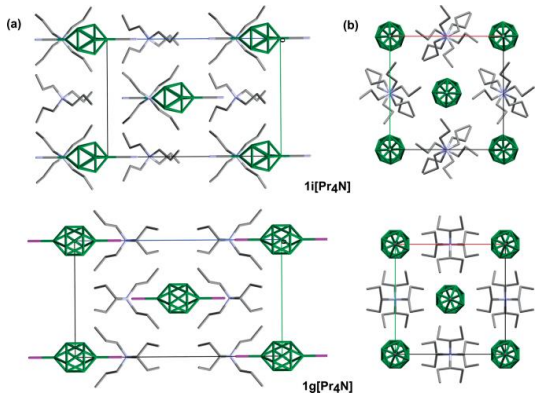

Figure 6. Crystal packing of **1i[Pr4N]** (top) and **1g[Pr4N]** (bottom) viewed along the *a* axis (a) and along the *c* axis (b).

Crystal systems of **1h-2H·[Bu_4N]Cl**, **1j** and **1k[Bu_4N]** contain a single molecule in the asymmetric unit and 4 molecules in the unit cell, while dinitrile **1i[Pr_4N]** crystallizes in a tetragonal system. In the latter, [*closo*-$B_{10}H_8$-1,10-$(CN)_2$]$^{2-}$ and $[Pr_4N]^+$ ions are positioned on a 4-fold rotation axis and 2-fold rotation axis, respectively. The symmetry of **1i** results in 2 formula units in the unit cell. In contrast, the asymmetric unit cell of **1f** contains 3 symmetrically independent molecules, while that for **1j** also contains a molecule of crystallization solvent (MeCN).

Data in Table 1 show that the {*closo*-B_{10}} cage dimensions in **1f** and **1h–1k** (Figure 3) are typical for {*closo*-B_{10}} derivatives as exemplified with the parent **A** and derivatives **1a**,[23] **1g**,[12] and also [*closo*-1-$B_{10}H_8$-1,10-$(NC_5H_5)_2$] (**1o**)[24] and [*closo*-1-$B_{10}H_8$-1,10-$(SMe_2)_2$] (**1p**).[25] Analysis of the data indicates that the cage geometry responds to the nature of the apical substituent. Thus, as observed before,[4b,26] the height of the square pyramid, B(1)···B(2–5), and the B(1)···B(10) increase with decreasing electron withdrawing character of the substituent and in series **1** they are in the order N_2^+ < $^+$IPh < $^+SMe_2$ < $^+OH_2$ ≈ $C_5H_5N^+$ < $[OCHNMe_2]^+$ < I < OCHO < CN < H (Table 1). An unusually strong effect on the {*closo*-B_{10}} cage geometry is observed for iodine-containing substituents, $^+$IPh and I. This is consistent with the previously reported higher-than-expected ^{1}H NMR chemical shifts of the C(1)–H in [*closo*-1-CB_9H_9-10-IPh].[26a] On the other hand, {*closo*-B_{10}} cage contraction observed in the 1,10-dicyano derivative is smaller than expected on the basis of the order of Hammett substituent parameters (CN > OCOR > I > H).[27] This discrepancy is presumably related to the particularly effective electronic interactions between the *sp*-hybridized CN group and C_4 symmetry apical boron atom.

It was noticed that the substituent effect on {*closo*-B_{10}} cage dimensions correlates well with the ^{1}H NMR chemical shifts of the C(1)–H in [*closo*-1-CB_9H_9-10-X] derivatives[26a] (Figure 4) indicating that similar electronic effects affect both the molecular structure and spectroscopic properties in 10-vertex clusters. This phenomenological correlation demonstrates consistency of the substituent electronic effects within the 10-vertex clusters, which are apparently different from those established in benzene derivatives.

The B–O interatomic distance in derivatives **1h-2H**, **1j** and **1k** is about 1.48 Å (Table 1). A comparison of **1j** with the reported[28] structure for [*closo*-$B_{10}H_9$-2-$(OCHNMe_2)$]$^-$ demonstrates that the B–O distance (avg 1.478 Å) in the former is shorter by 0.012 Å, while other dimensions of the $OCHNMe_2$ group are essentially the same within the experimental error. This difference in the B–O distance may result from different steric requirements of the apical B(1) vs. equatorial B(2) positions, different electronic interactions with the {*closo*-B_{10}} cluster at these two positions or the antipodal effect of the second DMF substituent at the B(10) position in **1j**. Similar comparisons of the substituent position on its geometrical parameters in the formyloxy derivatives **1k** and [*closo*-$B_{10}H_9$-2-(OCHO)]$^{2-}$ are not possible due to the significant positional disorder in the latter structure.[28,29]

The interatomic distances B–C and C≡N in the dinitrile **1i** are atypical and the former (avrg 1.566 Å) is longer, while the latter (avrg 1.084 Å) is significantly shorter than those in structurally similar boron cluster nitriles: 1.5420(3) Å and 1.1640(3) in [*closo*-B_6H_5-1-CN]$^{2-}$,[31] 1.542(2) Å and 1.157(2) in [*closo*-$B_{11}H_{10}$-2-CN]$^{2-}$,[32] and 1.550(3) Å and 1.133(4) in [*closo*-1-$CB_{11}H_{11}$-12-CN]$^-$.[15a] There is however a report of an unusually short C≡N

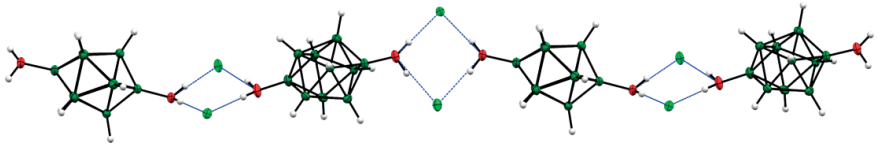

Figure 5. Undulating chain of **1h-2H** molecules connected through two Cl^- anions running along the [101] direction. Atomic displacement ellipsoid diagram drawn at 50 % probability.

© 2020 Wiley-VCH Verlag GmbH & Co. KGaA, Weinheim

Full Paper
doi.org/10.1002/ejic.202000456

distance found in [*closo*-1-$CB_{11}HMe_{10}$-12-CN]$^-$ anion (0.99(5) Å).[20] The B–I distances (avrg 2.178(7) Å) and B–I–C angles (avrg 98.2(3)°) in **1f** are similar to those in other phenyliodonium derivatives of *closo*-boranes.[33] The PhI groups in **1f** are pseudo *syn* to each other and oriented 1–21° (avrg 10(8)°) off the ideal staggered conformation with respect to the {*closo*-B_{10}} cage.

Substituents $[OCHNMe_2]^+$ and OCHO in **1j** and **1k**, respectively, are planar and adopt pseudo-staggered orientation with respect to the cage. The formate groups in **1k** are about 12.5° off the ideal staggered conformation and, consequently form an interplanar angle of 20.7°. In derivative **1j** one DMF substituent is nearly staggered (38.4° interplanar angle), while the second is closer to the eclipsed orientation (10.9°) relative to the {*closo*-B_{10}} cage.

The oxygen atoms in the two $^+OH_2$ substituents in **1h-2H** are pyramidalized and they are away from the plane, defined by 3 substituents at each oxygen atom (H, H, and B), by 0.206 Å and 0.253 Å. Further analysis indicates that oxygen atom lone pairs are about 19° and 29° off the ideal staggered orientation with respect to the cage.

The crystal packing in **1h-2H·[Bu_4N]Cl** is particularly noteworthy. It shows that the Cl^- ions are coordinated to both protons of each OH_2 group, which results in an undulating chain of **1h-2H** molecules connected through two Cl^- anions (Figure 5) with an average O···Cl distance of 2.94(3) Å (–0.33(3) Å inside the Van der Waals separation). The average O–H distance is 0.95(3) Å, while for the Cl···H it is 2.00(6) Å, which is –0.95(6) Å inside the Van der Waals separation or 0.725 Å longer that for the H–Cl bond in gas phase (1.2745 Å).[34]

The supramolecular assembly of the dicyano derivative **1i[Pr_4N]** appears to be isostructural to that observed in diiodo derivative **1g[Pr_4N]** (Figure 6). Unit cell dimensions *a* and *b* of **1i[Pr_4N]** and **1g[Pr_4N]** are nearly identical, while the *c* dimension is longer, which results in unit cell similarity[35] parameter Π = 0.04. The observed structural differences result from the substituent size (I vs. CN) and symmetry of the crystal structure (*I*422 vs. *P*4nc).

Molecular Modeling

For a better understanding of the observed reactivity, molecular geometries and electronic structures of selected derivatives **1** and some of their analogues (see the SI) were modeled at the B3LYP/TZVP level of theory. The resulting wavefunctions were subjected to NBO population analysis to obtain natural charges and bond order indices. Computational results were compared to the available experimental data and are shown in Table 2 and Table 3.

A comparison of geometries calculated in vacuo with experimental B(1)···B(10) distances (Table 1) demonstrated good correlation only for the anionic derivatives (**A**, **1g**, **1i**, **1k**), while the distances calculated for bis-zwitterions were typically too short (except for **1a**, Figure 7). This discrepancy is presumably due to the calculated high concentration of the positive charge on the atoms attached directly to the apical boron atoms, which gives rise to the minimal charge separation preferred in vacuo. A medium with a higher dielectric constant, such as that in the investigated solid crystals of **1**, would allow for charge diffusion and, in consequence, expansion of the {*closo*-B_{10}} cage, according to the general trend in Table 1.

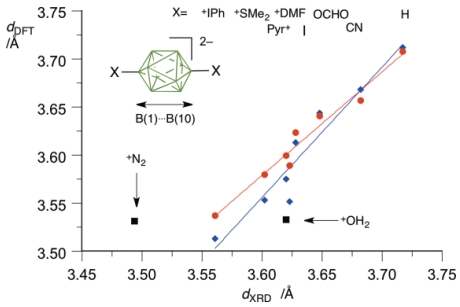

Figure 7. A comparison of experimental (XRD) and computational (B3LYP/TZVP) B(1)···B(10) distance in series **1**: calculations in vacuo (blue diamonds), best fit line: $d_{DFT} = -1.32(57) + 1.35(16) \times d_{XRD}$, $r^2 = 0.926$; calculations in PhCl dielectric medium, (red circles), best fit line: $d_{DFT} = 0.995(1) \times d_{XRD}$, $r^2 = 0.962$. The correlation does not include data for **1a** and **1h-2H** shown as black squares.

The effect of dielectric strength of the medium on molecular geometry and spectroscopic properties was investigated for two zwitterions **1a** and **1j** using the PCM model[36] and a set of five solvents with the dielectric constant ε ranging from 2.25 (benzene) to 78.39 (water).[37] Results demonstrate that the B(1)···B(10) distance, chosen as the geometrical probe, expands in both compounds with increasing value of ε and 80 % of the change is obtained for ε ≈ 6 for **1a** (Δ = 0.010 Å) and ε ≈ 7 for **1j** (Δ = 0.039 Å). The observed 4 times stronger dielectric medium effect on the geometry of **1j** than on **1a** is due to the resonance form **1j-II**, in which the positive charge is shifted away from the oxygen atom (Figure 8).

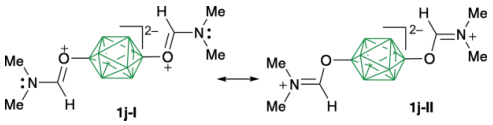

Figure 8. Two resonance forms of **1j** showing different distribution of the positive charge. Contribution of **1j-II** is expected to be important in high ε media.

Further analysis demonstrates that the dielectric medium also affects characteristic vibrational frequencies of functional groups, albeit to small extent. For instance, the $\nu_{N\equiv N}$ frequency in **1a** is shifted to higher energies by 15.5 cm^{-1}, while the C=N in **1j** by only 3.2 cm^{-1} in water relative to vacuum with most of the change taking place at about ε = 6–9. The vibrational frequency change in **1a** is substantial, while in **1j** is comparable to the experimental error. Since dielectric constant of solid compounds **1** and their analogues may vary significantly due to ionic or highly polar character of constituting molecules, dielectric constant of 5.62 (PhCl) was chosen arbitrarily for further investigation.

The B(1)···B(10) distance in structures **1** optimized in dielectric medium of PhCl (ε = 5.62) correlates much better with the

© 2020 Wiley-VCH Verlag GmbH & Co. KGaA, Weinheim

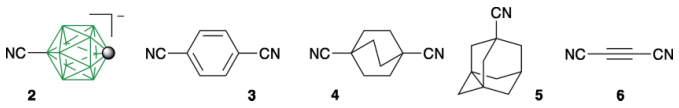

Figure 9. Structures of related nitriles.

experimental data affecting mainly the geometry of the zwitterions (Figure 7). The only outliers in this correlation are **1a** and **1h-2H**. In the latter, the $^{+}OH_2$ group is coordinated with Cl^{-} anions (Figure 5), which effectively diminishes the electron withdrawing character of the substituent and leads to the larger-than-calculated B(1)···B(10) distance. The calculated size of the {*closo*-B_{10}} cage in **1a** remains larger than that reported experimentally.[23] Assuming validity of the correlation in Figure 7, the expected B(1)···B(10) distances for **1a** and **1h-2H** are 3.549 Å and 3.551 Å, respectively. Also, selected experimental geometrical parameters in series **1**, such as B–X, C–O, C=O, C=N, S–C, and I–C distances, correlate well with the DFT-values calculated in PhCl dielectric medium.[37]

Analysis of structural data for **1i** and 11 other related nitriles revealed poor correlation of the calculated and experimental C≡N bond length, which all, except for **1i**, are in a range 1.133–1.164 Å. On the other hand, the X–C distance is well reproduced by the DFT calculations for all 12 derivatives with the worst result for **1i** (r^2 = 0.969 for all and r^2 = 0.986 without **1i**).[37]

NBO population analysis demonstrates significant differences in bonding and distribution of electron density in **1i** and model compounds representative for 12-vertex (**2**, Figure 9), aromatic (**3**), aliphatic (**4** and **5**) and acetylene (**6**, Table 2) derivatives. Thus, the bond order of the C≡N group for **1i** is the second lowest in the series and it increases in the order C≡C <{*closo*-B_{10}} < benzene < {*closo*-CB_{11}} < bicyclo[2.2.2]octane, which is consistent with the expected strength of π–π interactions in these compounds. Analysis of the X–C bond demonstrates that the bond order is generally lower in the boron cluster derivatives than in the hydrocarbon analogues. It is slightly higher for 10-vertex derivative **1i** than for the 12-vertex analogue **2**, which is in agreement with previous findings.[3c] Among the hydrocarbon analogues the X–C bond order is, as expected, related to the bond length $d_{C–CN}$ governed by the carbon atom hybridization and effectiveness of the π–π interactions: C≡C > benzene > bicyclo[2.2.2]octane. This relatively high effectiveness of electronic interactions between the {*closo*-B_{10}} clusters and the CN group is also apparent from the distribution of the FMOs in **1i** shown in Figure 10.

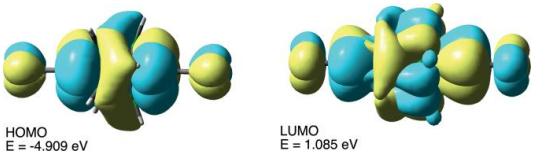

Figure 10. Contours and energies of frontier molecular orbitals for **1i** obtained at the B3LYP/TZVP level of theory in PhCl dielectric medium.

A consequence of the effective conjugation in dinitrile **1i** is significant delocalization of the negative charge density from the cluster to the CN group (Table 2). Thus, the CN group in **1i** has the highest electron density in the series (–0.254e) with the most negative N atom (–0.493e). Also, the electrophilicity of the carbon atom is among the lowest in the series, which is consistent with the observed resistance to hydrolysis and reduction.

IR Spectroscopy

Electronic interactions in derivatives of the [*closo*-$B_{10}H_{10}]^{2-}$ anion and its analogues were probed using IR spectroscopy. Data in Table 3 shows that the C≡N stretching frequency in **1i** ($\nu_{C≡N}$ = 2183 cm^{-1}) is significantly lower than that for the [*closo*-1-$CB_{11}H_{11}$-12-CN]$^{-}$ ($\nu_{C≡N}$ = 2215 cm^{-1})[15a] and hydrocarbon analogues, and similar to those measured for [*closo*-$B_{11}H_{10}$-2-CN]$^{2-}$ ($\nu_{C≡N}$ = 2180 cm^{-1})[32] and [*closo*-B_6H_5-1-CN]$^{2-}$ ($\nu_{C≡N}$ =

Table 2. Selected molecular parameters for **1i** and its analogues.[a]

		1i	2	3	4	6
$d_{C≡N}$ /Å	exp	1.084(20)	1.133(4)[b]	1.145(2)[c]	1.148(2)[d]	1.14[e]
	calcd	*1.160*	*1.156*	*1.154*	*1.153*	*1.157*
$d_{X–CN}$ /Å	exp	1.566(13)	1.550(3)[b]	1.441(1)[c]	1.475(2)[d]	1.37[e]
	calcd	*1.527*	*1.552*	*1.430*	*1.460*	*1.362*
Bond order[f]						
	C≡N	2.851	2.898	2.864	2.907	2.765
	X–C	0.995	0.982	1.091	1.029	1.198
Natural charge[g]						
	q_N	–0.493	–0.435	–0.329	–0.371	–0.222
	q_C	0.239	0.238	0.293	0.333	0.209
Total natural charge						
	$q_N + q_C$	–0.254	–0.197	–0.036	–0.038	–0.013

[a] Obtained at the B3LYP/TZVP level of theory in PhCl dielectric medium for structures in Figure 9. [b] Ref.[15a] [c] Ref.[38] [d] Data for 5-cyano-1,3-dehydroadamantane (**5**) Ref.[39] [e] Ref.[40] [f] NBO analysis: Wiberg bond index. [g] NBO analysis: natural charge.

© 2020 Wiley-VCH Verlag GmbH & Co. KGaA, Weinheim

Table 3. Selected molecular parameters for **1i** and its analogues.

X		**1**[a] ν /cm^{-1}	$[B_{10}H_9$-2-X$]^-$ ν /cm^{-1}	$[CB_{11}H_{11}$-12-X$]^-$ ν /cm^{-1}	Ph–X ν /cm^{-1}	*t*Bu-X ν /cm^{-1}
C≡N	exp	2183	–	2215[b]	2259[c]	2236[d]
	calcd[e]	*2265*	*2265*	*2311*	*2334*	*2340*
OC(H)=O	exp	1686	1697[f]	–	1739[g]	1723[h]
	calcd[e]	*1716*	*1716*	*1743*	*1802*	*1769*
$[OCH(=NMe_2)]^+$	exp	1671	–	–	–	–
	calcd[e]	*1704*	*1697*	*1700*	–	–

[a] Obtained in KBr. [b] In KBr; ref.[15a]. [c] Film; ref[41]. [d] Film; ref[43]. [e] B3LYP/TZVP level of theory in PhCl dielectric medium. [f] In Nujol; ref.[29]. [g] Neat; ref.[44]. [h] Neat; ref.[45]

2149 cm^{-1}).[31] The order of experimental vibrational frequencies, {*closo*-B_6} < {*closo*-B_{10}} ≈ {*closo*-B_{11}} < {*closo*-CB_{11}} < benzene < R_3C, generally follows that for bond order in the C≡N group (Table 2) and is well reproduced with DFT calculations for a total of 10 diverse nitriles (r^2 = 0.987).[37]

Analysis of experimental C=O vibrational frequencies in Table 3 demonstrates a markedly lower force constant in {*closo*-B_{10}} derivatives, **1k** and $[closo$-$B_{10}H_9$-2-OCHO$]^{2-}$, than in the hydrocarbon analogues, which is well reproduced with DFT calculations. The observed trends in vibration frequencies are consistent with those in 4-substituted benzonitrile ($\nu_{C\equiv N}$)[41] and phenyl benzoate ($\nu_{C=O}$)[42] derivatives, in which electron donating substituents reduce the bond order through the resonance effect and shift the position of the stretching vibration band to lower wavenumbers.

Discussion

Bis-phenyliodonium derivative $[closo$-$B_{10}H_8$-1,10-$(IPh)_2]$ (**1f**) serves as a convenient starting material for preparation of 1,10-disubstituted derivatives of the $[closo$-$B_{10}H_{10}]^{2-}$ anion and two such compounds have been obtained in high yields: dinitrile **1i** and bis DMF adduct **1j**. Attempted hydrolysis of the former to dicarboxylic acid $[closo$-$B_{10}H_8$-1,10-$(COOH)_2]^{2-}$ (**1e**) failed; it was unreactive under standard conditions, while under forcing conditions, used to hydrolyze $[closo$-1-$CB_{11}H_{11}$-12-CN$]^-$ (**2**),[15] a complex mixture of products was observed, presumably related to acetoxylation of the {*closo*-B_{10}} cluster.[16]

This difference in reactivity of the two nitriles is related to high negative charge density on the CN group in **1i** and hence its low electrophilicity on one hand, and higher energy of the HOMO in the {*closo*-B_{10}} cage (E = –4.91 eV in **1i**) relative to that in the {*closo*-CB_{11}} anion (E = –7.37 eV in **2**) on the other. Consequently, the {*closo*-B_{10}} cage is more susceptible to protonation and subsequent nucleophilic substitution reactions[1b] rather than hydrolysis of the nitrile group. This high electron density on the CN group in **1i**, resulting from effective electronic conjugation between {*closo*-B_{10}} and CN, is however desired for formation metal complexes[46] and these results will be reported elsewhere.

The issue of an alternative synthesis of diacid **1e** avoiding CO under high pressure still remains open. One potentially attractive approach to **1e** is Pd-catalyzed carbonylation of the readily available diiodide **1g**,[12] using CO surrogates.

The bis-phenyliodonium **1f** provides a convenient access to the previously unknown dihydroxy derivative **1h-2H**; it is available in 4 steps from the parent dianion **A** and 40 % overall yield. The only previously reported $[closo$-$B_{10}H_9$-1-OH$]^{2-}$ was obtained in 82 % yield by decomposition of monodinitrogen derivative $[closo$-$B_{10}H_9$-1-$N_2]^-$ in aqueous NaF,[47] while the equatorial isomer $[closo$-$B_{10}H_9$-2-OH$]^{2-}$ was easily prepared by alkaline hydrolysis of the formate or acetate ester.[16] The readily available[12] $[closo$-$B_{10}H_9$-1-IPh$]^-$ offers a potentially alternative route to the 1-hydroxy derivative following the sequence described for **1h-2H**.

Conditions for hydrolysis of DMF adduct **1j** to the dihydroxy derivative **1h-2H** deserve some comments. Bis-zwitterion **1j** is resistant to dilute acids, while formate **1k** is resistant to alkaline hydrolysis, conditions used to convert equatorial isomers e.g. *N*-methylpyrrolidinium **7**[9c] and 2-acyloxy **8**,[16,21] to 2-hydroxy derivative **9** (Scheme 4). This striking difference in reactivity of the 1- vs. 2-acyloxy derivatives suggests higher nucleophilicity of the ester group at the B(1) than at B(2) position. Surprisingly, DFT calculations did not reveal significant differences in the electronic structures of the two isomers. All these synthetic results provide additional evidence of unusually strong impact of boron clusters on reactivity of functional groups.

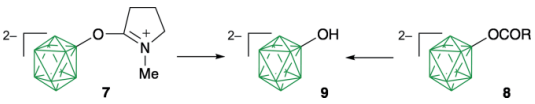

Scheme 4. Synthesis of $[closo$-$B_{10}H_9$-2-OH$]^{2-}$ from two precursors.

Single crystal XRD data permitted detailed analysis of trends in the substituent effect on the {*closo*-B_{10}} cluster geometry. Thus, analysis of experimental molecular structures in a series of $[closo$-$B_{10}H_8$-1,10-$X_2]^{2-}$ (**1**) demonstrated significant sensitivity of the apical position to the electronic nature of the substituent X: increasing withdrawal of electron density results in progressive contraction of the B(1)···B(10) distance in the cluster. Interestingly, the relative magnitude of the effect does not fully follow the order of the Hammett substituent constants σ_p indicating differences in interactions of substituents in benzene and boron cluster derivatives. This substituent effect on the {*closo*-B_{10}} cluster dimensions correlates well with the effect on the NMR spectra in derivatives of another 10-vertex cluster, {*closo*-CB_9}.

© 2020 Wiley-VCH Verlag GmbH & Co. KGaA, Weinheim

The phenomenon of cage contractions is also well reproduced with the B3LYP/TZVP computational method. High correlation of experimental and DFT-calculated values is obtained, when geometry optimizations are performed in a dielectric medium of a moderate strength. The inclusion of dielectric medium is particularly important for zwitterions, in which the charge separation (distribution) is medium-dependent, and hence concentration of the positive charge at the atom attached directly to the apical boron. This, in turn, impacts the apical position geometry. These geometrical effects are better seen in a series of compounds rather than in analyses of individual molecular models. Vibrational frequencies are dielectric strength dependent to a much smaller extent and this effect can be neglected when compared with experimental data.

Conclusions

The bis-phenyliodonium derivative [*closo*-$B_{10}H_8$-1,10-(IPh)$_2$] (**1f**) is convenient precursor for synthesis of 1,10-difunctionalized derivatives of the [*closo*-$B_{10}H_{10}$]$^{2-}$ anion (**A**) such as dinitrile **1i** and dihydroxy derivative **1h-2H**. While the former could not be converted into the dicarboxylic acid **1e**, it appears to be a potentially attractive ligand for metal complexes with strong binding nitrile. The dihydroxy **1h-2H** is considered as a new type of building block for construction of self-organizing materials. This work is in progress.

Analysis of experimental and computational structural data for a series of derivatives **1** revealed the importance of inclusion of dielectric medium in geometry optimization of boron cluster zwitterions. It also demonstrated that the substituent effect on the cluster geometry does not fully follow the Hammett substituent parameters σ_p established for benzene derivatives.

Computational Details

Quantum-mechanical calculations were carried out using Gaussian 09 suite of programs.[48] Geometry optimizations were performed with the B3LYP functional and Ahlrichs TZVP basis set,[49] which performed better than the standard 6-31G(2d,p) basis set, using tight convergence limits and appropriate symmetry constraints. The nature of stationary points was confirmed with vibrational frequency calculations. Zero-point energy (ZPE) corrections were scaled by 0.9806. Population analysis was performed with the NBO method. Solvent effects were implemented with the PCM model[36] using the SCRF(solvent=*name*) keyword. More details are provided in the SI.

Experimental Section

General. The bis-iodonium zwitterion [*closo*-$B_{10}H_8$-1,10-(IPh)$_2$] (**1f**) was obtained using a literature procedure.[10] NMR spectra were obtained at 500 MHz (^{1}H), 125.8 MHz (^{13}C) and 160.5 MHz (^{11}B) in [D$_6$]acetone, CD_3CN or D_2O unless indicated otherwise. Chemical shifts were referenced to the solvent ([D$_6$]acetone: 2.05 ppm for ^{1}H and 206.26 ppm for ^{13}C; CD_3CN: 1.94 ppm for ^{1}H and 118.26 ppm for ^{13}C; D_2O: 4.79 ppm for ^{1}H)[50] and to an external sample of neat BF_3·Et_2O in [D$_6$]acetone, CD_3CN and D_2O (^{11}B, δ = 0.0 ppm). More details are provided in the SI.

Preparation of [*closo*-$B_{10}H_8$-1,10-(OH$_2$)$_2$] (1h-2H). To a solution of [*closo*-$B_{10}H_8$-1,10-(OCOH)$_2$]$^{2-}$ 2[Bu_4N]$^+$ (**1k[Bu$_4$N]**, 500 mg, 0.72 mmol) in MeOH (6 mL) was added 6–7 drops of conc. HCl and allowed to stir at room temperature for 30 minutes. The reaction proceeded with initial bubbling and the progress was monitored using TLC (SiO_2, CH_2Cl_2/MeCN, 3:2). The solvent was evaporated, and the semi-solid residue was dissolved in water (8 mL) and the solution was washed twice with CH_2Cl_2 (2 × 5 mL). The aqueous layer was passed through Dowex-50 cation exchange resin and evaporated to give 80 mg (72 % yield) of **1h-2H** as an off white solid. The typical yield for the reaction was in a range 68–72 %: m.p. 95–100 °C dec.; ^{1}H NMR (500 MHz, D_2O) δ 0.38 (q, *J* = 117 Hz, 8H); ^{11}B NMR (160 MHz, D_2O) δ = –34.8 (d, *J* = 128 Hz, 8B), 14.7 (s, 2B); IR (ATR) $\nu_{ma\times}$ 3531 and 3385 (O-H), 2472 (B–H), 1210 cm^{-1}. Anal. Calcd for $H_{12}B_{10}O_2$: H, 7.95. Calcd for $H_{12}B_{10}O_2$·1/2H_2O: H, 8.13. Found: H, 8.11.

Preparation of [*closo*-$B_{10}H_8$-1,10-(OH$_2$)$_2$]·[Bu_4N]Cl (1h-2H·[Bu$_4$N]Cl). The aqueous layer obtained as described above from 500 mg (0.72 mmol) of **1k[Bu$_4$N]**, was washed with CH_2Cl_2, concentrated and left for crystallization. The resulting crystals were filtered and dried giving 350 mg (68 % yield) of the mixed salt **1h-2H·[Bu$_4$N]Cl**. The typical yield for the reaction was in a range 62–68 %: m.p. 95–100 °C; ^{1}H NMR (500 MHz, D_2O) δ 0.34 (q, *J* = 118, 8H), 0.91 (t, *J* = 7.5 Hz, 24H), 1.32 (sext, *J* = 7.4 Hz, 16H), 1.61 (qiunt, *J* = 8.0 Hz, 16H), 3.15 (t, *J* = 8.7 Hz, 16H); ^{11}B NMR (160 MHz, D_2O) δ –33.9 (d, *J* = 109 Hz, 8B), 15.5 (s, 2B); ^{13}C NMR (125 MHz, D_2O) δ 12.8, 19.1, 23.1, 58.0; IR (KBr) ν_{max} 3340 and 3210 (br, O-H), 2963 and 2875 (C-H), 2483 (B–H), 1483, 1197 cm^{-1}; HRMS ESI-TOF(–), calcd. for $B_{10}H_{10}O_2$ *m/z*: 152.1611, found 152.1610. Anal. Calcd for $H_{12}B_{10}O_2$·$C_{32}H_{72}Cl_2N_2$ (1:2 ratio): C, 54.28; H, 11.96; N, 3.96. Found: C, 55.79; H, 13.67; N, 3.98.

Preparation of [*closo*-$B_{10}H_8$-1,10-(CN)$_2$]$^{2-}$ 2[Et_4N]$^+$ (1i[Et$_4$N]). To a solution of [*closo*-$B_{10}H_8$-1,10-(IPh)$_2$] (**1f**, 200 mg, 0.38 mmol) in dry MeCN (1 mL) was added [Et_4N]$^+$CN$^-$ (179.0 mg, 1.14 mmol). The heterogeneous mixture was stirred at 65 °C for 24 h giving a homogeneous orange solution. The solvent was evaporated, and the residue was treated with cold MeOH. The resulting solid was filtered and recrystallized from MeOH to give 110 mg (67 % yield) of **1i[Et$_4$N]** as a colorless microcrystalline solid. The typical yield for the reaction was in a range 62–67 %: m.p. >250 °C; ^{1}H NMR (500 MHz, CD_3CN) δ 0.44 (q, *J* = 131 Hz, 8H), 1.22 (t, *J* = 7.3 Hz, 24H), 3.18 (q, *J* = 7.3 Hz, 16H); ^{13}C NMR (125 MHz, CD_3CN) δ 7.7, 53.0 (CN not observed); ^{11}B NMR (160 MHz, CD_3CN) δ = –24.4 (d, *J* = 130 Hz, 8B), –4.1 (s, 2B); IR (KBr) ν_{max} 2486 (B–H), 2183 (C≡N) cm^{-1} (lit.[13] for **1i[Cs]** in Nujol: 2175 cm^{-1}); HRMS ESI-TOF(–), calcd. for $C_2H_8B_{10}N_2$·Na *m/z*: 193.1516, found 193.1520. Anal. Calcd for $C_{18}H_{48}B_{10}N_4$: C, 50.43; H, 11.29; N, 13.07. Found: C, 50.21; H, 11.39; N, 12.89.

Exchange of the [Et_4N]$^+$ cation and formation of **1i[Bu$_4$N]** and **1i[Pr$_4$N]** salts was accomplished by passing MeCN solution of **1i[Et$_4$N]** through Dowex-50 cation exchange resin column, adding water removing MeCN and precipitation of the salt using appropriate [R_4N]$^+$Br$^-$. The yield was nearly quantitative.

1i[Pr$_4$N]: m.p. > 250 °C. Anal. Calcd for $C_{26}H_{64}B_{10}N_4$: C, 57.73; H, 11.93; N, 10.36. Found: C, 57.52; H, 11.85; N, 10.34.

1i[Bu$_4$N]: m.p. 170–175 °C. Anal. Calcd for $C_{34}H_{80}B_{10}N_4$: C, 62.52; H, 12.35; N, 8.58. Found: C, 62.19; H, 12.31; N, 8.41.

Preparation of [*closo*-$B_{10}H_8$-1,10-(OCHNMe$_2$)$_2$] (1j). A solution of [*closo*-$B_{10}H_8$-1,10-(IPh)$_2$] (**1f**, 500 mg, 0.95 mmol) in DMF (5 mL) was

© 2020 Wiley-VCH Verlag GmbH & Co. KGaA, Weinheim

stirred at 80 °C for 12 h. DMF was removed under vacuum and the oily residue was washed with Et_2O to yield an off white solid. The solid was recrystallized (MeCN) to give 180 mg (72 % yield) of pure adduct **1j**. The typical yield for the reaction was in a range 68–73 %: m.p. > 250 °C; ^{1}H NMR (500 MHz, CD_3CN) δ 0.62 (q, *J* = 129 Hz, 8H), 3.30 (s, 6H), 3.33 (s, 6H), 8.81 (s, 2H); ^{13}C NMR (125 MHz, CD_3CN) δ = 36.0, 41.0, 168.5; ^{11}B NMR (160 MHz, CD_3CN) δ = –30.6 (d, *J* = 129 Hz, 8B), 21.9 (s, 2B); IR (KBr) ν_{max} 2478 (B–H), 1671 (C=N), 1331 cm^{-1}; HRMS ESI-TOF(–), calcd. for $C_6H_{21}B_{10}N_2O_2$ *m/z*: 263.2534, found 263.2534. Anal. Calcd for $C_6H_{22}B_{10}N_2O_2$: C, 27.47; H, 8.45; N, 10.68. Found: C, 27.51; H, 8.47; N, 10.59.

The XRD quality crystals were obtained by slow evaporation of MeCN solution of **1j** at ambient temperature.

Preparation of [*closo*-$B_{10}H_8$-1,10-$(OCHO)_2$]$^{2-}$ 2[Bu_4N]$^+$ (1k[Bu_4N]). To a suspension of [*closo*-$B_{10}H_8$-1,10-$(OCHNMe_2)_2$] (**1j**, 100 mg, 0.38 mmol) in MeCN (3 mL) was added 40 wt.-% aqueous solution of [Bu_4N]$^+$OH$^-$ (0.49 mL, 0.76 mmol). The reaction mixture was stirred at 80 °C (to ensure full solubility of **1j**) for 2 h to get a turbid solution. The solvent was evaporated, and water was added to the residue. The resulting precipitation was filtered and dried to give 245 mg (94 % yield) of **1k[Bu_4N]** as a white solid. The typical yield for the reaction was in a range 81–94 %: m.p. 138–142 °C; ^{1}H NMR (500 MHz, [D_6]acetone) δ 0.51 (q, *J* = 94 Hz, 8H), 0.97 (t, *J* = 7.3 Hz, 24H), 1.44 (sext, *J* = 7.4 Hz, 16H), 1.81 (quint, *J* = 7.8 Hz, 16H), 3.32 (pseudo t, *J* = 8.5 Hz, 16H), 9.07 (s, 2H); ^{13}C NMR (125 MHz, [D_6]acetone) δ 14.0, 20.4, 24.5, 59.4, 169.0; ^{11}B NMR (160 MHz, [D_6]acetone) δ –31.9 (d, *J* = 101 Hz, 8B), 16.6 (s, 2B); IR (KBr) ν_{max} 2471 (B–H), 1686 (C=O), 1252 (C-O) cm^{-1}; HRMS ESI-TOF (–), calcd. for $C_2H_{10}B_{10}O_4$ *m/z*, 208.1510, found 208.1509. Anal. Calcd for $C_{34}H_{82}B_{10}N_2O_4$: C, 59.09; H, 11.96; N, 4.05. Found: C, 59.14; H, 12.03; N, 4.02.

XRD quality needle crystals were obtained by slow evaporation of an acetone/water solution of **1k[Bu_4N]**.

Preparation of [*closo*-$B_{10}H_8$-1,10-$(OCMeNMe_2)_2$] (1l). Following the procedure above for **1j**, a solution of **1f** (500 mg, 0.95 mmol) in DMA (5 mL) was stirred at 100 °C for 12 h. Volatiles were removed in vacuo and the oily residue was separated by column chromatography (SiO_2, CH_2Cl_2/MeCN, 15:1 ratio) to give 180 mg (65 % yield) of pure **1l** as a white powder. The typical yield for the reaction was in a range 64–67 %: m.p. > 250 °C; ^{1}H NMR (500 MHz, CD_3CN) δ 0.58 (q, *J* = 128 Hz, 8H), 2.89 (s, 6H), 3.31 (s, 6H), 3.35 (s, 6H); ^{13}C NMR (125 MHz, CD_3CN) δ 17.5, 38.5, 40.6, 178.2; ^{11}B NMR (160 MHz, CD_3CN) δ = –30.6 (d, *J* = 128 Hz, 8B), 19.6 (s, 2B); IR (KBr) ν_{max} 2480 (B–H), 1625 (C=N), 1262 cm^{-1}; HRMS ESI-TOF(–), calcd. for $C_8H_{26}B_{10}N_2O_2$ *m/z*: 292.2925, found 292.2936. Anal. Calcd for $C_8H_{26}B_{10}N_2O_2$: C, 33.09; H, 9.02; N, 9.65. Found: C, 32.79; H, 9.11; N, 9.61.

Preparation of [*closo*-$B_{10}H_8$-1,10-$(OCOMe)_2$]$^{2-}$ 2[Bu_4N]$^+$ (1m[Bu_4N]). Following the procedure for the preparation of diformate **1k[Bu_4N]**, a solution of [*closo*-$B_{10}H_8$-1,10-$(OCMeNMe_2)_2$] (**1l**, 100.0 mg, 0.34 mmol) in MeCN (3 mL) was treated with 40 wt.-% aqueous solution of [Bu_4N]$^+$OH$^-$ (0.446 mL, 0.68 mmol). The mixture was stirred for 1 h at r.t., while the progress of the reaction was monitored with TLC (CH_2Cl_2/CH_3CN, 8:2 ratio). When starting **1m** was no longer detected, the solvent was evaporated, and the residue was extracted with CH_2Cl_2/water mixture. The organic layer was dried (Na_2SO_4) and solvents were removed to give 230 mg (92 % yield) of salt **1m[Bu_4N]** as a white powder: m.p. 147–150 °C; ^{1}H NMR (500 MHz, [D_6]acetone) δ 0.45 (q, *J* = 107 Hz, 8H), 0.97 (t, *J* = 7.3 Hz, 24H), 1.43 (sext, *J* = 7.2 Hz 16H), 1.79 (quint, *J* = 7.7 Hz, 16H), 2.44 (s, 6H), 3.43 (t, *J* = 8.5 Hz, 16H); ^{13}C NMR (125 MHz, [D_6]acetone) δ 14.0, 20.4, 23.0, 24.6, 59.3, 174.7; ^{11}B NMR (160 MHz, [D_6]acetone) δ –31.3 (d, *J* = 122 Hz, 8B), 16.8 (s, 2B); IR (ATR) ν_{max} 2462 (B–H), 1671 (C=O), 1320, 1200, 713 cm^{-1}; HRMS ESI-TOF(–), calcd. for $C_4H_{14}B_{10}O_4$ *m/z*: 236.1823, found 236.1833. Anal. Calcd for $C_{36}H_{86}B_{10}N_2O_4$: C, 60.12; H, 12.05; N, 3.90. Found: C, 60.09; H, 12.11; N, 3.94.

Preparation of [*closo*-$B_{10}H_8$-1,10-$(OCOC_6H_5)_2$]$^{2-}$ 2[Bu_4N]$^+$ (1n[Bu_4N]). [*closo*-$B_{10}H_8$-1,10-$(OH)_2$] (**1h-2H**, 40.0 mg, 0.26 mmol) and [Bu_4N]$^+$Br$^-$ (186 mg, 0.58 mmol) was placed in a three-necked round-bottomed flask (25 mL volume) and filled with Ar by three pump-fill cycles. Dry THF (8 mL) was added followed by NaH (37 mg, 1.58 mmol) and C_6H_5COCl (0.067 mL, 0.58 mmol) and the reaction mixture was stirred for 2 h at r.t. under Ar atmosphere. Reaction progress was monitored using TLC (SiO_2, CH_2Cl_2/MeCN, 3:2). Water was added to quench excess NaH, THF was removed with rotary evaporator and the residue was extracted with CH_2Cl_2/water. The organic layer was dried (Na_2SO_4) and solvent was evaporated. The resulting crude product was purified by column chromatography (SiO_2, CH_2Cl_2/MeCN, 3:2) to give 89.0 mg (40 % yield) of pure **1n[Bu_4N]** as a pale greenish solid. The typical yield for the reaction was in a range 35–40 %: m.p. 210–215 °C dec.; ^{1}H NMR (500 MHz, CD_3CN) δ 0.41 (q, *J* = 120 Hz, 8H), 0.96 (t, *J* = 7.5 Hz, 24H), 1.34 (sext, *J* = 7.4 Hz, 16H), 1.58 (sext, *J* = 8.0 Hz, 16H), 3.07 (pseudo t, *J* = 8.6, 16H), 7.50 (t, *J* = 7.2 Hz, 4H), 7.55 (t, *J* = 6.5 Hz, 2H), 8.20 (d, *J* = 8.0 Hz, 4H); ^{13}C NMR (125 MHz, CD_3CN) δ 13.8, 20.2, 24.2, 59.2, 129.1, 130.3, 132.3, 135.1, 169.3; ^{11}B NMR (160 MHz, CD_3CN) δ –31.9 (d, *J* = 117 Hz, 8B), 16.0 (s, 2B); IR (KBr) ν_{max} 2469 (B–H), 1670 (C=O), 1370, 1294 cm^{-1}; HRMS ESI-TOF(–), calcd. for $C_{14}H_{18}B_{10}O_4$ *m/z*: 360.2136, found 360.2149. Anal. Calcd for $C_{46}H_{90}B_{10}N_2O_4$: C, 65.51; H, 10.76; N, 3.32. Found: C, 65.59; H, 10.81; N, 3.40.

Instead of pure **1h-H** and [Bu_4N]$^+$Br$^-$, co-crystals **1h-H·2[Bu_4N]Cl** can be to used to obtained diester **1n[Bu_4N]** with a similar effect.

Preparation of [*closo*-$B_{10}H_8$-1,10-$(OCOC_6H_5)_2$]$^{2-}$2[Me_4N]$^+$ (1n[Me_4N]). A solution of **1n[Bu_4N]** (80.0 mg, 0.095 mmol) in MeCN (5 mL) was passed through a Dowex-50 ion exchange column. Water was added (10 mL), MeCN and some water were removed under reduced pressure (water bath < 40 °C) and the aqueous phase was extracted with CH_2Cl_2. Residual CH_2Cl_2 was removed in vacuo and excess [Me_4N]$^+$Cl$^-$ (or [Me_4N]$^+$OH$^-$·5H_2O) was added. The resulting solution was cooled in an ice bath and the precipitated compound was filtered and dried to give 35.0 mg, (72 % yield) of pure **(1n[Me_4N])** as a white solid: m.p. >250 °C; ^{1}H NMR (500 MHz, CD_3CN) δ 0.47 (q, *J* = 114 Hz, 8H), 3.08 (s, 24H), 7.50 (t, *J* = 7.0 Hz, 4H), 7.56 (t, *J* = 7.3 Hz, 2H), 8.20 (d, *J* = 6.9 Hz, 4H); ^{13}C NMR (125 MHz, CD_3CN) δ = 56.1, 129.1, 130.2, 132.1,136.0, 168.7; ^{11}B NMR (160 MHz, CD_3CN) δ –31.7 (d, *J* = 125 Hz, 8B), 15.9 (s, 2B); IR (ATR) ν_{max} 2468 (B–H), 1671 (C=O), 1321, 1201, 717 cm^{-1}. Anal. Calcd for $C_{22}H_{42}B_{10}N_2O_4$: C, 52.15; H, 8.35; N, 5.53. Found: C, 52.04; H, 8.42; N, 5.65.

X-ray data collection. Single-crystal X-ray diffraction measurements for **1h-2H** and **1i[Pr_4N]** were performed with a Rigaku XtaLAB Synergy, Dualflex, Pilatus 300K diffractometer, for **1j** and **1k[Bu_4N]** with Rigaku XtaLAB SuperNova, Pilatus 200K diffractometer, and for **1f** with a Bruker APEX-II CCD instrument. The measurements were conducted at 100.0(1) K or 123(2) K (for **1f**) using rather the Cu-K_α radiation (λ = 1.54184 Å) or Mo-K_α radiation (λ = 0.71073 Å for **1f**). The data was collected and processed using CrysAlisPro program or Bruker SAINT and APEX2 software (for **1f**). Most structures were solved with the ShelXT structure solution program using intrinsic phasing, while **1f** was solved by direct methods as in ShelXS. All systems were refined by the full-matrix least-squares

© 2020 Wiley-VCH Verlag GmbH & Co. KGaA, Weinheim

minimization on F^2 with the ShelXL refinement software. All non-hydrogen atoms were refined anisotropically. C–H and B–H hydrogen atoms were generated geometrically and refined isotropically using a riding model. More details are provided in the SI.

Deposition Numbers 1036760 and 1990286–1990289 contain the supplementary crystallographic data for this paper. These data are provided free of charge by the joint Cambridge Crystallographic Data Centre and Fachinformationszentrum Karlsruhe Access Structures service www.ccdc.cam.ac.uk/structures.

Acknowledgments

This work was supported by the Foundation for Polish (TEAM/2016-3/24) and European Space Agency (NPI 542). We thank Dr. Bryan Ringstrand for supplying crystals of **1f** for XRD analysis.

Keywords: Boron · Cluster compounds · Synthesis design · Structure elucidation · Density functional calculations

[1] a) I. B. Sivaev, A. V. Prikaznov, D. Naoufal, *Collect. Czech. Chem. Commun.* **2010**, *75*, 1149–1199; b) K. Y. Zhizhin, A. P. Zhdanov, N. T. Kuznetsov, *Russ. J. Inorg. Chem.* **2010**, *55*, 2089–2127.

[2] a) J. Aihara, *J. Am. Chem. Soc.* **1978**, *100*, 3339–3342; b) R. B. King, *Chem. Rev.* **2001**, *101*, 1119–1152; c) J. Poater, M. Solà, C. Viñas, F. Teixidor, *Angew. Chem. Int. Ed.* **2014**, *53*, 12191–12195; *Angew. Chem.* **2014**, *126*, 12387; d) J. Poater, C. Viñas, I. Bennour, S. Escayola, M. Solà, F. Teixidor, *J. Am. Chem. Soc.* **2020**, *142*, 9396–9407.

[3] a) P. Kaszynski, *closo Boranes as π Structural Elements for Advanced Anisotropic Materials*, Vol. 798, ACS Symposium Series, Washington, D. C. **2001**; b) S. Pakhomov, P. Kaszynski, V. G. Young Jr., *Inorg. Chem.* **2000**, *39*, 2243–2245; c) P. Kaszynski, S. Pakhomov, V. G. Young Jr., *Collect. Czech. Chem. Commun.* **2002**, *67*, 1061–1083.

[4] a) A. Miniewicz, A. Samoc, M. Samoc, P. Kaszynski, *J. Appl. Phys.* **2007**, *102*, 033108; b) A. Jankowiak, A. Baliński, J. E. Harvey, K. Mason, A. Januszko, P. Kaszyński, V. G. Young Jr., A. Persoons, *J. Mater. Chem. C* **2013**, *1*, 1144–1159; c) D. G. Allis, J. T. Spencer, *Inorg. Chem.* **2001**, *40*, 3373–3380; d) A. Vöge, D. Gabel Boron Derivatives for Application in Nonlinear Optics in *Boron Science: New Technologies and Applications* (Ed.: N. S. Hosmane); CRS Press, New York **2012**, pp 295–317.

[5] a) M. O. Ali, D. Pociecha, J. Wojciechowski, I. Novozhilova, A. C. Friedli, P. Kaszyński, *J. Organomet. Chem.* **2018**, *865*, 226–233; b) P. Kaszynski, J. Huang, G. S. Jenkins, K. A. Bairamov, D. Lipiak, *Mol. Cryst. Liq. Cryst.* **1995**, *260*, 315–332.

[6] K. Y. Zhizhin, V. N. Mustyatsa, E. A. Malinina, L. V. Goeva, N. T. Kuznetsov, *Russ. J. Coord. Chem.* **2001**, *27*, 619–621.

[7] a) W. H. Knoth, J. C. Sauer, H. C. Miller, E. L. Muetterties, *J. Am. Chem. Soc.* **1964**, *86*, 115–116; b) W. H. Knoth, *J. Am. Chem. Soc.* **1966**, *88*, 935–939.

[8] R. N. Leyden, M. F. Hawthorne, *Inorg. Chem.* **1975**, *14*, 2444–2446.

[9] a) M. Komura, H. Nakai, M. Shiro, *J. Chem. Soc., Dalton Trans.* **1987**, 1953–1956; b) D. Naoufal, B. Grüner, B. Bennetot, H. Mongeot, *Polyhedron* **1999**, *18*, 931–939; c) A. V. Prikaznov, V. I. Bragin, M. N. Davydova, I. B. Sivaev, V. I. Bregadze, *Collect. Czech. Chem. Commun.* **2007**, *72*, 1689–1696.

[10] P. Kaszynski, B. Ringstrand, *Angew. Chem. Int. Ed.* **2015**, *54*, 6576–6581; *Angew. Chem.* **2015**, *127*, 6676.

[11] The n-X-m notation defines coordination of a hypervalent atom X, which contains n electrons in its vicinity and m attached ligands. For hypervalent iodine structure and reactivity see: M. Ochiai, *Top. Curr. Chem.* **2003**, *224*, 5–68.

[12] E. Rzeszotarska, I. Novozhilova, P. Kaszyński, *Inorg. Chem.* **2017**, *56*, 14351–14356.

[13] W. R. Hertler, W. H. Knoth, E. L. Muetterties, *J. Am. Chem. Soc.* **1964**, *86*, 5434–5439.

[14] a) *The Cyano Group*, Z. Rappoport (Eds.), Wiley&Sons, **1970**; b) R. C. Larock, *Comprehensive Organic Transformations: A Guide to Functional Group Preparations*, 2nd Ed., Wiley&Sons, **1999**, USA.

[15] a) A. J. Rosenbaum, D. H. Juers, M. A. Juhasz, *Inorg. Chem.* **2013**, *52*, 10717–10719; b) K. Zhang, Y. Shen, J. Liu, B. Spingler, S. Duttwyler, *Chem. Commun.* **2018**, *54*, 1698–1701.

[16] K. Y. Zhizhin, O. O. Vovk, E. A. Malinina, V. N. Mustyatsa, L. V. Goeva, I. N. Polyakova, N. T. Kuznetsov, *Russ. J. Coord. Chem.* **2001**, *27*, 613–618.

[17] N. M. Yoon, Y. S. Gyoung, *J. Org. Chem.* **1985**, *50*, 2443–2450.

[18] Y. M. Choi, M. Yoo, D. K. An, *Bull. Korean Chem. Soc.* **2010**, *31*, 473–474.

[19] S.-D. Cho, Y. D. Park, J.-J. Kim, J. R. Falck, Y.-J. Yoon, *Bull. Korean Chem. Soc.* **2004**, *25*, 407–409.

[20] F. Sembera, J. Plutnar, A. Higelin, Z. Janoušek, I. Císařová, J. Michl, *Inorg. Chem.* **2016**, *55*, 3797–3806.

[21] W. H. Knoth, J. C. Sauer, D. C. England, W. R. Hertler, E. L. Muetterties, *J. Am. Chem. Soc.* **1964**, *86*, 3973–3983.

[22] T. Ueda, H. Konishi, K. Manabe, *Org. Lett.* **2012**, *14*, 3100–3103.

[23] T. Whelan, P. Brint, T. R. Spalding, W. S. McDonald, D. R. Lloyd, *J. Chem. Soc., Dalton Trans.* **1982**, 2469–2473.

[24] M. Abdulmojeed, S. Kapuściński, T. Schafer, A. Pietrzak, O. Hietsoi, A. C. Friedli, P. Kaszyński, submitted.

[25] H. D. Hall, B. D. Ulrich, R. G. Kultyshev, J. Liu, S. Liu, E. A. Meyers, S. Gréau, S. G. Shore, *Collect. Czech. Chem. Commun.* **2002**, *67*, 1007–1024.

[26] a) R. Zurawinski, R. Jakubowski, S. Domagała, P. Kaszyński, K. Woźniak, *Inorg. Chem.* **2018**, *57*, 10442–10456; b) B. Ringstrand, P. Kaszynski, V. G. Young Jr., Z. Janoušek, *Inorg. Chem.* **2010**, *49*, 1166–1179.

[27] C. Hansch, A. Leo, R. W. Taft, *Chem. Rev.* **1991**, *91*, 165–195.

[28] V. V. Avdeeva, I. N. Polyakova, A. V. Churakov, A. V. Vologzhanina, E. A. Malinina, K. Y. Zhizhin, N. T. Kuznetsov, *Polyhedron* **2019**, *162*, 65–70.

[29] V. V. Avdeeva, I. N. Polyakova, L. V. Goeva, E. A. Malinina, N. T. Kuznetsov, *Russ. J. Inorg. Chem.* **2014**, *59*, 1247–1258.

[30] S. Mebs, R. Kalinowski, S. Grabowsky, D. Förster, R. Kickbusch, E. Justus, W. Morgenroth, C. Paulmann, P. Luger, D. Gabel, D. Lentz, *Inorg. Chem.* **2011**, *50*, 90–103.

[31] W. Preetz, A. Franken, M. Rath, *Z. Naturforsch. B* **1993**, *48*, 598–602.

[32] S. Z. Konieczka, F. Schlüter, C. Sindorf, C. Kerpen, E. Bernhardt, M. Finze, *Chem. Eur. J.* **2018**, *24*, 3528–3538.

[33] R. Jakubowski, A. Pietrzak, A. C. Friedli, P. Kaszyński, submitted.

[34] G. Jones, W. Gordy, *Phys. Rev. A* **1964**, *136*, 1229–1232.

[35] A. Kálmán, L. Párkányi, G. Argay, *Acta Crystallogr., Sect. B* **1993**, *49*, 1039–1049.

[36] M. Cossi, G. Scalmani, N. Rega, V. Barone, *J. Chem. Phys.* **2002**, *117*, 43–54, and references cited therein.

[37] For details see the SI.

[38] M. Colapietro, A. Domenicano, G. Portalone, G. Schultz, I. Hargittai, *J. Mol. Struct.* **1984**, *112*, 141–157.

[39] M. Bremer, H. Untenecker, P. A. Gunchenko, A. A. Fokin, P. R. Schreiner, *J. Org. Chem.* **2015**, *80*, 6520–6524.

[40] R. B. Hannan, R. L. Collin, *Acta Crystallogr.* **1953**, *6*, 350–352.

[41] S. Zheng, C. Yu, Z. Shen, *Org. Lett.* **2012**, *14*, 3644–3647.

[42] M. Arisawa, Y. Igarashi, H. Kobayashi, T. Yamada, K. Bando, T. Ichikawa, M. Yamaguchi, *Tetrahedron* **2011**, *67*, 7846–7859.

[43] X. Zhang, J. Sun, Y. Ding, L. Yu, *Org. Lett.* **2015**, *17*, 5840–5842.

[44] M. Ochiai, A. Yoshimura, K. Miyamoto, S. Hayashi, W. Nakanishi, *J. Am. Chem. Soc.* **2010**, *132*, 9236–9239.

[45] M. G. Dahlqvist, E. K. Euranto, *Spectrochim. Acta* **1978**, *34A*, 863–868.

[46] a) D. E. Richardson, H. Taube, *J. Am. Chem. Soc.* **1983**, *105*, 40–51; b) L. Bonniard, S. Kahlal, A. K. Diallo, C. Ornelas, T. Roisnel, G. Manca, J. Rodrigues, J. Ruiz, D. Astruc, J.-Y. Saillard, *Inorg. Chem.* **2011**, *50*, 114–124.

[47] V. I. Bragin, I. B. Sivaev, V. I. Bregadze, N. A. Votinova, *J. Organomet. Chem.* **2005**, *690*, 2847–2849.

[48] M. J. Frisch, G. W. Trucks, H. B. Schlegel, G. E. Scuseria, M. A. Robb, J. R. Cheeseman, G. Scalmani, V. Barone, B. Mennucci, G. A. Petersson, H. Nakatsuji, M. Caricato, X. Li, H. P. Hratchian, A. F. Izmaylov, J. Bloino, G. Zheng, J. L. Sonnenberg, M. Hada, M. Ehara, K. Toyota, R. Fukuda, J. Hasegawa, M. Ishida, T. Nakajima, Y. Honda, O. Kitao, H. Nakai, T. Vreven, J. A. Montgomery Jr., J. E. Peralta, F. Ogliaro, M. Bearpark, J. J. Heyd, E. Brothers, K. N. Kudin, V. N. Staroverov, R. Kobayashi, J. Normand, K. Raghavachari, A. Rendell, J. C. Burant, S. S. Iyengar, J. Tomasi, M. Cossi, N. Rega, J. M. Millam, M. Klene, J. E. Knox, J. B. Cross, V. Bakken, C. Adamo, J.

 © 2020 Wiley-VCH Verlag GmbH & Co. KGaA, Weinheim

Jaramillo, R. Gomperts, R. E. Stratmann, O. Yazyev, A. J. Austin, R. Cammi, C. Pomelli, J. W. Ochterski, R. L. Martin, K. Morokuma, V. G. Zakrzewski, G. A. Voth, P. Salvador, J. J. Dannenberg, S. Dapprich, A. D. Daniels, Ö. Farkas, J. B. Foresman, J. V. Ortiz, J. Cioslowski, D. J. Fox, Gaussian 09, Revision A.02, Gaussian, Inc., Wallingford CT, **2009**.

[49] a) A. Schäfer, H. Horn, R. Ahlrichs, *J. Chem. Phys.* **1992**, *97*, 2571–2577; b) A. Schäfer, C. Huber, R. Ahlrichs, *J. Chem. Phys.* **1994**, *100*, 5829–5835.

[50] G. R. Fulmer, A. J. M. Miller, N. H. Sherden, H. E. Gottlieb, A. Nudelman, B. M. Stoltz, J. E. Bercaw, K. I. Goldberg, *Organometallics* **2010**, *29*, 2176–2179.

Received: May 8, 2020

© 2020 Wiley-VCH Verlag GmbH & Co. KGaA, Weinheim

CHAPTER A3

Tunable intermolecular charge transfer in ionic liquid crystalline derivatives of the [*closo*-$B_{10}H_{10}$]$^{2-}$ anion.

(L. Jacob, E. Rzeszotarska, M. Koyioni, R. Jakubowski, D. Pociecha, A. Pietrzak, P. Kaszyński, *Chem. Mater.*, **2022**, *34*, 6476–6491, DOI: 10.1021/acs.chemmater.2c01-165)

3.1 Introduction

Liquid crystallinity is a feasible method to impose self-organization of molecules in fluid materials to achieve the anisotropy of the desired property. One such property of interest in ionic liquid crystals (ILC) is charge transport, which is attractive for technological applications such as photovoltaic cells, and electrochromic materials. ILC materials in which both ions are active and exhibit intermolecular charge transfer (CT) have been rarely studied. Typically, the focus is on one of the ions possessing the property of interest (e.g., photophysical or redox activity), while the counterion is a spectator necessary for charge balance.

The primary objective of this research project was to develop ionic liquid crystal (ILC) derivatives based on the [*closo*-$B_{10}H_{10}$]$^{2-}$ anion with controlled intermolecular charge transfer. By combining 1,10-disubstituted [*closo*-$B_{10}H_{10}$]$^{2-}$ anion derivatives with *N*-alkyl pyridinium cations as charge compensators, four series of liquid crystalline ion pairs were prepared, and their thermal and photophysical properties were investigated. Tunability of the intermolecular charge transfer in these two-component ILC derivatives was achieved by modifying FMO levels in the cation and the anion with appropriate substituents. This work demonstrated the first ionic liquid crystals based

on [*closo*-$B_{10}H_{10}]^{2-}$ anion and a new paradigm of ionic liquid crystals exhibiting tunable low energy intermolecular charge transfer bands. In addition, these derivatives are examples of molecules with anion-driven mesogenicity.

Broad-range smectic A phase with a high clearing temperature and tunable intermolecular charge transfer bands in the visible region was observed in all the ion pairs with substituted pyridinium cations. XRD and DSC analysis revealed that many ion pairs undergo a stepwise melting to the smectic A phase, with the initial melting of the alkyl chains and then the ionic cores as two independent thermodynamic events. Analysis of the electronic structure revealed effective electronic communication between the [*closo*-$B_{10}H_{10}]^{2-}$ anion with Ph and OR substituents. Also, the position of CT bands correlates well with the calculated energy difference between relevant FMOs and the σ_p parameters of the substituent on the pyridine ring for individual series.

Ms. Edyta Rzeszotarska, a former student, initiated this project. Although she succeeded in synthesizing derivatives of series **4[12]**, there were difficulties in the synthesis of series **3[11,12]**. Later on, Dr. Maria Koyioni took on this synthetic challenge and made progress in the synthesis. Due to problems associated with the low overall yields and difficulties in purification and optimization of the reaction conditions, further development of this project was hindered. Boron cluster chemistry is often tough due to the difficulties in functionalization, unusual reactions, involvement of the charged species, difficulties in purification, and lack of established reaction conditions. In addition, extraction and purification of these inorganic-organic hybrid ionic compounds require specialized knowledge and skills.

Dr. Mariya Koyioni entrusted me with this challenge, and I was able to successfully synthesize and characterize all of the target compounds in series **3[11,12]**, **2[12]**, and **1[11]**. I also

resynthesized and characterized all derivatives in series **4[12]**. Dr. Rafał Jakubowski contributed to the project by synthesizing some of the intermediate compounds. I performed all UV-vis spectroscopy (solution state and solid state) and polarized optical microscopy (POM) analyses. In addition, Dr. Damian Pociecha instructed me on how to conduct powder XRD measurements, which I performed on all liquid crystalline derivatives at Warsaw University. Dr. Anna Pietrzak obtained single crystal XRD structures. Prof. Piotr Kaszyński performed quantum mechanical calculations and validated the experimental findings.

3.2 Published text

CHEMISTRY OF MATERIALS

pubs.acs.org/cm Article

Tunable Intermolecular Charge Transfer in Ionic Liquid Crystalline Derivatives of the [*closo*-$B_{10}H_{10}$]$^{2-}$ Anion

Litwin Jacob, Edyta Rzeszotarska, Maria Koyioni, Rafał Jakubowski, Damian Pociecha, Anna Pietrzak, and Piotr Kaszynski*

Cite This: *Chem. Mater.* 2022, 34, 6476−6491 Read Online

ACCESS | Metrics & More | Article Recommendations | * Supporting Information

ABSTRACT: A new paradigm of ionic liquid crystals exhibiting low-energy charge transfer bands is demonstrated. Thus, four series of ion pairs of 1,10-disubstituted derivatives of the [*closo*-$B_{10}H_{10}$]$^{2-}$ anion and substituted pyridinium cations were prepared and their thermal and photophysical properties were investigated. All pyridinium ion pairs form a smectic A (SmA) phase with clearing temperatures above 200 °C and intermolecular charge transfer (CT) band in the solid and fluid states and in CH_2Cl_2 solutions. The CT band maximum is in the range of 320−510 nm and its position correlates with the difference in frontier molecular orbital (FMO) energies of the ions (highest occupied molecular orbital (HOMO) of the anions and the lowest unoccupied molecular orbital (LUMO) of the cations), which, in turn, correlate well with the substituent σ_p parameters. Experimental results are augmented with extensive density functional theory (DFT) calculations and X-ray diffraction (XRD) analyses.

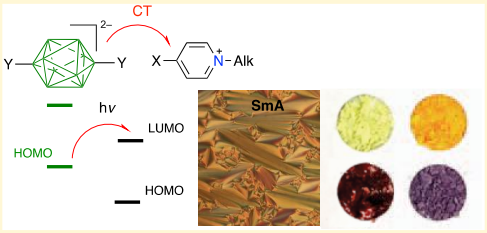

Downloaded via 188.146.250.197 on June 29, 2023 at 14:44:56 (UTC).
See https://pubs.acs.org/sharingguidelines for options on how to legitimately share published articles.

INTRODUCTION

Organic compounds exhibiting intermolecular charge transfer (CT) phenomena[1−3] constitute an important class of materials investigated in the context of organic solar cells, photodetectors, two-photon absorbers, and nonlinear optical systems.[4−9] One attractive approach to such materials involves self-organizing behavior of two-component liquid crystals (LCs), in which one constituent acts as an electron donor and the other as an electron acceptor.[10,11] Such materials offer advantages over other CT binary systems by more facile and reproducible preparation, predictable molecular organization, and modular approach. For these reasons, binary donor−acceptor (D−A) discotic LCs,[12−14] forming alternating columns, have been investigated as organic semiconductors, relatively efficient anisotropic charge conductors,[15,16] and laser addressable dichroics.[17] These materials typically involve electron-rich π systems, such as derivatives of triphenylene,[13,18,19] hexabenzocoronene,[12,15] and truxene,[20] and electron acceptors, for example, trinitrofluorenone,[14,16,18,21,22] naphthalenediimide,[23] perylenediimide,[12,15] mellitictriimide,[19,24] and tetracyanoquinodimethane (TCNQ).[25] It has been demonstrated that the energy of the CT interactions in alternating D−A discotic LCs can be adjusted using a series of electron donors and acceptors.[24,26] While most effort in self-organizing materials exhibiting low-energy CT behavior has been dedicated to discotic LCs, other types of such LCs, *eg.* calamitic and ionic, received little to no attention.

Functional ionic liquid crystals[27] (ILCs) are of increasing importance for contemporary technologies mainly in the context of ion transport in electrolytes, dye-sensitized solar cells, and electrochromic materials.[28−30] Typically, the focus is on one of the ions possessing the property of interest (*eg*, photophysical or redox activity), while the counterion is a spectator necessary for the charge balance. Consequently, materials in which both ions are active are rare and those exhibiting intermolecular CT are essentially neglected.[31] We report here the first, to our knowledge, ionic liquid crystals with tunable intermolecular CT bands based on the [*closo*-$B_{10}H_{10}$]$^{2-}$ anion.

The [*closo*-$B_{10}H_{10}$]$^{2-}$ anion[32] (Figure 1) is a three-dimensional (3-D) sigma aromatic system[33] with the D_{4d} molecular symmetry, a large highest occupied molecular orbital−lowest unoccupied molecular orbital (HOMO−LUMO) gap rendering practical transparency above 200 nm, and a high-lying doubly degenerate HOMO.[34] The orbital symmetry allows for efficient electronic interactions between the anion and π substituents,[35] and intense intramolecular cluster-to-π substituent CT bands have been observed in some

Received: April 20, 2022
Revised: June 2, 2022
Published: July 12, 2022

ACS Publications
© 2022 The Authors. Published by American Chemical Society

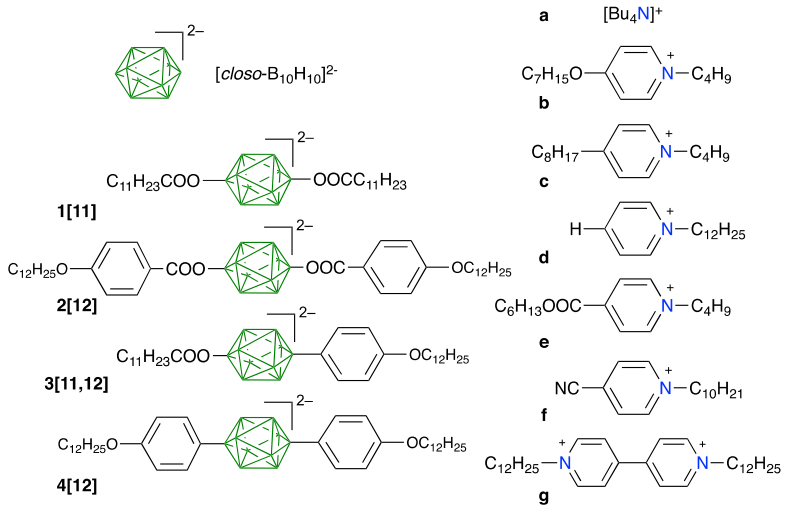

Figure 1. Structures of the $[closo\text{-}B_{10}H_{10}]^{2-}$ anion, its 1,10-disubstituted derivatives **1**[**n**]−**4**[**n**], and cations **a**−**g**. Each unsubstituted vertex represents a BH fragment. The number in the brackets represents the alkyl chain length.

zwitterionic derivatives substituted at the apical positions.[36−38] On the other hand, the high level of the HOMO in the $[closo\text{-}B_{10}H_{10}]^{2-}$ anion allows for CT interactions with certain cations,[39] such as pyridinium,[40,41] 2,2′-bipyridinium,[40,42−45] quinolinium,[40] and phenanthrolinium,[46] giving rise to colored, yellow, and orange solids. These findings hint at an intriguing possibility of unprecedented ionic LCs derived from the $[closo\text{-}B_{10}H_{10}]^{2-}$ anion and exhibiting CT phenomena.

Herein, we present a new paradigm in materials with intermolecular charge transfer: self-organizing ILC with tunable intermolecular CT absorption bands in the visible range. The ions are derived from $[closo\text{-}B_{10}H_{10}]^{2-}$ anions and *N*−alkyl pyridinium cations (Figure 1), in which substituents modify the frontier molecular orbital (FMO) levels and consequently the energy of the CT interactions. Thus, we report the synthesis of four series of ionic liquid crystalline derivatives **1**[**11**]−**4**[**12**] (Figure 1) and the investigation of their mesomorphic and photophysical properties. Anion $[closo\text{-}B_{10}H_{10}]^{2-}$ was substituted with long mesogenicity−inducing groups,[47] which through electronic interactions affect the level of the HOMO. Pyridinium cations **b**−**f** of approximately the same length are substituted with groups exerting different electronic effects on the pyridinium ring and its LUMO level ranging from electron-donating (OR) to strongly electron-withdrawing (CN). Paraquat derivative **g** was tested as the most electron-poor (lowest LUMO) pyridinium cation. Liquid crystalline properties of 17 ion pairs were investigated by polarized light optical microscopy (POM), differential scanning calorimetry (DSC), and powder X-ray diffraction (XRD) measurements, while photophysical properties in solutions and in the solid state were studied by electronic absorption spectroscopy and density functional theory (DFT) methods. Single-crystal XRD analysis of ion pair **4**[**7**]**b** (containing anion **4**[**7**] and cation **b**, Figure 1) sheds light on the molecular organization in the solid and in the ILC phase.

RESULTS AND DISCUSSION

Synthesis. *Preparation of 1[11]a and 2[12]a.* The requisite $[Bu_4N]^+$ salts **1**[**11**]**a** and **2**[**12**]**a** were obtained by esterification of dioxonium derivative[48] $[closo\text{-}B_{10}H_8\text{-}1,10\text{-}(OH_2)_2]$ cocrystals with $[Bu_4N]^+Cl^-$ (**5**·[**Bu**$_4$**N**]**Cl**, Scheme 1) with the appropriate acid chloride. Alternatively, a mixture

Scheme 1. Synthesis of Diester Ion Pairs 1[**11**]**a and 2**[**12**]**a**[a]

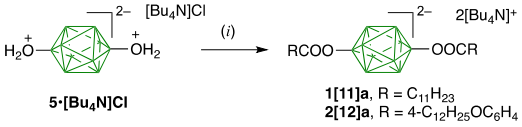

[a]Reagents and conditions: (i) NaH, RCOCl, tetrahydrofuran (THF), Ar, room temperature (rt), 2 h.

of pure **5** and $[Bu_4N]^+Cl^-$ can be used instead of **5**·[Bu_4N]Cl.[48] The presence of the $[Bu_4N]^+$ cation in the reaction mixture ensures solubility of the deprotonated **5** in the reaction medium and the reaction with RCOCl. The resulting esters were found to be unstable toward acidic conditions including silica gel. Therefore, pure derivatives **1**[**11**]**a** and **2**[**12**]**a** were obtained in about 70 and 60% yields, respectively, by column chromatography with basic alumina.

Preparation of 3[11,12]a. Unsymmetric derivative **3**-[**11,12**]**a** was obtained in a sequence of reactions shown in Scheme 2. Thus, iodo derivative[49] $[closo\text{-}B_{10}H_9\text{-}1\text{-}I]^{2-}$ (**6a**, Scheme 2) was arylated with 4-$C_{12}H_{25}OC_6H_4MgBr$ in the presence of 1 mol % PEPPSI-IPr catalyst, according to a previously demonstrated procedure.[49] Product **7a**, obtained in 88% yield, was selectively substituted at the B(10) position using $PhI(OAc)_2$, and the resulting unstable iodonium intermediate **8a** was thermolyzed in dry dimethylformamide (DMF) giving adduct **9a**, which was isolated by column chromatography in 35−43% yield based on **7a**. The

https://doi.org/10.1021/acs.chemmater.2c01165
Chem. Mater. 2022, 34, 6476−6491

Scheme 2. Synthesis of Ion Pair 3[11,12]a[a]

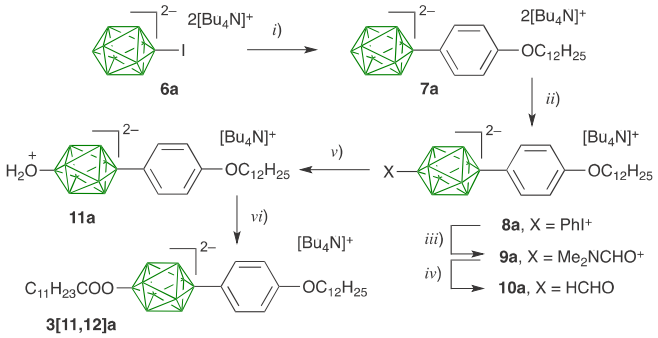

[a]Reagents and conditions: (i) 4-$C_{12}H_{25}OC_6H_4MgBr$, PEPPSI-IPr, THF, reflux, 24 h; (ii) $PhI(OAc)_2$, CH_3CN, 10 °C, 5 h; (iii) DMF, 60 °C, 12 h; (iv) $[Bu_4N]^+$ HO^-, CH_3CN, reflux, 2 h; (v) HCl, MeOH, rt (vi) $C_{11}H_{23}COCl$, NaH, THF, rt, 2 h.

Scheme 3. Synthesis of Derivative 4[12]a[a]

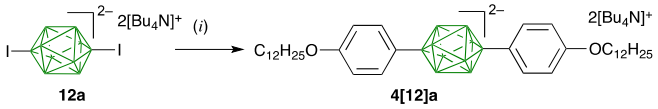

[a]Reagents and conditions: (i) 4-$C_{12}H_{25}OC_6H_4MgBr$, PEPPSI-IPr, THF, reflux, 24 h.

subsequent treatment of **9a** with $[Bu_4N]^+OH^-$ gave **10a** in 93% yield. Formate **10a** was treated with aqueous HCl to give unstable protonated 1-hydroxy intermediate **11a**, which was acylated with $C_{11}H_{23}COCl$ in the presence of NaH giving **3**[**11,12**]**a** in 34−40% yield.

Preparation of 4[n]a. Salt **4**[**12**]**a** was prepared in about 60% yield by the cross-coupling reaction of diiodo derivative[49] [*closo*-$B_{10}H_8$-1,10-I_2]$^{2-}$ (**12a**) with 4-$C_{12}H_{25}OC_6H_4MgBr$ using 2 mol % PEPPSI-IPr catalyst (Scheme 3). For single-crystal analysis, the shorter analogue, **4**[**7**]**a**, was also obtained under identical conditions.

Preparation of Pyridinium Cations. The requisite pyridinium bromides **b**[**Br**]−**f**[**Br**] were obtained by N-alkylation of substituted pyridines with appropriate alkyl bromides (Scheme 4), as reported before for **b**[**Br**].[50] Paraquat **g**[**Br**] was obtained in an analogous way from 4,4′-bipyridyl.[51]

Scheme 4. Synthesis of Pyridinium Salts b−f[a]

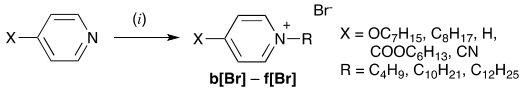

[a]Reagents and conditions: (i) RBr, MeCN, reflux. See the Supporting Information.

Cation Exchange. The initially obtained colorless $[Bu_4N]^+$ salts, **1**[**11**]**a**, **2**[**12**]**a**, and **3**[**11,12**]**a**, were converted to the pyridinium ion pairs in a biphasic CH_2Cl_2/H_2O solvent system, according to a general procedure.[50] Ion pair **1**[**11**]**g** containing the bipyridinium dication **g** was formed as an insoluble dark-purple material, which decomposed above 250 °C without melting. Cation exchange for compound **4**[**12**]**a** was accomplished in MeOH by stirring with the appropriate pyridinium bromide and subsequent filtering the precipitated product. The resulting ion pairs were purified by repeated recrystallization or precipitation from an appropriate solvent under ambient conditions giving pure products in 80−90% yields. Most ion pairs exhibited a color that depended on the pyridinium cation.

Molecular and Crystal Structures. Colorless triclinic crystals of ion pair **4**[**7**]**b** were obtained by slow evaporation of a CH_2Cl_2/acetone solution. The molecular structure of **4**[**7**]**b** along with pertinent geometrical parameters is shown in Figure 2. Crystallographic data collection and refinement details are provided in the Supporting Information (SI).

The intracage dimensions in anion **4**[**7**], such as the B−B bond distances, are typical for this class of derivatives, including the parent [*closo*-$B_{10}H_{10}$]$^{2-}$ anion[45] and its 1,10-disubstituted derivatives.[48] The height of two square pyramids in **4**[**7**], B(1)···B(2−6), is 1.102 and 1.105 Å, while the B(1)···

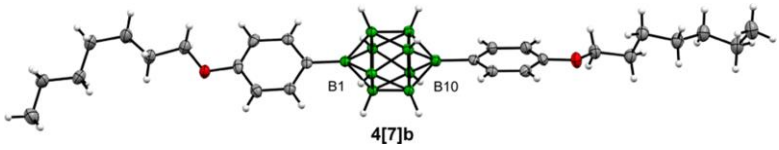

Figure 2. Atomic displacement ellipsoid representation for **4**[**7**]**b**. Minor disordered atomic sites and pyridinium cations are omitted for clarity. Pertinent distances: B(1)−C, 1.574(2) Å; B(10)−C, 1.573(2) Å; B(1)···B(10), 3.725(2) Å; O(1)···O(2), 15.298(2) Å.

https://doi.org/10.1021/acs.chemmater.2c01165
Chem. Mater. 2022, 34, 6476−6491

B(10) separation is 3.725(2) Å. Although within 3σ, the observed values appear to be larger than those found in the parent anion [*closo*-$B_{10}H_{10}]^{2-}$ (1.100 and 3.717(4) Å, respectively) and its derivatives[48] and are consistent[48] with a weak electron-donating effect of the alkoxyphenyl group (Hammett σ_p = −0.08).[52]

The benzene rings in **4**[7] form pseudostaggered orientations relative to the cage with the torsion angles of 0.5 and 9.1° away from the ideal staggered conformation. Consequently, the two benzene ring planes form a 36.0° interplanar angle. The CH_2O fragments are coplanar with the benzene ring. Both heptyl chains exhibit multiple gauche conformations and one of them is positionally disordered.

The butyl and alkoxy chains in the pyridinium cation **b** are oriented relative to the ring according to expectations (orthogonal and coplanar, respectively) with both alkyl chains exhibiting gauche conformations.

Analysis of crystal packing of **4**[7]**b** demonstrates that anions and cations are arranged in ionic planes, which are separated by 17.5 Å (Figure 3). This molecular arrangement is consistent with the propensity of the ion pair **4**[7]**b** to the formation of smectic liquid crystalline phases. In each ionic layer, the negatively charged {B_{10}} clusters are separated by the pyridinium cations pointing to the clusters with the positively charged nitrogen atoms. There are four unique distances between the long molecular axes of the anions with an average of 9.8 Å.

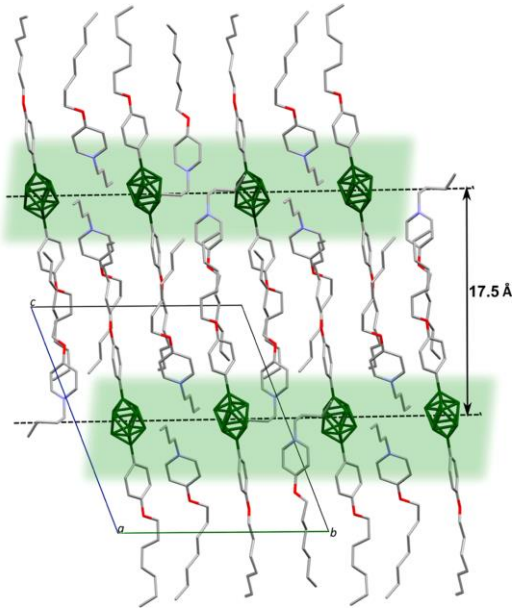

Figure 3. Partial crystal packing of **4**[7]**b** (view along the *a*-axis) with the ionic planes shaded. The distances between molecular long axes of the anions are in the range of 8.7−10.8 Å, and the distance between the ionic layers is 17.5 Å. Hydrogen atoms are omitted for clarity.

Liquid Crystalline Properties. Differential scanning calorimetry (DSC) and polarized light optical microscopy (POM) analyses revealed mesogenic behavior of all pyridinium ion pairs, and the results are presented in Table 1 and shown in Figures 4−6.

The analysis demonstrates that all derivatives form smectic phases[53] (Sm) and undergo a transition to the isotropic liquids (I) with decomposition typically above 200 °C (Table 1). For this reason, it was hard to obtain well-developed textures for detailed optical analyses. Only in the case of **1**[**11**]**e** and **3**[**11,12**]**e**, very brief heating above the clearing point and immediate cooling allowed to minimize the decomposition and resulted in the formation of a well-developed texture characteristic for a smectic A (SmA) phase (Figure 4). Shearing of these textures revealed large areas with homeotropic alignment consistent with the SmA phase.

Ion pairs in series **1**[**11**] exhibit relatively low melting temperatures, which increase in the order **b** < **e** < **c** < **f** < **d**. Ion pair **1**[**11**]**b** appears to exist as an Sm phase at ambient temperature, while **1**[**11**]**d** has the highest melting point in the series (105 °C, Figure 5 and Table 1). Derivatives **1**[**11**]**d** and **1**[**11**]**f** exhibit two endotherms on heating (Figure 5), which correspond to a crystal−crystal (Cr−Cr) transition and, the second with a lower enthalpy change, to the Cr−Sm transition. Other series of ion pairs with one (**3**[**11,12**]) and two (**2**[**12**] and **4**[**12**]) benzene rings in the anion's core have higher melting points. Ion pairs of **4**[**12**] with the most rigid core typically have the highest temperatures of melting to the Sm phase among all series.

DSC data combined with optical microscopy indicate that some compounds undergo clearing with decomposition at about 210 °C, while those with larger rigid cores, *e.g.*, series **2**[**12**], become isotropic with decomposition close to 300 °C.

To lower the clearing temperature of the ion pairs below that of their thermal decomposition, binary mixtures of **1**[**11**]**c** with structurally similar organic nonionic compounds were briefly investigated. Initial studies focused on mixtures of **1**[**11**]**c** with hydroquinone dilaurate (**H**[**11**]), which structurally resembles the anion. POM studies revealed phase separation and poor miscibility for mixtures containing either 50 or 25 mol % **H**[**11**].

It was speculated that hydroquinone dibutyrate (**H**[**3**]) could be a more compatible additive, and a 50 mol % mixture with **1**[**11**]**c** was investigated. In this case, the mixture exhibited a significantly lower SmA isotropic phase, however, with a broad biphasic region: the smectic phase started to appear at 207 °C, which was confirmed by the powder XRD diffraction pattern together with POM analysis (Figure 6).

XRD Measurements. Powder XRD analysis of LC phases obtained on heating confirmed smectic behavior of all pyridinium ion pairs **1**[**11**]−**4**[**12**]. X-ray diffraction patterns revealed sharp commensurate peaks at low diffraction angles and a diffuse scattering signal in the wide-angle region, which evidence a simple lamellar structure with no long-range positional order of molecules within the layers (Figure 7 and the SI). This is consistent with the SmA phase identified on the basis of sheering alignment. In all cases, the layer spacing *d* is significantly smaller than the length of the dianions calculated for their most extended conformations (Table 1). This is presumably due to partial interdigitation *I*, which is in the range of 30−50%. The highest interdigitation is observed in series **2**[**12**] (36−49%) and for ion pairs with cation **e** (*I* = 39−49%). In contrast, ion pairs containing the monosubstituted cation **d** exhibit the lowest in the series degree of interdigitation (*I* = 32−38%). The XRD data for smectic phases are consistent with molecular packing observed in the

https://doi.org/10.1021/acs.chemmater.2c01165
Chem. Mater. 2022, 34, 6476−6491

Table 1. Thermal, Powder XRD, and Photophysical Data for Ion Pairs 1[n]−4[n]

Compound	Thermal properties [a] Phase behavior T / °C (ΔH /kJmol^{-1})	Powder XRD Temp /°C	d [b] /Å	L [c] /Å	I [d] /%	CT electronic absorption λ_{CT} [e] solid /nm	λ_{CT} [f] CH_2Cl_2 /nm	ΔE_{FMO} [g] /eV
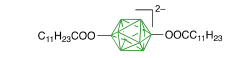	1[11]							
[4-$C_7H_{15}OC_5H_4N$-1-Bu]$^+$ **b**	Cr 38 (43.1) SmA >230 [h]	80	23.0	38.59	40	[i]	324	4.642
[4-$C_8H_{17}C_5H_4N$-1-Bu]$^+$ **c**	Cr 78 (46.2) SmA >290 [h]	180	24.0	38.59	38	343	374	4.291
[C_5H_5N-1-$C_{12}H_{25}$]$^+$ **d**	Cr_1 75 (58.7) Cr_2 105 (17.9) SmA >275 [h]	120	26.3	38.59	32	350	390	4.124
[4-$C_6H_{13}OOCC_5H_4N$-1-Bu]$^+$ **e**	Cr 53 (17.6) SmA >220 [h]	120	23.6	38.59	39	430	476	3.432
[4-NCC_5H_4N-1-Bu]$^+$ **f**	Cr_1 61 (40.9) Cr_2 96 (11.0) SmA >225 [h]	120	25.4	38.59	34	458	510	3.141
	2[12]							
[4-$C_7H_{15}OC_5H_4N$-1-Bu]$^+$ **b**	Cr_1 51 (21.4) Cr_2 77 (12.5) SmA >250 [h]	80	27.9 [j]	51.31	46	[i]	[i]	4.611
[C_5H_5N-1-$C_{12}H_{25}$]$^+$ **d**	Cr_1 97 (9.3) Cr_2 167 (40.4) SmA >290 [h]	180	32.8	51.31	36	353 [k]	[i]	4.093
[4-$C_6H_{13}OOCC_5H_4N$-1-Bu]$^+$ **e**	Cr_1 69 (5.2) Cr_2 159 (25.4) SmA >250 [h]	180	26.3	51.31	49	432	472	3.401
[4-NCC_5H_4N-1-Bu]$^+$ **f**	Cr_1 32 (3.5) Cr_2 138 (13.6) SmA >235 [h]	160	31.1	51.31	39	456	506	3.110
	3[11,12]							
[C_5H_5N-1-$C_{12}H_{25}$]$^+$ **d**	Cr 177 (27.0) SmA >210 [h]	180	26.8	42.51	37	386.5	414	3.797
[4-$C_6H_{13}OOCC_5H_4N$-*N*-Bu]$^+$ **e**	Cr_1 84 (33.2) Cr_2 129 (2.5) SmA >160 [h]	80	24.7	42.51	42	471 [k]	515	3.105
[4-NCC_5H_4N-1-Bu]$^+$ **f**	Cr 50 (3.0) SmA >190 [h]	130	26.8	42.51	37	465 [k]	530	2.814
	4[12]							
[4-$C_7H_{15}OC_5H_4N$-1-Bu]$^+$ **b**, n = 7 [l]	Cr_1 123 (25.4) Cr_2 144 (22.7) SmA >200 [h]	–	–	–	–	–	–	4.122
[4-$C_7H_{15}OC_5H_4N$-1-Bu]$^+$ **b**	Cr_1 106 (32.7) Cr_2 129 (20.7) SmA >205 [h]	160	27.4	46.67	41	[i]	[i]	4.122
[C_5H_5N-1-$C_{12}H_{25}$]$^+$ **d**	Cr_1 49 (4.0) Cr_2 191 (23.1) SmA >215 [h]	180	29.1	46.67	38	402 [k]	452	3.604
[4-$C_6H_{13}OOCC_5H_4N$-1-Bu]$^+$ **e**	Cr_1 104 (23.5) Cr_2 128 (17.4) SmA >210 [h]	110	27.7	46.67	41	496	580	2.912
[4-NCC_5H_4N-1-Bu]$^+$ **f**	Cr_1 111 (17.8) Cr_2 146 (11.3) SmA >160 [h]	130	30.1	46.67	36	524	582	2.621

[a]Peak temperature and change of enthalpy (in parentheses). Notation: Cr, crystalline; SmA, smectic A; I, isotropic phases. [b]Layer spacing. [c]Molecular length measured as the H···H distance without van der Waals radii of the terminal atoms for models obtained with the B3LYP/def2SVP method. [d]Degree of interdigitation $I = 100\% \times (L - d)/L$. [e]Maximum of absorption measured in the solid state, *ca.* 22 °C. [f]Maximum of absorption recorded in CH_2Cl_2 solutions ($c \sim 10^{-4}$ M). [g]$\Delta E_{FMO} = E_{LUMO} - E_{HOMO}$ for model compounds. Energies were obtained with the TD CAM-B3LYP/def2TZVP//B3LYP/def2TZVP method in the CH_2Cl_2 dielectric medium. For details, see the text. [h]Clearing temperature with decomposition determined by POM and DSC (50 K min^{-1}). [i]CT band under ion absorption bands. [j]Nearly constant value (±0.05 Å) in the temperature range of 80−180 °C. [k]After deconvolution. [l]Data for derivative **4**[7]**b**.

crystal structure of **4**[7]**b** (Figure 3), which revealed a significant overlap of aliphatic chains equivalent to about 48% of interdigitation.

Powder X-ray diffractograms of phases formed below the SmA phase revealed their crystalline character, as evident from multiple sharp reflections in the entire recorded 2θ range (1−25°). A detailed analysis of materials exhibiting trimorphism, such as **1**[**11**]**d**, suggests melting of alkyl chains at the Cr−Cr transition (for **1**[**11**]**d** at 75 °C; Figure 5), which is consistent with diminishing sharp reflections and increased background scattering at high angles (Figure 7). The second phase transition involves melting of the ionic cores and formation of the fluid SmA phase. This interpretation is consistent with the observed enthalpies of transitions, which are significantly higher for the first Cr−Cr transition than those for the second Cr−SmA (77 and 23 kJ mol^{-1} for **1**[**11**]**d**). Similar results are

https://doi.org/10.1021/acs.chemmater.2c01165
Chem. Mater. 2022, 34, 6476−6491

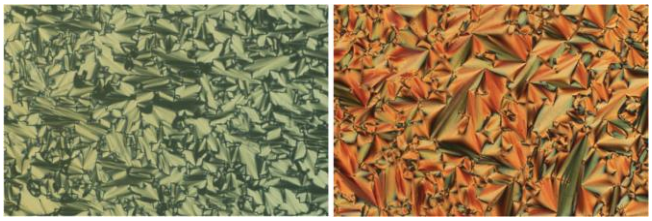

Figure 4. Optical textures for **3**[**11,12**]**e** in polarized light obtained on cooling from the isotropic phase at 126 °C (left) and 98 °C (right) for different areas of the sample.

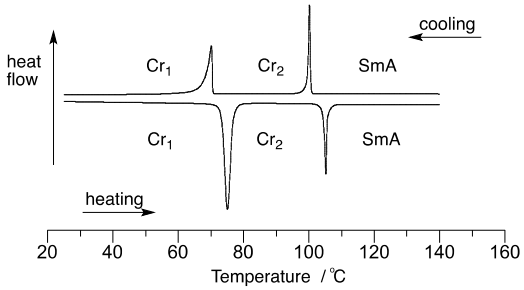

Figure 5. DSC trace of **1**[**11**]**d**. The heating and cooling rates are 10 K min^{-1}. Notation: Cr, crystalline phase; SmA, smectic A phase.

documented for **1**[**11**]**f** and **4**[**12**]**b** (see the SI), and it is believed that other systems exhibiting trimorphism on DSC scans (**2**[**12**]**b**, **2**[**12**]**f**, **3**[**11,12**]**e**, **4**[**12**]**b**, and **4**[**12**]**e**; Table 1 and the SI) also undergo a stepwise melting process. Analysis of enthalpy of transition to the SmA phases (Table 1) suggests that some other ion pairs may exist at ambient temperatures as solids with melted alkyl chains (*e.g.*, **1**[**11**]**e**, **3**[**11,12**]**d**, and **4**[**12**]**f**).

Analysis of temperature dependence of the layer spacing *d* is also consistent with the stepwise melting of the solid. For instance, the layer spacing in **1**[**11**]**d** increases on heating in the crystalline phases with a jump at the Cr−Cr phase transition by 1.5 Å to provide more space for mobile alkyl chains (Figure 7). At the Cr−SmA phase transition *d* abruptly decreases by 1.75 Å due to melted ionic cores and the spacing monotonously decreases with increasing temperature, which is typical for a SmA phase. This pattern of increasing layer spacing in crystalline phases and a steady decrease in SmA is also observed for other investigated ion pairs.[54]

Photophysical Properties. Electronic spectra of $[Bu_4N]^+$ ion pairs **1**[**11**]**a**, **2**[**12**]**a**, **3**[**11,12**]**a**, and **4**[**12**]**a** in MeCN revealed no absorption above 400 nm. Derivative **1**[**11**]**a** exhibits only a single, high-energy absorption band with a maximum at 226.5 nm ($\log \varepsilon = 4.04$) tailing to about 300 nm (Figure 8). Changing the undecanoate substituent in **1**[**11**] to dodecyloxybenzoate in **2**[**12**] resulted in the appearance of an absorption maximum at 247 nm ($\log \varepsilon = 4.53$) and a broad, intense absorption at 299 nm (after deconvolution)[54] tailing to about 400 nm due to the presence of the aromatic chromophore. Diaryl derivative **4**[**12**]**a** exhibits a broad and intense ($\log \varepsilon = 4.42$) absorption with a maximum at 277.5 nm (Figure 8). The absorption spectrum of the unsymmetric derivative **3**[**11,12**]**a** displays the most complex pattern with only one clear maximum at 273 nm ($\log \varepsilon = 4.15$) and three shoulder absorptions. Deconvolution of the low-energy portion of the spectrum gave two maxima at 270 and 294 nm.[54] Electronic absorption spectra of pyridinium bromides in MeCN typically exhibit multiple maxima below 300 nm (Figure 8 and the SI).

Similar results were obtained for the $[Bu_4N]^+$ ion pairs and the pyridinium bromides in CH_2Cl_2, which is transparent only above 230 nm. Maxima of absorption were shifted at most by a few nanometers and are generally less resolved, presumably due to the aggregation of ion pairs in the low-dielectric-strength solvent.

Analysis of pyridinium ion pairs in CH_2Cl_2 solutions showed absorption spectra, which were the sum of those of the individual ions. At higher concentrations ($c \sim 10^{-4}$ M), an additional, low-energy band appeared, which could be ascribed to intermolecular CT excitation and responsible for the color of the solids. Figure 9 shows that the maximum of the CT band in series **1**[**11**] systematically moves to higher wavelengths from 324 nm for **1**[**11**]**b** to 510 nm for **1**[**11**]**f**. A similar phenomenon is observed in other series, and the results

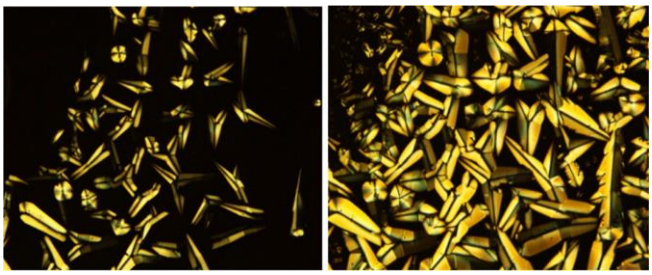

Figure 6. Optical textures for the **1**[**11**]**c**−**H**[**3**] 1:1 mixture in polarized light on cooling at 186 °C (left) and 130 °C (right).

https://doi.org/10.1021/acs.chemmater.2c01165
Chem. Mater. 2022, 34, 6476−6491

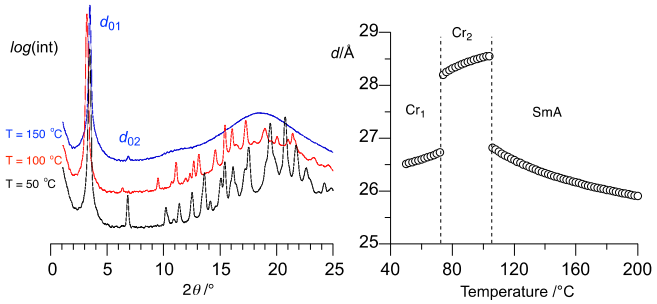

Figure 7. Left: wide-angle powder X-ray diffractograms for **1**[**11**]**d** obtained at three temperatures. Right: temperature dependence of layer thickness d obtained on heating. The dotted lines mark phase transitions.

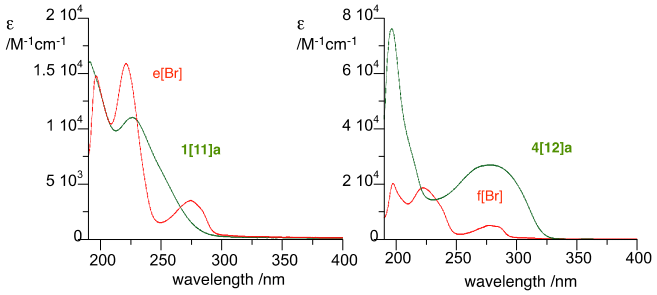

Figure 8. Left: absorption spectra of **1**[**11**]**a** (green) and **e**[**Br**] (red). Right: absorption spectra of **4**[**12**]**a** (green) and **f**[**Br**] (red) obtained in MeCN.

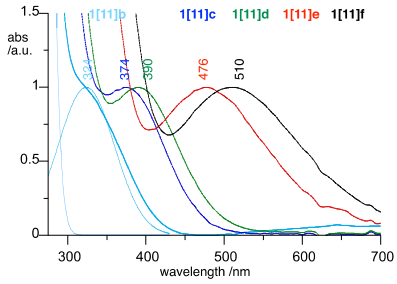

Figure 9. Normalized intermolecular charge transfer bands in pyridinium ion pairs of anion **1**[**11**] recorded in CH_2Cl_2 with the indicated λ_{max}. The low-energy portion of **1**[**11**]**b** (light blue) is deconvoluted.

are collected in Table 1. These additional low-energy absorption bands in pyridinium ion pairs of anions **1**[**11**]–**4**[**12**] are related to intermolecular charge transfer between anion's HOMO and cation's LUMO.

Analysis of two ion pairs in MeCN solutions, **1**[**11**]**e** and **4**[**12**]**e**, revealed a hypsochromic shift of the CT bands relative to those in CH_2Cl_2 solutions by about 40 nm or 0.24 and 0.15 eV, respectively (Figure 10). This indicates a negative solvatochromic effect in more polar MeCN (ε = 35.9), when compared to the lower dielectric strength CH_2Cl_2 (ε = 8.93), due to greater stabilization of the highly ionic ground state. This observation is consistent with solvent dependence of the position of the CT band in methyl *N*-ethylpyridinium-1-carboxylate iodide.[55]

Finally, photophysical properties of the pyridinium ion pairs were investigated in the solid state. Absorption spectra recorded for solid samples premelted between quartz plates revealed intense CT bands with maxima positioned close to those observed for solution spectra in MeCN. As shown for series **3**[**11,12**] in Figure 10, the CT band exhibits 20–25% intensity of the principal absorption bands below 400 nm. Maxima of the CT bands and the absorption edge are shifted to higher energies by 0.28(2) and 0.25(3) eV, respectively, relative to those recorded in CH_2Cl_2. Assuming a linear relationship between the energy of the CT band and the dielectric strength of the medium, it can be estimated that the ions experience a mean dielectric strength ε greater than 40 in the solid state.

DFT Analysis. For a better understanding of the observed photophysical effects, model anions and cations, in which the long alkyl chains were replaced with Me (anions) and Et (cations) groups, were investigated with the TD-DFT method[56] at the CAM-B3LYP/Def2TZVP//B3LYP/Def2TZVP level of theory in MeCN and CH_2Cl_2 dielectric media.

Results for the model anions revealed several excitations above 200 nm in which the lowest-energy excitations are typically of low intensity (small oscillator strength) and involve mainly the HOMO–LUMO transition. Anion **2**[**1**] is exceptional, and the lowest-energy excitation calculated at 260.6 nm has a large oscillator strength (f = 0.869) and corresponds to the maximum observed for **2**[**12**]**a** at 299 nm. Unlike in other anions, this excitation in **2**[**12**] has the intramolecular charge transfer character from the $\{B_{10}\}$ cluster to the benzoyl fragment, as evident from the density

https://doi.org/10.1021/acs.chemmater.2c01165
Chem. Mater. 2022, 34, 6476–6491

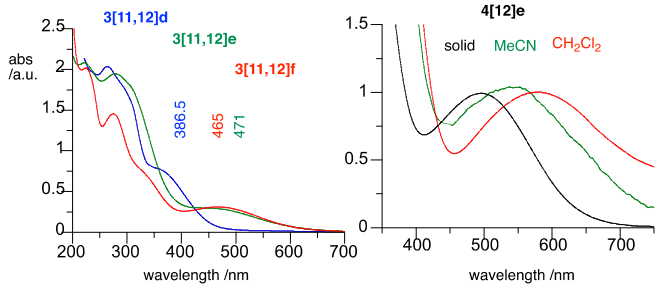

Figure 10. Left: normalized intermolecular charge transfer (ICT) bands recorded in the solid state for pyridinium ion pairs of anion **3**[**11,12**]. Right: normalized ICT bands recorded for **4**[**12**]**e** in MeCN (green), solid state (black), and CH_2Cl_2 (red).

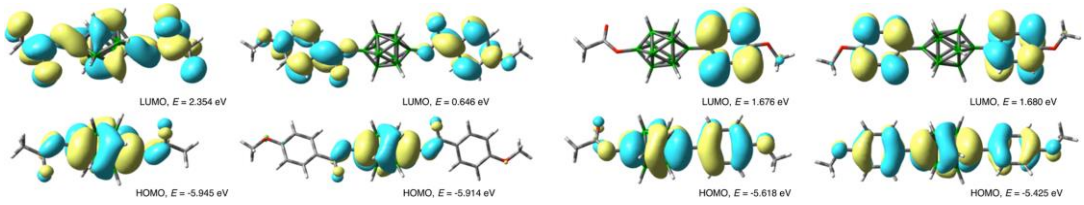

Figure 11. Time-dependent (TD) CAM-B3LYP/Def2TZVP//B3LYP/Def2TZVP-derived contours (isovalue = 0.0004) and energies of frontier molecular orbitals in the MeCN dielectric medium relevant to the lowest-energy excitations in model anions **1**[**1**], **2**[**1**], **3**[**1,1**], and **4**[**1**].

distribution of the involved HOMO and LUMO (Figure 11). Such CT processes are typically observed in pyridinium zwitterions of *closo*-borates.[36,37] Moderate- and high-oscillator-strength excitations that could be matched to the experimental absorption maxima in the other three anions are found as states 7 and 8 in **1**[**1**], state 2 in **3**[**1,1**], and state 3 in **4**[**1**]. A comparison of these time-dependent density functional theory (TD-DFT) excitation energies with experimental low energy λ_{max} shows good correlation and systematic overestimation by 0.50(3) eV.[54]

The distribution of the MO densities in the four anions (*e.g.*, FMO in Figure 11; see also the SI) indicates efficient electronic coupling of the $\{B_{10}\}$ cluster with the apical O atoms in esters **1**[**1**], **2**[**1**], and **3**[**1,1**] and with the phenyl substituent in **3**[**1,1**] and **4**[**1**]. Thus, substituents on the oxygen atoms (alkyl and acyl) and on the phenyl rings directly attached to the boron cluster affect its electronic structure and the energy of the HOMO of the anion. Similarly, substituents at the C(4) position of the pyridinium cation affect the energy of the LUMO. The relative positions of these two MOs define the energy of the intermolecular CT band in the ion pairs.

Analysis of model anions **1**[**1**]−**4**[**1**] and also those containing two MeO (**13**[**1**]), MeO, and 4-MeOPh (**14**[**1,1**]) and two COOMe groups (**15**[**1**]) at the apical positions demonstrates that the energy of the HOMO obtained in the CH_2Cl_2 dielectric medium depends on the substituent and correlates well with the sum of Hammett σ_p parameters[52] (Figure 12). Parameter σ_p for 4-MeOPhCOO was assumed to be 0.10 on the basis of σ_p for PhCOO (0.13),[52] while the value of σ_p = 0.00 was used for AcO.[36] Similarly, the DFT-calculated energy of the LUMO, E_{LUMO}, of the cation is a linear function of the σ_p parameter (Figure 12).

Correlations in Figure 12 indicate that the increasing electron-donating character of the substituent on the $\{B_{10}\}$ cluster increases the energy of the HOMO, while increasing

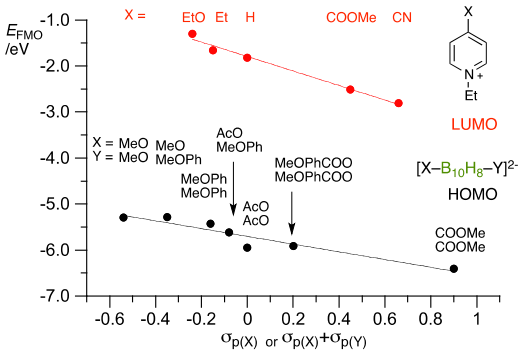

Figure 12. Energy E_{HOMO} for model anions (black) and E_{LUMO} for model cations (red) obtained with the TD-DFT method in the CH_2Cl_2 dielectric medium *vs* σ_p substituent parameter (for cations) or sum of σ_p parameters (for anions). Best fit lines: $E_{HOMO} = -5.70(5) - 0.84(12) \times (\sigma_{pX} + \sigma_{pY})$, $r^2 = 0.90$; $E_{LUMO} = -1.79(4) - 1.57(11) \times \sigma_{pX}$, $r^2 = 0.98$.

electron-withdrawing substituents decrease the energy of the LUMO of the pyridinium cation. The substituent effect is twice stronger for pyridinium than that for the $\{B_{10}\}$ cluster, as evident from the slopes of the correlations. A similar result was found for pyridinium zwitterions of the $\{B_{10}\}$ cluster exhibiting intramolecular CT.[36] The established correlations can be used for predicting FMO energy levels of other ions on the basis of Hammett σ_p parameters.[52]

The E_{HOMO} and E_{LUMO} energies calculated in the MeCN dielectric medium are 0.59(3) eV lower and 0.33(1) eV higher, respectively, than those obtained in CH_2Cl_2, and they exhibit similar correlation with σ_p parameters.[54] The resulting larger calculated HOMO−LUMO difference, ΔE_{FMO}, in MeCN is

https://doi.org/10.1021/acs.chemmater.2c01165
Chem. Mater. 2022, 34, 6476−6491

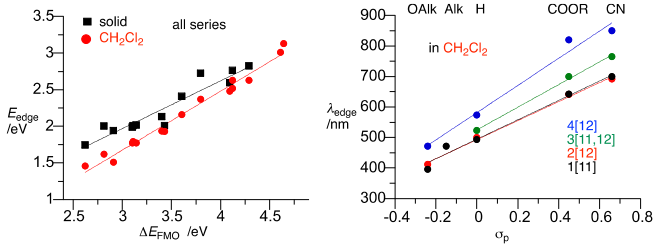

Figure 13. Left: absorption edge energy in CH_2Cl_2 (red dots) and in the solid state (black squares) *vs* calculated HOMO−LUMO energy difference, ΔE_{FMO}. Best fit lines: E_{edge}(DCM) = −0.74(11) + 0.805(30) × ΔE_{FMO}, r^2 = 0.980; E_{edge}(solid) = 0.656(9) × ΔE_{FMO}, r^2 = 0.90. Right: absorption edge in CH_2Cl_2 for each series *vs* σ_p substituent parameter. Best fit lines: **1**[**11**] λ_{edge} = 501(6) + 306(16) × σ_p, r^2 = 0.992; **2**[**12**] λ_{edge} = 493(6) + 312(14) × σ_p, r^2 = 0.996; **3**[**11,12**] λ_{edge} = 525(9) + 372(19) × σ_p, r^2 = 0.997; **4**[**12**] λ_{edge} = 582(19) + 446(46) × σ_p, r^2 = 0.98.

consistent with the observed hypsochromic shift of the CT band in MeCN relative to that in the CH_2Cl_2 solutions.

The energy of the observed intermolecular CT band in the pyridinium ion pairs is related to the ability of the anion to donate an electron and the ability of the cation to accept an electron, and, consequently, to the relative energy of the HOMO and the LUMO of the ions. Indeed, the energies of the CT band onset, E_{edge}, and peak,[54] E_{CT}, correlate well with the DFT-derived ΔE_{FMO}, as shown in Figure 13 for all four series. The correlation indicates that for the insoluble paraquat ion pair **4**[**12**]**g** the absorption peak is expected at 615 ± 12 nm and the edge at 861 ± 30 nm in the solid state. These values are predicted to be even more red-shifted in CH_2Cl_2 solutions.[54] Ion pairs of 1,10-dialkoxy derivatives **13**[**n**] with the highest in the series level of the HOMO (−5.29 eV) are expected to exhibit the most red-shifted CT bands. For instance, **13**[**n**]**f** is predicted to exhibit the CT peak at 554 ± 12 nm and absorption edge at 761 ± 30 nm in the solid state.[54] On the other hand, ion pairs of the dicarboxylic acid esters **15**[**n**] are expected to have CT bands significantly blue-shifted.[54] This demonstrates that the position of the CT band can be controlled in the visible range with a judicious choice of the substituents.

The position of the CT peak and absorption edge in each series also correlates with the σ_p parameter[52] of the substituent on the pyridinium cation (Figure 13, right and the SI). Analysis of the data for absorption edge in CH_2Cl_2 predicts that the ion pair of anion **1**[**11**] with the pyridinium cation containing the NO_2 group (σ_p = 0.78)[52] should exhibit the onset of the CT band at 740 ± 13 nm and the CT peak at 538 ± 14 nm in CH_2Cl_2, which is about 50 and 30 nm, respectively, red-shifted relative to that for **1**[**11**]**f**.

■ CONCLUSIONS

We have demonstrated the first ionic liquid crystals derived from 1,10-disubstituted [*closo*-$B_{10}H_{10}$]$^{2-}$ anion. These ion pairs with substituted pyridinium cations exhibit broad range SmA phases with high clearing temperatures and tunable intermolecular charge transfer bands in the visible range. This represents a new paradigm in the area of ILC.

XRD and DSC analyses indicate that many ion pairs undergo stepwise melting to the SmA phase: first the alkyl chains and then the ionic cores, as two independent thermodynamic events. The intermediate phase with melted alkyl chains constitutes an interesting system with sheets of rigid arrangements of electroactive ions, which are of general interest for organic semiconductors.

The tunability of the intermolecular charge transfer band in ionic liquid crystals has been accomplished by controlling the HOMO of the anions and the LUMO of the cations with judiciously selected substituents. The relevant FMO energies of the ions linearly depend on the substituent constant σ_p. Stronger substituent effects are observed for pyridinium cations than those for {B_{10}} anion. This reflects the lower efficiency of the electronic coupling between the substituent and the {B_{10}} cluster when compared to interactions of substituents and the pyridine ring. These findings indicate that a combination of anions **1**[**n**]−**4**[**n**] with other electron-poor (low LUMO) organic π cations may provide some additional means of controlling the CT band position in these ion pairs.

Analysis of the electronic structure revealed that the [*closo*-$B_{10}H_{10}$]$^{2-}$ anion exhibits effective electronic coupling with Ph and OR substituents. The 1,10-diphenyl derivative **4**[**n**] exhibits extensive electronic conjugation with the {B_{10}} cluster and represents the first example of a promising class of structural elements for molecular electronics.

The position of the CT bands correlates well with the DFT-derived differences between the energies of the relevant FMOs ($\Delta E_{FMO} = E_{LUMO} - E_{HOMO}$) and the σ_p parameters of the substituent on the pyridine ring for individual series. The established correlations offer a guide for designing materials with desired absorption characteristics. Thus, a judicious choice of substituents on both the anion and the cation allows for tuning the position of the CT band in the visible spectral range, which is of general interest for application in energy harvesting and processing.

■ COMPUTATIONAL DETAILS

Quantum−mechanical calculations were carried out with the B3LYP[57,58] method and Def2SVP and Def2TZVP basis sets[59,60] using the Gaussian 09 package[61] for model compounds, in which the alkyl chains were replaced by Me in anions and Et groups in cations. Initial geometry optimizations in appropriate symmetry constraints were undertaken at the B3LYP/Def2SVP level of theory using tight convergence limits in a PhCl dielectric medium requested with the self-consistent reaction field (SCRF) polarizable continuum model (PCM), solvent = C_6H_5Cl. The presence of a weak dielectric medium was demonstrated to be particularly effective for obtaining accurate molecular geometries.[48] The ground-state nature of the stationary points was verified with vibrational frequency calculations. The obtained structures and frequencies were used as starting points for B3LYP/Def2TZVP level geometry optimizations in the PhCl dielectric medium,

https://doi.org/10.1021/acs.chemmater.2c01165
Chem. Mater. 2022, 34, 6476−6491

for which guess = check and RCFC were requested from lower-level theory results.

Equilibrium geometries of anion **1**[**11**]−**4**[**12**] in the most extended conformations were obtained at the B3LYP/Def2SVP level of theory with default convergence limits.

Electronic excitation energies were obtained for model compounds at the CAM-B3LYP/Def2TZVP//B3LYP/Def2TZVP level using time-dependent DFT calculations[56] supplied in the Gaussian package. The solvent effect on electronic excitations was included using the PCM model[62] [keywords: SCRF (PCM, solvent = CH_2Cl_2)].

EXPERIMENTAL SECTION

General. Reagents and solvents were obtained commercially. Derivatives [*closo*-$B_{10}H_8$-1,10-$(OH_2)_2$] (**5**·[**Bu$_4$N**]**Cl**), [*closo*-$B_{10}H_9$-1-I]$^{2-}$ (**6a**), and [*closo*-$B_{10}H_8$-1,10-I_2]$^{2-}$ (**12a**) were obtained according to literature procedures.[48,49] Thin-layer chromatography (TLC) analyses were conducted on silica gel or neutral aluminum oxide plates 60-F254. Column chromatography was performed using 70−230 mesh silica gel (Merck) or basic aluminum oxide (Merck). NMR spectra were obtained at 500 MHz (^{1}H), 125 MHz (^{13}C), 160 MHz (^{11}B) or 400 MHz (^{1}H), 100 MHz (^{13}C), 128 MHz (^{11}B) in $CDCl_3$ and referenced to the solvent (δ = 7.26 ppm for ^{1}H and δ = 77.16 ppm for ^{13}C) or in acetone-d_6 and referenced to the solvent (δ = 2.05 ppm for ^{1}H and δ = 206.26 ppm for ^{13}C) or in CD_3CN and referenced to the solvent (δ = 1.94 ppm for ^{1}H and δ = 118.26 ppm for ^{13}C) or in CD_2Cl_2 and referenced to the solvent (δ = 5.32 ppm for ^{1}H and δ = 53.84 ppm for ^{13}C)[63] or to an external sample of neat BF_3·Et_2O in $CDCl_3$, acetone-d_6, CD_3CN, and CD_2Cl_2 (^{11}B NMR, δ = 0.0 ppm). ^{11}B NMR chemical shifts were taken from the H-decoupled spectra.

IR spectra were recorded using a Nexus Fourier transform infrared (FT-IR) Thermo Nicolet IR spectrometer in KBr tablets. Optical microscopy and phase identification were performed using a polarized microscope equipped with a hot stage. Thermal analysis was performed on a TA Discovery DSC 2500 using samples of about 1.0 mg at a heating rate of 10 K min^{-1} under a flow of nitrogen gas. Melting points were determined on a Melt-Temp II apparatus in capillaries and were uncorrected. High-resolution mass spectrometry was conducted with the TOF-MS ES method.

Electronic absorption spectra for the pyridinium salts **b**[**Br**]−**f**[**Br**] and [NBu_4]$^+$ salts were recorded in spectrophotometric-grade CH_2Cl_2 and MeCN for three concentrations, and the molar extinction coefficients ε were determined using Beer's law.

Details of single-crystal and powder X-ray diffraction experiments are provided in the SI.

Preparation of [*closo*-$B_{10}H_8$-1,10-$(OOCC_{11}H_{23})_2$]$^{2-}$ 2[Bu_4N]$^+$ (1[11]a). A solution of [*closo*-$B_{10}H_8$-1,10-$(OH_2)_2$]·[Bu_4NCl] (**5**·[**Bu$_4$N**]**Cl**, 400 mg, 0.57 mmol)[48] was placed in a three-necked, round-bottomed flask and filled with Ar by three pump-fill cycles. Dry THF (12 mL) was added followed by NaH (81 mg, 3.39 mmol) and $C_{11}H_{23}COCl$ (0.287 mL, 1.24 mmol), and the reaction mixture was stirred for 2 h at room temperature under Ar atm. The reaction progress was monitored using TLC (neutral Al_2O_3, CH_2Cl_2/MeCN, 4:1). Water was added to quench excess NaH, THF was removed, and the organic products were extracted with CH_2Cl_2. The organic layer was dried (Na_2SO_4), and the solvent was removed. The resulting crude product was purified by column chromatography (basic Al_2O_3, CH_2Cl_2/MeCN, 4:1) to give 386 mg (68% yield) of pure **1**[**11**]**a** as a colorless oil. The typical yield of the reaction was in a range of 65−70%: ^{1}H NMR (CD_3CN, 500 MHz): δ 3.09 (pseudo t, J = 8.6 Hz, 16H), 2.60 (t, J = 7.5 Hz, 4H), 1.68−1.64 (m, 4H), 1.59 (quint, J = 8.0 Hz, 16H), 1.39−1.29 (m, 48H), 0.96 (t, J = 7.4 Hz, 24H), 0.89 (t, J = 6.9 Hz, 6H), 0.34 (q, J = 112 Hz, 8H). ^{13}C{^{1}H} NMR (CD_3CN, 125 MHz): δ 177.5, 59.2, 37.0, 32.6, 30.4 (2C), 30.4, 30.2, 30.1, 26.6, 24.3, 23.4, 20.3, 14.4, 13.8. ^{11}B NMR (CD_3CN, 160 MHz): δ 15.2 (s, 2B), −32.7 (d, J = 126 Hz, 8B). IR (KBr) ν 2919, 2850, 2472, 1681, 1467, 1248 cm^{-1}. UV, λ_{max} (log ε) 230 (4.01) nm in CH_2Cl_2 and 226.5 (4.04) in MeCN. High-resolution mass spectrometry (HRMS) (electrospray ionization-time-of-flight mass spectrometry (ESI-TOF)) m/z: [M]$^-$ calcd for $C_{24}H_{54}B_{10}O_4$ 517.5031; found 517.5013. Anal. Calcd for $C_{56}H_{126}B_{10}O_4N_2$: C, 67.28; H, 12.70; N, 2.80. Found: C, 67.23; H, 12.97; N, 2.93.

Preparation of [*closo*-$B_{10}H_8$-1,10(OOCC$_6$H$_4$OC$_{12}$H$_{25}$)$_2$]$^{2-}$ 2-[Bu_4N]$^+$ (2[12]a). A solution of [*closo*-$B_{10}H_8$-1,10-$(OH_2)_2$]·[Bu_4NCl] (**5**·[**Bu$_4$N**]**Cl**, 200 mg, 0.28 mmol) was placed in a three-necked, round-bottomed flask and filled with Ar by three pump-fill cycles. Dry THF (8 mL) was added followed by NaH (41 mg, 1.71 mmol), and this was stirred for 5 min. To this, $C_{12}H_{25}OC_6H_4COCl$ (0.200 mL, 0.62 mmol) was added, and the reaction mixture was stirred for 2 h at room temperature under Ar atm. The reaction completion was monitored using TLC (neutral Al_2O_3, CH_2Cl_2/MeCN, 4:1). Water was added to the reaction mixture to quench the excess NaH. THF was removed in a rotary evaporator, and extraction was done in CH_2Cl_2/water. The organic layer was dried over Na_2SO_4 and evaporated. The resulting crude product was purified by column chromatography (basic Al_2O_3, CH_2Cl_2/MeCN, 4:1) to give 206 mg (68% yield) of pure **2**[**12**]**a** as a white powder. The typical yield of the reaction was in a range of 55−68%: mp 250−254 °C. ^{1}H NMR (CD_3CN, 500 MHz): δ 8.13 (d, J = 8.8 Hz, 4H), 6.99 (d, J = 8.8 Hz, 4H), 4.06 (t, J = 6.6 Hz, 4H), 3.06 (pseudo t, J = 8.6 Hz, 16H), 1.80 (quint, J = 7.0 Hz, 4H), 1.55 (quint, J = 7.8 Hz, 16H), 1.50−1.45 (m, 4H), 1.37−1.29 (m, 48H), 0.94 (t, J = 7.4 Hz, 24H), 0.89 (t, J = 6.9 Hz, 6H), 0.71−0.08 (m, 8H). ^{13}C{^{1}H} NMR (CD_3CN, 125 MHz): δ 168.3, 162.5, 132.1, 128.7, 114.6, 68.9, 59.1, 32.6, 30.33, 30.32, 30.28, 30.0 (2C), 29.9, 26.7, 24.3, 23.4, 20.3, 14.4, 13.8. ^{11}B{^{1}H} NMR (CD_3CN, 160 MHz): δ 16.2 (s, 2B), −31.7 (br d, 8B). IR (KBr) ν 2960, 2872, 2467, 1677, 1331 cm^{-1}. UV, λ_{max} (log ε) 249 (4.55) in CH_2Cl_2 and 247 (4.53) in MeCN. HRMS (ESI-TOF) m/z: [M]$^-$ calcd for $C_{38}H_{66}B_{10}O_6$ 728.5790; found 728.5837. Anal. Calcd for $C_{70}H_{138}B_{10}O_6N_2$: C, 69.37; H, 11.48; N, 2.31. Found: C, 69.25; H, 11.49; N, 2.34.

Preparation of [*closo*-$B_{10}H_8$-1-($C_6H_4OC_{12}H_{25}$)-10-$OOCC_{11}H_{23}$]$^{2-}$ 2[Bu_4N]$^+$ (3[11,12]a). To a solution of formate **10a** (106 mg, 0.12 mmol) in MeOH (2 mL) was added 4−5 drops of concentrated HCl, and the mixture was stirred at rt for 20 min. The reaction completion was monitored using TLC (basic Al_2O_3, CH_2Cl_2/MeCN, 3:2). The solution was passed through a pipette plugged with cotton wool and washed with MeOH. The solvent was evaporated to dryness, and the resulting oxonium intermediate **11a** was dried in high vacuum. NaH (24 mg, 0.6 mmol) was added to the residue, and the flask was evacuated and filled with Ar. Dried and deaired THF (2 mL) was added followed by lauryl chloride (142 μL, 0.6 mmol), and the reaction mixture was stirred for 2 h at rt under Ar atm. Reaction progress was monitored using TLC (basic Al_2O_3, CH_2Cl_2/MeCN, 4:1). Water was added to quench excess NaH, THF was removed, and organic products were extracted with CH_2Cl_2. The organic layer was dried (Na_2SO_4), solvents were removed, and the resulting crude product was purified by column chromatography (basic Al_2O_3, CH_2Cl_2/MeCN, 4:1), giving 52 mg (37% yield) of pure **3**[**11,12**]**a** as a colorless oil. The typical yield of the reaction was in the range of 34−40%: ^{1}H NMR (CD_2Cl_2, 400 MHz): δ 7.92−7.60 (m, 2H), 7.05−6.55 (m, 2H; molecular aggregation resulted in an atypical splitting pattern of aromatic signals), 3.98 (t, J = 6.6 Hz, 2H), 2.99 (pseudo t, J = 8.2 Hz, 16H), 2.71 (t, J = 7.6 Hz, 2H), 1.80−1.69 (m, 4H), 1.48 (quint, J = 8.3 Hz, 16H), 1.41−1.28 (m, 50H), 0.95 (t, J = 7.2 Hz, 24H), 0.88 (t, J = 6.6 Hz, 6H), 0.71−0.08 (br m, 8H). ^{13}C{^{1}H} NMR (CD_2Cl_2, 100 MHz): δ 176.3, 160.0, 137.0, 129.2, 126.9, 122.0, 112.9, 109.6, 67.9, 58.8, 36.3, 32.31, 32.29, 30.2, 30.15, 30.13, 30.1−29.9 (8C), 29.8, 29.7, 26.7, 26.3, 24.3, 23.1 (2C), 20.0, 14.3 (2C), 13.9. ^{11}B{^{1}H} NMR (CD_2Cl_2, 128 MHz): δ 18.0 (s, 1B), 1.8 (s, 1B), −30.3 (d, 8B). IR (KBr) ν 2925, 2854, 2461, 1676, 1466, 1380 cm^{-1}. UV, λ_{max} (log ε) 274 (4.26) nm in CH_2Cl_2 and 273 (4.15) nm in MeCN. HRMS (ESI-TOF) m/z: [M]$^-$ calcd for [$C_{30}H_{61}B_{10}O_3$]$^-$ 579.5551; found 579.5528. Anal. Calcd for $C_{62}H_{132}B_{10}N_2O_3$: C, 70.13; H, 12.53; N, 2.64. Found: C, 70.15; H, 12.49; N, 2.71.

https://doi.org/10.1021/acs.chemmater.2c01165
Chem. Mater. 2022, 34, 6476−6491

Synthesis of [*closo*-$B_{10}H_8$-1,10-(C_6H_4OR)$_2$]$^{2-}$ 2[Bu_4N]$^+$ (4[n]a). *General Procedure.* To a solution of [*closo*-$B_{10}H_8$-1,10-I_2]$^{2-}$ 2[Bu_4N]$^+$ (**12a**, 214 mg, 0.25 mmol) in dry THF (1 mL) were added 4-alkoxyphenylmagnesium bromide (8 mL, 0.5 M) in THF and PEPPSI-IPr catalyst (3 mg, 2 mol %). The mixture was refluxed for 12 h. The resulting dark solution was treated with a saturated solution of NH_4Cl (4 mL), and THF was evaporated. The organic products were extracted with CH_2Cl_2 (3 × 5 mL), the combined extracts were dried (Na_2SO_4), and the solvent was evaporated. The residue was washed with MeCN (3 × 2 mL), and the combined MeCN extracts were evaporated to dryness to obtain a colorless oily residue. The residue was triturated with toluene (2 mL), and the formed precipitate was filtered and washed with additional toluene. Recrystallization from *n*-hexane/CH_2Cl_2 gave **4**[**n**]**a** as colorless crystals.

[closo-$B_{10}H_8$-1,10-($C_6H_4OC_7H_{15}$)$_2$]$^{2-}$ 2[Bu_4N]$^+$ (4[7]a). Product **4**[**7**]**a** was obtained in 89% yield (219 mg) using 4-heptyloxyphenylmagnesium bromide as colorless microcrystals: mp 130−134 °C. ^{1}H NMR (CD_2Cl_2, 400 MHz): δ 7.92 (br d, J = 5.1 Hz, 4H), 6.75 (br d, J = 7.8 Hz, 4H), 3.95 (t, J = 7.4 Hz, 4H), 2.88 (pseudo t, J = 5.1 Hz, 16H), 1.79 (quint, J = 7.1 Hz, 4H), 1.48 (quint, J = 7.3 Hz, 4H), 1.43−1.29 (m, 44H), 0.96−0.90 (m, 30H), 0.9−0.2 (br m, 8H). ^{13}C{^{1}H} NMR (CD_2Cl_2, 100 MHz): δ 156.5, 136.7, 112.9, 68.3, 58.7, 32.3, 30.1, 29.6, 26.5, 24.3, 23.0, 20.0, 14.3, 13.9 (C nucleus attached to the cage was not observed). ^{11}B{^{1}H} NMR (CD_2Cl_2, 128 MHz): δ 7.3 (s, 2B), −27.6 (br d, 8B). HRMS (ESI-TOF) m/z: [M]$^-$ calcd for $C_{26}H_{47}B_{10}O_2$ 501.4550; found: 501.4507. Anal. Calcd for $C_{58}H_{118}B_{10}N_2O_2$: C, 70.82; H, 12.09; N, 2.85. Found: C, 70.79; H, 12.16; N, 2.97.

[closo-$B_{10}H_8$-1,10-($C_6H_4OC_{12}H_{25}$)$_2$]$^{2-}$ 2[Bu_4N]$^+$ (4[12]a). Product **4**[**12**]**a** was obtained in 60% yield (169 mg) using 12-dodecyloxyphenylmagnesium bromide as a white solid: mp 175−182 °C. ^{1}H NMR (CD_3CN, 400 MHz): δ 7.84 (d, J = 8.2 Hz, 4H), 6.73 (d, J = 8.5 Hz, 4H), 3.97 (t, J = 6.6 Hz, 4H), 3.02 (pseudo t, J = 8.6 Hz, 16H), 1.76 (quint, J = 7.1 Hz, 4H), 1.59−1.45 (m, 20H), 1.38−1.28 (m, 48H), 0.95 (t, J = 7.4 Hz, 24H), 0.89 (t, J = 6.9 Hz, 6H), 0.7−0.0 (br m, 8H). ^{13}C{^{1}H} NMR (CD_2Cl_2, 100 MHz): δ 156.4, 136.7, 112.9, 68.3, 58.5, 32.3, 30.04 (2C), 30.01 (3C), 29.9, 29.7, 29.6, 26.6, 24.2, 23.0, 20.0, 14.2, 13.9 (C nucleus attached to the cage was not observed). ^{11}B{^{1}H} NMR (CD_3CN, 128 MHz): δ 9.1 (s, 2B), −25.4 (d, J = 124 Hz, 8B). IR (KBr) ν 2925, 2853, 2448, 1482, 1224 cm^{-1}. UV (CH_2Cl_2), λ_{max} (log ε) 274 (4.38) nm in CH_2Cl_2 and 277.5 (4.42) nm in MeCN. HRMS (ESI-TOF) m/z: [M]$^-$ calcd for $C_{36}H_{67}B_{10}O_2$ 641.6072; found 641.6057. Anal. Calcd for $C_{68}H_{138}B_{10}N_2O_2$: C, 72.67; H, 12.38; N, 2.49. Found: C, 72.71; H, 12.43; N, 2.52.

Preparation of Ion Pairs of Anions 1[11], 2[12], and 3[11,12]. *General Procedure for Cation Exchange.* To a solution of **1**[**11**]**a** (250.0 mg, 0.25 mmol), **2**[**12**]**a**, (312.5 mg, 0.25 mmol), or **3**[**11,12**]**a** (277.8 mg, 0.25 mmol) in CH_2Cl_2 (2 mL), the appropriate pyridinium bromide (0.50 mmol) was added in one portion. The solution was stirred for 30 min, water (4 mL) was added, and vigorous stirring was continued to extract [Bu_4N]$^+$Br$^-$ into the water layer. The organic layer was separated and dried (Na_2SO_4), and the solvent was removed to give the corresponding pyridinium ion pair. Pure ion pairs were obtained by repeated precipitation or by recrystallization from the appropriate solvents.

Ion Pair 1[11]b. The ion pair obtained from **1**[**11**]**a** (150 mg, 0.15 mmol) and pyridinium bromide **b**[**Br**] (99 mg, 0.30 mmol) was further purified by precipitating from cold EtOH to give pure **1**[**11**]**b** as a pale-yellow waxy material in 83% yield (127 mg): ^{1}H NMR (CD_3CN, 500 MHz): δ 8.51 (d, J = 7.4 Hz, 4H), 7.37 (d, J = 7.4 Hz, 4H), 4.34 (t, J = 7.4 Hz, 4H), 4.28 (t, J = 6.6 Hz, 4H), 2.57 (t, J = 7.5 Hz, 4H), 1.89−1.77 (m, 8H), 1.65 (quint, J = 7.5 Hz, 4H), 1.45 (quint, J = 6.9 Hz, 4H), 1.36−1.28 (m, 48H), 0.86−0.94 (m, 18H), −0.3−0.8 (m, 8H). ^{13}C{^{1}H} NMR (CD_3CN, 125 MHz): δ 176.5, 171.4, 146.9, 114.7, 72.2, 60.4, 36.7, 33.7, 32.6, 32.4, 30.4 (3C), 30.3, 30.1, 29.5, 29.1, 26.6, 26.2, 23.4, 23.3, 19.8, 14.4, 14.3, 13.7. ^{11}B NMR (CD_3CN, 160 MHz): δ 15.4 (s, 2B), −32.0 (d, J = 114 Hz, 8B). IR (KBr) ν 3059, 2957, 2952, 2472, 1679, 1467, 1323 cm^{-1}. Anal. Calcd for $C_{56}H_{110}B_{10}O_6N_2$: C, 66.23; H, 10.92; N, 2.76. Found: C, 66.08; H, 11.15; N, 2.79.

Ion Pair 1[11]c. The ion pair obtained from **1**[**11**]**a** (100 mg, 0.10 mmol) and pyridinium bromide **c**[**Br**] (66 mg, 0.20 mmol) was further purified by precipitation from cold EtOAc to give a pure product as a light-yellow powder in 87% yield (88 mg): ^{1}H NMR (CD_3CN, 500 MHz): δ 8.64 (d, J = 6.5 Hz, 4H), 7.84 (d, J = 6.4 Hz, 4H), 4.48 (t, J = 7.5 Hz, 4H), 2.86 (t, J = 7.8 Hz, 4H), 2.56 (t, J = 7.5 Hz, 4H), 1.89 (quint, J = 7.6 Hz, 4H), 1.71−1.62 (m, 8H), 1.35−1.28 (m, 56H), 0.94−0.87 (m, 18H), 0.8 to −0.3 (m, 8H). ^{13}C{^{1}H} NMR (CD_3CN, 125 MHz): δ 176.3, 164.3, 144.8, 128.9, 61.6, 36.7, 36.1, 33.9, 32.6, 32.5, 30.4 (2C), 30.35 (3C), 30.3, 30.1, 29.9, 29.8, 29.7, 26.7, 23.4, 23.3, 19.9, 14.4 (2C), 13.7. ^{11}B NMR (CD_3CN, 160 MHz): δ 15.3 (s, 2B), −32.0 (d, J = 104 Hz, 8B). IR (KBr) ν 3061, 2920, 2478, 1682, 1640, 1470, 1322 cm^{-1}. Anal. Calcd for $C_{58}H_{114}B_{10}O_4N_2$: C, 68.86; H, 11.36; N, 2.77. Found: C, 68.75; H, 11.28; N, 2.81.

Ion Pair 1[11]d. The ion pair obtained from **1**[**11**]**a** (150 mg, 0.15 mmol) and pyridinium bromide **d**[**Br**] (99 mg, 0.30 mmol) was further purified by recrystallization from MeCN at room temperature to give a pure product as yellow microcrystals in 85% yield (129 mg): ^{1}H NMR ($CDCl_3$, 500 MHz): δ 8.98 (d, J = 5.7 Hz, 4H), 8.13 (t, J = 7.7 Hz, 2H), 7.94 (t, J = 6.8 Hz, 4H), 4.51 (t, J = 7.6 Hz, 4H), 2.57 (t, J = 7.7 Hz, 4H), 1.88 (t, J = 7.4 Hz, 4H), 1.74−1.68 (m, 4H), 1.37−1.20 (m, 68H), 0.88−0.85 (m, 12H), 0.8−0.2 (m, 8H). ^{13}C{^{1}H} NMR ($CDCl_3$, 125 MHz): δ 176.4, 145.4, 144.0, 128.7, 62.0, 36.9, 32.2, 32.0 (2C), 29.90, 29.86 (3C), 29.83, 29.80 (2C), 29.77, 29.6, 29.5, 29.48, 29.44, 26.2, 26.0, 22.8 (2C), 14.2 (2C). ^{11}B{^{1}H} NMR ($CDCl_3$, 160 MHz,): δ 14.1 (s, 2B), −33.7 (br d, 8B). IR (KBr) ν 3059, 2920, 2491, 1693, 1468, 1245 cm^{-1}. Anal. Calcd for $C_{58}H_{114}B_{10}O_4N_2$: C, 68.86; H, 11.36; N, 2.77. Found: C, 68.92; H, 11.29; N, 2.83.

Ion Pair 1[11]e. The ion pair obtained from **1**[**11**]**a** (213 mg, 0.21 mmol) and pyridinium bromide **e**[**Br**] (147 mg, 0.43 mmol) was further purified by precipitation from cold EtOH to give a pure product as a reddish waxy material in 88% yield (196 mg): ^{1}H NMR (CD_3CN, 500 MHz): δ 9.02 (d, J = 6.4 Hz, 4H), 8.42 (d, J = 6.2 Hz, 4H), 4.65 (t, J = 7.5 Hz, 4H), 4.38 (t, J = 6.7 Hz, 4H), 2.56 (t, J = 7.5 Hz, 4H), 1.97−1.90 (m, 4H), 1.78 (quint, J = 6.7 Hz, 4H), 1.66 (quint, J = 7.5 Hz, 4H), 1.44 (quint, J = 7.2 Hz, 4H), 1.37−1.28 (m, 48H), 0.94−0.87 (m, 18H), 0.7 to −0.2 (m, 8H). ^{13}C{^{1}H} NMR (CD_3CN, 125 MHz): δ 176.6, 163.0, 147.6, 145.3, 128.6, 68.1, 62.9, 36.9, 34.3, 32.7, 32.1, 30.5, 30.4, 30.3, 30.1, 29.1, 26.7, 26.2, 23.4, 23.3, 20.0, 14.5, 14.4, 13.9. ^{11}B NMR (CD_3CN, 160 MHz): δ 15.4 (s, 2B), −31.9 (d, J = 106 Hz, 8B). IR (KBr) ν 2925, 2853, 2470, 1737, 1683, 1463, 1287 cm^{-1}. Anal. Calcd for $C_{56}H_{106}B_{10}O_8N_2$: C, 64.45; H, 10.24; N, 2.68. Found: C, 64.39; H, 10.28; N, 2.75.

Ion Pair 1[11]f. The ion pair obtained from **1**[**11**]**a** (187 mg, 19 mmol) and pyridinium bromide **f**[**Br**] (122 mg, 38 mmol) was further purified by precipitation from cold MeCN to give a pure product as a reddish powder in 86% yield (162 mg): ^{1}H NMR ($CDCl_3$, 500 MHz): δ 9.34 (d, J = 4.5 Hz, 4H), 8.30 (d, J = 5.1 Hz, 4H), 4.59 (br s, 4H), 2.61 (t, J = 7.3 Hz, 4H), 1.92 (br s, 4H), 1.76−1.71 (m, 4H), 1.40 (br s, 4H), 1.40−1.22 (m, 56H), 0.85−0.88 (m, 12H), 0.8 to −0.1 (m, 8H). ^{13}C{^{1}H} ($CDCl_3$, 125 MHz): δ 176.7, 147.3, 131.3, 127.1, 114.0, 63.2, 36.9, 32.4, 32.04, 31.98, 29.89, 29.87, 29.82, 29.78, 29.79, 29.7, 29.6, 29.5, 29.4, 29.35, 26.3, 25.9, 22.8 (2C), 14.2 (2C). ^{11}B{^{1}H} NMR ($CDCl_3$, 160 MHz): δ 13.7 (s, 2B), −33.7 (br d, 8B). IR (KBr) ν 2921, 2851, 2477, 1674, 1466, 1332 cm^{-1}. Anal. Calcd for $C_{56}H_{104}B_{10}O_4N_4$: C, 66.89; H, 10.42; N, 5.57. Found: C, 66.84; H, 10.51; N, 5.60.

Ion Pair 1[11]g. The ion pair was obtained in 94% yield (94 mg) from **1**[**11**]**a** (100 mg, 0.10 mmol) and *N*,*N*′-didodecyl-4,4′-bipyridinium dibromide (**g**[**Br**], 66 mg, 0.10 mmol) as a purple powder insoluble in any solvent: mp 235−240 °C (dec). Anal. Calcd for $C_{58}H_{108}B_{10}O_4N_2$: C, 69.27; H, 10.82; N, 2.79. Found: C, 69.19; H, 10.90; N, 2.81.

Ion Pair 2[12]b. The ion pair obtained from **2**[**12**]**a** (100 mg, 0.08 mmol) and pyridinium bromide **b**[**Br**] (55 mg, 0.16 mmol) was further purified by precipitation from MeCN to give a pale-yellow

https://doi.org/10.1021/acs.chemmater.2c01165
Chem. Mater. 2022, 34, 6476−6491

powder in 85% yield (86 mg): ^{1}H NMR ($CDCl_3$, 500 MHz): δ 8.73 (d, J = 6.2 Hz, 4H), 8.15 (d, J = 8.5 Hz, 4H), 7.23 (d, J = 6.4 Hz, 4H), 6.86 (d, J = 8.6 Hz, 4H), 4.20 (br s, 4H), 3.97 (br t, J = 6.3 Hz, 4H), 3.89 (br t, J = 6.3 Hz, 4H), 1.78 (br quint, J = 6.9 Hz, 4H), 1.64 (br quint, J = 7.8 Hz, 4H), 1.57 (br quint, J = 7.3 Hz, 4H), 1.45 (quint, J = 7.3 Hz, 4H), 1.26−1.22 (m, 48H), 1.10 (sext, J = 7.6 Hz, 4H), 0.89−0.85 (m, 12H), 0.68 (t, J = 7.2 Hz, 6H), 0.8−0.0 (m, 8H). ^{13}C{^{1}H} NMR ($CDCl_3$, 125 MHz,): δ 169.6, 168.9, 161.9, 146.8, 131.8, 127.1, 113.9, 113.6, 70.9, 68.2, 59.6, 33.5, 32.0, 31.7, 29.8, 29.78, 29.74, 29.71, 29.6, 29.5, 29.4, 29.0, 28.6, 26.2, 25.8, 25.7, 22.8, 22.7, 19.2, 14.22, 14.17, 13.7. ^{11}B{^{1}H} NMR ($CDCl_3$, 160 MHz): δ 14.6 (s, 2B), −33.2 (br d, 8B). IR (KBr) ν 2923, 2470, 1670, 1604, 1520, 1327 cm^{-1}. Anal. Calcd for $C_{70}H_{122}B_{10}O_8N_2$: C, 68.47; H, 10.01; N, 2.28. Found: C, 68.41; H, 9.98; N, 2.32.

Ion Pair ***2[12]d.*** The ion pair obtained from **2**[**12**]**a** (100 mg, 0.08 mmol) and pyridinium bromide **d**[**Br**] (54 mg, 0.16 mmol) was further purified by recrystallization from cold MeCN to give yellow microcrystals in 88−92% yield (89 mg): ^{1}H NMR ($CDCl_3$, 500 MHz): δ 8.89 (br d, J = 4.5 Hz, 4H), 8.12 (d, J = 8.2 Hz, 4H), 8.01 (t, J = 7.2 Hz, 2H), 7.75 (br t, J = 6.0 Hz, 4H), 6.85 (d, J = 8.4 Hz, 4H), 4.47 (br s, 4H), 3.96 (br t, J = 6.6 Hz, 4H), 1.78 (br quint, J = 7.2 Hz, 4H), 1.68 (br s, 4H), 1.45 (br quint, J = 7.0 Hz, 4H), 1.27−1.11 (m, 52H), 1.04−0.97 (m, 16H), 0.89−0.85 (m, 12H), 0.8−0.0 (m, 8H). ^{13}C{^{1}H} NMR ($CDCl_3$, 125 MHz): δ 168.9, 162.0, 145.1, 144.5, 131.7, 128.5, 126.7, 113.7, 68.2, 61.9, 32.2, 32.1, 32.0, 29.82 (5C), 29.78 (2C), 29.70, 29.57, 29.54, 29.48 (2C), 29.39, 26.26, 26.19, 22.8, 14.2 (2C). ^{11}B{^{1}H} NMR ($CDCl_3$, 160 MHz): δ 14.3 (s, 2B), −33.6 (br d, 8B). IR (KBr) ν 3063, 2921, 2472, 1671, 1487, 1309, 1284 cm^{-1}. Anal. Calcd for $C_{72}H_{126}B_{10}O_6N_2$: C, 70.66; H, 10.38; N, 2.29. Found: C, 70.61; H, 10.42; N, 2.33.

Ion Pair ***2[12]e.*** The ion pair obtained from **2**[**12**]**a** (130 mg, 11 mmol) and pyridinium bromide **e**[**Br**] (74 mg, 0.22 mmol) was further purified by the recrystallization from cold EtOH to give a reddish sticky solid in 92% yield (124 mg): ^{1}H NMR (acetone-d_6, 500 MHz): δ 9.46 (d, J = 6.1 Hz, 4H), 8.45−8.41 (m, 4H), 8.13 (d, J = 8.6 Hz, 4H), 6.97 (d, J = 8.7 Hz, 4H), 4.86 (t, J = 7.5 Hz, 4H), 4.40−4.35 (m, 2H), 4.32 (t, J = 6.8 Hz, 2H), 4.08 (t, J = 6.5 Hz, 4H), 1.96 (quint, J = 7.2 Hz, 4H), 1.80 (quint, J = 7.0 Hz, 4H), 1.73 (quint, J = 7.2 Hz, 2H), 1.50 (quint, J = 7.4 Hz, 4H), 1.39−1.30 (m, 38H), 1.25−1.20 (m, 4H), 1.17−1.12 (m, 8H), 0.90−0.85 (m, 12H), 0.75 (t, J = 7.1 Hz, 6H), 0.8−0.0 (m, 8H). ^{13}C{^{1}H} NMR (acetone-d_6, 125 MHz) δ 169.1, 162.9, 162.7, 147.9, 144.6, 132.3, 128.5, 128.4, 114.5, 68.8, 67.8, 63.8, 63.1, 32.7, 32.2, 32.1, 30.41, 30.37, 30.3, 30.2, 29.1, 26.9, 26.4, 26.2, 23.4, 23.4, 23.2, 14.42, 14.39, 14.34. ^{11}B{^{1}H} NMR (acetone-d_6, 160 MHz): δ 17.5 (s, 2B), −30.4 (br d, 8B). IR (KBr) ν 3056, 2925, 2472, 1734, 1666, 1466, 1332 cm^{-1}. Anal. Calcd for $C_{70}H_{118}B_{10}O_{10}N_2$: C, 66.95; H, 9.47; N, 2.23. Found: C, 66.92; H, 9.51; N, 2.30.

Ion Pair ***2[12]f.*** The ion pair obtained from **2**[**12**]**a** (100 mg, 0.08 mmol) and pyridinium bromide **f**[**Br**] (54 mg, 0.16 mmol) was further purified by precipitation from cold MeCN to give pure product as a red powder in 85% yield (85 mg): ^{1}H NMR ($CDCl_3$, 500 MHz, 313 K): δ 9.21 (s, 4H), 8.11 (br s, 8H), 6.89 (br s, 4H), 4.54 (br s, 4H), 3.98 (br s, 4H), 1.77 (br s, 8H), 1.46 (br s, 4H), 1.29 (br s, 36H), 1.16 (br s, 8H), 1.03 (br s, 16H), 0.89−0.85 (m, 12H), 0.8−0.0 (m, 8H). ^{13}C{^{1}H} NMR ($CDCl_3$, 125 MHz, 313 K): δ 169.3, 162.6, 146.9, 131.9, 131.5, 127.0, 126.3, 114.2, 68.4, 63.5, 32.1 (2C), 32.0, 29.84 (3C), 29.81 (2C), 29.73, 29.68, 29.58, 29.55, 29.50 (2C), 29.47, 29.3, 26.3, 22.8 (2C), 14.2 (2C). ^{11}B{^{1}H} NMR ($CDCl_3$, 160 MHz, 313 K): δ 14.4 (s, 2B), −33.3 (br d, 8B). IR (KBr) ν 3048, 2923, 2472, 1667, 1467, 1328 cm^{-1}. Anal. Calcd for $C_{70}H_{116}B_{10}O_6N_4$: C, 69.04; H, 9.60; N, 4.60. Found: C, 68.97; H, 9.42; N, 4.59.

Ion Pair ***3[11,12]d.*** The ion pair obtained from **3**[**11,12**]**a** (100 mg, 0.09 mmol) and pyridinium bromide **d**[**Br**] (62 mg, 0.19 mmol) was further purified by recrystallization from MeCN to give a pure product as a yellow microcrystalline powder in 90% yield (91 mg): ^{1}H NMR (CD_2Cl_2, 400 MHz): δ 8.62 (d, J = 6.1 Hz, 4H), 8.14 (t, J = 7.8 Hz, 2H), 7.73 (t, J = 6.9 Hz, 4H), 7.62−7.54 (m, 2H), 7.09−6.61 (m, 2H; molecular aggregation resulted in an atypical splitting pattern of aromatic signals), 4.33 (t, J = 7.4 Hz, 4H), 3.95 (t, J = 6.7 Hz, 2H), 2.59 (t, J = 7.7 Hz, 2H), 1.80−1.70 (m, 10H), 1.44−1.18 (m, 68H), 0.91−0.86 (m, 12H), 0.7−0.0 (br m, 8H). ^{13}C{^{1}H} NMR (CD_2Cl_2, 100 MHz): δ 176.2, 158.5, 145.1, 144.7, 128.8, 127.7, 121.5, 110.6, 68.1, 62.5, 37.0, 32.4, 32.3, 32.1, 30.2−30.0, 29.85, 29.82, 29.79, 29.6, 26.7, 26.4, 26.3, 23.1, 14.3. ^{11}B{^{1}H} NMR (CD_2Cl_2, 128 MHz): δ 17.5 (s, 1B), 1.8 (s, 1B), −30.1 (br d, 8B). IR (KBr) ν 3062, 2923, 2464, 1690, 1501, 1467, 1226 cm^{-1}. Anal. Calcd for $C_{64}H_{120}B_{10}O_3N_2$: C, 71.59; H, 11.26; N, 2.61. Found: C, 71.48; H, 11.23; N, 2.64.

Ion Pair ***3[11,12]e.*** The ion pair obtained from **3**[**11,12**]**a** (100 mg, 0.09 mmol) and pyridinium bromide **e**[**Br**] (65 mg, 0.19 mmol) was further purified by precipitation from cold EtOH to give a pure product as a red powder in 90% yield (94 mg): ^{1}H NMR (CD_2Cl_2, 400 MHz): δ 8.89 (d, J = 6.2 Hz, 4H), 8.08 (d, J = 6.1 Hz, 4H), 7.86−7.54 (m, 2H; molecular aggregation resulted in an atypical splitting pattern of aromatic signals), 4.46 (t, J = 7.4 Hz, 4H), 4.38 (t, J = 6.9 Hz, 4H), 3.91 (t, J = 6.7 Hz, 2H), 2.61 (t, J = 7.7 Hz, 2H), 1.84−1.69 (m, 12H), 1.42−1.27 (m, 46H), 1.17 (sext, J = 7.4 Hz, 4H), 1.01−0.82 (m, 18H), 0.7−0.0 (br m, 8H). ^{13}C{^{1}H} NMR (CD_2Cl_2, 100 MHz): δ 176.2, 162.1, 158.6, 146.7, 144.4, 128.8, 127.9, 127.8, 121.4, 111.0, 68.0, 67.9, 62.6, 36.9, 34.3, 32.3, 31.8, 30.2−30.0, 29.78, 29.76, 28.8, 26.6, 26.2, 25.9, 23.1, 22.9, 19.6, 14.3, 14.2, 13.7. ^{11}B{^{1}H} NMR (CD_2Cl_2, 128 MHz): δ 17.8 (s, 1B), 1.9 (s, 1B), −29.9 (br d, 8B). IR (KBr) ν 3055, 2925, 2450, 1731, 1680, 1458, 1288 cm^{-1}. Anal. Calcd for $C_{62}H_{112}B_{10}O_7N_2$: C, 67.35; H, 10.21; N, 2.53. Found: C, 67.42; H, 10.35; N, 2.72.

Ion Pair ***3[11,12]f.*** The ion pair obtained from **3**[**11,12**]**a** (135 mg, 0.13 mmol) and pyridinium bromide **f**[**Br**] (82 mg, 0.26 mmol) was further purified by precipitation from EtOH/EtOAc mixture to give a pure product as a deep purple powder in 92% yield (125 mg): ^{1}H NMR (CD_2Cl_2, 400 MHz): δ 8.92 (d, J = 6.1 Hz, 4H), 7.74 (d, J = 6.0 Hz, 4H), 7.53−7.49 (m, 2H), 7.18−6.75 (m, 2H; molecular aggregation resulted in an atypical splitting pattern of aromatic signals), 4.38 (t, J = 7.3 Hz, 4H), 3.98 (t, J = 6.8 Hz, 4H), 2.61 (t, J = 7.8 Hz, 2H), 1.76 (br s, 8H), 1.45−1.18 (m, 60H), 0.90−0.85 (m, 12H), 0.7−0.0 (br m, 8H). ^{13}C{^{1}H} NMR (CD_2Cl_2, 100 MHz): δ 176.4, 159.0, 157.9, 146.9, 137.2, 131.3, 129.0, 128.5, 127.3, 122.4, 114.2, 110.6, 68.3, 63.4, 37.1, 32.4, 32.33, 32.3, 30.2−30.1, 29.98, 29.83−29.78, 29.7, 29.4, 26.6, 26.4, 26.3, 23.1, 14.1. ^{11}B{^{1}H} NMR (CD_2Cl_2, 128 MHz): δ 17.4 (s, 1B), 1.5 (s, 1B), −30.5 (br d, 8B). IR (KBr) ν 3051, 2923, 2470, 1676, 1459, 1230 cm^{-1}. Anal. Calcd for $C_{62}H_{110}B_{10}O_3N_4$: C, 69.75; H, 10.38; N, 5.25. Found: C, 69.44; H, 10.43; N, 5.21.

Preparation of Ion Pairs of Anions 4[n]. *General Procedure for Cation Exchange.* To a solution of **4a** (0.25 mmol) in MeOH (2 mL), appropriate pyridinium bromide (0.50 mmol) was added in one portion. The resulting colored precipitate was filtered and washed with MeOH (2 mL). The product was further purified by repeated recrystallization or precipitation from appropriate solvents.

Ion Pair ***4[7]b.*** The ion pair obtained from **4**[**7**]**a** (100 mg, 10 mmol) and pyridinium bromide **b**[**Br**] (67 mg, 20 mmol) was recrystallized from MeCN to give a pure compound as yellow crystals in 94% yield (96 mg): ^{1}H NMR (CD_2Cl_2, 400 MHz): δ 8.27 (d, J = 7.1 Hz, 4H), 7.97 (d, J = 7.8 Hz, 4H), 6.83−6.79 (m, 8H), 4.06 (t, J = 7.3 Hz, 4H), 4.01−3.94 (m, 8H), 1.84−1.73 (m, 8H), 1.63 (quint, J = 7.6 Hz, 4H), 1.51−1.31 (m, 32H), 1.18 (sext, J = 7.5 Hz, 4H), 0.93−0.89 (m, 12H), 0.85 (t, J = 7.3 Hz, 6H), 0.8−0.0 (br m, 8H). ^{13}C{^{1}H} NMR (CD_2Cl_2, 100 MHz): δ 170.2, 156.9, 146.4, 136.7, 113.8, 113.5, 71.5, 68.3, 59.9, 33.6, 32.3, 32.1, 30.1, 29.7, 29.4, 29.0, 26.6, 26.1, 23.1, 23.0, 19.5, 14.2, 13.7 (C nucleus attached to the cage was not observed). ^{11}B{^{1}H} NMR (CD_2Cl_2, 128 MHz): δ 7.4 (s, 2B), −27.4 (br d, 8B). Anal. Calcd for $C_{58}H_{102}B_{10}N_2O_4$: C, 69.69; H, 10.29; N, 2.80. Found: C, 69.81; H, 10.12; N, 2.85.

Ion Pair ***4[12]b.*** The ion pair obtained from **4**[**12**]**a** (100 mg, 0.09 mmol) and pyridinium bromide **b**[**Br**] (59 mg, 0.18 mmol) was recrystallized from a CH_2Cl_2/acetone mixture to give pure product **4**[**12**]**b** as pale-yellow crystals in 94% yield (95 mg): ^{1}H NMR (CD_2Cl_2, 400 MHz): δ 8.26 (d, J = 6.6 Hz, 4H), 7.96 (d, J = 7.8 Hz, 4H), 6.80 (d, J = 6.8 Hz, 4H), 6.61 (d, J = 6.8 Hz, 4H), 4.00 (t, J = 8.4 Hz, 4H), 3.96−3.89 (m, 8H), 1.83−1.71 (m, 8H), 1.60−1.30 (m, 56H), 1.09 (sext, J = 7.4 Hz, 4H), 0.97−0.87 (m, 12H), 0.80 (t, J =

https://doi.org/10.1021/acs.chemmater.2c01165
Chem. Mater. 2022, 34, 6476−6491

7.4 Hz, 6H), 0.8−0.0 (br m, 8H). $^{13}C\{^1H\}$ NMR (CD_2Cl_2, 100 MHz): δ 170.2, 156.9, 146.4, 136.7, 113.8, 113.4, 71.5, 68.3, 59.9, 33.6, 32.3, 32.1, 30.2−30.0, 29.8, 29.4, 29.0, 26.7, 26.1, 23.1, 23.0, 19.4, 14.29, 14.28, 13.7 (C nucleus attached to the cage was not observed). $^{11}B\{^1H\}$ NMR (CD_2Cl_2, 128 MHz): δ 7.5 (s, 2B), −27.3 (br d, 8B). IR (KBr) ν 3048, 2930, 2441, 1640, 1478, 1225 cm^{-1}. Anal. Calcd for $C_{68}H_{122}B_{10}N_2O_4$: C, 71.65; H, 10.79; N, 2.45. Found: C, 71.59; H, 10.65; N, 2.48.

Ion Pair ***4[12]d***. The ion pair obtained from **4**[**12**]**a** (100 mg, 0.09 mmol) and pyridinium bromide **d**[**Br**] (58 mg, 0.18 mmol) was recrystallized from a CH_2Cl_2/acetone mixture to give pure product **4**[**12**]**d** as orange microcrystals in 94% yield (95 mg): ^1H NMR (CD_2Cl_2, 400 MHz): δ 8.38 (d, *J* = 6.0 Hz, 4H), 7.99 (t, *J* = 7.9 Hz, 2H), 7.89 (d, *J* = 7.8 Hz, 4H), 7.39 (t, *J* = 6.9 Hz, 4H), 6.77 (d, *J* = 8.0 Hz, 4H), 4.09 (t, *J* = 4.1 Hz, 4H), 3.95 (t, *J* = 6.7 Hz, 4H), 1.79 (quint, *J* = 6.7 Hz, 4H), 1.55−1.45 (m, 8H), 1.36−1.15 (m, 64H), 0.99 (br quint, *J* = 7.9 Hz, 4H), 0.89−0.86 (m, 12H), 0.8−0.0 (br m, 8H). $^{13}C\{^1H\}$ NMR (CD_2Cl_2, 100 MHz): δ 157.0, 145.0, 144.6, 136.5, 128.4, 113.5, 68.3, 62.2, 32.4, 32.3, 32.0, 30.2−30.0, 29.9, 29.82, 29.79, 29.6, 26.7, 26.2, 23.1 (2C), 14.3 (2C) (C nucleus attached to the cage was not observed). $^{11}B\{^1H\}$ NMR (CD_2Cl_2 128 MHz): δ 7.3 (s, 2B), −27.4 (br s, 8B). IR (KBr) ν 3058, 2923, 2449, 1632, 1467, 1229 cm^{-1}. Anal. Calcd for $C_{70}H_{126}B_{10}N_2O_2$: C, 74.02; H, 11.18; N, 2.47. Found: C, 74.11; H, 11.32; N, 2.49.

Ion Pair ***4[12]e***. The ion pair obtained from **4**[**12**]**a** (150 mg, 0.13 mmol) and pyridinium bromide **e**[**Br**] (92 mg, 0.26 mmol) was precipitated from cold EtOH to give pure product **4**[**12**]**e** as a purple powder in 90% yield (140 mg): ^1H NMR (CD_2Cl_2, 400 MHz): δ 8.67 (d, *J* = 6.3 Hz, 4H), 7.90 (br s, 4H), 7.55 (d, *J* = 6.3 Hz, 4H), 6.77 (br s, 4H), 4.37−4.30 (m, 8H), 3.95 (s, 4H), 1.82−1.77 (m, 8H), 1.56−1.29 (m, 54H), 1.04−0.99 (m, 4H), 0.96−0.88 (m, 12H), 0.75 (t, *J* = 7.3 Hz, 6H), 0.8−0.0 (br m, 8H). $^{13}C\{^1H\}$ NMR (CD_2Cl_2, 100 MHz): δ 162.2, 157.4, 146.6, 144.1, 136.6, 127.6, 113.7, 68.3, 67.6, 62.3, 34.3, 32.34, 32.30, 31.8, 30.2−30.0, 29.8, 28.8, 26.7, 25.9, 23.1, 23.0, 19.4, 14.3, 14.2, 13.7. The signal corresponding to the carbon of the C−B bond was not observed. $^{11}B\{^1H\}$ NMR (CD_2Cl_2 128 MHz): δ 7.3 (s, 2B), −27.8 (br s, 8B). IR (KBr) ν 3046, 2922, 2445, 1738, 1456, 1282 cm^{-1}. Anal. Calcd for $C_{68}H_{118}B_{10}O_6N_2$: C, 69.94; H, 10.18; N, 2.40. Found: C, 69.98; H, 10.21; N, 2.43.

Ion Pair ***4[12]f***. The ion pair obtained from **4**[**12**]**a** (150 mg, 0.13 mmol) and pyridinium bromide **f**[**Br**] (87 mg, 0.26 mmol) was precipitated from cold EtOH to give pure product **4**[**12**]**f** as a deep purple powder in 94% yield (142 mg): ^1H NMR (CD_2Cl_2, 400 MHz): δ 8.74 (d, *J* = 6.1 Hz, 4H), 7.87 (d, *J* = 7.7 Hz, 4H), 6.95 (d, *J* = 6.1 Hz, 4H), 6.89 (t, *J* = 7.8 Hz, 4H), 4.25 (br s, 4H), 4.04 (t, *J* = 6.6 Hz, 4H), 1.85−1.80 (m, 4H), 1.60−1.53 (m, 4H), 1.40−1.15 (m, 58H), 1.00−0.96 (m, 6H), 0.91−0.85 (m, 12H), 0.8−0.0 (br s, 8H). $^{13}C\{^1H\}$ NMR (CD_2Cl_2, 100 MHz): δ 158.0, 146.7, 137.1, 130.6, 127.0, 114.1, 68.6, 62.9, 32.4, 32.3, 30.2−30.0, 29.9, 29.81, 29.78, 29.74, 29.4, 26.6, 26.0, 23.13, 23.11, 14.3 (2C) (C nucleus attached to the cage was not observed). $^{11}B\{^1H\}$ NMR (CD_2Cl_2, 128 MHz): δ 7.3 (s, 2B), −28.0 (br s, 8B). IR (KBr) ν 3046, 2923, 2441, 1637, 1453, 1230 cm^{-1}. Anal. Calcd for $C_{68}H_{116}B_{10}O_2N_4$: C, 72.29; H, 10.35; N, 4.96. Found: C, 72.24; H, 10.31; N, 4.92.

Preparation of [*closo*-$B_{10}H_9$-1-($C_6H_4OC_{12}H_{25}$)]$^{2-}$ 2[Bu_4N]$^+$ (7a). To a suspension of [*closo*-$B_{10}H_9$-1-I]$^{2-}$ 2[Bu_4N]$^+$ (**6a**, 3.5 g, 5.0 mmol) in dry THF (21 mL) was added 4-dodecyloxyphenylmagnesium bromide (50 mL, 0.5 M) in THF, followed by the PEPPSI-IPr catalyst (35 mg, 1 mol %). The mixture was refluxed overnight. The reaction mixture was quenched with a sat. solution of NH_4Cl (30 mL), and THF was removed using a rotary evaporator. The aqueous phase was extracted with CH_2Cl_2 (4 × 30 mL), the combined organic extracts were dried (Na_2SO_4), and the solvent was evaporated *in vacuo*. The resulting residue was treated with MeOH and filtered, and the filtrate was evaporated to dryness. The resulting crude product was purified by column chromatography (SiO_2, CH_2Cl_2/CH_3CN, 4:1) to give 3.68 g (88% yield) of pure **7a** as a light-yellow oil, which solidified on freeze-drying to an off-white solid: mp 85−87 °C. ^1H NMR (acetone-d_6, 400 MHz): δ 7.99 (d, *J* = 7.7 Hz, 2H), 6.68 (d, *J* = 7.7 Hz, 2H), 3.94 (t, *J* = 6.5 Hz, 2H), 3.31 (pseudo t, *J* = 8.5 Hz, 16H), 1.80−1.76 (m, 2H), 1.69 (quint, *J* = 7.4 Hz, 16H), 1.54−1.45 (m, 2H), 1.42 (sext, *J* = 7.4 Hz, 16H), 1.31 (br s, 16H), 0.95 (t, *J* = 7.4 Hz, 24H), 0.88 (t, *J* = 6.8 Hz, 3H), 0.8−0.0 (m, 8H). $^{13}C\{^1H\}$ NMR (acetone-d_6, 100 MHz) δ 156.5, 137.3, 112.9, 68.4, 59.3, 32.7, 30.6, 30.5, 30.4, 30.2, 30.0, 27.1, 24.7, 23.4, 20.5, 14.5, 14.1 (C nucleus attached to the cage was not observed). ^{11}B NMR (acetone-d_6, 128 MHz): δ 9.8 (s, 1B), −1.3 (d, *J* = 140 Hz, 1B), −26.2 (d, *J* = 157 Hz, 4B), −27.6 (d, *J* = 160 Hz, 4B). HRMS (ESI-TOF) *m*/*z*: $[M]^-$ calcd for $C_{18}H_{38}B_{10}O$ 380.3853; found 380.3876. Anal. Calcd for $C_{50}H_{110}B_{10}N_2O$: C, 69.54; H, 12.84; N, 3.24. Found: C, 69.27; H, 12.69; N, 3.31.

Preparation of [*closo*-$B_{10}H_8$-1-($C_6H_4OC_{12}H_{25}$)-10-OCHN-$(Me)_2$]$^-$ [Bu_4N]$^+$ (9a). A solution of [*closo*-$B_{10}H_9$-1-($C_6H_4OC_{12}H_{25}$)]$^{2-}$ 2[Bu_4N]$^+$ (**7a**, 200 mg, 0.23 mmol) in dry MeCN (2 mL) under argon was cooled at 0 °C, and PhI(OAc)$_2$ (82 mg, 0.25 mmol) was added to one portion. After 5 h (during this time, the temperature was allowed to gradually reach 10 °C (*ca.* 2 h) and was maintained at 10 °C), the solvent was removed *in vacuo* (at temp <20 °C). The resulting pale green oily residue was dissolved in CH_2Cl_2 (5 mL) and washed with 5% aq $NaHCO_3$ (3 × 10 mL). The organic layer was dried (Na_2SO_4), and the solvent was evaporated *in vacuo* (at temp <20 °C), giving crude, unstable phenyliodonium derivative **8a**. The crude product was freeze-dried and immediately dissolved in dry DMF (4 mL), and the solution was heated at 60 °C under nitrogen for 12 h (the commercial anhydrous DMF from Sigma-Aldrich Sure/Seal was dried over CaH_2, freshly distilled, and stored over 4 Å molecular sieves prior to use to avoid hydrolysis of the reaction product). Excess DMF was removed by distillation under high vacuum, and the residue was purified by column chromatography (SiO_2, CH_2Cl_2/CH_3CN 4:1). The resulting colorless oily material was crystallized (MeOH) at ambient temperature to give 60 mg (38% yield) of pure **9a** as a colorless microcrystalline powder. The typical yield of the reaction was in the range of 35−43%: mp 140−142 °C. ^1H NMR (acetone-d_6, 400 MHz): δ 8.95 (s, 1H), 7.97 (d, *J* = 7.7 Hz, 2H), 6.71 (d, *J* = 7.8 Hz, 2H), 3.95 (t, *J* = 6.5 Hz, 2H), 3.59 (s, 3H), 3.41 (s, 3H), 3.25 (pseudo t, *J* = 8.3 Hz, 8H), 1.80−1.75 (m, 2H), 1.68 (quint, *J* = 7.9 Hz, 8H), 1.50 (quint, *J* = 7.6 Hz, 2H), 1.41−1.31 (br m, 24H), 0.95 (t, *J* = 7.4 Hz, 12H), 0.89 (t, *J* = 6.6 Hz, 3H), 0.8−0.0 (br m). $^{13}C\{^1H\}$ NMR (acetone-d_6, 100 MHz): δ 168.8, 157.0, 137.3, 113.1, 68.3, 59.2, 40.5, 35.6, 32.7, 30.5, 30.4 (2C), 27.1, 24.5, 23.4, 20.4, 14.4, 14.0 (C nucleous attached to the cage was not observed). $^{11}B\{^1H\}$ NMR (acetone-d_6, 128 MHz): δ 22.0 (s, 1B), 6.3 (s, 1B), −27.6 (d, *J* = 119 Hz, 4B), −28.6 (d, *J* = 134 Hz, 4B). IR (KBr) ν 2958, 2924, 2464, 1676, 1481, 1336, 1224 cm^{-1}. HRMS (ESI-TOF) *m*/*z*: $[M]^-$ calcd for $[C_{21}H_{44}B_{10}NO_2]^-$ 452.4303; found: 452.4329. Anal. Calcd for $C_{37}H_{80}B_{10}N_2O_2$: C, 64.11; H, 11.63; N, 4.04. Found: C, 63.95; H, 11.78; N, 4.21.

Preparation of [*closo*-$B_{10}H_8$-1-($C_6H_4OC_{12}H_{25}$)-10-OCHO]$^{2-}$ 2[Bu_4N]$^+$ (10a). To a solution of DMF adduct **9a** (70 mg, 0.1 mmol) in MeCN (2 mL) was added [*n*-Bu_4N]$^+OH^-$ (40 w/w % in water, 72.6 μL, 0.11 mmol), and the mixture was refluxed for 1 h. The solvent was evaporated *in vacuo*, and the resulting residue was dissolved in CH_2Cl_2 (3 mL) and washed with water (10 mL). The organic layer was evaporated, giving 85 mg of the pure product **10a** as a colorless oil (93% yield): ^1H NMR (acetone-d_6, 400 MHz): δ 9.25 (s, 1H), 7.97 (d, *J* = 7.9 Hz, 2H), 6.69 (d, *J* = 7.8 Hz, 2H), 3.92 (t, *J* = 6.5 Hz, 2H), 3.28 (pseudo t, *J* = 8.6 Hz, 16H), 1.79−1.76 (m, 2H), 1.69 (quint, *J* = 7.9 Hz, 16H), 1.54−1.46 (m, 4H), 1.40 (sext, *J* = 7.4 Hz, 16H), 1.31 (br s, 14H), 0.95 (t, *J* = 7.4 Hz, 24H), 0.87 (t, *J* = 7.1 Hz, 3H), 0.7−0.0 (br m, 8H). $^{13}C\{^1H\}$ NMR (acetone-d_6, 100 MHz): δ 169.1, 156.7, 137.5, 113.0, 68.3, 59.2, 32.7, 30.48, 30.42, 30.39 29.3, 27.0, 24.5, 23.4, 20.4, 14.4, 14.0. The signal corresponding to the carbon of C−B bond was not observed. ^{11}B NMR (acetone-d_6, 128 MHz): δ 20.4 (s, 1B), 3.3 (s, 1B), −28.8 (d, *J* = 125 Hz, 8B). IR (KBr) ν 2961, 2929, 2458, 1674, 1469, 1226 cm^{-1}. HRMS (ESI-TOF) *m*/*z*: $[M]^-$ calcd for $C_{19}H_{39}B_{10}O_3$ 425.3830; found 425.3797. Anal. Calcd for $C_{51}H_{110}B_{10}N_2O_3$: C, 67.50; H, 12.22; N, 3.09. Found: C, 67.23; H, 12.05; N, 3.14.

https://doi.org/10.1021/acs.chemmater.2c01165
Chem. Mater. 2022, 34, 6476−6491

■ ASSOCIATED CONTENT

Supporting Information

The Supporting Information is available free of charge at https://pubs.acs.org/doi/10.1021/acs.chemmater.2c01165.

Additional synthetic details, NMR spectra, XRD collection and refinement details, DSC measurements, powder XRD data, UV−vis spectra, computational details, and archive for DFT results (PDF)

■ AUTHOR INFORMATION

Corresponding Author

Piotr Kaszyński − *Centre of Molecular and Macromolecular Studies, Polish Academy of Sciences, 90-363 Łódź, Poland; Faculty of Chemistry, University of Łódź, 91-403 Łódź, Poland; Department of Chemistry, Middle Tennessee State University, Murfreesboro, Tennessee 37130, United States;* orcid.org/0000-0002-2325-8560; Email: piotr.kaszynski@chemia.uni.lodz.pl

Authors

Litwin Jacob − *Centre of Molecular and Macromolecular Studies, Polish Academy of Sciences, 90-363 Łódź, Poland;* orcid.org/0000-0001-5128-1381

Edyta Rzeszotarska − *Centre of Molecular and Macromolecular Studies, Polish Academy of Sciences, 90-363 Łódź, Poland*

Maria Koyioni − *Centre of Molecular and Macromolecular Studies, Polish Academy of Sciences, 90-363 Łódź, Poland*

Rafał Jakubowski − *Centre of Molecular and Macromolecular Studies, Polish Academy of Sciences, 90-363 Łódź, Poland;* orcid.org/0000-0002-3305-1352

Damian Pociecha − *Faculty of Chemistry, University of Warsaw, 02-089 Warsaw, Poland;* orcid.org/0000-0001-7734-3181

Anna Pietrzak − *Faculty of Chemistry, Łódź University of Technology, 90-924 Łódź, Poland;* orcid.org/0000-0003-3415-8650

Complete contact information is available at: https://pubs.acs.org/10.1021/acs.chemmater.2c01165

Author Contributions

The manuscript was written through the contribution of all authors. All authors have given approval to the final version of the manuscript.

Notes

The authors declare no competing financial interest.

■ ACKNOWLEDGMENTS

Financial support from FNP (TEAM-3/2016-3/24) and the European Space Agency (NPI 542) is greatly acknowledged.

■ ABBREVIATIONS

POM, polarized optical microscopy; DSC, differential scanning calorimetry; XRD, X-ray diffraction; SQUID, superconductive quantum interference device; TLC, thin-layer chromatography

■ REFERENCES

(1) Wang, W.; Luo, L.; Sheng, P.; Zhang, J.; Zhang, Q. Multifunctional features of organic charge-transfer complexes: Advances and perspectives. *Chem. - Eur. J.* **2021**, *27*, 464−490.

(2) Goetz, K. P.; Vermeulen, D.; Payne, M. E.; Kloc, C.; McNeil, L. E.; Jurchescu, O. D. Charge-transfer complexes: New perspectives on an old class of compounds. *J. Mater. Chem. C* **2014**, *2*, 3065−3076.

(3) Das, A.; Ghosh, S. Supramolecular assemblies by charge-transfer interactions between donor and acceptor chromophores. *Angew. Chem., Int. Ed.* **2014**, *53*, 2038−2054.

(4) Deibel, C.; Strobel, T.; Dyakonov, V. Role of the charge transfer state in organic donor−acceptor solar cells. *Adv. Mater.* **2010**, *22*, 4097−4111.

(5) Gotoh, T.; Kondoh, T.; Egawa, K.; Kubodera, K.-i. Exceptionally large third-order optical nonlinearity of the organic charge-transfer complex. *J. Opt. Soc. Am. B* **1989**, *6*, 703−706.

(6) Baeg, K. J.; Binda, M.; Natali, D.; Caironi, M.; Noh, Y. Y. Organic light detectors: Photodiodes and phototransistors. *Adv. Mater.* **2013**, *25*, 4267−4295.

(7) Sun, L.; Zhu, W.; Wang, W.; Yang, F.; Zhang, C.; Wang, S.; Zhang, X.; Li, R.; Dong, H.; Hu, W. Intermolecular charge-transfer interactions facilitate two-photon absorption in styrylpyridine−tetracyanobenzene cocrystals. *Angew. Chem., Int. Ed.* **2017**, *56*, 7831−7835.

(8) Siegmund, B.; Mischok, A.; Benduhn, J.; Zeika, O.; Ullbrich, S.; Nehm, F.; Böhm, M.; Spoltore, D.; Fröb, H.; Körner, C.; Leo, K.; Vandewal, K. Organic narrowband near-infrared photodetectors based on intermolecular charge-transfer absorption. *Nat. Commun.* **2017**, *8*, No. 15421.

(9) Prasanthkumar, S.; Ghosh, S.; Nair, V. C.; Saeki, A.; Seki, S.; Ajayaghosh, A. Organic donor−acceptor assemblies form coaxial p−n heterojunctions with high photoconductivity. *Angew. Chem.* **2015**, *127*, 960−964.

(10) Kumar, M.; Kumar, S. Liquid crystals in photovoltaics: A new generation of organic photovoltaics. *Polym. J.* **2017**, *49*, 85−111.

(11) Sergeyev, S.; Pisula, W.; Geerts, Y. H. Discotic liquid crystals: A new generation of organic semiconductors. *Chem. Soc. Rev.* **2007**, *36*, 1902−1929.

(12) Pisula, W.; Kastler, M.; Wasserfallen, D.; Robertson, J. W. F.; Nolde, F.; Kohl, C.; Müllen, K. Pronounced supramolecular order in discotic donor−acceptor mixtures. *Angew. Chem., Int. Ed.* **2006**, *45*, 819−823.

(13) Arikainen, E. O.; Boden, N.; Bushby, R. J.; Lozman, O. R.; Vinter, J. G.; Wood, A. Complimentary polytopic interactions. *Angew. Chem.* **2000**, *112*, 2423−2426.

(14) Kouwer, P. H. J.; Jager, W. F.; Mijs, W. J.; Picken, S. J. Charge transfer complexes of discotic liquid crystals: A flexible route to a wide variety of mesophases. *Macromolecules* **2002**, *35*, 4322−4329.

(15) Schmidt-Mende, L.; Fechtenkötter, A.; Müllen, K.; Moons, E.; Friend, R. H.; MacKenzie, J. D. Self-organized discotic liquid crystals for high-efficiency organic photovoltaics. *Science* **2001**, *293*, 1119−1122.

(16) Percec, V.; Glodde, M.; Bera, T. K.; Miura, Y.; Shiyanovskaya, I.; Singer, K. D.; Balagurusamy, V. S. K.; Heiney, P. A.; Schnell, I.; Rapp, A.; Spiess, H. W.; Hudson, S. D.; Duan, H. Self-organization of supramolecular helical dendrimers into complex electronic materials. *Nature* **2002**, *419*, 384−387.

(17) Van Winkle, M.; Scrymgeour, D. A.; Kaehr, B.; Reczek, J. J. Laser rewritable dichroics through reconfigurable organic charge-transfer liquid crystals. *Adv. Mater.* **2018**, *30*, No. 1706787.

(18) Otmakhova, O. A.; Piryazev, A. A.; Bondarenko, G. N.; Shandryuk, G. A.; Maryasevskaya, A. V.; Merekalov, A. S.; Ivanov, D. A.; Talroze, R. V. New complexes of liquid crystal discotic triphenylenes: Induction of the double gyroid phase. *Phys. Chem. Chem. Phys.* **2021**, *23*, 16827−16836.

(19) Park, L. Y.; Hamilton, D. G.; McGehee, E. A.; McMenimen, K. A. Complementary C_3-symmetric donor-acceptor components: cocrystal structure and control of mesophase stability. *J. Am. Chem. Soc.* **2003**, *125*, 10586−10590.

(20) Wang, J.-Y.; Yan, J.; Ding, L.; Ma, Y.; Pei, J. One-dimensional microwires formed by the co-assembly of complementary aromatic donors and acceptors. *Adv. Funct. Mater.* **2009**, *19*, 1746−1752.

(21) Li, J.; He, Z.; Zhao, H.; Gopee, H.; Kong, X.; Xu, M.; An, X.; Jing, X.; Cammidge, A. N. Homeotropic alignment through charge-transfer-induced columnar mesophase formation in an unsymmetrically substituted triphenylene derivative. *Pure Appl. Chem.* **2010**, *82*, 1993−2003.
(22) Stępień, M.; Donnio, B.; Sessler, J. L. Supramolecular liquid crystals based on cyclo[8]pyrrole. *Angew. Chem., Int. Ed.* **2007**, *46*, 1431−1435.
(23) Reczek, J. J.; Villazor, K. R.; Lynch, V.; Swager, T. M.; Iverson, B. L. Tunable columnar mesophases utilizing C_2 symmetric aromatic donor-acceptor complexes. *J. Am. Chem. Soc.* **2006**, *128*, 7995−8002.
(24) Leight, K. R.; Esarey, B. E.; Murray, A. E.; Reczek, J. J. Predictable tuning of absorption properties in modular aromatic donor−acceptor liquid crystals. *Chem. Mater.* **2012**, *24*, 3318−3328.
(25) Iguchi, H.; Furutani, H.; Kimizuka, N. Ionic charge-transfer liquid crystals formed by alternating supramolecular copolymerization of liquid π-donors and TCNQ. *Front. Chem.* **2021**, *9*, No. 657246.
(26) Bé, A. G.; Tran, C.; Sechrist, R.; Reczek, J. J. Strongly dichroic organic films via controlled assembly of modular aromatic charge-transfer liquid crystals. *Org. Lett.* **2015**, *17*, 4834−4837.
(27) Salikolimi, K.; Sudhakar, A. A.; Ishida, Y. Functional ionic liquid crystals. *Langmuir* **2020**, *36*, 11702−11731.
(28) Goossens, K.; Lava, K.; Bielawski, C. W.; Binnemans, K. Ionic liquid crystals: Versatile materials. *Chem. Rev.* **2016**, *116*, 4643−4807.
(29) Axenov, K. V.; Laschat, S. Thermotropic ionic liquid crystals. *Materials* **2011**, *4*, 206−259.
(30) Binnemans, K. Ionic liquid crystals. *Chem. Rev.* **2005**, *105*, 4148−4204.
(31) Liu, X.; Liu, J. L.; Cai, B.; Ren, X. M. A charge transfer salt consisted of bis(maleonitriledithiolato)zincate dianion and 1,1′-didecyl-4,4′-bipyridinium exhibiting uncommon nematic mesophase behavior. *Inorg. Chem. Commun.* **2011**, *14*, 1428−1431.
(32) Sivaev, I. B.; Prikaznov, A. V.; Naoufal, D. Fifty years of the *closo*-decaborate anion chemistry. *Collect. Czech. Chem. Commun.* **2010**, *75*, 1149−1199.
(33) Poater, J.; Solà, M.; Viñas, C.; Teixidor, F. πAromaticity and three-dimensional aromaticity: Two sides of the same coin? *Angew. Chem.* **2014**, *126*, 12387−12391.
(34) Kaszynski, P. *closo* Boranes as Pi Structural Elements for Advanced Anisotropic Materials. In *Anisotropic Organic Materials-Approaches to Polar Order*; Glaser, R.; Kaszynski, P., Eds.; ACS Symposium Series: Washington, D.C., 2001; Vol. *798*, pp 68−82.
(35) Kaszynski, P.; Pakhomov, S.; Young, V. G., Jr. Investigation of electronic interactions between *closo*-boranes and their triple-bonded substituents. *Collect. Czech. Chem. Commun.* **2002**, *67*, 1061−1083.
(36) Kapuściński, S.; Abdulmojeed, M. B.; Schafer, T. E.; Pietrzak, A.; Hietsoi, O.; Friedli, A. C.; Kaszyński, P. Photonic materials derived from the $[closo\text{-}B_{10}H_{10}]^{2-}$ anion: Tuning photophysical properties in $[closo\text{-}B_{10}H_8\text{-}1\text{-}X\text{-}10\text{-}(4\text{-}Y\text{-}NC_5H_5)]^-$. *Inorg. Chem. Front.* **2021**, *8*, 1066−1082.
(37) Jankowiak, A.; Baliński, A.; Harvey, J. E.; Mason, K.; Januszko, A.; Kaszyński, P.; Young, V. G., Jr.; Persoons, A. $[closo\text{-}B_{10}H_{10}]^{2-}$ as a structural element for quadrupolar liquid crystals: A new class of liquid crystalline NLO chromophores. *J. Mater. Chem. C* **2013**, *1*, 1144−1159.
(38) Kaszynski, P.; Huang, J.; Jenkins, G. S.; Bairamov, K. A.; Lipiak, D. Boron clusters in liquid crystals. *Mol. Cryst. Liq. Cryst. Sci. Technol., Sect. A* **1995**, *260*, 315−332.
(39) Sivaev, I. B. Nitrogen heterocyclic salts of polyhedral borane anions: From ionic liquids to energetic materials. *Chem. Heterocycl. Compd.* **2017**, *53*, 638−658.
(40) Muetterties, E. L.; Balthis, J. H.; Chia, Y. T.; Knoth, W. H.; Miller, H. C. Chemistry of boranes. VIII. Salts and acids of $B_{10}H_{10}^{-2}$ and $B_{12}H_{12}^{-2}$. *Inorg. Chem.* **1964**, *3*, 444−451.
(41) Virovets, A. V.; Vakulenko, N. N.; Volkov, V. V.; Podberezskaya, N. V. Crystal structure of di(1-*n*-dodecylpyridine) decahydro-*closo*-decaborate(2-) $(C_5H_5N\text{-}C_{12}H_{25})_2[B_{10}H_{10}]$. *J. Struct. Chem.* **1994**, *35*, 339−344.
(42) Fuller, D. J.; Kepert, D. L.; Skelton, B. W.; White, A. H. Structure, stereochemistry and novel 'hydrogen bonding' in two bipyridinium salts of the $B_{10}H_{10}^{2-}$ anion. *Aust. J. Chem.* **1987**, *40*, 2097−2105.
(43) Mebs, S.; Kalinowski, R.; Grabowsky, S.; Förster, D.; Kickbusch, R.; Justus, E.; Morgenroth, W.; Paulmann, C.; Luger, P.; Gabel, D.; Lentz, D. Charge transfer via the dative N−B bond and dihydrogen contacts. Experimental and theoretical electron density studies of four deltahedral boranes. *J. Phys. Chem. A* **2011**, *115*, 1385−1395.
(44) Chantler, C. T.; Maslen, E. N. Charge transfer and three-centre bonding in monoprotonated and diprotonated 2,2′-bipyridylium decahydro-*closo*-decaborate(2-). *Acta Crystallogr., Sect. B: Struct. Sci.* **1989**, *45*, 290−297.
(45) Mebs, S.; Kalinowski, R.; Grabowsky, S.; Förster, D.; Kickbusch, R.; Justus, E.; Morgenroth, W.; Paulmann, C.; Luger, P.; Gabel, D.; Lentz, D. Real-space indicators for chemical bonding. Experimental and theoretical electron density studies of four deltahedral boranes. *Inorg. Chem.* **2011**, *50*, 90−103.
(46) Avdeeva, V. V.; Vologzhanina, A. V.; Malinina, E. A.; Kuznetsov, N. T. Dihydrogen bonds in salts of boron cluster anions $[B_nH_n]^{2-}$ with protonated heterocyclic organic bases. *Crystals* **2019**, *9*, 330.
(47) Goodby, J. W.; Davis, E. J.; Mandle, R. J.; Cowling, S. J. Chemical Structure and Mesogenic Properties. In *Hanbook of Liquid Crystals*; Goodby, J. W.; Collings, P. J.; Kato, T.; Tschierske, C.; Gleeson, H. F.; Raynes, P., Eds.; Wiley-VCH: Mörlenbach, Germany, 2014; Vol. *1*, pp 231−260.
(48) Jacob, L.; Rzeszotarska, E.; Pietrzak, A.; Young, V. G., Jr.; Kaszyński, P. Synthesis, structural analysis, and functional group interconversion in the $[closo\text{-}B_{10}H_8\text{-}1,10\text{-}X_2]^{2-}$ (X = CN, $[OCRNMe_2]^+$, OCOR, and $[OH_2]^+$) derivatives. *Eur. J. Inorg. Chem.* **2020**, *2020*, 3083−3093.
(49) Rzeszotarska, E.; Novozhilova, I.; Kaszyński, P. Convenient synthesis of $[closo\text{-}B_{10}H_9\text{-}1\text{-}I]^{2-}$ and $[closo\text{-}B_{10}H_8\text{-}1,10\text{-}I_2]^{2-}$ anions. *Inorg. Chem.* **2017**, *56*, 14351−14356.
(50) Ringstrand, B.; Monobe, H.; Kaszynski, P. Anion-driven mesogenicity: Ionic liquid crystals based on the $[closo\text{-}1\text{-}CB_9H_{10}]^-$ cluster. *J. Mater. Chem.* **2009**, *19*, 4805−4812.
(51) Narendran, R. L.; Patnaik, A. Synergistic effect of hydrophobic and hydrogen bonding interaction-driven viologen−pyranine charge-transfer aggregates: Adenosine monophosphate recognition. *Soft Matter* **2021**, *17*, 903−914.
(52) Hansch, C.; Leo, A.; Taft, R. W. A survey of Hammett substituent constants and resonance and field parameters. *Chem. Rev.* **1991**, *91*, 165−195.
(53) Goodby, J. W. Structures and Properties of Smectic Liquid Crystals. In *Hanbook of Liquid Crystals*; Goodby, J. W.; Collings, P. J.; Kato, T.; Tschierske, C.; Gleeson, H. F.; Raynes, P., Eds.; Wiley-VCH: Mörlenbach, Germany, 2014; Vol. *4*, pp 43−68.
(54) For details see the SI.
(55) Kosower, E. M. The effect of solvent on spectra. I. A new empirical measure of solvent polarity: Z-values. *J. Am. Chem. Soc.* **1958**, *80*, 3253−3260.
(56) Stratmann, R. E.; Scuseria, G. E.; Frisch, M. J. An efficient implementation of time-dependent density-functional theory for the calculation of excitation energies of large molecules. *J. Chem. Phys.* **1998**, *109*, 8218−8224.
(57) Becke, A. D. Density-functional thermochemistry. III. The role of exact exchange. *J. Chem. Phys.* **1993**, *98*, 5648−5652.
(58) Lee, C.; Yang, W.; Parr, R. G. Development of the Colle-Salvetti correlation-energy formula into a functional of the electron density. *Phys. Rev. B* **1988**, *37*, 785−789.
(59) Weigend, F. Accurate Coulomb-fitting basis sets for H to Rn. *Phys. Chem. Chem. Phys.* **2006**, *8*, 1057−1065.
(60) Weigend, F.; Ahlrichs, R. Balanced basis sets of split valence, triple zeta valence and quadruple zeta valence quality for H to Rn: Design and assessment of accuracy. *Phys. Chem. Chem. Phys.* **2005**, *7*, 3297−3305.

https://doi.org/10.1021/acs.chemmater.2c01165
Chem. Mater. 2022, 34, 6476−6491

(61) Frisch, M. J.et al.*Gaussian 09*, revision C.01; Gaussian, Inc.: Wallingford CT, 2011.
(62) Cossi, M.; Scalmani, G.; Rega, N.; Barone, V. New developments in the polarizable continuum model for quantum mechanical and classical calculations on molecules in solution. *J. Chem. Phys.* 2002, *117*, 43−54. and references therein.
(63) Fulmer, G. R.; Miller, A. J. M.; Sherden, N. H.; Gottlieb, H. E.; Nudelman, A.; Stoltz, B. M.; Bercaw, J. E.; Goldberg, K. I. NMR chemical shifts of trace impurities: Common laboratory solvents, organics, and gases in deuterated solvents relevant to the organometallic chemist. *Organometallics* 2010, *29*, 2176−2179.

https://doi.org/10.1021/acs.chemmater.2c01165
Chem. Mater. 2022, 34, 6476−6491

3.3 Additional information

3.3.1 Additional synthetic details

Hexyl isonicotinate (12e). To isonicotinic acid (200 mg, 1.62 mmol), $SOCl_2$ (471 μL, 6.49 mmol) was added and the reaction mixture was stirred for 3 h at 40 °C. Excess of $SOCl_2$ was removed by distillation. To the obtained solid, a solution of 1-hexanol (224 μL, 1.78 mmol) in dry CH_2Cl_2 (5 mL) was added and the mixture was refluxed for 12 h. The reaction mixture was cooled to rt and washed with saturated solution of Na_2CO_3 (2 × 8 mL) and distilled water (2 × 8 mL). The organic layer was dried over Na_2SO_4, filtered and the solvent was evaporated *in vacuo* to give a colorless liquid, which was passed through a pad of silica gel using CH_2Cl_2/MeCN (5:1) as eluent to give 285 mg (85% yield) of hexyl isonicotinate as a colorless oil: ^{1}H NMR ($CDCl_3$, 500 MHz): δ 8.76 (d, *J* = 6.0 Hz, 2H), 7.83 (d, *J* = 6.1 Hz, 2H), 4.33 (t, *J* = 6.7 Hz, 2H), 1.75 (quint, *J* = 7.1 Hz, 2H), 1.42 (quint, *J* = 7.5 Hz, 2H), 1.33–1.30 (m, 4H), 0.89 (t, *J* = 7.0 Hz, 3H). ^{13}C{^{1}H} NMR ($CDCl_3$, 125 MHz): δ 165.2, 150.6, 137.6, 123.0, 66.1, 31.5, 28.6, 25.7, 22.6, 14.1.

Preparation of *N*-butyl-4-(hexyloxycarbonyl)pyridinium bromide (e[Br]). A solution of hexyl isonicotinate (**12e**, 200 mg, 0.96 mmol) and 1-bromobutane (350 μL, 1.44 mmol) in dry MeCN (5 mL) was refluxed for 24 h. The solvent was evaporated and the obtained crude product was dissolved in EtOAc and hexane was added to precipitate 240 mg (72% yield) of pure compound as a yellow sticky material: ^{1}H NMR ($CDCl_3$, 500 MHz) δ 9.94 (d, *J* = 5.5 Hz, 2H), 8.37 (d, *J* = 6.5 Hz, 2H), 4.98 (t, *J* = 7.9 Hz, 2H), 4.25 (t, *J* = 6.6 Hz, 2H), 1.95 (t, *J* = 7.4 Hz, 2H), 1.62 (t, *J* = 7.3 Hz, 2H), 1.30–1.15 (m, 8H), 0.82–0.71 (m, 6H). ^{13}C{^{1}H} NMR ($CDCl_3$, 125 MHz): 161.3, 146.7, 144.1, 127.3, 67.4, 61.7, 33.7, 31.0, 28.1, 25.2, 22.2, 19.1, 13.7, 13.3. HRMS (ESI-TOF) *m/z*: $[M]^-$ calcd for $C_{16}H_{26}NO_2$ 264.1964; found 264.1955.

Preparation of *N*-decyl-4-cyanopyridinium bromide (f[Br]). A solution of 4-cyanopyridine (**12f**, 500 mg, 4.80 mmol) and 1-bromodecane (1.1 mL, 5.28 mmol) in dry MeCN (5 mL) was refluxed for 12 h. The solvent was evaporated and the obtained crude product was dissolved in EtOAc (5 mL) and hexane was added to precipitate the pure compound. The formed precipitate was filtered off and washed with hexane giving 1.10 g (71% yield) of pure compound as a yellow powder: mp 196–200 °C. ^{1}H NMR ($CDCl_3$, 500 MHz): δ 9.93 (d, *J* = 6.3 Hz, 2H), 8.53 (d, *J* = 6.3 Hz, 2H), 5.04 (t, *J* = 7.4 Hz, 2H), 2.03 (quint, *J* = 7.6 Hz, 2H), 1.36–1.27 (m, 4H), 1.21–1.16 (m, 10H), 0.79 (t, *J* = 6.9 Hz, 3H). ^{13}C{^{1}H} NMR ($CDCl_3$, 125 MHz): δ 147.0, 131.1, 127.8, 113.8, 63.2, 32.0, 31.7, 29.4, 29.3, 29.2, 29.0, 26.1, 22.6, 14.1. HRMS (ESI-TOF) *m/z*: $[M]^-$ calcd for $C_{16}H_{25}N_2$ 245.2018; found 245.2013. Anal. Calcd for $C_{16}H_{25}N_2Br$: C, 59.08; H, 7.75; N, 8.61. Found: C, 59.11; H, 7.49; N, 8.58.

Preparation of hydroquinone dibutyrate H[3]. To a suspension of hydroquinone (100 mg, 0.91 mmol) in dry CH_2Cl_2 (10 mL) was added butyric acid (0.167 mL, 1.82 mmol), DCC (413 mg, 2.00 mmol), DMAP (44 mg, 0.36 mmol) and the resulting mixture was stirred for 8 h at room temperature under Ar atmosphere. Water was added into the reaction mixture and extraction was done in CH_2Cl_2/water. The organic layer was dried over Na_2SO_4 and evaporated. The resulting crude product was purified by column chromatography (SiO_2, petroleum ether/EtOAc, 4:1). Further purification was done by precipitation from cold ethanol to give 205 mg (90% yield) of pure dibutyrate **H[3]** as a white crystalline powder: mp 40−42 °C. ^{1}H NMR ($CDCl_3$, 400 MHz): δ 7.08 (s, 4H), 2.53 (t, *J* = 7.4 Hz, 4H), 1.78 (sext, *J* = 7.4 Hz, 4H), 1.04 (t, *J* = 7.4 Hz, 6H). ^{13}C{^{1}H} NMR ($CDCl_3$, 100 MHz): δ 172.1, 148.2, 122.5, 36.3, 18.5, 13.7. HRMS (ESI-TOF) *m/z*: $[M]^+$ calcd for $C_{14}H_{19}O_4$ 251.1284; found 251.1284. Anal. Calcd for $C_{14}H_{18}O_4$: C, 67.18; H, 7.25. Found: C, 67.12; H, 7.21.

Preparation of hydroquinone didodecanoate H[11]. To a solution of hydroquinone (100 mg, 0.91 mmol) and KOH (101 mg, 1.82 mmol) in dry CH_2Cl_2 (5 mL) was added $C_{11}H_{23}COCl$ (0.420 mL, 1.82 mmol) and the reaction mixture was stirred for 2 h at room temperature under Ar atmosphere. The reaction was quenched by adding water and extraction was done in CH_2Cl_2/water. The organic layer was dried over Na_2SO_4 and evaporated. The resulting crude product was purified by precipitating from ethanol at ambient temperature to give 380 mg (88% yield) of pure product **H[11]** as a white powder: mp 83−85 °C. ^{1}H NMR ($CDCl_3$, 400 MHz): δ 7.08 (s, 4H), 2.54 (t, *J* = 7.5 Hz, 4H), 1.74 (quint, *J* = 7.5 Hz, 4H), 1.42–1.19 (m, 32H), 0.88 (t, *J* = 6.8 Hz, 6H). ^{13}C{^{1}H} NMR ($CDCl_3$, 100 MHz): δ 172.3, 148.2, 122.5, 34.5, 32.0, 29.7 (2C), 29.6, 29.5, 29.4, 29.2, 25.1, 22.8, 14.3. HRMS (ESI-TOF) m/*z*: $[M]^+$ calcd for $C_{30}H_{51}O_4$ 475.3787; found 475.3777. Anal. Calcd for $C_{30}H_{50}O_4$: C, 75.90; H, 10.62. Found: C, 75.91; H, 10.63

3.3.2 DSC measurements

DSC data were obtained with a DSC-2500 instrument and are shown in Figures 1-17. Heating and cooling rates were 10 K min^{-1}.

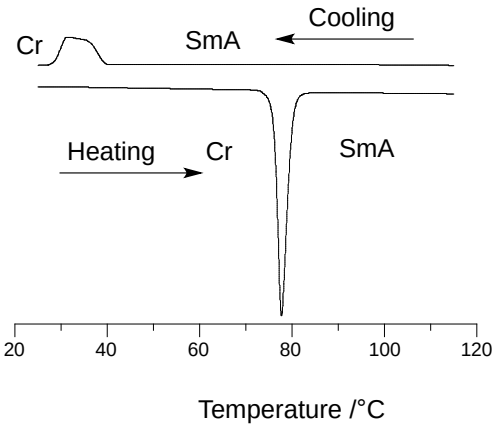

Figure 1. DSC trace of **1[11]c**.

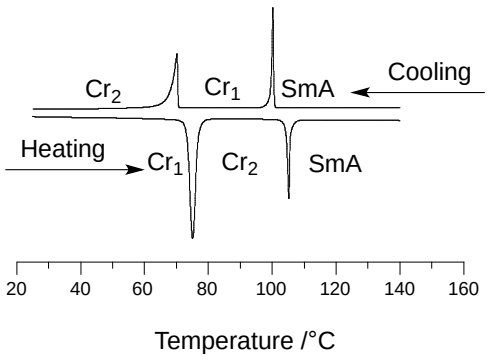

Figure 2. DSC trace of **1[11]d**.

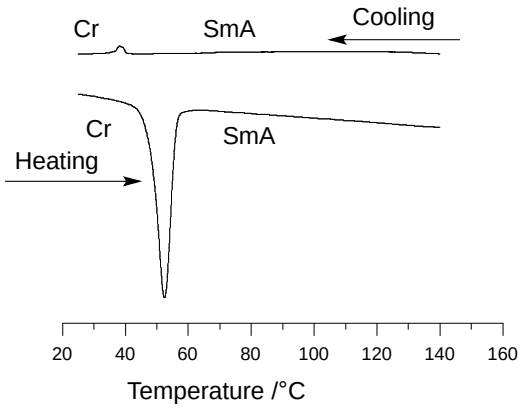

Figure 3. DSC trace of **1[11]e**.

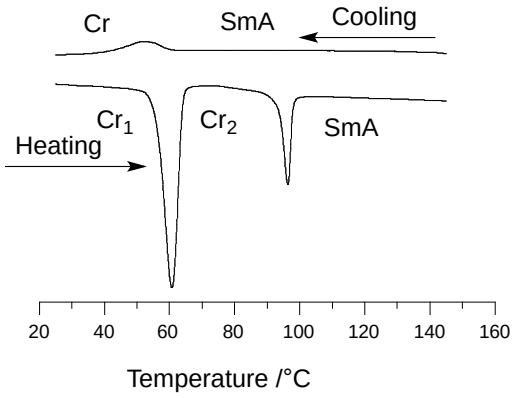

Figure 4. DSC trace of **1[11]f**.

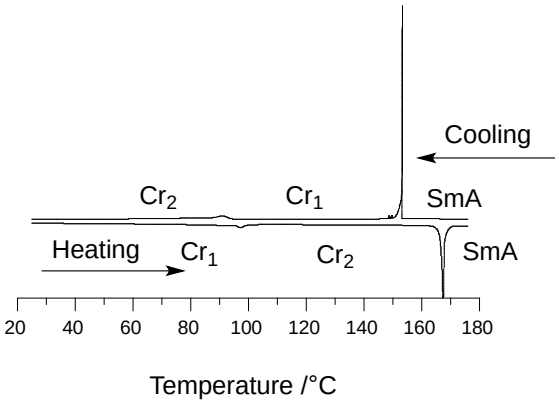

Figure 5. DSC trace of **2[12]d**.

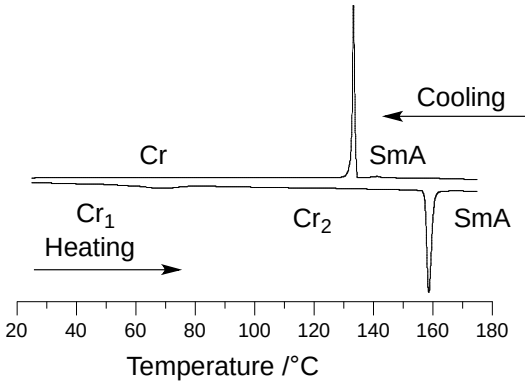

Figure 6. DSC trace of **2[12]e**.

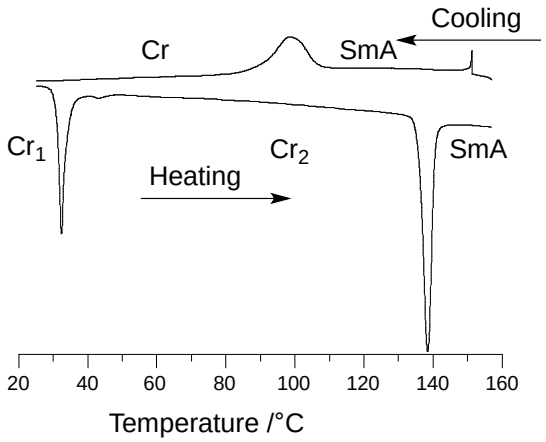

Figure 7. DSC trace of **2[12]f**.

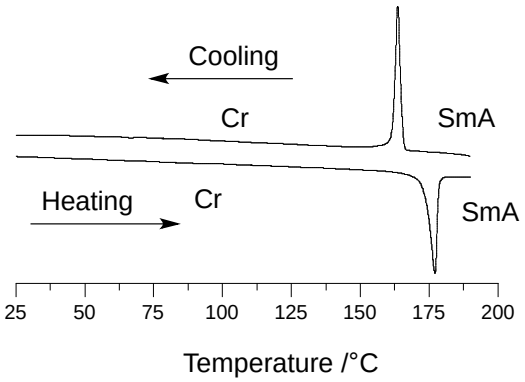

Figure 8. DSC trace of **3[11,12]d**.

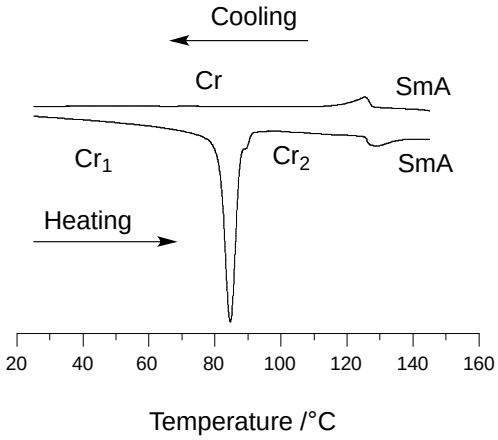

Figure 9. DSC trace of **3[11,12]e**.

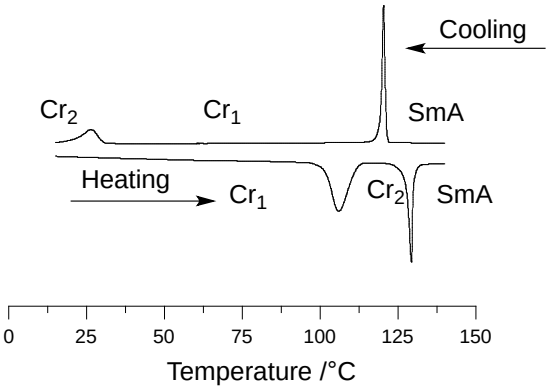

Figure 10. DSC trace of **4[12]b**.

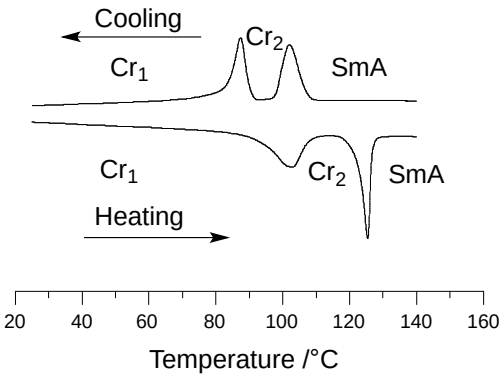

Figure 11. DSC trace of **4[12]e**.

3.3.3 Powder XRD data

Wide-angle diffractogram for the compounds obtained by integration of 2D pattern taken at suitable temperature.

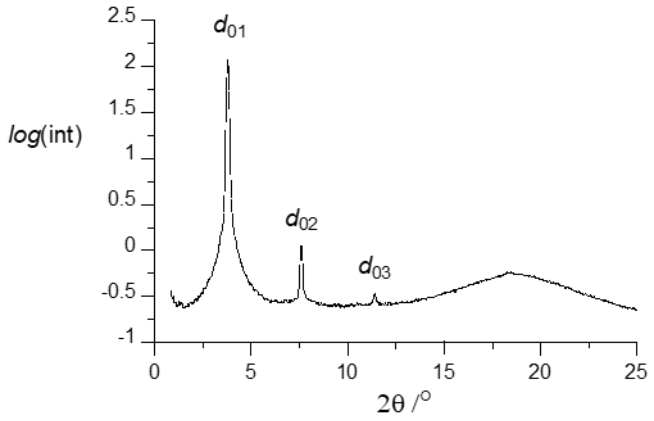

Figure 12. Powder X-ray diffractogram for ion pair **1[11]b** at 80 °C

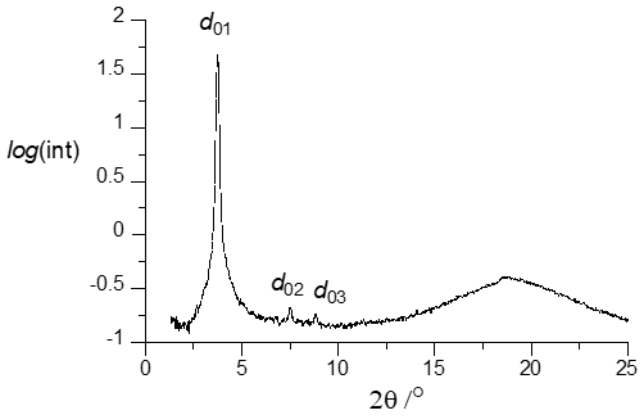

Figure 13. Powder X-ray diffractogram for ion pair **1[11]c** at 180 °C

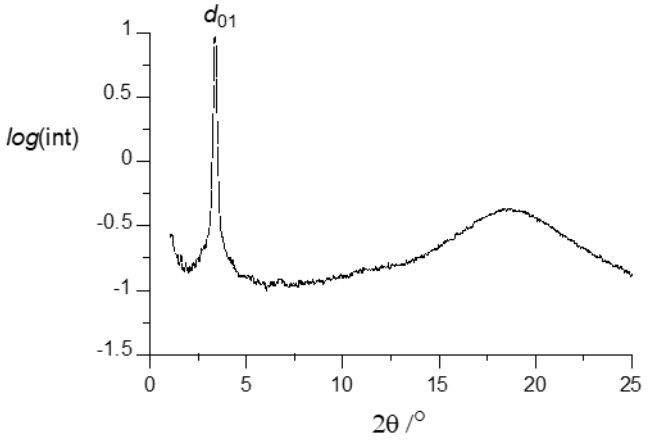

Figure 14. Powder X-ray diffractogram for ion pair **1[11]d** at 120 °C

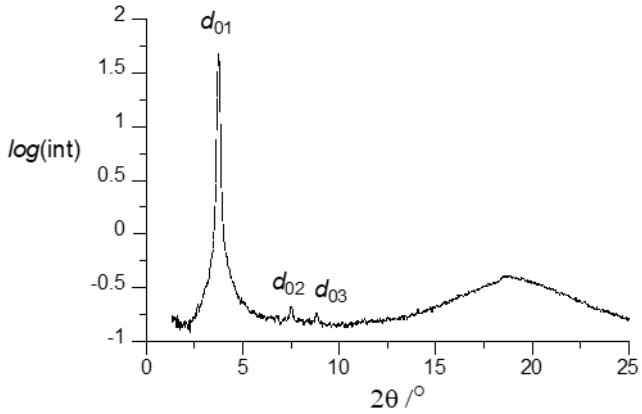

Figure 15. Powder X-ray diffractogram for ion pair **1[11]e** at 120 °C

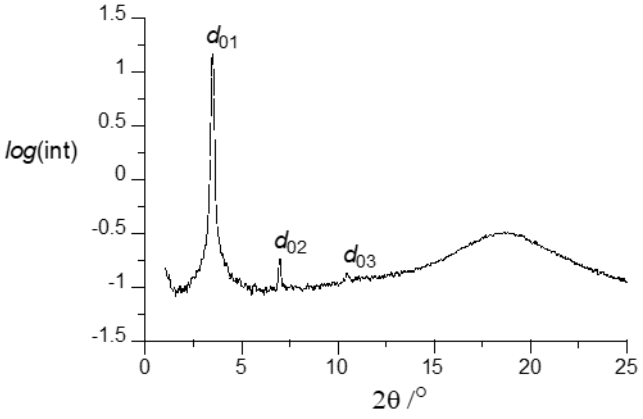

Figure 16. Powder X-ray diffractogram for ion pair **1[11]f** at 120 °C

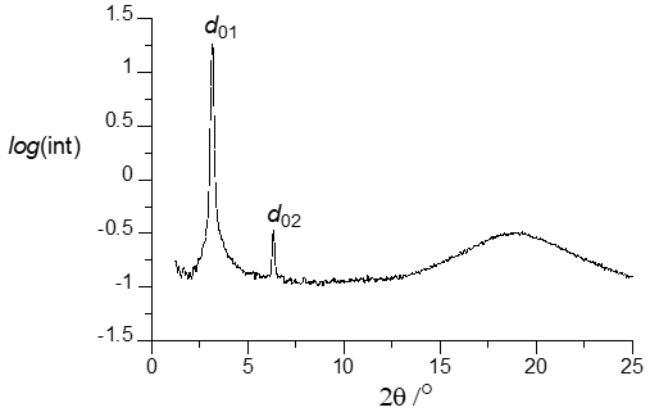

Figure 17. Powder X-ray diffractogram for ion pair **2[12]b** at 80 °C

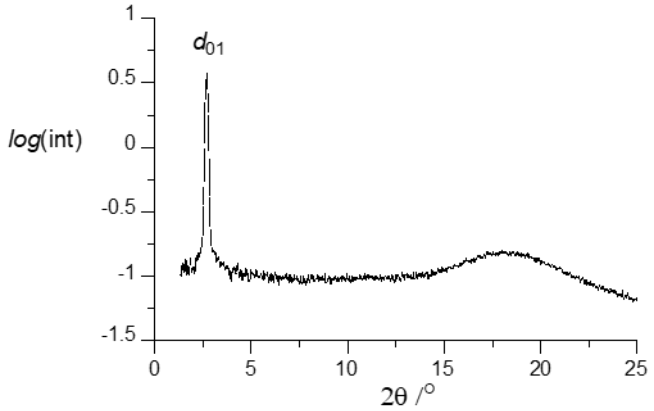

Figure 18. Powder X-ray diffractogram for ion pair **2[12]d** at 180 °C

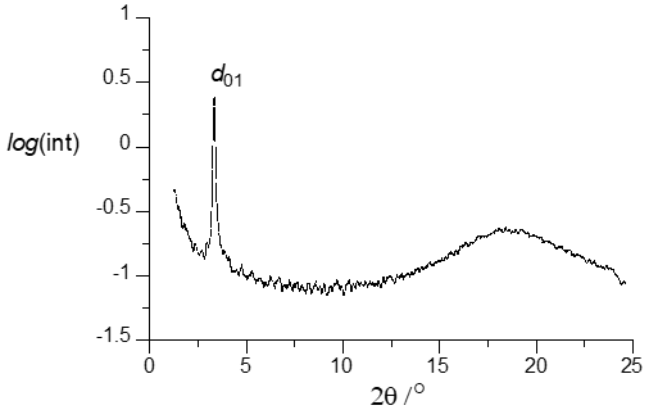

Figure 19. Powder X-ray diffractogram for ion pair **2[12]e** at 180°C

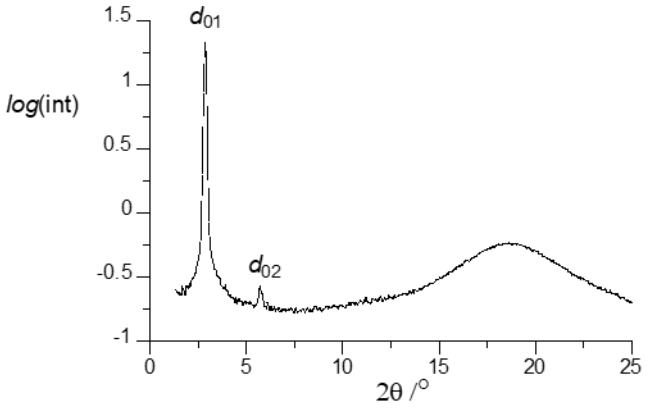

Figure 20. Powder X-ray diffractogram for ion pair **2[12]f** at 160 °C

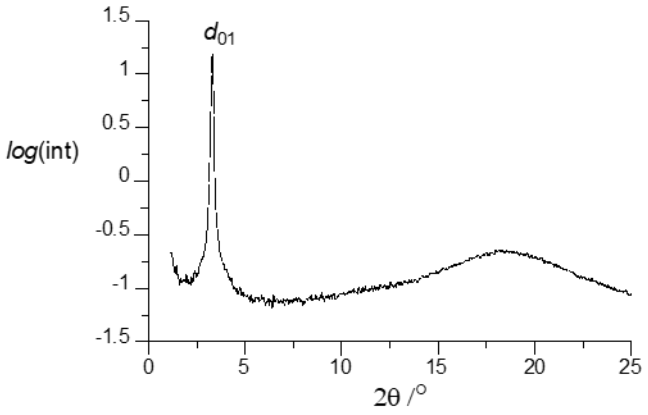

Figure 21. Powder X-ray diffractogram for ion pair **3[11,12]d** at 180 °C

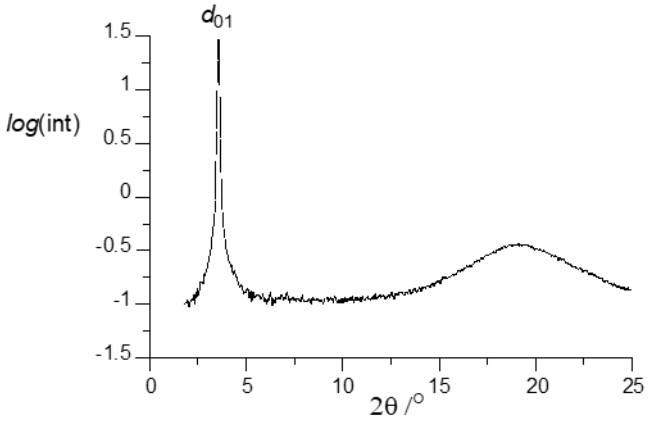

Figure 22. Powder X-ray diffractogram for ion pair **3[11,12]e** at 80 °C

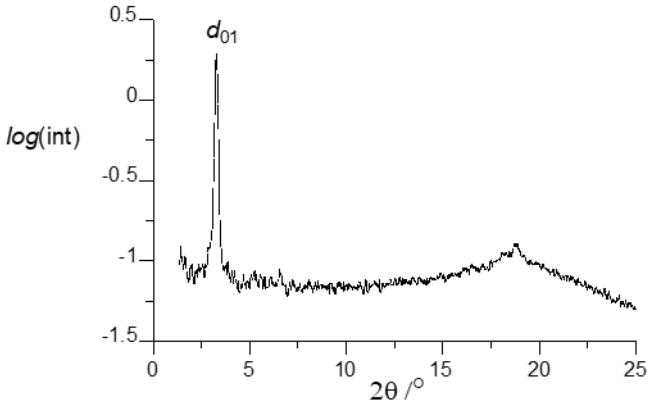

Figure 23. Powder X-ray diffractogram for ion pair **3[11,12]f** at 130 °C

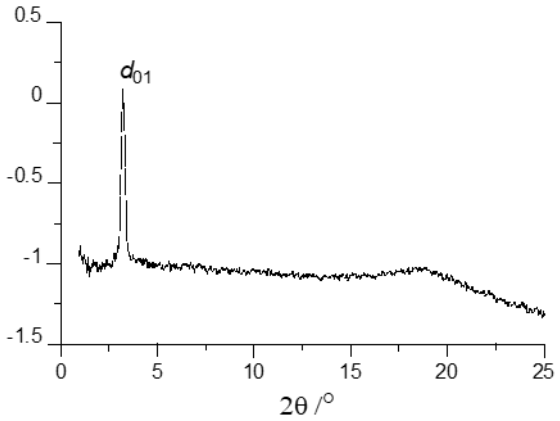

Figure 24. Powder X-ray diffractogram for ion pair **4[12]b** at 160 °C

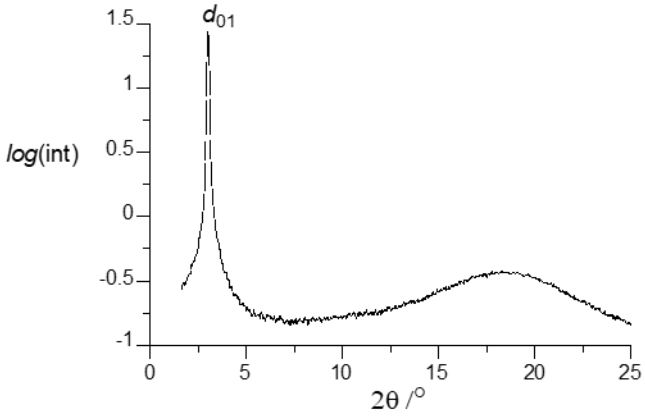

Figure 25. Powder X-ray diffractogram for ion pair **4[12]d** at 180 °C

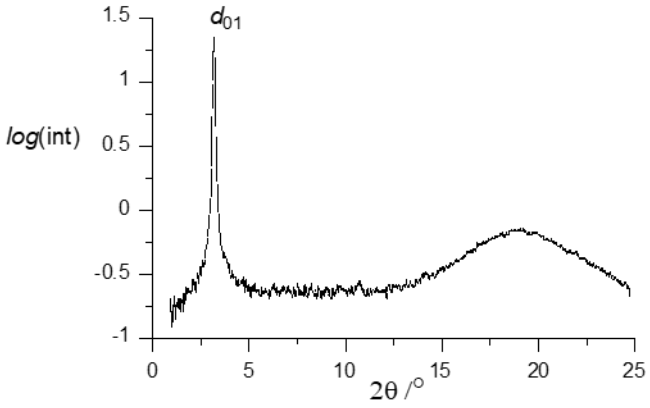

Figure 26. Powder X-ray diffractogram for ion pair **4[12]e** at 130 °C

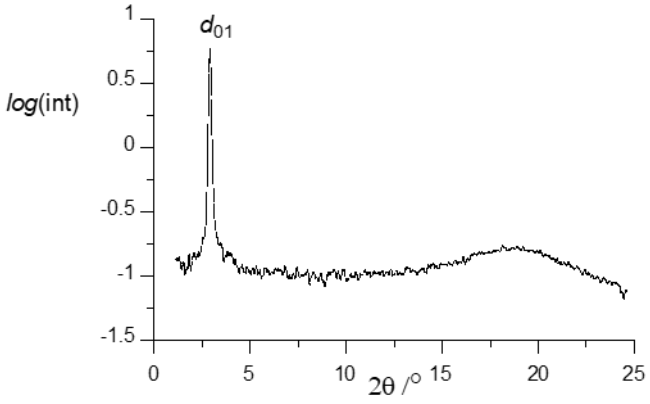

Figure 27. Powder X-ray diffractogram for ion pair **4[12]f** at 130 °C

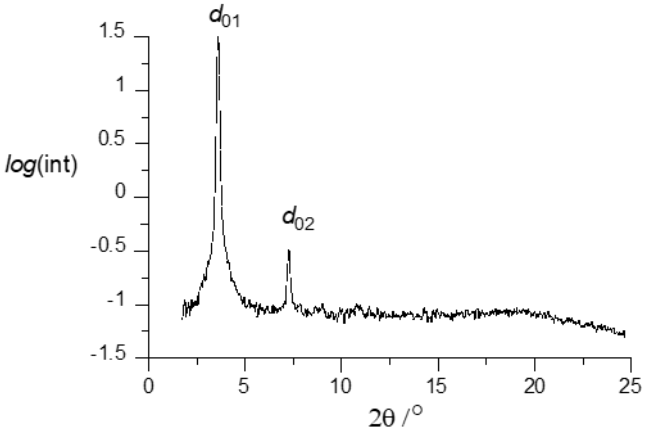

Figure 28. Powder X-ray diffractogram for 50 mol% mixture of ion pair **1[11]c** with hydroquinone dibutyrate **H[3]** at 120 °C.

PART B

Development of new efficient electrolytes based on [*closo*-1-$CB_{11}H_{12}$]$^-$ for Li-ion battery applications

As stated in the beginning of the main introduction, efficient energy storage and conversion technologies are crucial for space exploration, whereas current Li-ion batteries have numerous limitations for such applications. Part B of the thesis focuses on addressing some of these issues by developing anisotropic ion-conductive materials based on the [*closo*-1-$CB_{11}H_{12}$]$^-$ anion (**G**). In this approach we combine anisotropic ion transport of a liquid crystal (LC) with boron clusters as anions for Li-ion electrolytes. Here, the goal is to obtain a parallelly aligned polymeric host containing an oligoethylene fragment (for Li-ion coordination and solubility reasons) and a Li^+ salt with anion structurally similar/compatible with the host. The resulting thin polymeric film will be tested as a solid-state electrolyte for a CR2032 type battery. The key challenges in this project involves extensive synthesis and characterization of the liquid crystalline electrolyte sample, parallel alignment of the electrolyte sample using different surface treatment methods, photopolymerization of the parallel aligned liquid crystalline electrolytes, and finally cell assembly and battery test.

Part B of the thesis begins with a general overview (Chapter B1) of battery requirements for space exploration and electrolytes for Li-ion batteries. Initial investigations of liquid crystalline electrolytes derived from the 1,12-disubstituted [*closo*-1-$CB_{11}H_{12}$]$^-$ anion are described in Chapter B2. Unpublished results are reported in Chapters B3 and B4, which deal with anisotropy in Li-ion transport and polymer electrolytes, respectively, based on a liquid crystalline electrolyte containing Li^+ salt of the anionic [*closo*-1-$CB_{11}H_{12}$]$^-$ derivative.

CHAPTER B1

Electrolytes for Li-ion batteries

1.1 Introduction

The development of Li-ion batteries (LIBs) has received extraordinary significance worldwide in the last three decades due to the increasing demand for safe, reliable, and high energy-density storage and conversion [1-2]. Significant progress has been made in LIB technologies ever since their first commercial application in 1991 [3-4]. Due to their high energy density, light weight, and increased lifespan [5-6], they are currently utilized in numerous modern technologies, including portable electronic devices such as computers, smartphones, etc., and electric vehicles [7-12]. In addition, LIBs play a significant role in decarbonization via the electrification of transportation and their application in contemporary high-tech electronic products [13-14].

LIBs play a significant role in space missions, and they are emerging as the primary energy source for spacecraft, launch vehicles, interplanetary missions, the space station, etc. As of now, almost 107 space agencies are currently engaged in a variety of space-related endeavors, including meteorology, navigation, telecommunications, exploration of other planets, etc. [15]. In all this, rechargeable batteries with a primary energy source (solar cells) are essential to store energy and provide an uninterrupted power supply, especially in long-duration missions and satellites [16].

In order to ensure smooth battery operation in space, they have to overcome several challenges, including temperature and gravitational fluctuations, high-energy particles, radiation environments, hard ultraviolet light, etc. [17]. In addition, LIBs are susceptible to aging and degradation. Typically, the battery requirements for a space application vary based on the mission type and duration. Ag-Zn batteries, Ni-Cd batteries, and Ni-H_2 batteries are rechargeable batteries

that are commonly used in space applications [16]. Although some of these batteries, such as Ni-H_2, have a number of benefits, such as a long cycle life (>50,000 cycles) and reliable and consistent battery performance, their large size and poor performance at low temperatures remain obstacles [18-19]. The majority of conventional batteries have low energy density, poor performance at extreme temperatures, electrolyte leakage, capacity loss, and a short lifespan [18-22]. Other limitations include battery failure due to an internal short circuit, degradation of the separator, and electrode corrosion [23-24].

Li-ion batteries (LiBs) have several advantages over conventional batteries because of their high energy density, long cycle life, and light weight (a 50% weight reduction over Ni–H_2 is possible) [2]. Li-ion batteries are currently used in geostationary earth orbit (GEO) and low earth orbit (LEO) spacecraft, planetary missions, and also landers and rovers [16]. However, when operating at elevated temperatures, LIBs are susceptible to numerous electrolyte-related safety issues, including leakage, volatility, flammability, and decomposition [2]. For instance, the toxic and non-toxic gases released during the decomposition of the electrolyte material and Li-salt can lead to the expansion and explosion of a battery. Therefore, the development of an effective electrolyte system is crucial to the realization of safer LIBs with a high energy density. Extensive studies are in search of an efficient and reliable solid-state ion-transport material for the application in LIBs due to its easy processability and application in portable and flexible electronics.

1.2 Li-ion batteries

The primary components in the general design of a Li-ion battery include two electrodes (a positive cathode and a negative anode), an electrolyte, separators, and current collectors (Cu foil at the anode and Al foil at the cathode) [25-27]. Cathode materials are typically metal oxides or phosphates with varying electrochemical potentials, such as $LiCoO_2$ [28], $LiMn_2O_4$ [29-30], and

$LiFePO_4$ [31-32]. Commonly used anode material is either graphite [33-34] or lithium titanium oxide ($Li_4Ti_5O_{12}$) [35]. Throughout the charge-discharge cycle, electrolytes serve as the medium through which Li-ion is transported between the two electrodes. They consist of electronically insulating solutions, polymers, or inorganic solids containing lithium salts. $LiPF_6$, $LiAsF_6$, $LiCF_3SO_3$, $LiBF_4$, $LiClO_4$, and $LiN(CF_3SO_2)_2$ [36] are some of the commonly used lithium salts in electrolytes. The separators prevent direct contact between the electrodes while permitting the Li-ion to pass through them. A schematic description of LIB is shown in Figure 1.

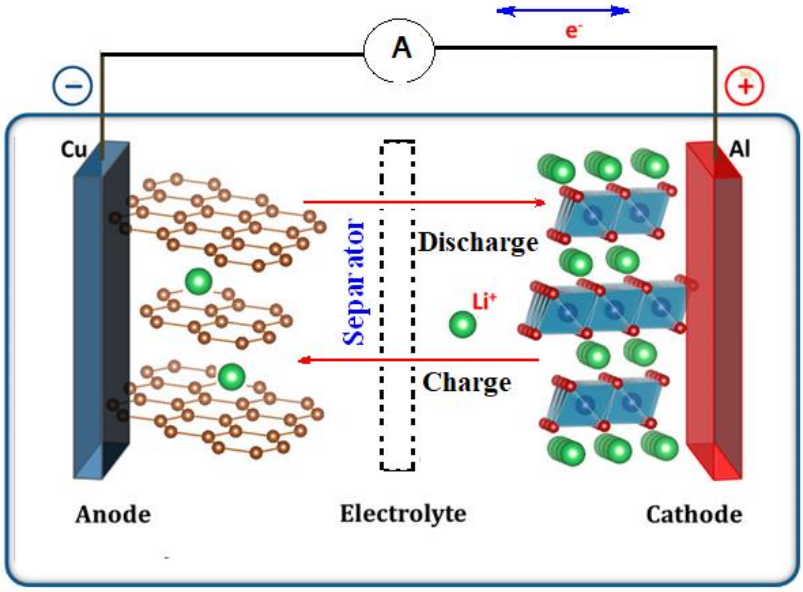

Figure 1. Schematic representation of a Li-ion battery

LIBs operate on the basis of electrochemical oxidation and reduction reactions (redox reactions) occurring in the cell during the charge and discharge processes [37-39]. Cells convert electrical energy to chemical energy through redox reactions. When the battery is being charged, electrons migrate from the cathode (oxidation) to the anode (reduction) through an external circuit, and Li-ions migrate from the cathode to the anode through the electrolyte in order to balance the charge. Additionally, electrolyte materials provide enough concentrations of lithium ions to facilitate ion transport. During the discharge of a battery, the movement of Li-ions from the anode

(oxidation) to the cathode (reduction) generates an electron flow from one electrode to the other, thereby generating an electric current in the external circuit. Depending on their reusability, Li-ion batteries are classified as either non-rechargeable (primary) or rechargeable (secondary).

1.3 Electrolytes for Li-ion batteries

The battery's ionic conductivity, charge-discharge cycles, coulombic efficiency, and safety depend mostly on the electrolyte. Consequently, electrolytes are as important as cathode and anode active materials for the development of an efficient LIB. The electrolyte in LIBs is desired to have high ionic conductivity, stability at high oxidation potential and low reduction potential, and safe operation under extreme conditions.

Conventionally used liquid organic electrolytes raise numerous safety concerns due to their high volatility, flammability, possibility of electrolyte leakage, high potential for toxic gas production, and poor resistance to impact (which is an important criterion for LIB application in space) [40-42]. Despite numerous attempts to improve the safety of liquid electrolytes, the flammability of these substances remained a concern. Therefore, it was necessary to develop a superior electrolyte system with high ionic conductivity to overcome these limitations [43].

Recently, solid-state electrolytes (SSEs) have received a lot of interest as a promising alternative to liquid electrolytes due to their thermal stability, high energy density, and broad operating temperature range [44-45]. SSEs are divided into organic solid electrolytes (OSEs) and inorganic solid electrolytes (ISEs) based on their chemical composition [46]. Although some inorganic solid electrolytes (ISEs), such as $Li_{10}GeP_2S_{12}$ and $70Li_2S\text{-}30P_2S_{5,}$ exhibit promising room temperature ionic conductivities of 1.2×10^{-2} and 3.2×10^{-3} S cm^{-1}, respectively [47a-47b], the majority of ISEs suffer from poor interfacial compatibility with electrode material, processing difficulties, and generally low ionic conductivity [47]. Compared to inorganic solid electrolytes,

organic solid electrolytes are typically more flexible and compatible with electrode interfaces. For this reason, current research focuses primarily on the development of organic solid electrolytes (OSEs). OSEs are further classified as solid polymer electrolytes (SPEs) [48-51], plastic crystal electrolytes (PCEs) [52-54], metal organic framework-based electrolytes (MOFEs) [55], and covalent organic framework-based electrolytes (COFEs) [56]. Among them, solid polymer electrolytes (SPEs) are of great interest due to their easy processability, low cost, and excellent film forming ability.

Recently, nanostructured liquid crystals (LC) have received attention for the development of electrolytes due to their ability to form nano-channels for efficient Li-ion transport [57-68]. LC polymer electrolytes were also obtained by the polymerization of LC electrolytes. In the context of this research, polymer electrolytes, LC electrolytes (LCEs), and LC polymer electrolytes (LCPEs) are of significance; this will be elaborated in the subsequent sections.

1.3.1 Solid polymer electrolytes

Solid polymer electrolytes (SPEs) are promising solid-state electrolytes that can satisfy the requirements of high voltage device applications. Compared to inorganic solid polymer electrolytes, they have enhanced electrochemical and thermal stability, interfacial compatibility, mechanical properties, easy processability, low cost, and improved safety [69-70]. SPEs can function as ionic conductors and an electronically insulating separator. SPEs are prepared by dissolving Li-salts, such as LiTFSI, LiFSI, $LiN(FSO_2)_2$, $LiCF_3SO_3$, and $LiClO_4$, in an appropriate polymer matrix [71-74]. In the polymer electrolyte system, Li^+ salts form a complex with polar groups such as –C–O–C–, –N–, and –S– present in the polymer matrix. Solid polymer electrolytes with high ionic conductivity and good mechanical properties are desirable for device applications [75]. The ionic conductivity of the polymer electrolyte is determined primarily by the dissolution

of the Li^+ salt and the dissociation energy of the Li-ion in the complex [76]. Polyethylene oxide-based (PEO) polymer electrolytes are the most commonly used among the various types of polymer electrolytes (polyethylene oxide, polyacrylonitrile, polyvinylidene fluoride, etc.) due to their ability to dissolve a variety of Li^+ salts, efficient coordination of the Li-ion, mechanical stability, good interfacial properties, and ability to facilitate ion transport [77-78].

Li-ion transport in polymer electrolytes is complex due to the presence of multiphase structures and distinct ion transport pathways [79]. Several ion transport mechanisms, including the cation hopping mechanism and the free ion transport mechanism have been proposed to explain the Li-ion transport in polymer electrolytes based on PEO [80-81]. In the cation-hopping mechanism, the Li-ion coordinates with the oxygens in the PEO and diffuses through the electrolytes in conjunction with the segmental motion of the polymer backbone. In general, Li-ion transport in polymer electrolytes made from PEO depends on Li-ion hopping between and within chains and relaxation of polymer segments [82].

Meziane and co-workers developed a solvent-free polymer electrolyte in an earlier attempt, but it exhibited a low ionic conductivity in the range of 10^{-6} to 10^{-7} S cm^{-1} [83]. A hybrid solid polymer electrolyte composed of PEO polymer and ZnO nanoparticles exhibited a high ionic conductivity of 4.2×10^{-4} S cm^{-1} at room temperature and excellent lithium plating and stripping performance at 40 °C [84]. Recent study demonstrated an improved ionic conductivity of 1.7×10^{-4} S cm^{-1} in a PEO-based polymer electrolyte containing Li_2S_6 salt [85]. This electrolyte system was found to inhibit dendrite growth, and its electrochemical performance in cells was remarkable.

The poor ionic conductivity at room temperature (10^{-6} to 10^{-7} S cm^{-1}) is the major hurdle in the application of solid polymer electrolytes in LIBs. This is mainly attributable to the sluggish Li-ion diffusion through its crystalline phase [70b, 86-87]. In addition, the formation of dendrites is a serious problem in batteries that use solid polymer electrolytes.

1.3.2 Liquid crystalline electrolytes

The ability of liquid crystalline (LC) electrolytes to self-organize and to provide 1D [61-62], 2D [63-65], and 3D [66-68] ion-conductive pathways for the efficient transport of Li-ions has received significant attention. The nanostructured smectic LC forms highly ion-conductive 2D pathways [88], which are thought to be free of order defects compared to 1D and 3D pathways. For this reason, it is anticipated that 2D pathways will increase ionic conductivity by providing appropriate molecular orientation for ion transport [89]. Despite the fact that LC has lower order and density than solids, it can be easily aligned to achieve the desired properties. Its light weight, ability to nanosegregate immiscible components spontaneously, rapid self-assembly, film-forming capability, and simple processability [90] make it a promising alternative to conventional electrolytes. The liquid-like mobility of ordered structures in the liquid crystalline phase is also advantageous for ion diffusion and the formation of the robust solid electrolyte interface (SEI). Yet another advantage of using LC in electrolytes is its ability to inhibit the formation of dendrites during the charge-discharge process [91]. In addition, it is possible to obtain solid-polymer electrolytes by immobilizing the ion conducting channels in the aligned LC phase by polymerization. These electrolytes ought to be nonvolatile, thermally stable, and flexible [92-94].

In general, LC-based electrolytes are generated by combining metal ion salts with LC matrices at a predetermined concentration. Polar LC containing carbonates or PEO chains [63] and ionic LC containing imidazolium [62,65], phosphonium, or ammonium [66] groups are primarily used in electrolyte applications due to their miscibility with ionic salts. Carbonate-base LC derivatives are suitable for use as electrolytes due to their high electrochemical stability and dielectric constant for the dissociation of Li^+ salts [40]. PEO in the LC structure has several advantages due to its ability to solvate a wide variety of Li^+ salts and its easy processability [95]. In addition, the incorporation of PEO into the LC structure can improve nanosegregation in the LC

phase and ion transport via the segmental motion of PEO. Figure 2 shows several examples of electrolytes that are derived from liquid crystals.

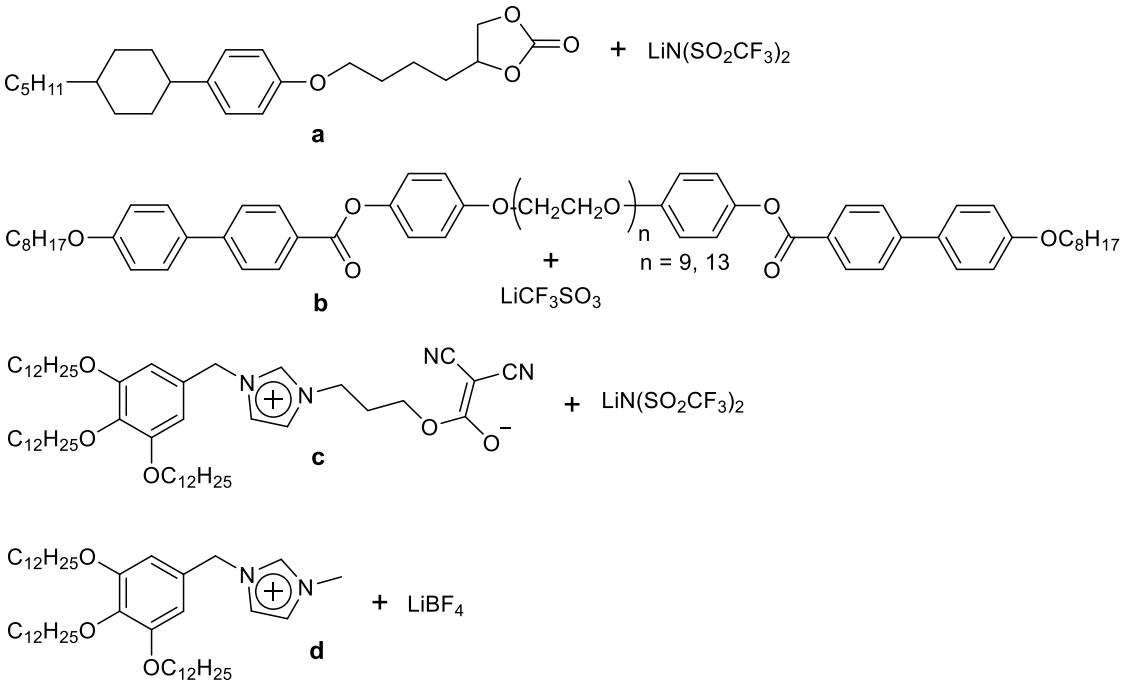

Figure 2. Examples of liquid crystalline electrolytes based on (a) carbonate-based LC [100], (b) dimeric LC containing oxyethylene moieties [63], (c) zwitterionic LC [67], and (d) ionic LC [62] containing Li^+ salts.

LC electrolytes showed remarkable thermal stability and are nonvolatile over a wide range of temperature and those utilized in dye-sensitized solar cells (DSSCs) were discovered to be functional even at elevated temperatures [96-98]. Such electrolytes offering greater ionic conductivities over a broad temperature range will be advantageous for use in Li-ion batteries for space exploration.

For the first time in 2015, Kato and co-workers showed that LC electrolytes could be used in Li-ion batteries [99]. In this study, the electrolyte was generated through a combination of a cyclic carbonate-based LC molecule and LiTFSI salt. These materials showed 2D ion-conductive

pathways in the smectic A (SmA) phase with moderate ionic conductivities [10^{-6} to 10^{-5} S cm^{-1}]. They showed excellent electrochemical stability and reversible charge-discharge characteristics in the $LiFe_4PO_4/LiTi_5O_{12}$ electrode system [99].

In a new approach to improve ionic conductivity in LC electrolytes through weak noncovalent interactions, low molecular weight carbonates (ethylene or propylene) were incorporated into the 2D structure of a liquid crystalline electrolyte derived from lithium bis(trifluoromethylsulfonyl)imide (LiTFSI) salt and carbonate-based LC. The newly obtained electrolyte system exhibited high ionic conductivity (10^{-4} to 10^{-5} S cm^{-1}), while preserving its 2D nanostructure. Good ionic conductivity was observed even at room temperature and its use was demonstrated in the first LC electrolyte-based LIBs operating at room temperature [100].

Studies on an electrolyte system composed of zwitterionic liquid crystals, LiTFSI salt, and propylene carbonate revealed excellent ionic conductivities of up to 10^{-4} S cm^{-1} [67]. Ober and co-workers demonstrated an electrolyte system based on LiTFSI salt and oligothiophene based LC containing oxyethylene units, showing a high ionic conductivity of 5.2×10^{-4} S cm^{-1} at 70 °C [101]. A detailed study on this electrolyte system revealed that the high ionic conductivity in the smectic phase is associated with the formation of 2D ion transport channels due to nanosegregation of the oligothiophene and oxyethylene moieties and π-stacking of the thiophene rings.

Wang and co-workers demonstrated a solvent-free electrolyte system based on ILCs that combined the properties of Li^+ salt and an organic solvent or plasticizer. It showed good room-temperature ionic conductivity (3×10^{-3} S cm^{-1}) and electrochemical stability. Here also, detailed studies revealed that the observed high ionic conductivity was associated with the formation of efficient ion-conductive channels in the LC phase [102].

Electrochemical stability of the electrolytes at high voltages is critical for the application of advanced LIBs, which work in the voltage range of 0 to 5.0 V. LC electrolytes have shown good

electrochemical stability up to 4.3 V versus the Li/Li^+ reference electrode. Furthermore, LC electrolytes having high oxidative resistance have been found to suppress the electrolysis of active electrode materials during the charge-discharge process [103].

Lithium metal is a natural choice for use in rechargeable Li-ion batteries as an anode material due to its high negative electrochemical potential (−3.040 V vs the standard hydrogen electrode), high theoretical specific capacity (3860 mAh g^{-1}), and low density (0.534 g cm^{-3}) [8, 104-106]. However, their use in high performance LIBs is limited because of the Li-dendrite formation during the continued lithium deposition and stripping process and poor cycle life. This leads to the disruption of the electrochemical reactions due to the unavailability of enough Li-ions, increased resistance, and poor coulombic efficiency. Eventually, this leads to battery failure and short-circuiting which could result in an explosion. Recent studies have shown that the use of LC electrolytes with high ionic conductivity can suppress dendrite formation by forming a robust solid electrolyte interface (SEI) over a wide temperature range [91b]. This was demonstrated in a recent study that shows only a negligible change in the polarization of the cell, even after 850 hours of continues lithium plating and stripping, which indicates smooth cycling with minimal dendrite formation [91b].

1.3.3 Liquid crystalline polymer electrolytes

LCs are also utilized in the synthesis of anisotropic polymer electrolytes, which combine the properties of liquid crystal electrolytes and polymer electrolytes [107-108]. This is obtained by the polymerization of the liquid crystalline electrolyte material in a LC phase. The introduction of the LC property allows tuning the size and orientation of the ion-conducting channels in the polymer for efficient Li-ion transport [108]. In addition, liquid-crystalline polymer electrolytes

(LCPEs) provide high mechanical stability, a broad operating temperature range, reduced electrolyte leakage, and low flammability [109].

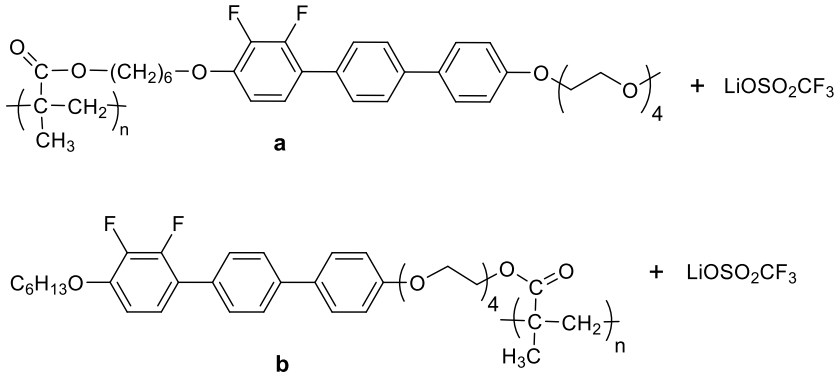

Figure 3. Examples of typical examples of polymer electrolyte systems based on liquid crystals [110].

Kato and co-workers prepared such a liquid crystalline polymer electrolyte in 2005 by photopolymerizing a PEO-based LC monomer containing a polymerizable methacrylate unit. It exhibited ionic conductivity in the range of 10^{-3} S cm^{-1} at room temperature (Figure 3). Even after polymerization, the ethylene oxide moiety retained its mobility [110]. Zhang and co-workers recently created a solid polymer electrolyte by combining a nematic LC and an ionic liquid; it exhibited high ionic conductivity at room temperature of 2.14×10^{-3} S cm^{-1}, a wide electrochemical window of 4.8 V, and excellent compatibility with lithium metal [111].

1.4 Boron clusters in solid-state electrolytes

Anionic boron clusters have attracted significant interest as components of new solid-state electrolytes due to their highly delocalized negative charge in their 3-dimensional sigma framework (weakly coordinating anions) as well as their high electrochemical and thermal stability. In addition, it was observed that the large size of polyhedral boron clusters has an advantage over the simple metal borohydride $M[BH_4]$ by providing interstitial channels for facile ion diffusion

with low activation energy. In general, the disordered high-temperature phase exhibits up to three orders of magnitude greater ionic conductivity than the ordered low-temperature phase. Metal salts of boron clusters, including [*closo*-$B_{10}H_{10}]^{2-}$ (**A**), [*closo*-1-$CB_9H_{10}]^-$ (**B**), and [*closo*-1-$CB_{11}H_{12}]^-$ (**G**), have been extensively studied as halogen-free electrolyte materials for all-solid-state battery applications. Solid-state electrolytes have several advantages over liquid electrolytes, including high oxidative stability, high energy density, and lower risk of flammability [112-116].

1.4.1 Electrolytes based on boron clusters

In the disordered high-temperature phase of metal salts of the boron clusters, there are more interstitial voids in the crystal lattice, resulting in increased metal ion mobility through it. As a consequence, Na^+ salts of the dianions [*closo*-$B_{10}H_{10}]^{2-}$ (**A**) and [*closo*-$B_{12}H_{12}]^{2-}$ (**F**) (Structures in Figure 2 of the main Introduction) exhibit superionic conductivity (0.01 to 0.1 S cm^{-1}) above their respective order-disorder phase transition temperatures of 373 K and 573 K [117-119]. Li^+ salts of these dianions exhibit high ionic conductivity with a transition temperature greater than 600 K [120]. The phase transition temperatures of the Li^+ and Na^+ salts of [*closo*-1-$CB_{11}H_{12}]^-$ (**G**) were determined to be 400 K and 380 K, respectively, which is significantly lower than the transition temperature for the salts of the anion **A**. In their disordered cubic phases, Li^+ and Na^+ salts of the anion **G** exhibit superionic conductivities of 0.15 S cm^{-1} and 0.12 S cm^{-1}, respectively [121]. Due to its low phase transition temperature of 363 K, [*closo*-1-$CB_9H_{10}]^- Li^+$ has been intensively studied and they have demonstrated ionic conductivity of 8.1×10^{-2} S cm^{-1} in their high temperature phase [122]. As an alternative to Li-ion batteries, other metal ions such as Mg^{2+} and Ca^{2+} are being extensively studied [123-126].

Compared to metal salts of dianionic *closo*-borates, salts of monoanionic carboranes are indeed superior electrolyte components due to the lower cation to anion ratio in their lattices, which

allows for greater cation diffusion. In addition, it has been observed that the carbon atoms in carborane decrease the order-disorder phase transition temperature by increasing the intrinsic disorder. In addition to the increased anion orientational mobility, the weak coulombic attraction also facilitates cation diffusion in carbaborate salts [127-128]. However, from the standpoint of using these electrolytes in ion batteries, a high ionic conductivity at low temperature is desired.

One of the ways in which high ionic conductivity at a lower temperature was achieved is by mixing different boron cluster salts. A study of a solid solution of $0.7Li[CB_9H_{10}]$-$0.3Li[CB_{11}H_{12}]$ revealed a low transition temperature to a chemically and electrochemically stable phase with an ionic conductivity of 6.7×10^{-3} S cm^{-1} at 25 °C [129]. Similarly, ionic conductivities of a solid solution of $0.6Li[CB_9H_{10}]$-$0.4Li_2[B_{12}H_{12}]$ at 25 °C were 1.7×10^{-3} S cm^{-1} [130]. Also, an electrolyte system of $0.5Na[B_{12}H_{12}]$-$0.5Na[B_{10}H_{10}]$ was utilized to create a stable 3 V solid-state battery [131].

Although anionic boron clusters as structural elements for solid-state electrolytes are extremely promising, achieving ionic conductivities comparable to those of liquids (10^{-2} to 10 S cm^{-1}) remains difficult. This is primarily due to steric interactions and coulombic forces, which make diffusion of metal ions through the crystal lattice difficult [116]. One approach to achieve good ionic conductivity is by developing a new electrolyte system by incorporating *closo*-borate metal salts as additives to a suitable organic matrix. This approach was primarily constrained by the incompatibility and poor solubility of the salts in organic matrices. Currently, several functionalized carbaborates suitable for electrolyte applications are available. Part B of this thesis is focused solely on this new area of electrolyte research, in which functionalized [*closo*-1-$CB_{11}H_{12}]^-$ derivatives are used as Li^+ salt additives to liquid crystalline matrices to generate liquid crystalline electrolytes. The final goal of the project is to obtain a free standing and flexible solid polymer electrolyte and to test its performance in a Li-ion battery.

1.5 Principles of electrochemical impedance spectroscopy

Electrochemical impedance spectroscopy (EIS) is a widely used technique for understanding the characteristics of electrolytes, the mobility of ions, interfacial reactions between electrodes and electrolytes, as well as the physical and chemical phenomena occurring within lithium-ion batteries (LIBs) [132]. Monitoring the battery's performance in real time is crucial for ensuring its safety, quality, and efficiency. As a non-destructive technique, EIS can be used as a diagnostic tool in various battery stages and over a broad frequency range without compromising the battery's integrity [133-135]. EIS is also used to characterize energy storage and conversion devices such as fuel cells [136] and capacitors [137].

Impedance, Z, is the resistance to current flow through a battery when an AC voltage is applied. It has a direct effect on the battery's efficiency, operating voltage, rate capability, and capacity. Due to this, measuring impedance is helpful for estimating the operational limits, performance, and internal aging state of batteries [138-139]. The internal impedance of a battery is complex due to contributions (resistive, capacitive, and inductive impedance) from its many individual components, such as electrodes, electrolyte, current collectors, and separators [140]. EIS is conducted over a broad frequency range under varying temperature and state of charge (SOC) conditions to gather impedance information (real part, imaginary part, phase). EIS is faster and more accurate than traditional methods based on voltage and current alone [141-142].

EIS measurements, either in a potentiostatic mode (constant voltage) or in a galavanostatic mode (constant current), can be used to obtain the characteristic impedance spectrum [143]. In the potentiostatic mode, a sinusoidal voltage of a certain amplitude and frequency is applied to the battery over a specific frequency range (typically kHz to MHz), and the output current and phase are analyzed with a frequency response analyzer (FRA). Typically, the measurements provide

information regarding the various elementary reactions occurring in the cell, including electron transfer from the current collector to the electrode, electron migration and Li-ion migration through the electrode thickness, double layer charging at the interfaces, coupled diffusion of active and non-active ions in porous electrodes, and diffusion of ions in the separator [144]. This technique allows for the investigation of these distinct processes with distinct time constants.

Typically, Nyquist or Bode plots are employed to analyze the results of impedance measurements (the output signal and the current response of the system). Using a Nyquist or Bode plot, the resistance, capacitance, and inductance contributions of various cell components and processes can be determined. The Nyquist plot is generated by plotting the imaginary part (Z'') of the impedance against the real part (Z'). In a Bode plot, Z'' and Z', or magnitude and phase, are plotted as functions of frequency [145]. One can determine resistance from the X-axis and reactance from the Y-axis using the Nyquist plot.

Although EIS is an easy-to-use technique, deconvolution and interpretation of the massive amount of data from the poorly resolved arcs in the impedance spectrum are frequently challenging [146]. Through a series of studies evaluating the changes in the measured EIS spectra in relation to the changes in the cell components, scientists were able to connect particular electrochemical processes to particular regions of the spectra [147-148]. By constructing equivalent circuits, it is also possible to assign each region of the plot to a distinct physical process and component of the battery. Using various electric field elements, the basic shape of measured spectra can be easily matched in equivalent circuit analysis. Figure 4 depicts a schematic example of a typical Nyquist plot.

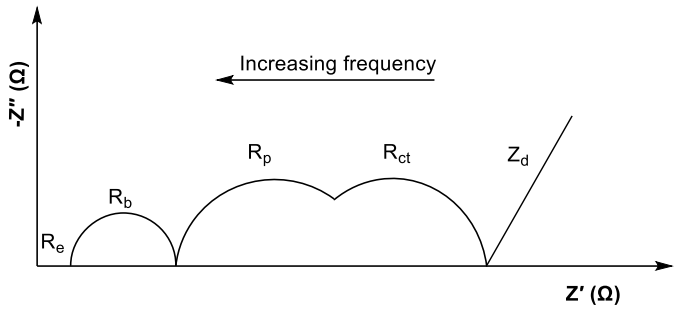

Figure 4. A typical Nyquist plot of a symmetrical lithium battery. The meaning of labels is discussed in the text.

In Figure 4, R_e in the highest frequency region represents the electrode resistance between the current collector and the electrode [149]. The next region of the spectrum corresponds to the electrolyte resistance, R_b, and it is the resistance for the movement of active Li-ions and counterions in the electrolyte. Impedance arcs in the next region, resulting from the passive layer resistance, R_p, and charge transfer resistance, R_t, are overlapped. This is due to their similar time constants, and this region of the spectrum is often called interfacial layer impedance due to the practical meaning it has. This region combines resistive and capacitive effects [150]. The lowest frequency region of the spectrum corresponds to the Warburg impedance Z_d. This is the resistance related to the ambipolar diffusion in the solid-state crystallites of the insertion material.

1.6 References

1. C. Bubulinca, N. E. Kazantseva, V. Pechancova, N. Joseph, H. Fei, M. Venher, A. Ivanichenko, P. Saha, Development of all-solid-state Li-ion batteries: from key technical areas to commercial use, *Batteries*, **2023**, *9*,157–182.
2. M. Li, J. Lu, Z. Chen, K. Amine, 30 years of lithium-ion batteries, *Adv. Mater.*, **2018**, *30*, 1800561.

3. C. A. Vincent, Lithium batteries: A 50-year perspective, *Solid State Ion.*, **2000**, *134*, 159–167.
4. S. S. Shin, Y. K. Sun, K. Amine, Synthesis and electrochemical properties of $Li[Li_{(1-2x)/3}Ni_xMn_{(2-x)/3}]O_2$ as cathode materials for lithium secondary batteries, *J. Power Sources*, **2002**, *112*, 634–638.
5. J. Mei, T. F. Yi, X. Y. Li, Y. R. Zhu, Y. Xie, C. F. Zhang, Robust strategy for crafting $Li_5Cr_7Ti_6O_{25}@CeO_2$ composites as high-performance anode material for lithium-ion battery, *ACS Appl. Mater. Inter.*, **2017**, *9*, 23662–23671.
6. W. Xing, D. F. Du, T. H. Cai, X. C. Li, J. Zhou, Y. M. Chai, Q. Z. Xue, Z. F. Yan, Carbonencapsulated CoSe nanoparticles derived from metal-organic frameworks as advanced cathode material for Al-ion battery, *J. Power Sources*, **2008**, *401*, 6–12.
7. A. R. Armstrong, P. G. Bruce, Synthesis of layered $LiMnO_2$ as an electrode for rechargeable lithium batteries, *Nature*, **1996**, *381*, 499–500.
8. J. M. Tarascon, J. Armand, Issues and challenges facing rechargeable lithium batteries, *Nature*, **2001,** *414*, 359–367.
9. F. Jiao, P. G. Bruce, Mesoporous crystalline b-MnO_2-a reversible positive electrode for rechargeable lithium batteries, *Adv. Mater.*, **2007**, *19*, 657–660.
10. P. G. Bruce, B. Scrosati, J. M. Tarascon, Nanomaterials for rechargeable lithium batteries, *Angew. Chem. Int. Ed.*, **2008**, *47*, 2930–2946.
11. D. Mecerreyes, Polymeric ionic liquids: Broadening the properties and applications of polyelectrolytes, *Prog. Polym. Sci.*, **2011**, *36*, 1629–1648.
12. X. Xu, Z. F. Dou, E. L. Gu, L. Si, X. S. Zhou, J. C. Bao, Uniformly-distributed Sb nanoparticles in ionic liquid-derived nitrogen-enriched carbon for highly reversible sodium storage, *J. Mater. Chem. A*, **2017**, *5*, 13411–13420.

13. S. Sripad, V. Viswanathan, Evaluation of current, future, and beyond Li-ion batteries for the electrification of light commercial vehicles: Challenges and opportunities. *J. Electrochem. Soc.*, **2017**, 167, 3635–3646.
14. M. D. Moore, 52nd Aerospace sciences meeting in *AIAA SciTech Forum* (American Institute of Aeronautics and Astronautics, 2014).
15. WMO OSCAR, List of all space agencies. https://space.oscar.wmo .int/spaceagencies.
16. A. D. Pathak, S. Saha, V. K. Bharti, M. M Gaikwad, C. S. Sharma, A review on battery technology for space application, *J. Energy Storage*, **2023**, *61*, 106792–106815.
17. A. F. Hepp, P. N. Kumta, O. I. Velikokhatnyi, M. K. Datta, Batteries for aeronautics and space exploration: Recent developments and future prospects, *Lithium-Sulfur Batteries*, **2022**, 531–595.
18. J. Mondt, K. Burke, B. Bragg, G. Rao, S.Vukson, Energy storage technology for future space science missions, National Aeronautics and Space Administration, Technical Report, **2004,** JPL D-30268, Rev. A.
19. G. Halpert, H. Frank, S. Surampudi, Batteries and fuel cells in space, *Electrochem. Soc. Interface*, **1999**, *8*, 25–32.
20. T. Jiang, W. Chen, Nickel hydrogen gas batteries: From aerospace to grid-scale energy storage applications, *Curr. Opin. Electrochem.*, **2021**, *30*, 100859.
21. G. Van Ommering, C. W.Koehler, Bipolar nickel-hydrogen battery system design, *Proc., Intersoc. Energy Convers. Eng. Conf. United States*,**1984**, *1*, 840804.
22. W. Chen, Y. Jin, J. Zhao, N. Liu, Y. Cui, Nickel-hydrogen batteries for large-scale energy storage, *Proc. Natl. Acad. Sci. U. S. A.*, **2018,** *115*, 11694–11699.

23. X. Fan, B. Liu, J. Liu, J. Ding, X. Han, Y. Deng, X. Lv, Y. Xie, B. Chen, W. Hu, C. Zhong, Battery technologies for grid-level large-scale electrical energy storage, *Trans. Tianjin Univ.*, **2020**, *26*, 92–103.

24. A. Mondal, H. Das, Energy storage batteries: Basic feature and applications, in *Ceramic Science and Engineering*, **2022**, *13*, 323–351.

25. R. C. Agrawal, R. K. Gupta, Superionic solid: Composite electrolyte phase–an overview, *J. Mater. Sci.*, **1999**, *34*, 1131–1162.

26. G.B. Appetecchi, B. Scrosati, Lithium-ion polymer battery, *Electrochim. Acta*, **1998**, *43*, 1105–1107.

27. J. Y. Kim, S. H. Kim, Ionic conduction behavior of network polymer electrolytes based on phosphate and polyether copolymers, *Solid State Ion.*, **1999**, *124*, 91–99.

28. Z. Chen, Z. Lu, J. R. Dahn, Staging phase transitions in Li_xCoO_2, *J. Electrochem. Soc.*, **2002**, *149*, 1604–1610.

29. M. Thackeray, W. David, P. Bruce, J. Goodenough, Lithium insertion into manganese spinels, *Mater. Res. Bull.*, **1983**, *18*, 461–472.

30. J. M. Tarascon, W. R. McKinnon, F. Coowar, T. N. Bowmer, G. Amatucci, D. Guyomard, Synthesis conditions and oxygen stoichiometry effects on Li insertion into the spinel $LiMn_2O_4$, *J. Electrochem. Soc.*, **1994**, *141*, 1421–1431.

31. A. K. Padhi, Phospho-olivines as positive-electrode materials for rechargeable lithium batteries, *J. Electrochem. Soc.*, **1997**, *144*, 1188–1196.

32. B. Kang, G. Ceder, Battery materials for ultrafast charging and discharging, *Nature*, **2009**, *458*, 190–193.

33. M Winter, J. O. Besenhard, M. E. Spahr, P. Novak, Insertion electrode materials for rechargeable lithium batteries, **1998**, *Adv. Mater.*, *10*, 725–763.

34. S. Flandrois, B. Simon, Carbon materials for lithium-ion rechargeable batteries, *Carbon*, **1999**, *37*, 165–180.

35. E. Ferg, Spinel anodes for lithium-ion batteries, *J. Electrochem. Soc.*, **1994**, *141*, 147–151.

36. Y. An, X. Han, Y. Liu, A. Azhar, J. Na, A. K. Nanjundan, S. Wang, J. Yu, Y. Yamauchi, Progress in solid polymer electrolytes for lithium-ion batteries and beyond, *Small*, **2022**, *18*, 2103653.

37. K. W. Wong, W. K. Chow, Principle for the working of the lithium-ion battery, *J. Mod. Phys.*, **2020**, *11*, 1743–1750.

38. N. Chawla, N. Bharti, S. Singh, Recent advances in non-flammable electrolytes for safer lithium-ion batteries, *Batteries*, **2019**, *5*, 19–44.

39. X. Zhang, W. Zhang, G. Lei, A review of Li-ion battery equivalent circuit models, *Trans. Electr.*, **2016**, *17*, 311–316.

40. K. Xu, Nonaqueous liquid electrolytes for lithium-based rechargeable batteries, *Chem. Rev.*, **2004**, *104*, 4303−4418.

41. E. M. Erickson, E. Markevich, G. Salitra, D. Sharon, D. Hirshberg, E. de la Llave, I. Shterenberg, A. Rozenman, A. Frimer, D. Aurbach, Development of advanced rechargeable batteries: A continuous challenge in the choice of suitable electrolyte solutions. *J. Electrochem. Soc.*, **2015**, *162*, 2424−2438.

42. M. Watanabe, M. L. Thomas, S. Zhang, K. Ueno, T. Yasuda, K. Dokko, Application of ionic liquids to energy storage and conversion materials and devices, *Chem. Rev.*, **2017**, *117*, 7190−7239.

43. S. J. Kwon, B. M. Jung, T. Kim, J. Byun, J. Lee, S. B. Lee, U. H. Choi, Influence of Al_2O_3 nanowires on ion transport in nanocomposite solid polymer electrolytes, *Macromolecules*, **2018**, *51*, 10194–10201.

44. S. Chen, K. Wen, J. Fan, Y. Bando, D. Golberg, Progress and future prospects of high-voltage and high-safety electrolytes in advanced lithium batteries: From liquid to solid electrolytes, *J. Mater. Chem. A*, **2018**, *6*, 11631–11663.

45. A. Arya, A. L. Sharma, A glimpse on all-solid-state Li-ion battery (ASSLIB) performance based on novel solid polymer electrolytes: a topical review, *J. Mater. Sci.*, **2020**, *55*, 6242–6304.

46. J. Janek, W. G. Zeier, A solid future for battery development, *Nat. Energy*, **2016**, *1*, 1–4.

47. (a) N. Kamaya, K. Homma, Y. Yamakawa, M. Hirayama, R. Kanno, M. Yonemura, T. Kamiyama, Y. Kato, S. Hama, K. Kawamoto, A. Mitsui, A lithium superionic conductor, *Nat. Mater.*, **2011**, *10*, 682–686; (b) F. Mizuno, A. Hayashi, K. Tadanaga, M. Tatsumisago, New, highly ion-conductive crystals precipitated from Li_2S–P_2S_5 glasses, *Adv. Mater.*, **2005**, *17*, 918–921; (c) T. Minami, A. Hayashi, M. Tatsumisago, Recent progress of glass and glass-ceramics as solid electrolytes for lithium secondary batteries, *Solid State Ion.*, **2006**, *177*, 2715–2720; (d) P. Knauth, Inorganic solid Li ion conductors: An overview, *Solid State Ion.*, **2009**, *180*, 911–916.

48. H. Zhang, C. Li, M. Piszcz, E. Coya, T. Rojo, L. M. Rodriguez-Martinez, M. Armand, Z. Zhou, Single lithium-ion conducting solid polymer electrolytes: Advances and perspectives, *Chem. Soc. Rev*., **2017**, *46*, 797−815.

49. P. V. Wright, Polymer electrolytes the early days, *Electrochim. Acta*, **1998**, *43*, 1137−1143.

50. W. H. Meyer, Polymer electrolytes for lithium-ion batteries, *Adv. Mater*, ***1998***, *10*, 439−448.

51. F. Croce, G. B. Appetecchi, L. Persi, B. Scrosati, Nanocomposite polymer electrolytes for lithium batteries, *Nature*, **1998**, *394*, 456−458.

52. J. M. Pringle, Recent progress in the development and use of organic ionic plastic crystal electrolytes, *Phys. Chem. Chem. Phys.*, **2013**, *15*, 1339−1351.

53. D. R. Macfarlane, J. Huang, M. Forsyth, Lithium-doped plastic crystal electrolytes exhibiting fast ion conduction for secondary batteries, *Nature*, ***1999***, *402*, 792−794.

54. P. J. Alarco, Y. Abu-Lebdeh, A. Abouimrane, M. Armand, The plastic-crystalline phase of succinonitrile as a universal matrix for solid-state ionic conductors, *Nat. Mater.*, **2004**, *3*, 476−481.

55. L. Shen, H. B. Wu, H. F. Liu, J. L. Brosmer, G. R. Shen, X. F. Wang, J. I. Zink, Q. F. Xiao, M. Cai, G. Wang, et al. Creating lithium-ion electrolytes with biomimetic ionic channels in metal-organic framework, *Adv. Mater.*, **2018**, *30*, 1707476−1707484.

56. K. Jeong, S. Park, G. Y. Jung, S. H. Kim, Y. H. Lee, S. K. Kwak, S. Y. Lee, Solvent-free, single lithium-ion conducting covalent organic frameworks, *J. Am. Chem. Soc.*, **2019**, *141*, 5880–5885.

57. T. Kato, From nanostructured liquid crystals to polymer-based electrolytes, *Angew. Chem. Int. Ed.*, **2010**, *49*, 7847−7848.

58. M. Yoshio, T. Kato, Liquid crystals as ion conductors in handbook of liquid crystals, 2nd ed.; J. W. Goodby, P. J. Collings, T. Kato, C. Tschierske, H. Gleeson, P. Raynes, Eds.; *Wiley-VCH:Weinheim*, **2014**, *8*, 727−749.

59. B. K. Cho, Nanostructured organic electrolytes, *RSC Adv.*, **2014**, *4*, 395−405.

60. B. R. Wiesenauer, D. L. Gin, Nanoporous polymer materials based on self-organized, bicontinuous cubic lyotropic liquid crystal assemblies and their applications, *Polym. J.*, **2012**, *44*, 461−468.

61. H. Shimura, M. Yoshio, A. Hamasaki, T. Mukai, H. Ohno, T. Kato, Electric-field-responsive lithium-ion conductors of propylenecarbonate-based columnar liquid crystals, *Adv. Mater.*, **2009**, *21*, 1591−1594.

62. M. Yoshio, T. Mukai, H. Ohno, T. Kato, One-dimensional ion transport in self-organized columnar ionic liquids, *J. Am. Chem. Soc.*, **2004**, *126*, 994−995.

63. T. Ohtake, M. Ogasawara, K. Ito-Akita, N. Nishina, S. Ujiie, H. Ohno, T. Kato, Liquid-crystalline complexes of mesogenic dimers containing oxyethylene moieties with $LiCF_3SO_3$: Self- organized ion conductive materials, *Chem. Mater.*, **2000**, *12*, 782−789.

64. A. Eisele, K. Kyriakos, R. Bhandary, M. Schönhoff, C. M. Papadakis, B. Rieger, Structure and ionic conductivity of liquid crystals having propylene carbonate units, *J. Mater. Chem. A*, **2015**, *3*, 2942−2953.

65. J. H. Lee, K. S. Han, J. S. Lee, A. S. Lee, A. S. K. Park, S. Y. Hong, J. C. Lee, K. T. Mueller, S. M. Hong, C. M. Koo, Facilitated ion transport in smectic ordered ionic liquid crystals, *Adv. Mater.*, **2016**, *28*, 9301−9307.

66. T. Ichikawa, M. Yoshio, A. Hamasaki, S. Taguchi, F. Liu, X. B. Zeng, G. Ungar, H. Ohno, T. Kato, Induction of thermotropic bicontinuous cubic phases in liquid crystalline ammonium and phosphonium salts, *J. Am. Chem. Soc.*, **2012**, *134*, 2634−2643.

67. B. Soberats, M. Yoshio, T. Ichikawa, H. Ohno, T. Kato, Zwitterionic liquid crystals as 1D and 3D lithium-ion transport media, *J. Mater. Chem. A*, **2015**, *3*, 11232−11238.

68. T. Kobayashi, T. Ichikawa, T. Kato, H. Ohno, Development of glassy bicontinuous cubic liquid crystals for solid proton-conductive materials, *Adv. Mater.*, **2017**, *29*, 1604429−1604435.

69. Q. Zhao, S. Stalin, C. Z. Zhao, L. A. Archer, Designing solid-state electrolytes for safe, energy-dense batteries, *Nat. Rev. Mater.*, **2020**, *5*, 229−252.

70. (a) J. W. Fergus, Ceramic and polymeric solid electrolytes for lithium-ion batteries, *J. Power Sources*, **2010**, *195*, 4554−4569; (b) Z. Xue, D. He, X. Xie, Poly (ethylene oxide)-based electrolytes for lithium-ion batteries, *J. Mater. Chem. A*, **2015**, *3*, 19218−19253; (c) A. Manthiram, X. Yu, S. Wang, Lithium battery chemistries enabled by solid-state electrolytes, *Nat. Rev. Mater.*, **2017**, *2*, 1–16; (d) C. Sun, J. Liu, Y. Gong, D. P. Wilkinson, J. Zhang, Recent advances in all-solid-state rechargeable lithium batteries, *Nano Energy*, **2017**, *33*, 363–386.

71. Z. Wang, W. Gao, X. Huang, Y. Mo, L. Chen, Ion transport in polyacrylonitrile-based electrolytes with high LiTFSI contents, *Electrochem. Solid-State Lett.*, **2001**, *4*, 148−151.

72. X. Zhang, S.Wang, C. Xue, C. Xin, Y. Lin, Y. Shen, L. Li, C. W. Nan, Self-suppression of lithium dendrite in all-solid-state lithium metal batteries with poly (vinylidene difluoride)-based solid electrolytes, *Adv. Mater.*, **2019**, *31*, 1806082−1806091.

73. S. Skaarup, K. West, B. Zachau-Christiansen, Mixed phase solid electrolytes, *Solid State Ion.*, **1988**, *28*, 975–978.

74. R. Marom, O. Haik, D. Aurbach, I. C. Halalay, Revisiting $LiClO_4$ as an electrolyte for rechargeable lithium-ion batteries, *J. Electrochem. Soc.*, **2010**, *157*, 972–984.

75. J. C. Bachman, S. Muy, A. Grimaud, H. H. Chang, N. Pour, S. F. Lux, O. Paschos, F. Maglia, S. Lupart, P. Lamp, L. Giordano, Y. Shao-Horn, Inorganic solid-state electrolytes

for lithium batteries: mechanisms and properties governing ion conduction, *Chem. Rev.*, **2016**, *116*, 140–162.

76. Y. Zhao, L. Wang, Y. Zhou, Z. Liang, N. Tavajohi, B. Li, T. Li, Solid polymer electrolytes with high conductivity and transference number of Li ions for Li-based rechargeable batteries, *Adv. Sci.*, **2021**, *8*, 2003675–2003697.
77. J. W. Kim, K. S. Ji, J. P. Lee, J. W. Park, Electrochemical characteristics of two types of PEO-based composite electrolyte with functional SiO_2, *J. Power Sources*, **2003**, *119*, 415–421.
78. (a) M. Armand, Polymer solid electrolytes-an overview, *Solid State Ion.*, **1983**, *9*, 745–754; (b) W. H. Meyer, Polymer electrolytes for lithium-ion batteries, *Adv. Mater.*, **1998**, *10*, 439–448.
79. Y. Wang, A. P. Sokolov, Design of superionic polymer electrolytes, *Curr. Opin. Chem. Eng.*, **2015**, *7*, 113–119.
80. S. Rajendran, R. Kannan, O. Mahendran, Study on Li ion conduction behavior of the plasticized polymer electrolytes based on poly acrylonitrile, *Mater. Lett.*, **2001**, *48*, 331–335.
81. S. Mogurampelly, V. Ganesan, Effect of nanoparticles on ion transport in polymer electrolytes, *Macromolecules*, **2015**, *48*, 2773–2786.
82. A. Maitra, A. Heuer, Cation transport in polymer electrolytes: a microscopic approach, *Phys. Rev. Lett.*, **2007**, *98*, 227802–227806.
83. R. Meziane, J. P. Bonnet, M. Courty, K. Djellab, M. Armand, Single-ion polymer electrolytes based on a delocalized polyanion for lithium batteries, *Electrochim. Acta*, **2011,** *57*, 14–19.

84. S. Nematdoust, R. Najjar, D. Bresser, S. Passerini, Understanding the role of nanoparticles in PEO-based hybrid polymer electrolytes for solid-state lithium–polymer batteries, *J. Phys. Chem. C,* **2020**, *124*, 27907–27915.

85. R. Fang, B. Xu, N. S. Grundish, Y. Xia, Y. Li, C. Lu, Y. Liu, N. Wu, J. B. Goodenough, Li_2S_6-integrated PEO-based polymer electrolytes for all-solid-state lithium-metal batteries, *Angew. Chem. Int. Ed.*, **2021**, *60*, 17842–17847.

86. F.M. Gray, *Polymer Electrolytes*, **1997**, (Royal Society of Chemistry, London)

87. J. B. Goodenough, Y. Kim, Challenges for rechargeable Li batteries, *Chem. Mater*., **2010**, *22*, 587–603.

88. (a) T. Ohtake, K. Ito, N. Nishina, H. Kihara, H. Ohno, T. Kato, Liquid crystalline complexes of a lithium salt with twin oligomers containing oxyethylene spacers. An approach to anisotropic ion conduction, *Polym. J*., **1999**, *31*, 1155–1158; (b) Y. Iinuma, K. Kishimoto, Y. Sagara, M. Yoshio, T. Mukai, I. Kobayashi, H. Ohno, T. Kato, Uniaxial parallel alignment of a smectic A liquid-crystalline rod−coil molecule and its lithium salt complexes using rubbed polyimides, *Macromolecules*, **2007**, *40*, 4874–4878; (c) G. S. McHattie, C. T. Imrie, M. D. Ingram, Ionically conducting side chain liquid crystal polymer electrolytes, *Electrochim. Acta*, **1998**, *43*, 1151–1154; (d) M. Yoshio, T. Mukai, K. Kanie, M. Yoshizawa, H. Ohno, T. Kato, Liquid-crystalline assemblies containing ionic liquids: An approach to anisotropic ionic materials, *Chem. Lett.*, **2002**, *31*, 320–321; (e) C. J. Bowlas, D. W. Bruce, K. R. Seddon, Liquid-crystalline ionic liquids, *Chem. Commun.*, **1996**, *14*,1625–1626.

89. W. Pisula, M. Zorn, J. Y. Chang, K. Müllen, R. Zentel, Liquid crystalline ordering and charge transport in semiconducting materials, *Macromol. Rapid Commun.*, **2009,** *30*, 1179–1202.

90. C. Ruiz, E. M. García-Frutos, G. Hennrich, B. Gómez-Lor, Organic semiconductors toward electronic devices: High mobility and easy processability, *J. Phys. Chem. Lett*., **2012**, *3*, 1428–1436.

91. (a) Z. Ahmad, Z. Hong, V. Viswanathan, Design rules for liquid crystalline electrolytes for enabling dendrite-free lithium metal batteries, *Proc. Natl. Acad. Sci.*, **2020**, *117*, 26672–26680; (b) D. Gopalakrishnan, S.Alkatie, A. Cannon, S. Rajendran, N. K. Thangavel, N. Bhagirath,E. M. Ryan, L. M. R. Arava, Anisotropic mass transport using ionic liquid crystalline electrolytes to suppress lithium dendrite growth, *Sustain. Energy Fuels*, **2021**, *5*, 1488–1497.

92. T. Kato, From nanostructured liquid crystals to polymer-based electrolytes, *Angew. Chem. Int. Ed.*, **2010**, *43*, 7847–7848.

93. K. Kishimoto, T. Suzawa, T. Yokota, T. Mukai, H. Ohn, T. Kato, Nano-segregated polymeric film exhibiting high ionic conductivities, *J. Am. Chem. Soc.*, **2005**, *127*, 15618–15623.

94. (a) M. Yoshio, T. Kagata, K. Hoshino, T. Mukai, H. Ohno, T. Kato, One-dimensional ion-conductive polymer films: Alignment and fixation of ionic channels formed by self-organization of polymerizable columnar liquid crystals, *J. Am. Chem. Soc.* **2006**, *128*, 5570−5577; (b) T. Ichikawa, M. Yoshio, A. Hamasaki, J. Kagimoto, H. Ohno, T. Kato, 3D interconnected ionic nano-channels formed in polymer films: Self-organization and polymerization of thermotropic bicontinuous cubic liquid crystals, *J. Am. Chem. Soc.*, **2011**, *133*, 2163−2169; (c) K. Kishimoto, M. Yoshio, T. Mukai, M. Yoshizawa, H. Ohno, T. Kato, Nanostructured anisotropic ion-conductive films, *J. Am. Chem. Soc.*, **2003**, *125*, 3196−3197; (d) K. Hoshino, M. Yoshio, T. Mukai, K. Kishimoto, H. Ohno, T. Kato, Nanostructured ion-conductive films: Layered assembly of a side-chain liquid-crystalline

polymer with an imidazolium ionic moiety, *J. Polym. Sci. Part A: Polym. Chem.*, **2003**, *41*, 3486−3492; (e) A. Yamashita, M. Yoshio, S. Shimizu, T. Ichikawa, H. Ohno, T. Kato, Columnar nanostructured polymer films containing ionic liquids in supramolecular one-dimensional nanochannels, *J. Polym. Sci. Part A: Polym. Chem.*, **2015**, *53*, 366−371.

95. M. Yoshizawa, T. Mukai, T. Ohtake, K. Kanie, T. Kato, H. Ohno, Ion-conductive mechanism in liquid crystalline molecules having polyether segment, *Solid State Ion.*, **2002**, *154*, 779−787.
96. D. Högberg, B. Soberats, S. Uchida, M. Yoshio, L. Kloo, H. Segawa, T. Kato, Nanostructured two-component liquid crystalline electrolytes for high-temperature dye-sensitized solar cells, *Chem. Mater*., **2014**, *26*, 6496−6502.
97. D. Högberg, B. Soberats, R. Yatagai, S. Uchida, M. Yoshio, L. Kloo, H. Segawa, T. Kato, Liquid crystalline dye-sensitized solar cells: Design of two-dimensional molecular assemblies for efficient ion transport and thermal stability, *Chem. Mater*., **2016**, *28*, 6493−6500.
98. N. Yamanaka, R. Kawano, W. Kubo, N. Masaki, T. Kitamura, Y. Wada, M. Watanabe, S. Yanagida, Dye-sensitized TiO_2 solar cells using imidazolium-type ionic liquid crystal systems as effective electrolytes, *J. Phys. Chem. B*, **2007**, *111*, 4763−4769.
99. J. Sakuda, E. Hosono, M. Yoshio, T. Ichikawa, T. Matsumoto, H. Ohno, H. Zhou, T. Kato, Liquid crystalline electrolytes for lithium-ion batteries: Ordered assemblies of a mesogen-containing carbonate and a lithium salt, *Adv. Funct. Mater*., **2015**, *25*, 1206−1212.
100. T. Onuma, E. Hosono, M. Takenouchi, J. Sakuda, S. Kajiyama, M. Yoshio, T. Kato, Noncovalent approach to liquid-crystalline ion conductors: High-rate performances and room-temperature operation for Li-ion batteries, *ACS omega*, **2018**, *3*, 159−166.

101. Z**.** Liu, B. X. Dong, M. Misra, Y. Sun, J. Strzalka, S. N. Patel, F. A. Escobedo, P. F. Nealey, C. K. Ober, Self-assembly behavior of an oligothiophene-based conjugated liquid crystal and its implication for ionic conductivity characteristics, *Adv. Funct. Mater.*, **2019**, *29*, 1805220−1805232.

102. F. Yuan, S. Chi, S. Dong, X. Zou, S. Lv, L. Bao, J. Wang, Ionic liquid crystal with fast ion-conductive tunnels for potential application in solvent-free Li-ion batteries, *Electrochim. Acta*, **2019**, *294*, 249−259.

103. Kuwabara, Atsushi, Mayu Enomoto, Eiji Hosono, Kazuma Hamaguchi, Taira Onuma, Satoshi Kajiyama, Takashi Kato, Nanostructured liquid-crystalline Li-ion conductors with high oxidation resistance: molecular design strategy towards safe and high-voltage-operation Li-ion batteries, *Chem. Sci.*, **2020**, *11*, 10631−10637.

104. P. G. Bruce, S. A. Freunberger, L. J. Hardwick J. M. Tarascon, Li–O_2 and Li–S batteries with high energy storage, *Nat. Mater*., **2011**, *11*, 19−29.

105. F. Croce, G. B. Appetecchi, L. Persi, B. Scrosati, Nanocomposite polymer electrolytes for lithium batteries, *Nature*, **1998**, *394*, 456−458.

106. J. C. Jones, S. Rajendran, A. Pilli, V. R. Lee, N. Chugh, L. M. R. Arava, J. A. Kelber, In situ X-ray photoelectron spectroscopy study of lithium carbonate removal from garnet-type solid-state electrolyte using ultra high vacuum techniques, *J. Vac. Sci. Technol. A*, **2020**, *38*, 23201−23212.

107. D. Ndaya, R. Bosire, S. Vaidya, R. M. Kasi, Molecular engineering of stimuli-responsive, functional, side-chain liquid crystalline copolymers: Synthesis, properties and applications, *Polym. Chem.*, **2020**, *11*, 5937−5954.

108. X. L. Lyu, A. Q. Xiao, D. Shi, Y. J. Li, Z. H. Shen, E. Q. Chen, S. J. Zheng, X. H. Fan, Q. F. Zhou, Liquid crystalline polymers: Discovery, development, and the future, *Polymer*, **2020**, *202*, 122740−122781.

109. A. Kuwabara, M. Enomoto, E. Hosono, K. Hamaguchi, T. Onuma, S. Kajiyama, T. Kato, Nanostructured liquid-crystalline Li-ion conductors with high oxidation resistance: molecular design strategy towards safe and high-voltage-operation Li-ion batteries, *Chem. Sci.*, **2020**, *11*, 10631−10637.

110. K. Kishimoto, T. Suzawa, T. Yokota, T. Mukai, H. Ohno, T. Kato, Nano-segregated polymeric film exhibiting high ionic conductivities, *J. Am. Chem. Soc.*, **2005**, *127*, 15618−15623.

111. S. Wang, Q. Zeng, A. Wang, X. Liu, J. Chen, Z. Wang, L. Zhang, Constructing stable ordered ion channels for a solid electrolyte membrane with high ionic conductivity by combining the advantages of liquid crystal and ionic liquid, *J. Mater. Chem. A*, **2019**, *7*, 1069−1075.

112. F. Zheng, M. Kotobuki, S. Song, M. O. Ali, L. Lu, Review on solid electrolytes for all-solid-state lithium-ion batteries, *J. Power Sources*, **2018**, *389*, 198−213.

113. Z. Gao, H. Sun, L. Fu, F. Ye, Y. Zhang, W. Luo, Y. Huang, Promises, challenges, and recent progress of inorganic solid-state electrolytes for all-solid-state lithium batteries, *Adv. Mater.*, **2018**, *30*, 1705702−1705723.

114. C. Zhao, L. Liu, X. Qi, Y. Lu, F. Wu, J. Zhao, Y. Yu, Y. -S. Hu, L. Chen, Solid-state sodium batteries, *Adv. Energy Mater.*, **2018**, *8*, 1703012−1703032.

115. Y. Wang, W. D. Richards, S. P. Ong, L. J. Miara, J. C. Kim, Y. Mo, G. Ceder, Design principles for solid-state lithium superionic conductors, *Nat. Mater.*, **2015**, *14*, 1026−1031.

116. H. Zhang, C. Li, M. Piszcz, E. Coya, T. Rojo, L. M. Rodriguez- Martinez, M. Armand, Z. Zhou, Single lithium-ion conducting solid polymer electrolytes: Advances and perspectives, *Chem. Soc. Rev.*, **2017**, *46*, 797−815.

117. N. Verdal, J.-H. Her, V. Stavila, A. V. Soloninin, O. A. Babanova, A. V. Skripov, T. J. Udovic, J. J. Rush, Complex high-temperature phase transitions in $Li_2B_{12}H_{12}$ and $Na_2B_{12}H_{12}$, *J. Solid State Chem.*, **2014**, *212*, 81–91.

118. A. V. Skripov, O. A. Babanova, A. V. Soloninin, V. Stavila, N. Verdal, T. J. Udovic, J. J. Rush, Nuclear magnetic resonance study of atomic motion in $A_2B_{12}H_{12}$ (A= Na, K, Rb, Cs): Anion reorientations and Na^+ mobility, *J. Phys. Chem. C*, **2013**, *117*, 25961–25968.

119. T. J. Udovic, M. Matsuo, A. Unemoto, N. Verdal, V. Stavila, A. V. Skripov, J. J. Rush, H. Takamura, S. Orimo, Sodium superionic conduction in $Na_2B_{12}H_{12}$, *Chem. Commun.*, **2014**, *50*, 3750–3752.

120. T. J. Udovic, M. Matsuo, W. S. Tang, H. Wu, V. Stavila, A. V. Soloninin, R. V. Skoryunov, O. A. Babanova, A. V. Skripov, J. J. Rush, A. Unemoto, H. Takamura, S. Orimo, Exceptional superionic conductivity in disordered sodium decahydro-*closo*-decaborate, *Adv. Mater.*, **2014**, *26*, 7622–7626.

121. W. S. Tang, A. Unemoto, W. Zhou, V. Stavila, M. Matsuo, H. Wu, S. I. Orimo, T. J. Udo1vic, Unparalleled lithium and sodium superionic conduction in solid electrolytes with large monovalent cage-like anions, *Energy Environ. Sci.*, **2015**, *8*, 3637–3645.

122. W. S. Tang, M. Matsuo, H. Wu, V. Stavila, W. Zhou, A. A. Talin, A. V. Soloninin, R. V. Skoryunov, O. A. Babanova, A. V. Skripov, Liquid-like ionic conduction in solid lithium and sodium monocarba-*closo*-decaborates near or at room temperature, *Adv. Eergy Mater.*, **2016**, *6*, 1502237–1502249.

123. O. Tutusaus, R. Mohtadi, N. Singh, T. S. Arthur, F. Mizuno, Study of electrochemical phenomena observed at the Mg metal/electrolyte interface, *ACS Energy Lett.*, **2017**, *2*, 224−229.

124. K. Kisu, S. Kim, T. Shinohara, K. Zhao, A. Züttel, S. I. Orimo, Monocarborane cluster as a stable fluorine-free calcium battery electrolyte, *Sci. Rep*, **2021**, *11*,1–8.

125. N. T. Hahn, T. J. Seguin, K. -C. Lau, C. Liao, B. J. Ingram, K. A. Persson, K. R. Zavadil, Enhanced stability of the carba-*closo*-dodecaborate anion for high-voltage battery electrolytes through rational design, *J. Am. Chem. Soc.*, **2018**, *140*, 11076−11084.

126. W. Ren, M. Cheng, Y. Wang, D. Zhang, Y. Yang, J. Yang, J. Wang, Y. Nuli, Boron–based electrolytes for rechargeable magnesium batteries: Biography and perspective, *Batteries Supercaps*, **2022**, *5*, 202200263.

127. A. V. Soloninin, M. Dimitrievska, R. V. Skoryunov, O. A. Babanova, A. Skripov, W. S. Tang, V. Stavila, S. -I. Orimo, T. J. Udovic, Comparison of anion reorientational dynamics in MCB_9H_{10} and $M_2B_{10}H_{10}$ (M = Li, Na) via nuclear magnetic resonance and quasielastic neutron scattering studies, *J. Phys. Chem. C*, **2017**, *121*, 1000−1012.

128. A. V. Skripov, R. V. Skoryunov, A. V. Soloninin, O. A. Babanova, W. S. Tang, V. Stavila, T. J. Udovic, Anion reorientations and cation diffusion in $LiCB_{11}H_{12}$ and $NaCB_{11}H_{12}$: ^{1}H, ^{7}Li, and ^{23}Na NMR Studies, *J. Phys. Chem. C*, **2015**, *119*, 26912−26918.

129. S. Kim, H. Oguchi, N. Toyama, T. Sato, S. Takagi, T. Otomo, D. Arunkumar, N. Kuwata, J. Kawamura, S. -I Orimo, A complex hydride lithium superionic conductor for high-energy-density all-solid-state lithium metal batteries, *Nat. Commun.*, **2019**, *10*, 1–9.

130. S. Kim, K. Kisu, S. I. Orimo, Stabilization of superionic-conducting high-temperature phase of $Li(CB_9H_{10})$ via solid solution formation with $Li_2(B_{12}H_{12})$, *Crystals*, **2021**, *11*, 330–340.

131. L. Duchêne, R. S. Kühnel, E. Stilp, E. C. Reyes, A. Remhof, H. Hagemann, C. Battaglia, A stable 3 V all-solid-state sodium-ion battery based on a *closo*-borate electrolyte, *Energy Environ. Sci.*, **2017**, *10*, 2609–2615.

132. A. Barai, K. Uddin, M. Dubarry, L. Somerville, A. McGordon, P. Jennings, I. Bloom, A comparison of methodologies for the non-invasive characterization of commercial Li-ion cells, *Prog. Energy Combust. Sci*., **2019**, *72*, 1–31.

133. U. Troltzsch, O. Kanoun, H. R. Trankler, Characterizing aging effects of lithium-ion batteries by impedance spectroscopy, *Electrochim. Acta*, **2006**, *51*, 1664–72.

134. H. Piret, P. Granjon, N. Guillet, V. Cattin, Tracking of electrochemical impedance of batteries, *J. Power Sources*, **2016**, *312*, 60–69.

135. R. Koch, A. Jossen, Temperature measurement of large format pouch cells with impedance spectroscopy, in 28th international electric vehicle symposium and exhibition 2015, EVS, **2015**, 1–9.

136. Z. He, F. Mansfeld, Exploring the use of electrochemical impedance spectroscopy (EIS) in microbial fuel cell studies, *Energy Environ. Sci*., **2009**, *2*, 215−219.

137. M. Zhi, F. Yang, F. Meng, M. Li, A. Manivannan, N. Wu, Effects of pore structure on performance of an activated-carbon supercapacitor electrode recycled from scrap waste tires, *ACS Sustainable Chem. Eng*., **2014**, *2*, 1592−1598.

138. A. Barai, K. Uddin, W. D. Widanage, A. McGordon, P. Jennings, A study of the influence of measurement timescale on internal resistance characterisation methodologies for lithium-ion cells, *Sci. Rep*., **2018**, *8*, 1–13.

139. C. Fleischer, W. Waag, H. M. Heyn, D. U. Sauer, On-line adaptive battery impedance parameter and state estimation considering physical principles in reduced order equivalent

circuit battery models part 2. Parameter and state estimation, *J. Power Sources*, **2014**, *262*, 457–482.

140. K.W. Beard, Linden's handbook of batteries, fifth ed., McGraw-Hill Education, **2019.**
141. K. McCarthy, H. Gullapalli, T. Kennedy, Real-time internal temperature estimation of commercial Li-ion batteries using online impedance measurements, *J. Power Sources*, **2022**, *519*, 230786.
142. H. Nara, T. Yokoshima, T. Osaka, Technology of electrochemical impedance spectroscopy for an energy-sustainable society, *Curr. Opin. Electrochem*, **2020**, *20*, 66–77.
143. J. Li, C. Arbizzani, S. Kjelstrup, J. Xiao, Y. Y. Xia, Y. Yu, Y. Yang, I. Belharouak, T. Zawodzinski, S. T. Myung, R. Raccichini, S. Passerini, Good practice guide for papers on batteries for the Journal of Power Sources, *J. Power Sources*, **2020,** *452*, 1016–1020.
144. J. Moškon, M. Gaberšček, Transmission line models for evaluation of impedance response of insertion battery electrodes and cells, *J. Power Sources Adv*., **2021**, *7*, 100047–100059.
145. E. Barsoukov, J. R. Macdonald (Eds.), Impedance spectroscopy: Theory, experiment, and applications, third ed., Wiley, **2018**.
146. L. A. Middlemiss, A. J. Rennie, R. Sayers, A. R. West, Characterisation of batteries by electrochemical impedance spectroscopy. *Energy Rep.*, **2020**, *6*, 232–241.
147. J. Moškon, J. Žuntar, S. Drvarič Talian, R. Dominko, M. Gaberšček, A powerful transmission line model for analysis of impedance of insertion battery cells: A case study on the NMC-Li system, *J. Electrochem. Soc*., **2020**, *167*, 140539–140561.
148. B. A. Mei, O. Munteshari, J. Lau, B. Dunn, L. Pilon, Physical interpretations of Nyquist plots for EDLC electrodes and devices. *J. Phys. Chem. C*, **2018**, *122*, 194–206.

149. E. C. Shin, P. A. Ahn, H. H. Seo, J. M. Jo, S. D. Kim, S. K. Woo, J. H. Yu, J. Mizusaki, J. S. Lee, Polarization mechanism of high temperature electrolysis in a Ni-YSZ/YSZ/ LSM solid oxide cell by parametric impedance analysis, *Solid State Ion.*, **2013**, *232*, 80–96.

150. S. M. M. Alavi, C. R. Birkl, D. A. Howey, Time-domain fitting of battery electrochemical impedance models, *J. Power Sources*, **2015**, *288*, 345–352.

CHAPTER B2

Liquid crystalline electrolytes derived from the 1,12-disubstituted [*closo*-$CB_{11}H_{12}]^-$ anion.

(J. Guschlbauer, L. Niedzicki, L. Jacob, E. Rzeszotarska, D. Pociecha, P. Kaszyński, *J. Mol. Liq.* **2023**, *377*, 121525, DOI: 10.1016/j.molliq.2023.121525)

2.1 Introduction

This research investigated a novel paradigm for anisotropic electrolytes. A new LC electrolyte system was investigated in which the anion of the Li-salt is a 1,12-disubstituted [*closo*-$CB_{11}H_{12}]^-$ derivative that is structurally similar to the molecules of the LC host exhibiting smectic C and nematic phases. The significance of this electrolyte design was that the anion behaves, in principle, like the host molecule, and this may permit to avoid using extraneous anions accumulating in the conductive layer, which could be beneficial for the liquid crystalline phase stability and Li^+ ion transport properties. Electrolytes with different concentrations of salts (5, 10, and 15 mol%) were studied, and the results showed that the ionic conductivity in the LC phase monotonically increased from 10^{-8} to 10^{-4} S cm^{-1}, with increasing concentration of Li-ion and temperature (20 to 120 ^oC). The electrochemical stability window of the 15 mol% electrolyte was determined to be between 1.3 and 4.6 volts relative to the Li metal anode. This suggests the compatibility of the electrolyte system with most Li^+ ion electrodes.

This project was started by Ms. Edyta Rzeszotarska, a former student, who initially worked on the synthesis of the LC host. Dr. Jannick Guschlbauer was subsequently able to synthesize and characterize the LC host and lithium salt based on a 1,12-disubstituted [*closo*-$CB_{11}H_{12}]^-$ derivative. He also prepared the electrolyte samples. I contributed to the project by providing the [*closo*-1-$CB_{11}H_{12}]^-$ cluster and by resynthesizing the LC host and lithium salt to obtain larger amounts for

studies. I also contributed to the thermal behavior analysis and powder XRD measurements of the samples. Dr. Damian Pociecha performed the temperature dependent powder XRD measurements. Dr. Leszek Niedzicki performed the electrochemical impedance spectroscopy (EIS) and linear sweep voltammetry (LSV). Prof. Piotr Kaszyński validated all experimental results.

2.2 Published text

Journal of Molecular Liquids 377 (2023) 121525

Contents lists available at ScienceDirect

Journal of Molecular Liquids

journal homepage: www.elsevier.com/locate/molliq

Liquid crystalline electrolytes derived from the 1,12-disubstituted [*closo*-$CB_{11}H_{12}$]$^-$ anion

Jannick Guschlbauer [a], Leszek Niedzicki [b], Litwin Jacob [a], Edyta Rzeszotarska [a], Damian Pociecha [c], Piotr Kaszyński [a,d,e,*]

[a] Centre of Molecular and Macromolecular Studies, Polish Academy of Sciences, 90-363 Łódź, Poland
[b] Faculty of Chemistry, Warsaw University of Technology, 00-664 Warsaw, Poland
[c] Faculty of Chemistry, University of Warsaw, Żwirki i Wigury 101, 02-089 Warsaw, Poland
[d] Faculty of Chemistry, University of Łódź, 91-403 Łódź, Poland
[e] Department of Chemistry, Middle Tennessee State University, Murfreesboro, TN 37130, USA

ARTICLE INFO

Article history:
Received 17 November 2022
Revised 18 January 2023
Accepted 21 February 2023
Available online 24 February 2023

Keywords:
Ionic liquid crystals
Smectic phase
Carborane
Ionic conductivity

ABSTRACT

A new approach to anisotropic liquid electrolytes is explored. Thus, a non-ionic liquid crystalline host exhibiting SmC and N phases is doped with a lithium salt containing an anion structurally similar to the host and derived from the weakly-nucleophilic [*closo*-$CB_{11}H_{12}$]$^-$ cluster. The resulting unaligned 5, 10, and 15 mol% solutions of the lithium salt in the host were investigated by optical, thermal, powder XRD and impedance spectroscopy methods in a broad temperature range. The results showed that the increasing concentration of the ionic additives essentially does not affect the mesophase stability, but expands the lamellar SmA phase possessing ion conducting channels. At the same time ionic conductivity, σ, monotonically increases from 10^{-8} to 10^{-4} S cm^{-1} with increasing temperature (20–120 °C) and with increasing Li^+ ion concentration. The Arrhenius analysis of the conductivity data revealed progressively decreasing activation energy E_{aIC} from crystalline (~102 kJ mol^{-1}), to SmA (~70 kJ mol^{-1}) and to nematic (~30 kJ mol^{-1}) phases. The electrochemical stability window of the 15 mol% electrolyte was determined as 1.3–4.6 V vs Li metal anode.

© 2023 Elsevier B.V. All rights reserved.

1. Introduction

Organic electrolytes [1–3] are of increasing importance for energy storage and processing, in particular for Li-ion batteries [4–10]. One promising avenue to such electrolytes involves liquid crystals (LCs), which can serve as effective nanostructured anisotropic solvents for lithium salts [11–14]. Research over the past two decades has shown that such an approach provides substantial benefits, when compared to conventional liquid lithium salt solutions [15]. Thus, these materials offer reasonable ionic conductivity, safe processibility with decreased danger of leakage, reduced inflammability, and the perspective for immobilization by polymerization [16]. For instance, ionic conductivity of 10^{-6}–10^{-5} S cm^{-1} was obtained for smectic materials [17,18], which was improved by 60 times upon addition of ethylene carbonate [19]. The inherent anisotropy of liquid crystals that arises from nano-segregation leads to formation of 1D [20,21], 2D [22–25] or 3D [26–28] ion-conductive nanopathways with liquid-like ion mobility. For instance, aligned smectic materials have been shown to increase ionic conductivity up to three orders of magnitude for Li^+ migration along the ionic planes, when compared to the transport through the same material with unaligned polydomain structures [29,30]. These studies typically involved solutions of lithium salts, *e.g.* lithium triflate or $(CF_3SO_2)_2NLi$, in an LC host containing ionic or chelating O-donor groups, such as alkylcarbonate [17,18,20,24,26,31] or oligo(ethylene oxide) [22,29,30,32–35]. There are also recent reports on liquid crystalline lithium salts, both low molecular weight and polymeric as single-ion conductors [36–38].

Lithium salts used to formulate electrolytes typically contain weakly nucleophilic anions, such as $(CF_3SO_2)_2N^-$, $CF_3SO_3^-$, PF_6^-, and BF_4^- [39,40]. Particularly interesting in this context are *closo*-borate anions [41,42], which are weakly nucleophilic [43], inorganic, three-dimensional, σ-aromatic [44,45] boron hydrides. Over the past four decades several lithium [46–51] and, more recently, also magnesium [52,53] salts of the parent and halogenated *closo*-borates were tested as ionic additives to organic electrolytes and

* Corresponding author at: Centre of Molecular and Macromolecular Studies, Polish Academy of Sciences, 90-363 Łódź, Poland.
E-mail address: piotr.kaszynski@mtsu.edu (P. Kaszyński).

https://doi.org/10.1016/j.molliq.2023.121525
0167-7322/© 2023 Elsevier B.V. All rights reserved.

also as solid electrolytes.[54–57] On the other hand, these *closo*-borates have been demonstrated to be effective structural elements of polar [58] and ionic liquid crystals [59–62]. Therefore, it was speculated that incorporation of a *closo*-borate anion into a molecular structure resembling that of a mesogenic compound might led to effective electrolyte systems, in which the anion behaves, in principle, like a molecule of the host. This approach may permit to avoid the use of extraneous anions accumulating in the conductive layer, which could be beneficial for the liquid crystalline phase stability and Li^+ ion transport properties. For this purpose, we considered a non-ionic host molecule **LC[n]** and its close structural analogue **1[Li]** as the source of lithium cations (Fig. 1).

Herein we present a new approach to anisotropic liquid electrolytes, in which a mesogenic non-ionic host **LC[n]** is doped with lithium salt **1[Li]** containing an anion structurally similar to the host molecule. In this preliminary report we formulate 5, 10, and 15 mol% solutions and investigate them for liquid crystalline behavior, ionic conductivity, and voltage stability of unaligned samples to set the foundation of a new class of ion transport materials.

2. Results and discussion

2.1. Synthesis

The preparation of liquid crystalline hosts **LC[n]** and the ionic additive **1[Li]** is shown in Scheme 1. Thus, a Steglich-type esterification of biphenyl-4-ol **2[n]** with 4-hexylbenzoic acid in the presence of dicyclohexylcarbodiimide (DCC) and catalytic amounts of 4-dimethylaminopyridine (DMAP) gave **LC[3]** and **LC[4]** in 77% and 61% yields, respectively, after chromatographic purification. Using the same reaction conditions, biphenyl-4-ol **2[n]** was esterified with acid [62] [*closo*-1-$CB_{11}H_{10}$-1-COOH-12-C_6H_{13}]$^-$[Et_4N]$^+$. Acidic workup of the reaction mixture gave the protonated form of the ester (**1[H]**), which was converted to the [Et_4N]$^+$ salt **1[Et$_4$N]** and purified by column chromatography. The ion pair was converted to the Li^+ salt **1[Li]** by removing the [Et_4N]$^+$ cation and then extracting the Li^+ salt from the aqueous to the CH_2Cl_2 layer.

The requisite biphenyl-4-ols **2[3]** and **2[4]** were obtained in 86% and 58% yield, respectively, by alkylation of 4,4′-dihydroxybiphenyl with appropriate tosylate **3[n]** [63,64] in the presence of one equivalent of *t*-BuOK (Scheme 2). This procedure was more efficient than the two-step method of alkylation of benzyl mono-protected 4,4′-dihydroxybiphenyl [65] (**4**) to form **5[3]** followed by reductive debenzylation in the presence of a Pd/C catalyst.

Electrolyte mixtures, **LC[3]–1[Li]5**, **LC[3]–1[Li]10**, and **LC[3]–1[Li]15** for impedance analysis containing 5, 10 and 15 mol% of salt **1[Li]** in host **LC[3]**, respectively, were prepared by dissolving exact amounts in CH_2Cl_2, followed by evaporation of the clear solutions and drying in *vacuo*.

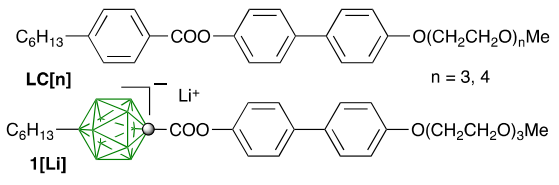

Fig. 1. Structures of the LC host and the ionic additive **1[Li]**. In the boron cage of **1[Li]** each unsubstituted vertex (green) is a BH fragment and the dot represents a carbon atom. (For interpretation of the references to color in this figure legend, the reader is referred to the web version of this article.)

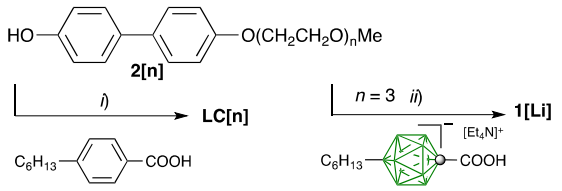

Scheme 1. Preparation of hosts **LC[n]** and additive **1[Li]**. Reagents and conditions: *i*) 1.2 eq. DCC, 0.2 eq. DMAP, CH_2Cl_2, rt, 18 h, yield 77% (**LC[3]**) and 61% (**LC[4]**); *ii*) 1. 1.2 eq. DCC, 0.2 eq. DMAP, CH_2Cl_2, rt, 18 h. 2. aq. HCl (10%), 3. LiOH/LiCl, H_2O/CH_2Cl_2, rt, yield 65%.

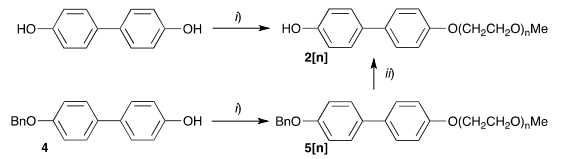

Scheme 2. Preparation of biphenyl-4-ols **2[n]**. Reagents and conditions: *i*) *t*-BuOK, $TsO(CH_2CH_2O)_nMe$ (**3[n]**), EtOH, yield 86% (**2[3]**), 58% (**2[4]**), 66% (**5[3]**); *ii*) H_2, Pd/C, AcOEt, rt, 18 h, 93% yield.

2.2. Liquid crystalline behavior

Mesogenic behavior of hosts **LC[n]** and mixtures **LC[3]–1[Li]x** was investigated with differential scanning calorimetry (DSC) and polarized optical microscopy[66,67] (POM). Results are shown in Table 1 and Figs. 2–4.

Compounds **LC[3]** and **LC[4]** exhibit two crystalline (Cr), smectic (Sm),[68] and nematic (N) phases with the overall higher mesophase stability for the former derivative (Table 1). Both compounds undergo a Cr–Cr transition at about 50 °C and melt to a smectic phase at 70 and 58 °C, respectively, as shown for **LC[3]** in Fig. 2. The enthalpy change at the Cr–Cr transition is substantial (about 30 kJ mol^{-1}, Table 1) and twice higher than that for the melting, which suggests a two–stage process: first melting of the coiled oligo(ethylene oxide) chains followed by melting of the aromatic cores. This is consistent with the fact that the Cr–Sm transition is reversible with a small hysteresis (about 8 K at a rate of 10 K min^{-1}), while the Cr–Cr transition is not observed on cooling (Fig. 2). The latter suggests freezing of the oligo(ethylene oxide) chains rather than their crystallization. Such a sequential melting to lamellar phases has been observed recently for compounds with incompatible rigid cores and alkyl chains [61,69].

The enantiotropic smectic phase was identified as a tilted smectic C (SmC) phase on the basis of its schlieren texture and also a fingerprint texture observed at the N–Sm transition in a slowly cooled

Table 1
Thermotropic properties of **LC[n]** and mixtures **LC[3]–1[Li]x**.[a]

Compound	Transition temperature (°C) and enthalpy (kJ mol^{-1})
LC[3] [b]	Cr_1 49(26.9) Cr_2 70(14.1) (SmI 69)[c] SmC 80(4.3) N 117(0.9) I
LC[4] [b]	Cr_1 53(33.6) Cr_2 58(13.3) SmC 60(5.1) N 91(0.4) I
LC[3]–1[Li]x [d]	
x = 5	Cr 68 SmA 102 N 114 I
x = 10	Cr_1 43 Cr_2 61 SmA 110 N 116 I
x = 15	Cr 44 SmA 116 (N 115)[c] I

[a] Cr–crystalline phase, SmA, SmC, SmI–smectic phases, N–nematic, I–isotropic phase.
[b] Peak of the transition recorded on the first heating at 10 K min^{-1}; enthalpy in kJ mol^{-1} (in parentheses).
[c] Monotropic transition.
[d] Peak of the transition recorded on the second heating at 10 K min^{-1}.

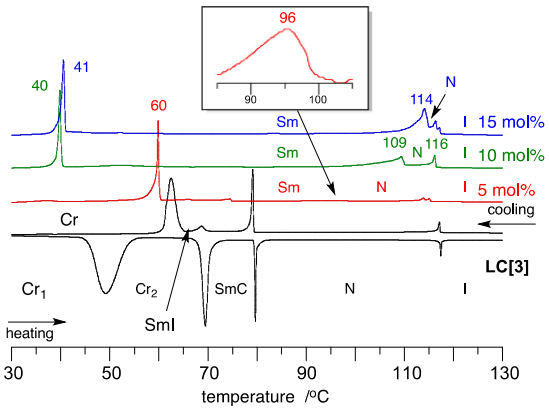

Fig. 2. DSC trace of the host **LC[3]** (black), obtained on first heating and cooling cycle, and mixtures with **1[Li]**: 5 mol% (red), 10 mol% (green) and 15 mol% (blue) obtained on second cooling after the 25 → 180 → 25 → 180 °C cycle (10 K min^{-1}). (For interpretation of the references to color in this figure legend, the reader is referred to the web version of this article.)

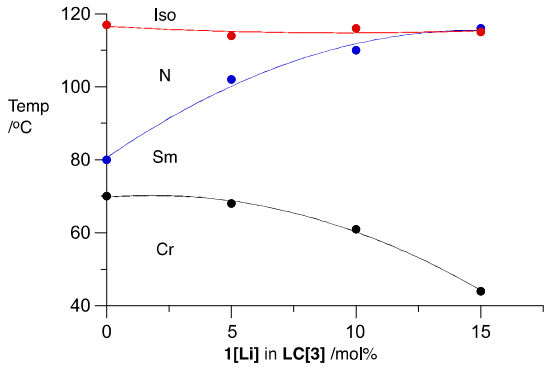

Fig. 4. Partial phase diagram of **1[Li]** and **LC[3]** obtained on second heating (See Table 1).

sample without the top cover (Fig. 3b). The narrow range SmC phase (10 K for **LC[3]** and 2 K for **LC[4]**) is followed by a nematic phase and clearing to the isotropic phase at 117 and 91 °C, respectively. The cooling cycle revealed a narrow monotropic phase below the SmC phase only for **LC[3]** (Fig. 2). The schlieren texture suggests a smectic I (SmI) phase as shown in Fig. 3c. Overall, higher mesophase stability and a broader smectic phase observed in **LC[3]** suggested it as a more suitable host for the ionic additive **1[Li]**.

Addition of the ion pair **1[Li]** to **LC[3]** converts the SmC phase in pure **LC[3]** to a smectic A (SmA) phase, as evident from the homeotropic texture of the sample without the top cover glass [70]. Increasing concentration of the ionic additive progressively expands the smectic phase range at the expense of the N phase, as shown in a partial phase diagram in Fig. 4. For 15 mol% of **1[Li]**, the nematic phase is nearly fully replaced with a SmA phase with a narrow range (1 K) monotropic nematic phase.

2.3. Powder XRD analysis

The formation of SmC in pure hosts **LC[3]** and **LC[4]**, and SmA in solutions of **1[Li]** in **LC[3]** were confirmed with powder X-ray diffraction methods (PXRD). Results are shown in Figs. 5 and 6.

Diffraction patterns obtained for the smectic C phase in **LC[3]** and **LC[4]** were typical for a fluid lamellar phase, consisting of a set of sharp, commensurate signals in the small angle region and a broad diffused high angle signal (Fig. 5). The transition to a hexatic phase below the SmC phase in **LC[3]** was accompanied by a considerable narrowing of the high angle diffraction signal due to the growing correlation length of in-plane positional order. The equatorial position of the high-angle signal, with respect to layer reflections, strongly suggests a SmI phase, in which the molecules are tilted to the nearest neighbour. Unfortunately, full characterization of the phase was hampered by its metastable nature and partial crystallization during the measurements. In addition, the temperature dependence of the layer spacing *d* shows an S–like shape, which is typical for the SmC–hexatic phase transition (Fig. 6).

XRD patterns for the smectic A phase of the electrolyte mixtures were qualitatively the same as those taken for SmC phase of the pure host (Fig. 5). However the low angle signal position indicated a considerably higher layer spacing of about 33 Å in all mixtures vs about 26 Å in the pure host. This observed larger layer spacing might be attributed to the orthogonal character of the smectic phase in the mixtures and also to a reorganization of the tri(ethylene oxide) layer resulting from coordination of the Li^+ ions with at least partial incorporation of the *closo*-borate fragment into the ionic layer. Analysis of temperature dependence of the layer spacing *d* revealed the appearance of an additional diffraction signal at

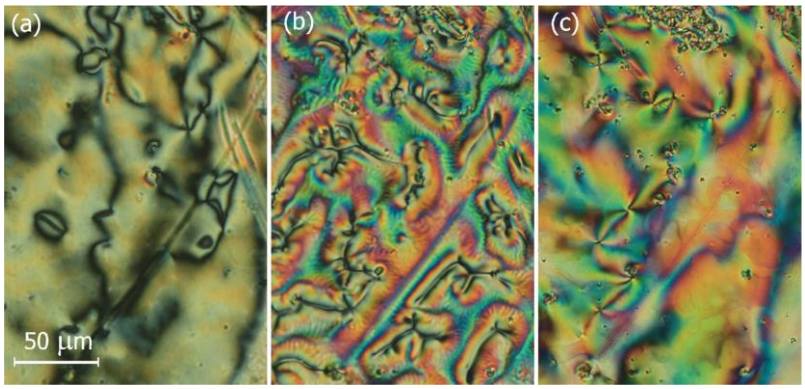

Fig. 3. Optical textures obtained on cooling and observed in polarized light for the same sample region of **LC[3]**: a) nematic phase at 90 °C, b) SmC phase just below N–SmC transition at 79 °C, c) hexatic SmI at 68 °C.

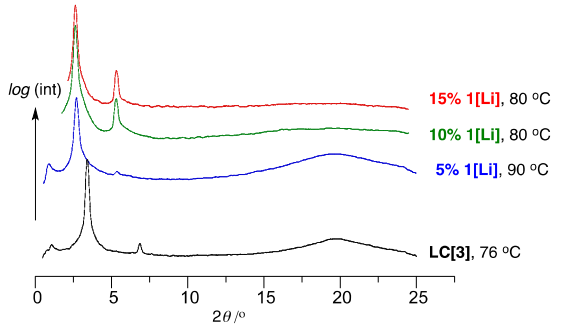

Fig. 5. Powder XRD patterns for smectic phases in **LC[3]** (bottom) and mixtures **LC[3]–1[Li]x**.

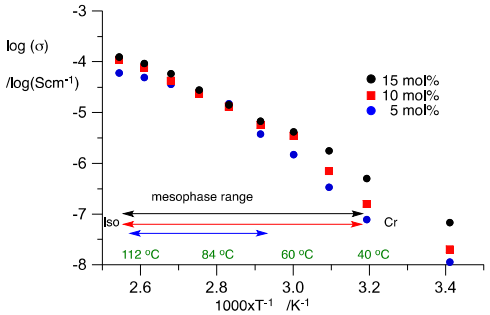

Fig. 7. Temperature dependent Li^+ conductivity obtained by the EIS method in 10 K steps from 20 °C to 120 °C.

76 °C for 5 mol% and at 53 °C for 10 mol% mixture (Fig. 6 and the SI), whose position coincides with that for the SmC phase of the pure host [70]. This observation suggests a macroscopic phase separation at lower temperatures, which narrows the range of homogeneous solutions for reliable characterization by impedance spectroscopy.

2.4. Impedance spectroscopy

Ionic conductivity σ was measured for unaligned samples of **1[Li]** in non-ionic **LC[3]** in the temperature range of 20–120 °C and for three concentrations, 5, 10, and 15 mol% (approximately 0.1, 0.2, and 0.3 M, respectively) by an Electrochemical Impedance Spectroscopy (EIS) method. Results in Fig. 7 demonstrate that conductivity σ increases monotonically in the entire temperature range from crystalline, through SmA to the nematic phase for all three concentrations of ionic additive **1[Li]**. Importantly, above 110 °C the conductivity reaches 0.1 mS cm^{-1}, which is in a range of interest for practical applications. The observed trends in logσ (T^{-1}) are consistent with those for Li^+ salts with small anions, such as ClO_4^-, up to about 0.5 M solutions [71–73], above which ionic conductivity typically decreases by up to an order of magnitude in liquid crystal [18] and ionic liquid [74,75] solutions.

Detailed analysis of the conductivity data demonstrated that solutions with higher concentrations generally have higher conductivity. The only exception is the region of the SmA phase between 80 °C and 90 °C, in which the 10 mol% mixture, **LC[3]–1[Li]10**, surprisingly has lower conductivity than that of the 5 mol % solution, **LC[3]–1[Li]5** (Fig. 7). Regardless of the phase type, the ratio of ionic conductivity σ of the 15 mol% vs. the 10 mol% mixture is in a range of 1.15 to 1.4 at temperatures above 60 °C. The analogous ratio of conductivity for the 10 mol% to the 5 mol% solution is much higher (up to 1.78), except for 80 °C and 90 °C, at which the ratio is below 1.0 (0.87 and 0.96, respectively). This observation indicates anomalous behavior of the 5 mol% mixture (**LC[3]–1[Li]5**), which may be related to phase segregation taking place just below 80 °C.

Further analysis of the electrolyte solutions focused on the activation energy (E_{aIC}) of the conductivity process in each phase determined by Arrhenius analysis of lnσ(T^{-1}) plots, as shown for 10 mol% solution **LC[3]–1[Li]10** in Fig. 8. A limited number of datapoints allowed only for estimates, which are tabularized in Fig. 8, and which permit a semi-quantitative discussion. Thus, the E_{aIC} for the nematic phase was determined only for the 5 mol% solution, and E_{aIC} for the SmA and crystalline phases could reliably be obtained for 10 and 15 mol% solutions. Analysis of the data demonstrates that the activation energy E_{aIC} increases from the nematic phase (32 ± 3 kJ mol^{-1} for **LC[3]–1[Li]5**) through the SmA phase to the highest in the crystalline phase, which was expected on the basis of increasing organization of the phase and, consequently, its viscosity. The E_{aIC} values determined for the SmA phase in the two high concentration solutions are about 70 kJ mol^{-1}, which are significantly higher than the estimated E_{aIC} of 56 kJ mol^{-1} for the 5 mol% solution, **LC[3]–1[Li]5**. This indicates again anomalous behavior of the 5 mol% solution.

The generally high E_{aIC} values in the **LC[3]–1[Li]x** system, especially in the crystalline phase, are responsible for the observed steep, by over two orders of magnitude increase of conductivity σ in a 40 K range (20 °C to 60 °C). Such a high E_{aIC} value in the

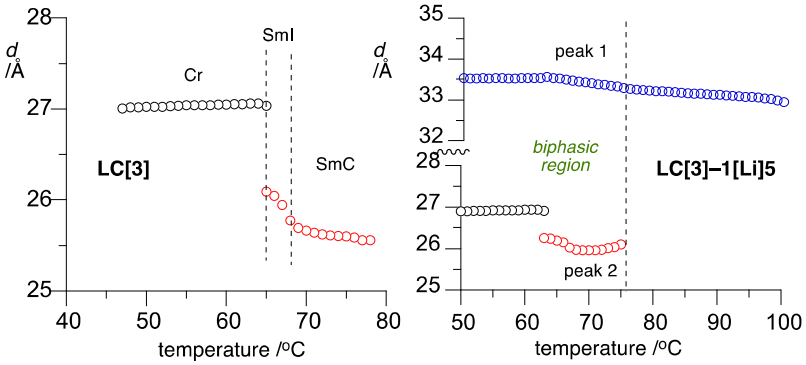

Fig. 6. Temperature dependence of the layer spacing *d* for **LC[3]** (left) and mixture **LC[3]–1[Li]5** (right). The vertical dotted line on the right indicates phase separation.

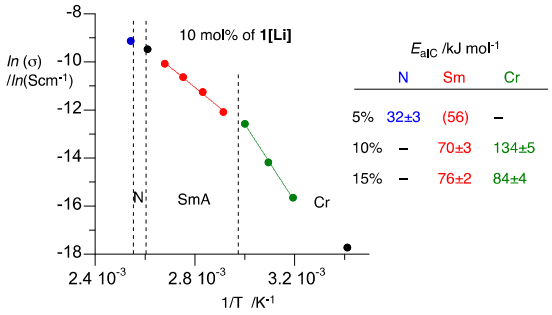

Fig. 8. Left: Arrhenius analysis of conductivity of 10 mol% solution **LC[3]–1[Li]10**: nematic phase (blue), SmA phase (red), crystalline phase (green), points not used for analysis (black, blue). Right: calculated activation energy E_{aIC} for all three concentrations. Details are provided in the SI. (For interpretation of the references to color in this figure legend, the reader is referred to the web version of this article.)

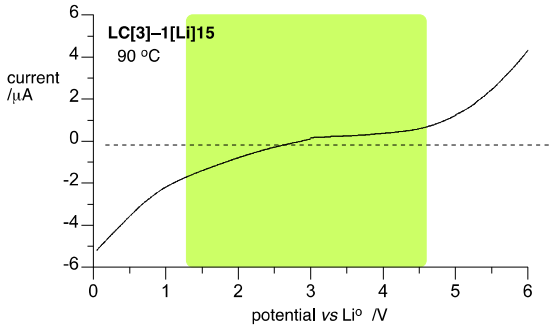

Fig. 9. Linear sweep voltammogram (LSV) of 15 mol% **1[Li]** in **LC[3]** at 90 °C. The shaded area indicates the electrochemical window of compatibility with the Li metal anode.

crystalline phases is typical for solid polymer electrolytes and polymerized ionic liquids [76,77], while E_{aIC} values in a range of 70 kJ mol^{-1} observed for the smectic phase are typical for ionic liquid and liquid polymer electrolytes [75,78].

Analysis of the E_{aIC} values for the SmA phase shows an increasing trend with increasing concentration of the Li^+ salt, which suggests an increasing order of the ionic layer. Support for this assertion is provided by the XRD results, which demonstrate higher intensity of the first harmonic reflection in the SmA phase for higher concentration solutions (Fig. 5). The observed relatively small increase in conductivity σ and in the E_{aIC} values (vide supra) between 10 and 15 mol% (relatively to 5 vs 10 mol%) indicates that the system is close to an optimum concentration for obtaining a homogeneous, broad temperature range mesophase. This may also suggest that a further increase in concentration may not result in a substantial increase in ionic conductivity.

Changes in the E_{aIC} values observed between the crystal and SmA phases provide an additional insight into the structure of the conductive layer. Thus, the decrease in E_{aIC} is much bigger for the 10 mol% mixture (ΔE_{aIC} = –64 kJ mol^{-1}) than for the 15 mol% solution (ΔE_{aIC} = –8 kJ mol^{-1}). The small change for the latter solution is due to the already low activation barrier for ion conduction in the crystalline phase. This observation suggests that the optimum concentration of Li^+ ions is achieved with about 15 mol%, and the structure of the conductive layer, consisting of about 6 tri(ethylene oxide) chains per Li^+ ion in the crystalline phase, more closely resembles that in the smectic A layer. Consistent with this suggestion is the observed in the series diminishing tendency of the solutions to macrosegregate the pure host **LC[3]**, as perhaps a way to achieve this favorable ratio of **1[Li]** to **LC[3]** (at 76 °C for 5 mol%, at 54 °C for 10 mol%, and none for 15 mol% mixture, vide supra).

Finally, electrochemical stability window for the 15 mol% solution **LC[3]–1[Li]15** at 90 °C (SmA phase) was assessed by Linear Sweep Voltammetry (LSV) using a Li° | electrolyte | Pt° cell. Reduction and oxidation limits were obtained for independent samples starting the sweep at 3 V vs the Li° anode (Fig. 9). Experiments demonstrated that the stability window for **LC[3]–1[Li]15** at 90 °C spans from 1.3 to 4.6 V vs Li° anode (Fig. 9), which suggests good compatibility with most Li^+ ion electrodes. This stability window compares favourably to that of solid solutions of [*closo*-1-CB_9H_{10}]$^-$$Li^+$ and [*closo*-$B_{12}H_{12}$]2$^-$ 2Li^+ salts (up to 5 V vs Li° anode),[54,55] and to a similar solid solution of [*closo*-1-$CB_{11}H_{12}$]$^-$$Li^+$ and [*closo*-1-CB_9H_{10}]$^-$$Li^+$ salts, which exhibits electrochemical stability only up 2.9 V vs Li° anode.[56,57] This latter result suggests lower electrochemical stability of the [*closo*-1-$CB_{11}H_{12}$]$^-$ anion than the two other *closo*-borane anions and reported here **LC[3]–1[Li]15**.

3. Conclusions

We have demonstrated a new approach to anisotropic electrolytes by using a non-ionic LC host and ionic additive with the anion structurally similar to the host and comprising of the appropriately substituted [*closo*-1-$CB_{11}H_{12}$]$^-$ cluster. Experiments show that such a host–ion additive system exhibits good compatibility: the additive essentially does not affect thermal stability of the mesophase, it expands the range of the lamellar phase, and a homogenous solution with concentrations up to 15 mol% (~0.3 M solutions) can be obtained. This represents a promising direction in electrolyte formulations.

Impedance spectroscopy revealed favourable electrochemical properties of unaligned samples of the electrolyte solutions: the ion conductivity generally increases with increasing concentration and with increasing temperatures reaching the range of about 0.1 mS cm^{-1}. It is expected that aligned samples will exhibit much higher conductivities with significant anisotropy. For these reasons such systems are promising for obtaining practical materials after alignment and additional molecular optimizations. Further analysis demonstrated that the activation energy of the ion conduction, E_{aIC}, in unaligned samples is about 70 kJ mol^{-1} in the SmA phase, which is similar to ionic liquid and polymeric electrolytes.

Structures optimization, alignment of the smectic phases, and preparation of anisotropic polymers are underway.

4. Experimental section

4.1. General procedures

Reagents and solvents were obtained commercially. Toluene, THF, and CH_2Cl_2 used in reactions were passed through alumina in a solvent purification system after drying according to established procedures [79]. Acid [*closo*-1-$CB_{11}H_{10}$-1-COOH-12-C_6H_{13}]$^-$[Et_4N]$^+$ [62], tosylates TsO(CH_2CH_2O)$_n$Me [63] (**3[n]**), and 4′-(benzyloxy)biphenyl-4-ol [65] (**4**) were synthesized according to the literature. Reactions were performed in an inert-gas atmosphere (balloons) using oven-dried glassware. Workups were done in air. Heat for reactions requiring elevated temperatures was supplied using oil baths. NMR spectra were recorded on a Bruker AV III 400 or a AV III 500 spectrometer in $CDCl_3$, CD_2Cl_2 or DMSO d_6. ^{1}H and ^{13}C NMR chemical shifts were internally referenced to the

solvent signals ($CDCl_3$: δ_H 7.26 ppm, δ_C 77.16 ppm; CD_2Cl_2: δ_H 5.32 ppm, δ_C 53.84 ppm; DMSO d_6: δ_H 2.50 ppm, δ_C 39.52 ppm) [80] and for ^{7}Li and ^{11}B NMR spectra using external references, LiCl in D_2O and $BF_3{\cdot}Et_2O$, respectively, set to δ = 0.0 ppm. Melting points were determined on a Stuart SMP30 Melting Point Apparatus and are uncorrected.

4.2. Preparation of 4-(4-hexylbenzoyloxy)-4′-[2-(2-(2-methoxyethoxy)ethoxy)ethoxy]biphenyl (LC**[3]**)

To a solution of biphenyl-4-ol **2[3]** (0.838 g, 2.52 mmol, 1.0 eq.) and 4-hexylbenzoic acid (0.624 g, 3.03 mmol, 1.2 eq.) in CH_2Cl_2 (30 mL) were added dicyclohexylcarbodiimide (DCC, 0.624 g, 3.03 mmol, 1.2 eq.) and *N,N*-dimethylaminopyridine (DMAP, 0.062 g, 0.50 mmol, 0.2 eq.). The clear solution turned to a white suspension after 30 min. It was stirred for 18 h until thin layer chromatography (TLC) indicated the absence of the starting **2[3]**. The suspension was filtered and the volatiles were removed in *vacuo*. The residue was separated by column chromatography (SiO_2, pet. ether/EtOAc 3:2) and the product was dried in vacuo giving 1.012 g (1.94 mmol, 77% yield) of **LC[3]** as a colorless solid, which was purified further by recrystallization (*i*-PrOH): ^{1}H NMR (400 MHz, $CDCl_3$) δ 8.13 (d, *J* = 7.9 Hz, 2H), 7.58 (d, *J* = 8.3 Hz, 2H), 7.51 (d, *J* = 8.4 Hz, 2H), 7.32 (d, *J* = 7.8 Hz, 2H), 7.25 (d, *J* = 8.1 Hz, 2H), 6.99 (d, *J* = 8.4 Hz, 2H), 4.18 (t, *J* = 4.9 Hz, 2H), 3.89 (t, *J* = 4.4 Hz, 2H), 3.79–3.65 (m, 6H), 3.59–3.54 (m, 2H), 3.38 (s, 3H), 2.70 (t, *J* = 7.7 Hz, 2H), 1.66 (quint, *J* = 7.9 Hz, 2H), 1.40–1.28 (m, 6H), 0.89 (t, *J* = 6.4 Hz, 3H) ppm. ^{13}C{^{1}H} NMR (100 MHz, $CDCl_3$) δ 165.5, 158.5, 150.1, 149.5, 138.6, 133.3, 130.4, 128.8, 128.2, 127.8, 127.1, 122.1, 115.1, 72.1, 71.0, 70.8, 70.7, 69.9, 67.6, 59.2, 36.2, 31.8, 31.2, 29.0, 22.7, 14.2 ppm. HRMS ESI(+) *m*/*z* calcd. for $C_{32}H_{41}O_6$ [M + H]$^+$: 521.2903, found: 521.2895. Anal. Calcd. for $C_{32}H_{40}O_6$: C, 73.82; H, 7.74. Found: C, 74.05; H, 7.81 %.

4.3. Preparation of 4-(4-hexylbenzoyloxy)-4′-(2-(2-(2-(2-methoxyethoxy)ethoxy)ethoxy)ethoxy)biphenyl (***LC[4]***)

The ester was prepared following the procedure for **LC[3]** using **2[4]** (0.251 g, 0.67 mmol, 1.0 eq.), 4-hexylbenzoic acid (0.165 g, 0.80 mmol, 1.2 eq.), DCC (0.165 g, 0.80 mmol, 1.20 eq.) and DMAP (0.016 g, 0.13 mmol, 0.2 eq.). Crude product was purified by column chromatography (SiO_2, pet. ether/EtOAc 2:3) giving 0.234 g (0.41 mmol, 61% yield) of **LC[4]** as a microcrystalline solid, which further recrystallized (*i*-PrOH):): ^{1}H NMR (400 MHz, $CDCl_3$) δ 8.13 (d, *J* = 8.1 Hz, 2H), 7.58 (d, *J* = 8.5 Hz, 2H), 7.51 (d, *J* = 8.4 Hz, 2H), 7.32 (d, *J* = 8.1 Hz, 2H), 7.25 (d, *J* = 8.3 Hz, 2H), 6.99 (d, *J* = 8.5 Hz, 2H), 4.18 (t, *J* = 4.4 Hz, 2H), 3.89 (t, *J* = 4.4 Hz, 2H), 3.78–3.63 (m, 10*H*), 3.57–3.53 (m, 2H), 3.38 (s, 3H), 2.70 (t, *J* = 7.6 Hz, 2H), 1.66 (q, *J* = 7.3 Hz, 2H), 1.38–1.28 (m, 6H), 0.89 (t, *J* = 6.8 Hz, 3H) ppm. ^{13}C{^{1}H} NMR (100 MHz, $CDCl_3$) δ 165.5, 158.5, 150.1, 149.5, 138.6, 133.3, 130.4, 128.8, 128.2, 127.8, 127.0, 122.1, 115.1, 72.1, 71.0, 70.8 (3C), 70.7, 69.9, 67.6, 59.2, 36.2, 31.8, 31.2, 29.0, 22.7, 14.2 ppm. HRMS ESI(+) *m*/*z* calcd. for $C_{34}H_{45}O_7$ [M + H]$^+$: 565.3165, found: 565.3174. Anal. Calcd. for $C_{34}H_{44}O_7$: C, 72.31; H, 7.85. Found: C, 72.26; H, 7.89 %.

4.4. Preparation of [4-(12-C6H13CB11H10-1-COO)-4′-(2-(2-(2-methoxyethoxy)ethoxy)ethoxy)biphenyl]$^-$[Li]$^+$ (***1[Li]***)

The ester was prepared following the procedure for **LC[3]** using biphenyl-4-ol **2[3]** (0.301 g, 0.906 mmol, 1.0 eq.), acid [*closo*-1-$CB_{11}H_{10}$-1-COOH-12-C_6H_{13}]$^-$[NEt_4]$^+$ [62] (0.490 g, 1.00 mmol, 1.1 eq.), DCC (0.224 g, 1.09 mmol, 1.2 eq.) and DMAP (0.022 g, 0.18 mmol, 0.2 eq.). After 18 h the reaction mixture was filtered and the volatiles were removed in *vacuo*. The residue was separated by column chromatography (SiO_2, CH_2Cl_2/MeCN 9:1), the product was dried in *vacuo* and the resulting sticky oily **1[Et$_4$N]** (0.864 mg) was treated with 10% HCl (50 mL). The acidic form of the ester **1[H]** was extracted with Et_2O (1 × 100 mL, then 3 × 50 mL). A solution of LiOH (0.022 g, 0.91 mmol, 1.0 eq.) and LiCl (0.038 g, 0.91 mmol, 1.0 eq.) in H_2O (50 mL) was added to the combined organic layers. After addition of CH_2Cl_2 (50 mL), all organic volatiles were removed with a rotary evaporator. The obtained aqueous phase was extracted with CH_2Cl_2 (3 × 50 mL) and the organic layers were concentrated under reduced pressure. The resulting sticky solid was diluted in a minimum amount of CH_2Cl_2 upon which pet. ether was carefully layered. After 18 h a colorless precipitate was filtered, washed with pet. ether (10 mL) and dried in *vacuo* giving 0.348 mg (5.87 mmol, 65% yield) of **1[Li]** as a white microcrystalline powder: ^{1}H NMR (400 MHz, CD_2Cl_2) δ 7.37 (d, *J* = 8.5 Hz, 2H), 7.31 (d, *J* = 8.6 Hz, 2H), 6.96 (d, *J* = 8.6 Hz, 2H), 6.81 (d, *J* = 8.7 Hz, 2H), 4.17 (t, *J* = 4.6 Hz, 2H), 3.92 (t, *J* = 4.1 Hz, 2H), 3.81 (t*, 2H), 3.73 (t*, 2H), 3.67 (t*, 2H), 3.59 (t*, 2H), 3.24 (s, 3H), 1.90–1.10 (m, 18H), 0.86 (t, *J* = 6.8 Hz, 3H), 0.55 (t, *J* = 8.2 Hz, 3H) ppm (*poorly resolved triplet). ^{13}C{^{1}H} NMR (100 MHz, CD_2Cl_2) δ 170.2, 157.8, 150.5, 138.4, 134.1, 128.6, 127.9, 121.9, 115.4, 71.4, 69.5, 69.4 (2C), 69.2, 67.9, 59.4, 33.9, 33.4, 32.5, 30.8, 23.2, 14.4 ppm (signal for the carborane C nucleus was not observed). ^{11}B NMR (128.4 MHz, CD_2Cl_2) δ 4.8 (bs, 1B), –12.4 (d, *J* = 136 Hz, 5B), –14.8 (d, *J* = 126 Hz, 5B) ppm. ^{7}Li NMR (194 MHz, CD_2Cl_2) δ –0.5 (s) ppm. HRMS ESI(-) *m*/*z* calcd. for $C_{27}H_{46}B_{11}$ M$^-$: 587.4318, found: 587.4368. Anal. Calcd. for $C_{27}H_{46}O_6B_{11}Li$: C, 54.73; H, 7.83. Found: C, 54.68; H, 7.92 %.

4.5. Preparation of 4′-(2-(2-(2-methoxyethoxy)-ethoxy)ethoxy) biphenyl-4-ol (***2[3]***)

Method A. A mixture of 4,4′-dihydroxybiphenyl (0.279 g, 1.50 mmol 1.0 eq.) and KOtBu (0.185 g, 1.65 mmol, 1.1 eq.) in dry EtOH (30 mL) was heated to reflux under Ar for 30 min. to form a green solution. 2-(2-(2-Methoxyethoxy)ethoxy)ethyl tosylate [63] (**3[3]**, 0.500 g, 1.57 mmol, 1.1 eq.) was added at ambient temperature. The reaction mixture was heated at reflux for 18 h during which the green color vanished. After removing the solvent under reduced pressure, 10% aq HCl (20 mL) was added to the residue and the mixture was extracted with CH_2Cl_2 (3 × 20 mL). The solvent was evaporated and the residue was separated by column chromatography (SiO_2, CH_2Cl_2/EtOAc 2:1). After drying in vacuo the resulting oily product **2[3]** crystallized as a colorless solid (0.426 mg, 86% yield, 1.28 mmol). Further purification of **2[3]** was accomplished by carefully layering pet. ether on a saturated solution in Et_2O and slow diffusion overnight to yield colorless crystals: mp 34 °C. ^{1}H NMR (400 MHz, $CDCl_3$) δ 7.35 (d, *J* = 8.7 Hz, 2H), 7.33 (d, *J* = 8.6 Hz, 2H), 6.89 (d, *J* = 8.5 Hz, 2H), 6.85 (d, *J* = 8.6 Hz, 2H), 6.21 (bs, 1H), 4.06 (t, *J* = 4.9 Hz, 2H), 3.85 (t, *J* = 4.8 Hz, 2H), 3.78–3.67 (m, 6H), 3.61–3.57 (m, 2H), 3.38 (s, 3H) ppm. ^{13}C{^{1}H} NMR (100 MHz, $CDCl_3$) δ 157.7, 155.4, 133.7, 132.9, 127.8, 127.6, 115.8, 114.8, 71.9, 70.8, 70.7, 70.5, 69.9, 67.3, 59.0 ppm. HRMS ESI(+) *m*/*z* calcd. for $C_{19}H_{25}O_5$ [M + H]$^+$: 333.1702, found: 333.1713. Anal. Calcd. for $C_{19}H_{24}O_5$: C, 68.66; H, 7.28. Found: C, 68.71; H, 7.32 %.

Method B. 10% Pd/C (20 mg) was added to a solution of benzyloxy derivative **5[3]** (0.200 mg, 0.47 mmol) in 6 mL of EtOAc and the mixture was equipped with a H_2 filled balloon connected via a rubber septum. The mixture was stirred for 18 h at ambient temperature. The catalyst was removed by filtration through Celite® (washed with 10 mL of EtOAc), the volatiles were removed from the filtrate by rotary evaporator and the residue was purified by column chromatography (SiO_2, EtOAc/hexane 3:2). The product **2[3]** was obtained as a colorless oil, which slowly solidified during drying in vacuo overnight (0.141 g, 0.37 mmol, 90%).

*4.6. Preparation of 4′-(2-(2-(2-(2-methoxyethoxy)ethoxy)-ethoxy) ethoxy)biphenyl-4-ol (**2[4]**) [81]*

The phenol was obtained according to method A for the preparation of **2[3]** using 4,4′-dihydroxybiphenyl (0.245 g, 1.31 mmol 1.0 eq.), KOtBu (0.162 g, 1.45 mmol, 1.1 eq.), $MeO(CH_2CH_2O)_4Ts$ [63] (**3[4]**, 0.500 g, 1.38 mmol, 1.1 eq.). The crude product was purified using column chromatography (SiO_2, CH_2Cl_2/EtOAc 2:1) giving 0.289 mg (0.77 mmol, 58% yield) of **2[4]** as a viscous oil. Product was purified further by a second column chromatography (SiO_2, CH_2Cl_2/MeCN 3:4): ^{1}H NMR (400 MHz, $CDCl_3$) δ 7.35 (d, *J* = 9.2 Hz, 2H), 7.33 (d, *J* = 9.6 Hz, 2H), 6.89 (d, *J* = 8.5 Hz, 2H), 6.85 (d, *J* = 8.6 Hz, 2H), 6.1 (bs, 1H), 4.06 (t, *J* = 4.8 Hz, 2H), 3.84 (t, *J* = 4.8 Hz, 2H), 3.76–3.61 (m, 10*H*), 3.56–3.51 (m, 2H), 3.36 (s, 3H) ppm. ^{13}C{^{1}H} NMR (100 MHz, $CDCl_3$) δ 157.7, 155.6, 133.7, 132.7, 127.8, 127.5, 115.8, 114.8, 71.9, 70.8, 70.7, 70.6 (2C), 70.5, 69.8, 67.4, 59.0 ppm. HRMS ESI(+) *m/z* calcd. for $C_{21}H_{29}O_6$ $[M + H]^+$: 377.1964, found: 377.1969. Anal. Calcd. for $C_{21}H_{28}O_6$: C, 67.00; H, 7.50. Found: C, 66.88; H, 7.51 %.

*4.7. Preparation of 4-(benzyloxy)-4′-(2-(2-(2-methoxy-ethoxy) ethoxy)ethoxy)biphenyl (**5[3]**)*

A mixture of 4′-benzyloxybiphenyl-4-ol [65] (**4**, 0.950 g, 3.48 mmol, 1.0 equiv.) and KOtBu (0.424 g, 3.68 mmol, 1.1 eqiv.) in dry EtOH (20 mL) was refluxed for 30 min. The colorless solution was cooled and a solution of tosylate **3[3]** [63] (1.095 g, 3.44 mmol, 1.0 equiv.) in EtOH (10 mL) was added. The reaction mixture was refluxed for 18 h, cooled and treated with 10% HCl (30 mL). Removing all volatiles with rotary evaporator resulted in a suspension that was extracted into CH_2Cl_2 (3 × 50 mL). After evaporating the solvent, the crude product was separated by column chromatography (SiO_2, CH_2Cl_2/EtOAc 95:5). Product **5[3]** was obtained in 66% yield (0.959 g, 2.27 mmol) as a colorless solid after drying in vacuo: mp 117–119 °C. ^{1}H NMR (DMSO d_6, 500 MHz) δ 7.55–7.51 (m, 4H), 7.47 (d, *J* = 7.4 Hz, 2H), 7.40 (t, *J* = 7.4 Hz, 2H), 7.33 (t, *J* = 7.4 Hz, 1H), 7.06 (d, *J* = 8.8 Hz, 2H), 6.98 (d, *J* = 8.8 Hz, 2H), 5.14 (s, 2H), 4.11 (t, *J* = 4.5 Hz, 2H), 3.75 (t, *J* = 4.5 Hz, 2H), 3.60–3.49 (m, 6H), 3.42 (t, *J* = 4.5 Hz, 2H), 3.23 (s, 3H) ppm. ^{13}C{^{1}H} NMR (DMSO d_6, 125.75 MHz) δ 157.6, 157.4, 137.2, 132.5, 132.3, 128.5, 127.8, 127.7, 127.2 (2C), 115.2, 114.8, 71.3, 70.0, 69.8, 69.6, 69.2, 69.0, 67.2, 58.1 ppm. Anal. Calcd. for $C_{26}H_{30}O_5$: C, 73.91; H, 7.16. Found: C, 74.19; H, 6.99 %.

4.8. Impedance spectroscopy

Temperature dependent measurements of ionic conductivity have been performed by Electrochemical Impedance Spectroscopy (EIS) in a temperature rage of 20 120 °C. Samples of electrolytes were prepared in air and transferred to an argon-filled MBraun glovebox with less than 1 ppm of both moisture and oxygen content. Mixtures were placed between two stainless steel electrodes and sandwiched to form a cell. Before the measurements the mixtures were melted (>120 °C) to fill in the whole space between the electrodes. Cells were sealed under argon atmosphere into air-tight Swagelok-type tubes and sealed additionally with Parafilm.

Electrolyte samples geometry was measured with a 0.5% precision and calculated cell constants were in the 0.02–0.08 cm-1 range. The cells were placed in a cryostat-thermostat system (Haake K75 with a DC50 temperature controller) and thermostated for at least one hour for each temperature, until the sample resistances have stabilized. The sample temperature was stabilized with the accuracy of ± 0.05 K. All impedance measurements were carried out on the computer-interfaced multichannel potentiostat with frequency response analyzer option Bio-Logic Science Instruments VMP3 within 500 kHz–1 Hz frequency range with 10 points per decade and 5 mV A.C. signal amplitude. Measurements were repeated at least three times for each concentration for consistency. Details of Arrhenius analysis of the conductivity process are provided in the SI.

Linear Sweep Voltammetry (LSV) was performed using Biologic Science Instruments VMP3 module and a Li^o | electrolyte | Pt^o cell with lithium metal as the reference. The sweep rate was 1 mV s^{-1}.

4.9. Powder XRD data

Broad angle X-ray diffraction studies were performed with Bruker D8 GADDS system consisting of a sealed tube with copper anode as a radiation source, Göbel mirror monochromator and pinhole collimator forming parallel beam of Cu Kα radiation, modified Linkam heating stage and Vantec 2000 area detector. In order to precisely determine temperature dependence of smectic layer thickness, small angle diffraction experiments were executed with Bruker D8 Discover system (Cu Kα radiation, Göbel mirror, Anton Parr DCS350 heating stage, scintillation counter). Samples for both type experiments were prepared in a form of a droplet or a thin film on a heated surface, and the X-ray beam was incident nearly parallel to the sample surface.

Data availability

Data will be made available on request.

Declaration of Competing Interest

The authors declare that they have no known competing financial interests or personal relationships that could have appeared to influence the work reported in this paper.

Acknowledgements

Support for this project was provided by the Foundation for Polish Science (TEAM/2016-3/24) and European Space Agency (NPI 542) grants. The authors thank Dr. Brian Ringstrand for his technical assistance.

Appendix A. Supplementary data

Supplementary data to this article can be found online at https://doi.org/10.1016/j.molliq.2023.121525.

References

[1] J. Kalhoff, G.G. Eshetu, D. Bresser, S. Passerini, ChemSusChem. 8 (2015) 2154–2175.
[2] E. Quartarone, P. Mustarelli, J. Electrochem. Soc. 167 (2020) 050508.
[3] K. Xu, Chem. Rev. 114 (2014) 11503–11618.
[4] J., Ma Liquid Electrolyte Chemistry for Lithium Metal Batteries: Design, Mechanisms, Strategies, Wiley-VCH, 2022.
[5] Z. Xue, D. He, X. Xie, J. Mater. Chem. A. 3 (2015) 19218–19253.
[6] K. Chen, D. Xue, J. Mater. Chem. A. 4 (2016) 7522–7537.
[7] D. Zhou, D. Shanmukaraj, A. Tkacheva, M. Armand, G. Wang, Chem. 5 (2019) 2326–2352.
[8] M. Armand, P. Axmann, D. Bresser, M. Copley, K. Edström, C. Ekberg, D. Guyomard, B. Lestriez, P. Novák, M. Petranikova, W. Porcher, S. Trabesinger, M. Wohlfahrt-Mehrens, H. Zhang, J. Power Sourc. 479 (2020).
[9] Electrolytes for Lithium and Lithium-Ion Batteries; T.R. Jow, K. Xu, O. Borodin, M. Ue, Eds.; Springer: New York, 2014; Vol. 58.
[10] N.-S. Choi, Z. Chen, S.A. Freunberger, X. Ji, Y.-K. Sun, K. Amine, G. Yushin, L.F. Nazar, J. Cho, P.G. Bruce, Angew. Chem. Int. Ed. 51 (2012) 9994–10024.
[11] K. Goossens, K. Lava, C.W. Bielawski, K. Binnemans, Chem. Rev. 116 (2016) 4643–4807.
[12] K.V. Axenov, S. Laschat, Materials. 4 (2011) 206–259.
[13] J. Uchida, B. Soberats, M. Gupta, T. Kato, Adv. Mater. (2022) 2109063.
[14] B.-K. Cho, RSC Adv. 4 (2014) 395–405.

[15] M. Yoshio, T. Kato, Liquid crystals as ion conductors, in: J.W. Goodby, C. Tschierske, P. Raynes, H. Gleeson, T. Kato, P.J. Collings (Eds.), Handbook of Liquid Crystals, Vol. 8, Wiley-VCH, Weinheim, 2014, pp. 727–749.
[16] T. Kato, M. Yoshio, T. Ichikawa, B. Soberats, H. Ohno, M. Funahashi, Nat. Rev. Mater. 2 (2017) 17001.
[17] J. Sakuda, E. Hosono, M. Yoshio, T. Ichikawa, T. Matsumoto, H. Ohno, H. Zhou, T. Kato, Adv. Funct. Mater. 25 (2015) 1206–1212.
[18] A. Kuwabara, M. Enomoto, E. Hosono, K. Hamaguchi, T. Onuma, S. Kajiyama, T. Kato, Chem. Sci. 11 (2020) 10631–10637.
[19] T. Onuma, E. Hosono, M. Takenouchi, J. Sakuda, S. Kajiyama, M. Yoshio, T. Kato, ACS Omega. 3 (2018) 159–166.
[20] H. Shimura, M. Yoshio, A. Hamasaki, T. Mukai, H. Ohno, T. Kato, Adv. Mater. 21 (2009) 1591–1594.
[21] M. Yoshio, T. Mukai, H. Ohno, T. Kato, J. Am. Chem. Soc. 126 (2004) 994–995.
[22] K. Kishimoto, T. Suzawa, T. Yokota, T. Mukai, H. Ohno, T. Kato, J. Am. Chem. Soc. 127 (2005) 15618–15623.
[23] Y. Iinuma, K. Kishimoto, Y. Sagara, M. Yoshio, T. Mukai, I. Kobayashi, H. Ohno, T. Kato, Macromolecules. 40 (2007) 4874–4878.
[24] A. Eisele, K. Kyriakos, R. Bhandary, M. Schönhoff, C.M. Papadakis, B. Rieger, J. Mater. Chem. A. 3 (2015) 2942–2953.
[25] J.H. Lee, K.S. Han, J.S. Lee, A.S. Lee, S.K. Park, S.Y. Hong, J.-C. Lee, K.T. Mueller, S. M. Hong, C.M. Koo, Adv. Mater. 28 (2016) 9301–9307.
[26] T. Ichikawa, M. Yoshio, A. Hamasaki, J. Kagimoto, H. Ohno, T. Kato, J. Am. Chem. Soc. 133 (2011) 2163–2169.
[27] B. Soberats, M. Yoshio, T. Ichikawa, H. Ohno, T. Kato, J. Mater. Chem. A. 3 (2015) 11232–11238.
[28] T. Kobayashi, T. Ichikawa, T. Kato, H. Ohno, Adv. Mater. 29 (2017) 1604429.
[29] T. Ohtake, M. Ogasawara, K. Ito-Akita, N. Nishina, S. Ujiie, H. Ohno, T. Kato, Chem. Mater. 12 (2000) 782–789.
[30] K. Kishimoto, M. Yoshio, T. Mukai, M. Yoshizawa, H. Ohno, T. Kato, J. Am. Chem. Soc. 125 (2003) 3196–3197.
[31] R.L. Kerr, S.A. Miller, R.K. Shoemaker, B.J. Elliott, D.L. Gin, J. Am. Chem. Soc. 131 (2009) 15972–15973.
[32] M. Lee, N.-K. Oh, J. Mater. Chem. 6 (1996) 1079–1086.
[33] Y. Akachi, K. Kawamura, N. Koide, Polym. Adv. Technol. 12 (2001) 422–426.
[34] Y. Zheng, J. Lui, G. Ungar, P.V. Wright, Chem. Record. 4 (2004) 176–191.
[35] P.W. Majewski, M. Gopinadhan, W.-S. Jang, J.L. Lutkenhaus, C.O. Osuji, J. Am. Chem. Soc. 132 (2010) 17516–17522.
[36] D. Bresser, M. Leclere, L. Bernard, P. Rannou, H. Mendil-Jakani, G.-T. Kim, T. Zinkevich, S. Indris, G. Gebel, S. Lyonnard, L. Picard, ChemSusChem. 14 (2021) 655–661.
[37] H.-P. Liang, M. Zarrabeitia, Z. Chen, S. Jovanovic, S. Merz, J. Granwehr, S. Passerini, D. Bresser, Adv. Energ. Mater. 12 (2022) 2200013.
[38] Y. Wang, C.J. Zanelotti, X. Wang, R. Kerr, L. Jin, W.H. Kan, T.J. Dingemans, M. Forsyth, L.A. Madsen, Nat. Mater. 20 (2021) 1255–1263.
[39] L. Niedzicki, M. Kasprzyk, New strategies in designing salts and solutions for the new generation of electrolytes, in: W. Wieczorek, J. Płocharski (Eds.), Designing Electrolytes for Lithium-Ion and Post-Lithium Batteries, Jenny Stanford Publishing, New York, 2021, pp. 3–42.
[40] W.A. Henderson, Nonaqueous electrolytes: Advances in lithium salts, in: T.R. Jow, K. Xu, O. Borodin, M. Ue (Eds.), Electrolytes for Lithium and Lithium-Ion Batteries, Modern Aspects of Electrochemistry, Vol. 58, Springer, New York, 2014, pp. 1–92.
[41] S.P. Fisher, A.W. Tomich, S.O. Lovera, J.F. Kleinsasser, J. Guo, M.J. Asay, H.M. Nelson, V. Lavallo, Chem. Rev. 119 (2019) 8262–8290.
[42] R.N. Grimes, Carboranes, 3rd ed.:., Academic Press, New York, 2016.
[43] C.A. Reed, Acc. Chem. Res. 31 (1998) 133–139.
[44] J. Poater, M. Solà, C. Viñas, F. Teixidor, Angew. Chem. Int. Ed. 53 (2014) 12191–12195.
[45] J. Poater, C. Viñas, I. Bennour, S. Escayola, M. Solà, F. Teixidor, J. Am. Chem. Soc. 142 (2020) 9396–9407.
[46] J.W. Johnson, M.S. Whittingham, J. Electrochem. Soc. 127 (1980) 1653–1654.
[47] J.W. Johnson, J.F. Brady, J. Electrochem. Soc. 129 (1982) 2213–2219.
[48] Z. Chen, A.N. Jansen, K. Amine, Energy Environ. Sci. 4 (2011) 4567–4571.
[49] C.M. Ionica-Bousquet, D. Muñoz-Rojas, W.J. Casteel, R.M. Pearlstein, G. GirishKumar, G.P. Pez, M.R. Palacín, J. Power Sourc. 195 (2010) 1479–1485.
[50] Z. Chen, Y. Ren, A.N. Jansen, C.-K. Lin, W. Weng, K. Amine, Nat. Commun. 4 (2013) 1513.
[51] M. Green, K. Kaydanik, M. Orozco, L. Hanna, M.A.T. Marple, K.A.S. Fessler, W.B. Jones, V. Stavila, P.A. Ward, J.A. Teprovich Jr., Adv. Sci. (2022) 2106032.
[52] S.G. McArthur, R. Jay, L. Geng, J. Guo, V. Lavallo, Chem. Commun. 53 (2017) 4453–4456.
[53] R. Jay, A.W. Tomich, J. Zhang, Y. Zhao, A.D. Gorostiza, V. Lavallo, J. Guo, ACS Appl. Mater. Interfaces. 11 (2019) 11414–11420.
[54] S. Kim, K. Kisu, S.-I. Orimo, Crystals. 11 (2021) 330.
[55] S. Kim, K. Kisu, S. Takagi, H. Oguchi, S.-I. Orimo, ACS Appl. Energy Mater. 3 (2020) 4831–4839.
[56] R. Asakura, L. Duchêne, R.-S. Kühnel, A. Remhof, H. Hagemann, C. Battaglia, ACS Appl. Energy Mater. 2 (2019) 6924–6930.
[57] S.H. Payandeh, D. Rentsch, Z. Łodziana, R. Asakura, L. Bigler, R. Černý, C. Battaglia, A. Remhof, Adv. Funct. Mater. 31 (2021) 2010046.
[58] B. Ringstrand, P. Kaszynski, J. Mater. Chem. 21 (2011) 90–95.
[59] B. Ringstrand, H. Monobe, P. Kaszynski, J. Mater. Chem. 19 (2009) 4805–4812.
[60] P. Kaszyński. *closo*-Boranes as structural elements for liquid crystals. In: Hosmane NS, Eagling R, editors. Handbook of Boron Science. London: World Scientific; 2018; Vol. 3, p 57-114.
[61] L. Jacob, E. Rzeszotarska, M. Koyioni, R. Jakubowski, D. Pociecha, A. Pietrzak, P. Kaszyński, Chem. Mater. 14 (2022) 6476–6491.
[62] B. Ringstrand, A. Jankowiak, L.E. Johnson, P. Kaszynski, D. Pociecha, E. Górecka, J. Mater. Chem. 22 (2012) 4874–4880.
[63] S. Kohmoto, E. Mori, K. Kishikawa, J. Am. Chem. Soc. 129 (2007) 13364–13365.
[64] M.R.J. Vallée, P. Majkut, I. Wilkening, C. Weise, G. Müller, C.P.R. Hackenberger, Org. Lett. 13 (2011) 5440–5443.
[65] W. Wang, R. Li, G.W. Gokel, Chem. Eur. J. 15 (2009) 10543–10553.
[66] G.W. Gray, J.w.g., Goodby Smectic Liquid Crystals-Textures and Structures, Philadelphia, Leonard Hill, 1984.
[67] I., Dierking Textures of Liquid Crystals, Weinheim, Wiley-VCH, 2003.
[68] J.W. Goodby, Structures and Properties of Smectic Liquid Crystals, in: J.W. Goodby, C. Tschierske, P. Raynes, H. Gleeson, T. Kato, P.J. Collings (Eds.), Handbook of Liquid Crystals, Vol. 4, Wiley-VCH, Weinheim, 2014, pp. 43–68.
[69] M.O. Ali, D. Pociecha, J. Wojciechowski, I. Novozhilova, A.C. Friedli, P. Kaszyński, J. Organometal. Chem. 865 (2018) 226–233.
[70] For details see the SI.
[71] S. Ferrari, E. Quartarone, P. Mustarelli, A. Magistris, S. Protti, S. Lazzaroni, M. Fagnoni, A. Albini, J. Power Sourc. 194 (2009) 45–50.
[72] L. Niedzicki, E. Karpierz, M. Zawadzki, M. Dranka, M. Kasprzyk, A. Zalewska, M. Marcinek, J. Zachara, U. Domańska, W. Wieczorek, Phys. Chem. Chem. Phys. 16 (2014) 11417–11425.
[73] Z.P. Rosol, N.J. German, S.M. Gross, Green Chem. 11 (2009) 1453–1457.
[74] A. Martinelli, A. Matic, P. Jacobsson, L. Börjesson, A. Fernicola, B. Scrosati, J. Phys. Chem. B. 113 (2009) 11247–11251.
[75] F. Zhang, Y. Sun, Z. Wang, D. Fu, J. Li, J. Hu, J. Xu, X. Wu, ACS Appl. Mater. Interfaces. 12 (2020) 23774–23780.
[76] J.W. Fergus, J. Power Sourc. 195 (2010) 4554–4569.
[77] M. Lee, U.H. Choi, S. Wi, C. Slebodnick, R.H. Colby, H.W. Gibson, J. Mater. Chem. 21 (2011) 12280–12287.
[78] X. Wang, Y. Chi, T. Mu, J. Mol. Liq. 193 (2014) 262–266.
[79] W.L.F. Armarego Purification of laboratory chemicals; Eighth edition ed.; Butterworth-Heinemann: Kidlington, Oxford, United Kingdom; Cambridge, MA, 2017.
[80] G.R. Fulmer, A.J.M. Miller, N.H. Sherden, H.E. Gottlieb, A. Nudelman, B.M. Stoltz, J.E. Bercaw, K.I. Goldberg, Organometallics. 29 (2010) 2176–2179.
[81] A. Bubnov, M. Kašpar, V. Hamplová, U. Dawin, F. Giesselmann, Beilstein J. Org. Chem. 9 (2013) 425–436.

CHAPTER B3

Liquid crystalline electrolytes containing Li^+ salt of a [*closo*-$CB_{11}H_{12}]^-$ derivative: Synthesis, characterization, and anisotropic Li-ion transport

1. INTRODUCTION

Liquid crystals (LCs) [1] have gained considerable interest as electrolyte materials in the recent years due to their ability to form self-organized structures with ion conductive channels [2-3]. More specifically, the inherent partial organization of the LC electrolyte endow them with macroscopic ordering and the macroscopically aligned nonsegregated structures can be considered as 1D [4,5], 2D [6-9] or 3D [10-12] pathways suitable for the anisotropic ion transport. This property of LC electrolytes is advantageous over the conventional organic electrolytes [13-15], which have random molecular orientation (isotropic). Additionally, LC electrolytes can be aligned in specific directions and studies have shown increased ionic conductivity (up to three times) in the aligned monodomain smectic phase of the electrolyte compared to the unaligned electrolyte sample [16,17]. Consequently, LC electrolytes are expected to suppress the undesired side reactions, such as dissolution of electrodes and current collectors, dendrite growth formation, etc., that are commonly observed in the conventional electrolytes [18].

Although Li-ion transport in LCs have been known for the last few decades, Kato and coworkers in 2015 developed the first thermotropic LC electrolytes for the application in lithium-ion batteries [2]. It showed moderate ionic conductivity in the range of 10^{-6} to 10^{-5} S cm^{-1} and the Li-ion battery developed using such a LC electrolyte showed a reversable charge-discharge for both positive and negative electrodes. Kato and coworkers also studied the anisotropy in Li-ion transport in a parallelly aligned LC electrolyte system in which ionic conductivity in perpendicular

and parallel directions were found to be 3.1×10^{-6} S cm^{-1} and 3.9×10^{-7} S cm^{-1} respectively [19]. Recent studies of LC electrolytes revealed their ability to effectively suppress the Li dendrite growth during the charge discharge cycles without the aid of any external forces [20]. Vishwanathan and coworkers in 2020, theoretically demonstrated that the LC molecules can suppress dendrite growth and proposed molecular level design rules for LC electrolytes for dendrite free lithium metal batteries [20a]. LC electrolytes have also showed good electrochemical stability (up to 4.3 V versus the Li/Li^+ reference electrode) and high oxidative resistance, which are important for high voltage battery applications [3].

Typically, LC-based electrolytes are obtained by combining metal ion salts such as, $LiBF_4$, $LiAsF_6$, $LiPF_6$, $LiClO_4$, $LiN(SO_2CF_3)_2$, with LC matrices at a predetermined concentration. Due to their miscibility with ionic salts, polar LC containing organic carbonates or PEO chains [21.22] and ionic LC containing imidazolium [5,9], phosphonium, or ammonium [23] groups are predominantly used in electrolyte applications. Despite the availability of these halogenated lithium salts, there are still concerns related to their stability, environmental compatibility and accumulation of the anions in ion conductive layers. In order to address these intrinsic drawbacks, a new design of a stable and halogen-free lithium salt is important. Particularly interesting in this context are anionic boron clusters [24], which are weakly-nucleophilic, inorganic, three-dimensional, and σ-aromatic boron hydrides [25-26]. *closo*-Borate anions have recently received significant attention as new solid electrolyte systems, owing to their high ionic conductivity, high deformability, and superior chemical/electrochemical stability [27-30].

A combination of Li-salt of weakly coordinating anionic boron cluster derivatives, as a source of Li-ion, and anisotropic liquid crystals as matrix constitutes an intriguing system to investigate in the context of high-performance electrolytes for Li-ion batteries. Recently, we demonstrated the first such LC electrolytes based on anionic boron clusters in which the anion of

the Li-salt was a 1,12-disubstituted [*closo*-1-$CB_{11}H_{12}$]$^-$ derivative and structurally similar to the host LC matrix [32]. The ionic conductivity for the unaligned electrolyte sample was found to monotonically increase from 10^{-8} to 10^{-4} S cm^{-1} with increase in temperature and Li-ion concentration. The study of anisotropic Li-ion transport in an aligned electrolyte sample is also of interest. This chapter focuses exclusively on the progress made in the investigation of anisotropic Li-ion transport in a parallelly aligned LC electrolyte sample containing Li^+ salt of the structurally similar anionic [*closo*-1-$CB_{11}H_{12}$]$^-$ derivative.

2. RESULS AND DISCUSSION

2.1 Synthesis

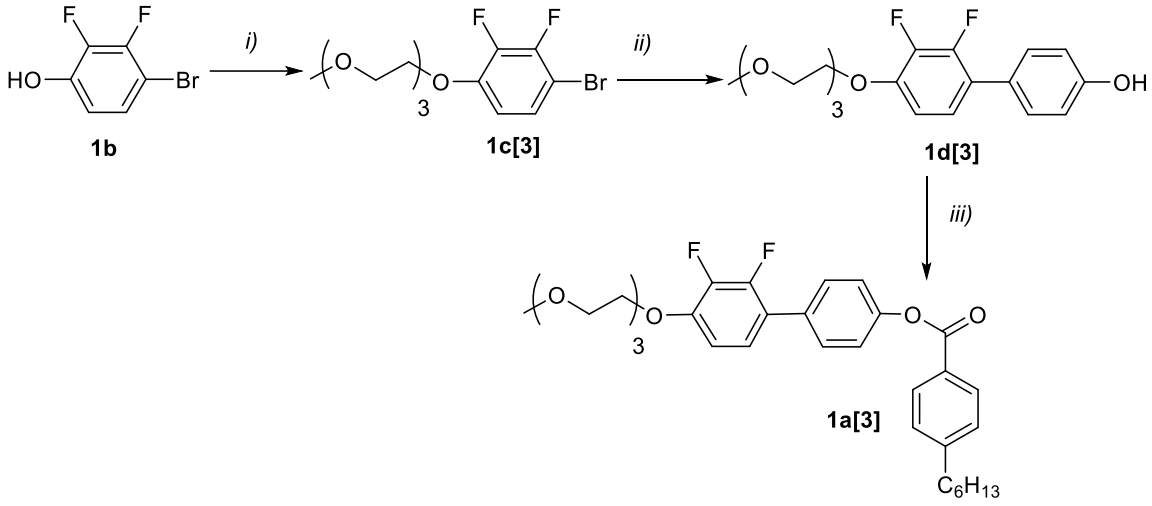

Scheme 1. Preparation of LC matrix **1a[3]**. Reagents and conditions: (*i*) *t*-BuOK, EtOH, $Me(OCH_2CH_2)_3OTs$, reflux, 18 h, 70–75% yield; (*ii*) 4-hydroxyphenylboronic acid, $Pd_2(dba)_3$, $[HPCy_4][BF_4]$, *t*-BuOK, THF/water, reflux, 48 h, 66–70% yield; (*iii*) 4-hexylbenzoic acid, DCC, DMAP, CH_2Cl_2, rt, 18 h, 84–89% yield.

*Preparation of LC host matrix **1a[3]***. 4-Bromo-2,3-difluorophenol (**1b**) on reaction with $Me(OCH_2CH_2)_3OTs$ [25] in the presence of *t*-BuOK gave **1c[3]** in 70–75% yield (Scheme 1). A

subsequent reaction of **1c[3]** with 4-hydroxyphenylboronic acid in the presence of tris(dibenzylideneacetone)dipalladium(0) ($Pd_2(dba)_3$) catalyst and $[HPCy_4][BF_4]$ ligand resulted in derivative **1d[3]** obtained in 66–70% yield. Steglich type esterification of **1d[3]** with 4-hexylbenzoic acid in the presence of dicyclohexylcarbodiimide (DCC) and catalytic amounts of 4-dimethylaminopyridine (DMAP) gave the LC matrix **1a[3]** in 84–89% yield.

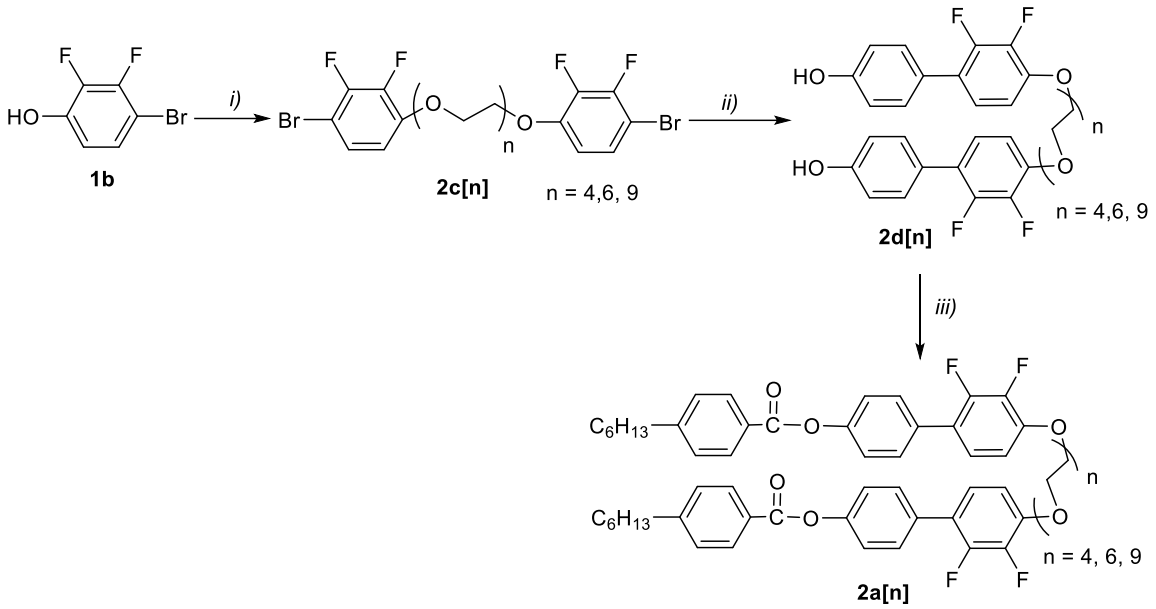

Scheme 2. Preparation of the dimeric LC matrix **2a[n]**. Reagents and conditions: *i)* Synthesis of dimeric LC matrix. Reagents and conditions: *i*) *t*-BuOK, EtOH, $Ts(OCH_2CH_2)_nOTs$, reflux, 18 h, 69–90% yield; *ii*) 4-hydroxyphenylboronic acid, $Pd_2(dba)_3$, $[HPCy_4][BF_4]$, *t*-BuOK, THF/water, reflux, 48 h, 61–74% yield; *iii*) 4-hexylbenzoic acid, EDC·HCl or DCC, DMAP, CH_2Cl_2, rt, 18 h, 60–78% yield.

*Preparation of LC host matrix **2a[4]**, **2a[6]**, and **2a[9]***. Thus, 4-bromo-2,3-difluorophenol (**1b**) was reacted with $Ts(OCH_2CH_2)_nOTs$ (n = 4, 6, 9) in the presence of *t*-BuOK to give **2c[n]** isolated in 69–90% yield after column chromatography (Scheme 2). Subsequent reaction of **2c[n]** with 4-hydroxyphenylboronic acid in the presence of $Pd_2(dba)_3$ catalyst and $[HPCy_4][BF_4]$ ligand

resulted in the derivative **2d[n]** obtained in 61–74% yield. Synthesis of the dimeric LC matrix **2a[4]** was achieved through the Steglich-type esterification of **2d[4]** with 4-hexylbenzoic acid in the presence of DCC and catalytic amounts of 4-dimethylaminopyridine (DMAP). Derivatives **2a[6]** and **2a[9]** were also obtained from **2d[6]** and **2d[9**], respectively, through the same esterification reaction; however, *N*-(3-dimethylaminopropyl)-*N′*-ethylcarbodiimide hydrochloride (EDC·HCl) was used instead of DCC in order to avoid contamination of the pure product with urea byproducts.

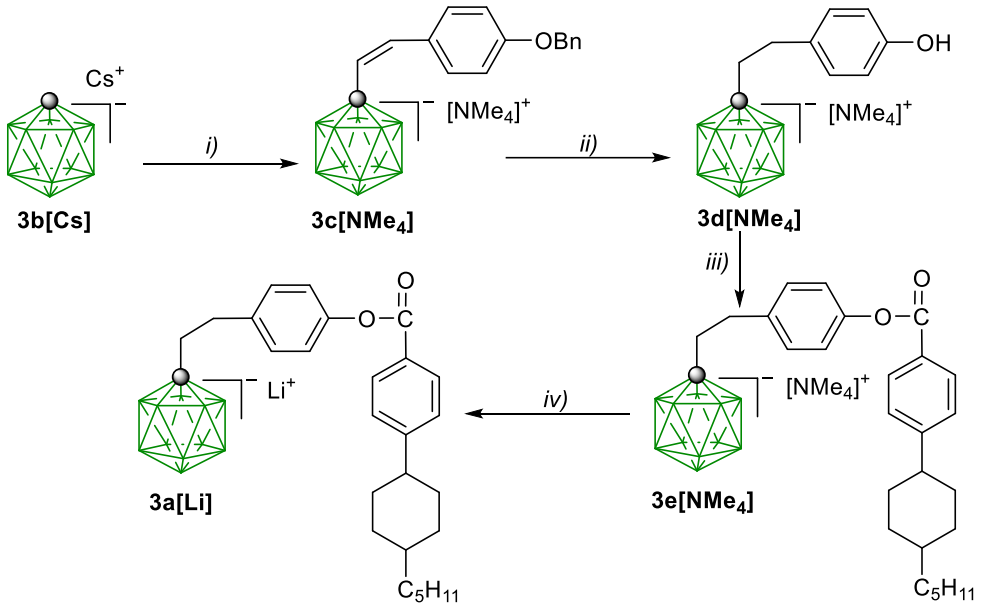

Scheme 3. Preparation of the lithium salt based on [*closo*-1-$CB_{11}H_{12}$]$^-$ derivative. Reagents and conditions: (*i*) 1). *n*-BuLi, THF, −78 →0 °C, 2). CuI, rt, 30 min., 3). $BnOC_6H_4CHCH$-Hal, $Pd(OAc)_2$, $(2\text{-}OMeC_6H_4)_3P$, rt, 12 h, 4). $[Me_4N]^+Cl^-$, 81% yield; (*ii*) H_2, Pd/C, EtOH/EtOAc, rt, 12 h; (*iii*) 4-(4-pentylcyclohexyl)benzoyl chloride, NaOH, THF, rt, 12 h, 61−69% yield; (*iv*) 1). 20% HCl, 2). LiOH.

*Preparation of the Li^+ salt **3a[Li]***. The phenolic derivative **3d[NMe_4]** was prepared from the derivative **3b[Cs]** according to a previously demonstrated procedure [31]. Subsequent esterification of **3d[NMe_4]** using freshly prepared 4-(4-pentylcyclohexyl)benzoyl chloride gave

3e[NMe$_4$] in a 61–69% yield (Scheme 3). Attempts at synthesis of **3e[NMe$_4$]** through Steglich-type esterification of **3d[NMe$_4$]** in the presence of DCC or EDC·HCl was not efficient due to the difficulty in removing the urea byproduct formed during the reaction. Li^+ salt **3a[Li]** was obtained by exchanging the $[NMe_4]^+$ cation in **3e[NMe$_4$]** with the Li^+ cation in a water/CH_2Cl_2 system [32].

Electrolyte samples under investigation were prepared by dissolving 10 mol% of Li^+ salt **3a[Li]** in appropriate LC matrix.

2.2 Liquid crystalline behavior

The investigation of the liquid crystalline behavior revealed smectic (Sm) and nematic (N) phases in the dimeric matrices and electrolyte samples. Optical textures observed for the dimeric LC matrix **2a[6]** are shown in Figure 1. Shearing of the smectic phase texture leads to a homeotropic alignment consistent with the SmA phase. Matrix **1a[3]** showed only a nematic phase.

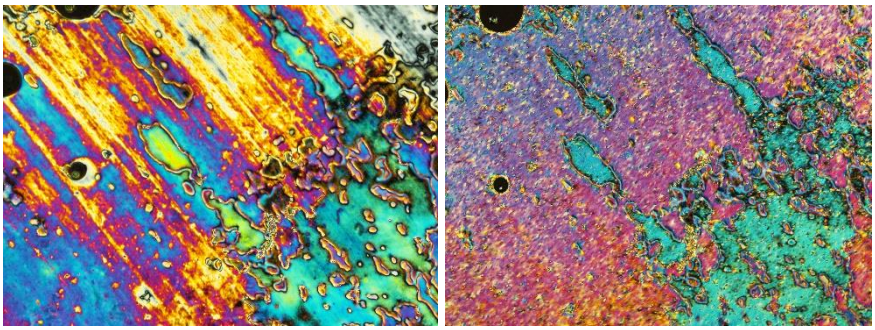

Figure 1. Optical textures for the dimeric matrix **2a[6]** observed in the same region on cooling: nematic phase at 90 °C (left), smectic phase just below N-Sm transition at 58 °C (right).

Depending on the length of the oligoethylene moiety present, the liquid crystalline properties of these matrices differed. Thermal behavior of the LC matrices is shown in Table 1.

Table 1. Thermotropic properties of the LC matrices recorded at 10 K min^{-1}.

Compound	**Transition temperature (**°C)
1a[3]	Cr 36 N 69 I
2a[4]	Cr 108 (SmA 84)[a] N 162 I
2a[6]	Cr_1 37 Cr_2 70 (SmA 58)[a] N 119 I
2a[9]	Cr 67 (SmA 62)[a] N 75 I
10 mol% Li^+ salt 3a[Li] in 2a[6]	Cr 63 (N 132) [a] SmA 134 I
10 mol% Li^+ salt 3a[Li] in 2a[9]	Cr 48 SmA 89 I

[a] monotropic transition. Notation: Cr, crystalline; SmA, smectic A; I, isotropic phases.

In general, the longer the oligoethylene chain, the lower the clearing temperature. For instance, the dimeric LC molecule **2a[4]** clears at 162 °C, whereas the higher homologues **2a[6]** and **2a[9]** clear at 119 °C and 75 °C, respectively. Derivative **1a[3]** cleared at 69 °C. Also, longer ethylene glycol units stabilize the N phase in favour of the Sm phase. Thus, compared to the derivatives **2a[4]** and **2a[6]**, which have only a narrow window of the smectic phase region (2 K and 6 K, respectively), derivative **2a[9]** has a wide window of the smectic phase region (30 K). Addition of the Li-salt **3a[Li]** to the LC matrix **2a[6]** raised the phase transition temperature (approximately 15 K increase in clearing temperature compared to pure host matrices) and stabilized the N phase in favour of the Sm phase. A representative DSC trace for matrix **2a[6]** and 10 mol% solution of **3a[Li]** in **2a[6]** are shown in Figure 2.

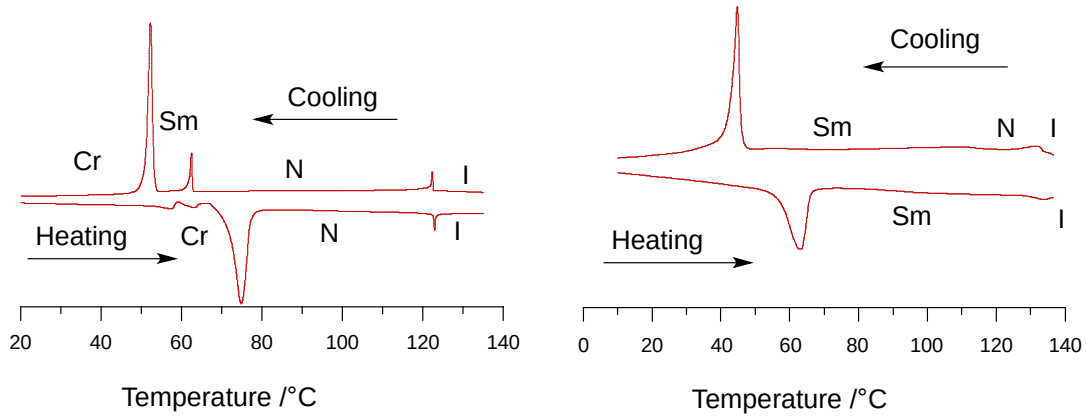

Figure 2. DSC trace for matrix **2a[6]** (left) and 10 mol% solution of **3a[Li]** in **2a[6]** (right). The heating and cooling rates are 10 K min^{-1}.

2.3 Powder XRD analysis

Powder XRD measurements (PXRD) confirmed the formation of a Sm phase in the dimeric LC matrices. The observed sharp signal in the small angle region and a broad diffused signal in the wide-angle region are typical for a fluid smectic phase, such as SmA. A representative powder XRD pattern observed for the derivatives **2a[6]** and **2a[9]** is shown in Figure 3.

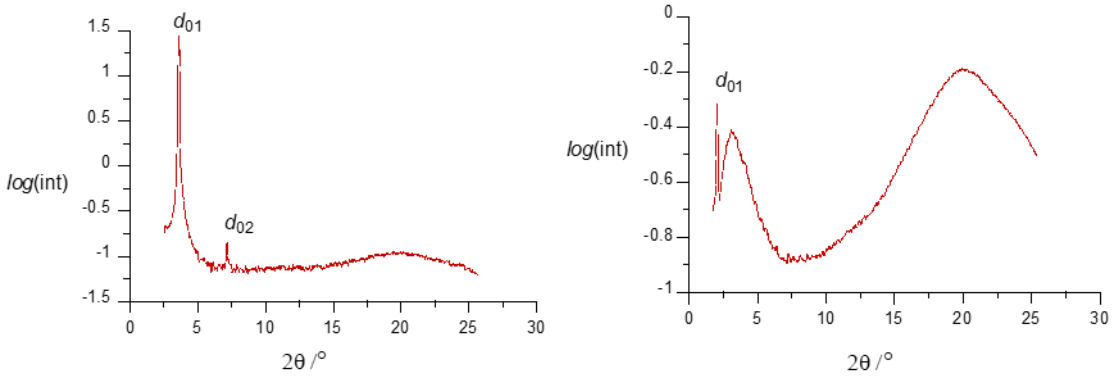

Figure 3. Powder XRD pattern for the derivative **2a[6**] and **2a[9]** in the smectic phase measured at 60 °C and 50 °C, respectively.

2.4 Impedance spectroscopy

Li-ion conduction in the parallelly aligned electrolyte sample (10 mol% solution of **3a[Li]** in **2d[6]**) in the smectic phase was investigated using electrochemical impedance spectroscopy (EIS) measurements. An interdigitated gold electrode with gap size 10 μm and an ITO cell with a thickness of 10 μm were used for measuring the parallel ($\sigma_{\parallel}$) and perpendicular ($\sigma_{\perp}$) ionic conductivity, respectively (Figure 4).

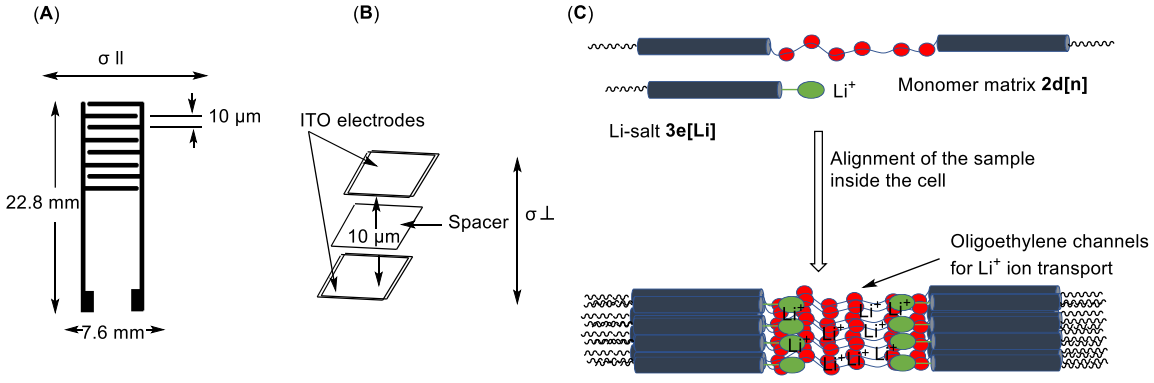

Figure 4. Schematic representation of the electrodes and electrolyte. **A**) Interdigitated gold electrode, **B**) ITO cell, **C**) parallelly aligned electrolyte sample inside the cell with oligoethylene channels for Li-ion transport.

Results of the measurements are shown in Figure 5. The Li-ion transport in the Sm phase of the electrolyte was found to increase with increasing temperature in both parallel and perpendicular directions. Although the ionic conductivity at 90 °C was the same (0.02 mS cm^{-1}) in both directions, further increase in temperature showed better ionic conductivity in the perpendicular direction, and it reached 0.09 mS cm^{-1} at 120 °C. This could be associated with the existance of a soft crystalline phase at lower temperature. The ionic conductivity at 120 °C measured in the parallel direction was 0.04 mS cm^{-1}. This value of ionic conductivity is comparable to that observed for amorphous polyethylene materials and liquid crystals containing oxyethylene

moieties [16]. Therefore, LC electrolytes containing Li^+ salts of a boron cluster derivative could be a potential candidate to replace the widely used organic electrolytes.

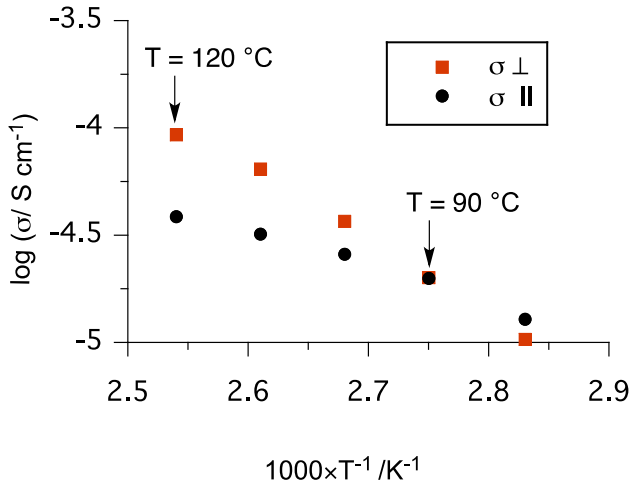

Figure 5. Temperature dependent anisotropic Li-ion transport in 10 mol% solution of **3a[Li]** in **2a[6]**.

3. SUMMARY AND CONCLUSIONS

Four liquid crystalline host matrices with varying oligoethylene chain lengths and a Li^+ salt **3a[Li]** containing anionic [*closo*-1-$CH_{11}H_{12}$]$^-$ derivative, structurally similar to the LC matrix were synthesized and characterized. Thermal properties of LC matrices were investigated, and it was found that the phase stability and transition temperature depend on the length of the oligoethylene moiety present in them. Longer oligoethylene units in the matrix have been found to decrease the clearing temperature and stabilize the N phase in favor of the Sm phase. The anisotropic Li^+ ion conductivity was measured for one of the electrolyte systems (10 mol% solution of **3a[Li]** in **2a[6]**). Preliminary results showed that the ionic conductivity in the perpendicular direction is up to 0.09 mS cm^{-1} at 120 °C, while it is only 0.04 mS cm^{-1} at the same temperature in the parallel direction.

These results are consistent with the previous studies, and investigations of the ionic conductivity in the remaining electrolyte systems are in progress.

4. EXPERIMENTAL SECTION

General procedure

Reagents and solvents were obtained commercially. Derivative **3d[NMe$_4$]** was obtained according to a literature procedure [31]. NMR spectra were obtained at 400 MHz (^{1}H), 100 MHz (^{13}C), 128 MHz (^{11}B), 376 MHz (^{19}F), in $CDCl_3$ and referenced to the solvent (δ = 7.26 ppm for ^{1}H and δ = 77.16 ppm for ^{13}C) or in CD_3CN and referenced to the solvent (δ = 1.94 ppm for ^{1}H and δ = 118.26 ppm for ^{13}C) or in DMSO-*d*$_6$ and referenced to the solvent (δ = 2.50 ppm for ^{1}H and δ = 39.52 ppm for ^{13}C) [33] or to an external sample of neat $BF_3{\cdot}Et_2O$ in $CDCl_3$ and CD_3CN (^{11}B NMR, δ = 0.0 ppm) or to an external sample of neat CF_3COOH in $CDCl_3$ and DMSO-*d*$_6$ (^{19}F NMR δ = 76.55 ppm). ^{11}B and ^{19}F NMR chemical shifts were taken from the H–decoupled spectra.

A polarized optical microscope with a hot stage was used to identify the liquid crystalline phase. TA Discovery DSC 2500 instrument was used for thermal analysis of the samples. Samples of about 1.0 mg under a flow of nitrogen gas was used for the thermal analysis and the heating and cooling rates were 10 K min^{-1}. Melting points were determined on a Melt-Temp II apparatus in capillaries. High-resolution mass spectrometry was conducted with the TOF-MS ES method. Broad angle X-ray diffraction studies were performed for unaligned samples using a Bruker D8 GADDS instrument (Cu Kα radiation, λ=1.54 Å, incident beam formed by Göbel mirror monochromator and point collimator 0.5 mm, two-dimensional detector Vantec 2000).

Impedance spectroscopy

Electrochemical impedance spectroscopy measurements were performed in the range of 80 to 120 °C. Two types of cells were used for measuring the ionic conductivity in the parallel and

perpendicular directions (interdigitated gold electrode and ITO cell, respectively). Electrolyte samples were filled into the cells by melting the sample at 140 °C. Before the measurement at each temperature, the cells were thermostated for a minimum of one hour in a cryostat-thermostat system (Haake K75 with a DC50 temperature controller). A computer-interfaced multichannel potentiostat with a frequency range of 500 kHz to 1 Hz and a 5 mV AC signal amplitude was used for the measurement. At each temperature point, the measurements were repeated for consistency.

Preparation of the binary mixture

Electrolyte samples under investigation were prepared by dissolving 10 mol% of Li^+ salt **3a[Li]** in appropriate LC matrix. Thus, a solution of the matrix **1a[3]** or **2a[n]** with 10 mol% of Li^+ salt **3a[Li]** in CH_2Cl_2 was evaporated to dryness in a rotary evaporator and dried under high vacuum to obtain the electrolyte samples.

Preparation of 1c[3]

A mixture of 4-bromo-2,3-difluorophenol (**1b**, 2.00 g, 9.57 mmol, 1.0 eq.) and *t*-BuOK (1.18 g, 10.53 mmol, 1.1 eq.) in EtOH (35 mL) was refluxed for 30 minutes until a green solution is obtained. To this solution $MeO(CH_2CH_2O)_3Ts$ (3.35 g, 10.53 mmol, 1.1 eq.) was added and the mixture was refluxed for another 18 h during which the green colour fades. EtOH was removed in a rotary evaporator and extraction was performed in CH_2Cl_2 (3 × 20 mL). The target compound was isolated by column chromatography (SiO_2, CH_2Cl_2/EtOAc, 2:1) to get 2.40 g (70% yield) of **1c[3]** as a colorless oil. $^1H\{^{19}F\}$ NMR (400 MHz, $CDCl_3$): δ 7.22–7.17 (m, 1H), 6.73–6.68 (m, 1H), 4.19 (t, J = 4.8 Hz, 2H), 3.87 (t, J = 4.8 Hz, 2H), 3.76–3.72 (m, 2H), 3.68–3.63 (m, 4H), 3.56–3.53 (m, 2H), 3.38 (s, 3H). $^{19}F\{^1H\}$ NMR (376 MHz, $CDCl_3$): δ -127.8 (d, J = 22.6 Hz), -152.9 (d, J = 22.6 Hz). $^{13}C\{^1H\}$ NMR (100 MHz, $CDCl_3$): δ 148.9 (d, $J_{F\text{-}C}$ = 244.1 Hz), 148.0 (d, $J_{F\text{-}C}$ = 11.4 Hz), 143.5 (d, $J_{F\text{-}C}$ = 15.4 Hz), 141.1, 126.4 (d, $J_{F\text{-}C}$ = 4.6 Hz), 111.0 (d, $J_{F\text{-}C}$ = 3.2 Hz), 101.2 (d,

J_{F-C} = 18.2 Hz), 72.0, 71.1, 70.8, 70.7, 70.7, 69.8, 69.6, 59.2. HRMS (ESI-TOF) *m/z*: $[M + H]^+$ calcd for $C_{13}H_{18}BrF_2O_4$: 355.0357, found: 355.0342. Anal. Calcd for $C_{13}H_{17}BrF_2O_4$: C 43.96, H 4.82. Found: C 43.97, H 4.77.

Preparation of 1d[3]

To a mixture of **1c[3]** (2.21 g, 6.19 mmol, 1.0 eq.), Pd_2dba_3 (113 mg, 0.12 mmol, 2 mol%), $[HPCy_3][BF_4]$ (91 mg, 0.25 mmol, 4 mol%), *t*-BuOK (28 mg, 0.25 mmol, 4 mol%), (4-hydroxyphenyl)boronic acid (854 mg, 6.19 mmol, 1.0 eq.) in THF (25 mL), a solution of K_2CO_3 (856 mg, 6.19 mmol, 1.0 eq.) in H_2O (25 mL) was added at room temperature. After refluxing the reaction mixture for 48 h, the reaction mixture was made acidic by adding 10% HCl at room temperature. The volatiles were removed *in vacuo* and the aqueous layer was extracted three times with 20 mL CH_2Cl_2. The target compound was isolated by column chromatography (SiO_2, CH_2Cl_2/EtOAc, 2:1) to get 1.63 g (70% yield) of **1d[3]** as a colorless, highly viscous oil that solidifies upon drying *in vacuo* to yield a colorless solid. $^1H\{^{19}F\}$ NMR (400 MHz, $CDCl_3$): δ 7.33 (d, *J* = 8.6 Hz, 2H), 6.96 (td, *J* = 8.5, 2.4 Hz, 1H), 6.89 (d, *J* = 8.7 Hz, 2H), 6.74–6.68 (m, 1H), 4.17 (t, *J* = 4.8 Hz, 2H), 3.89 (t, *J* = 4.9 Hz, 2H), 3.78–3.75 (m, 2H), 3.72–3.67 (m, 4H), 3.58–3.56 (m, 2H), 3.38 (s, 3H). $^{19}F\{^1H\}$ NMR (376 MHz, $CDCl_3$): δ -140.2 (d, *J* = 18.8 Hz), -156.5 (d, *J* = 18.8 Hz). $^{13}C\{^1H\}$ NMR (100 MHz, $CDCl_3$): δ 155.5, 147.0 (d, J_{F-C} = 8.9 Hz), 141.9 (d, J_{F-C} = 250.5 Hz), 130.0 (d, J_{F-C} = 3.0 Hz), 127.1, 123.3 (q, J_{F-C} = 12.2 Hz), 123.1, 115.5, 109.9, 71.9, 70.9, 70.7, 70.6, 69.6, 69.3, 59.0. HRMS (ESI-TOF) *m/z*: $[M + H]^+$ calcd for $C_{19}H_{22}F_2O_5$: 369.1514, found: 369.1496. Anal. Calcd for $C_{19}H_{22}F_2O_5$: C, 61.95; H, 6.02. Found: C, 62.00; H, 5.96.

Preparation of 1a[3]

To a suspension of **1d[3]** (1.43 g, 3.79 mmol, 1.0 eq.) and 4-hexylbenzoic acid (860 mg, 4.17 mmol, 1.1 eq.) in CH_2Cl_2 (20 mL), were added dicyclohexylmethanediimine (DCC, 939 mg,

4.55 mmol, 1.2 eq.) and 4-dimethylaminopyridine (DMAP, 93 mg, 0.76 mmol, 0.2 eq.). The reaction mixture was stirred overnight at room temperature. Progress in the reaction was monitored using TLC (SiO_2, EtOAc/Pet. ether, 3:2). After the reaction was complete, it was filtered and the collected filtrate was concentrated using a rotary evaporator to obtain the crude product. The target compound was isolated by column chromatography (SiO_2, EtOAc/Pet. Ether, 3:2) to give 1.95 g (92% yield) of **1a[3]** as a white solid. ^{1}H NMR (400 MHz, $CDCl_3$): δ 8.13 (d, *J* = 8.0 Hz, 2H), 7.55 (d, *J* = 6.8 Hz, 2H), 7.32 (d, *J* = 8.0 Hz, 2H), 7.28 (d, *J* = 8.6 Hz, 2H), 7.13–7.08 (m, 1H), 6.86–6.82 (m, 1H), 4.26 (t, *J* = 4.8 Hz, 2H), 3.91 (t, *J* = 4.8 Hz, 2H), 3.78–3.76 (m, 2H), 3.70–3.66 (m, 4H), 3.57–3.55 (m, 2H), 3.38 (s, 3H), 2.70 (t, *J* = 7.7 Hz, 2H), 1.66 (quint, *J* = 7.3 Hz, 2H), 1.37–1.29 (q, *J* = 6.5 Hz, 6H), 0.89 (t, *J* = 7.7 Hz, 3H). ^{19}F{^{1}H} NMR (376 MHz, $CDCl_3$): δ -140.6 (d, *J* = 18.8 Hz), -156.9 (d, *J* = 18.8 Hz).^{13}C{^{1}H} NMR (100 MHz, $CDCl_3$): δ 165.3, 150.7, 149.6, 149.0 (d, $J_{F\text{-}C}$ = 244.7 Hz), 147.7 (q, $J_{F\text{-}C}$ = 3.5 Hz), 142.1 (d, $J_{F\text{-}C}$ = 246.0 Hz), 132.5, 130.4, 130.0, 129.9 (d, $J_{F\text{-}C}$ = 3.0 Hz), 128.8, 126.9, 123.7, 122.8 (d, $J_{F\text{-}C}$ = 11.0 Hz), 122.0, 110.19, 110.16, 72.0, 71.1, 70.8, 70.7, 69.65, 69.59, 59.2, 36.2, 31.8, 31.2, 29.0, 22.7, 14.2. HRMS (ESI-TOF) *m/z*: $[M + H]^+$ calcd for $C_{32}H_{38}F_2O_6$: 557.2715, found: 557.2701. Anal. Calcd for $C_{32}H_{38}F_2O_6$: C, 69.05; H, 6.88. Found: C, 69.13; H, 6.84.

Preparation of 2a[4]

To a suspension of **2d[4]** (250 mg, 0.42 mmol, 1.0 eq.) and 4-hexylbenzoic acid (188 mg, 0.91 mmol, 2.2 eq.) in CH_2Cl_2 (10 mL), were added dicyclohexylmethanediimine (DCC, 205 mg, 0.99 mmol, 2.4 eq.) and 4-dimethylaminopyridine (DMAP, 20 mg, 0.17 mmol, 0.4 eq.). The reaction mixture was stirred overnight at room temperature. Progress in the reaction was monitored using TLC (SiO_2, CH_2Cl_2/EtOAc, 9:1). After the reaction was complete, it was filtered and the collected filtrate was concentrated using a rotary evaporator to obtain the crude product. The target

compound was isolated by column chromatography (SiO_2, CH_2Cl_2/EtOAc, 9:1) to give 319 mg (79% yield) of **2a[4]** as a white solid. $^1H\{^{19}F\}$ NMR (400 MHz, $CDCl_3$): δ 8.12 (d, *J* = 8.2 Hz, 4H), 7.54 (d, *J* = 7.0 Hz, 4H), 7.32 (d, *J* = 8.1 Hz, 4H), 7.27 (d, *J* = 8.9 Hz, 4H), 7.10 (td, *J* = 8.4, 2.2 Hz, 2H), 6.85–6.81 (m, 2H), 4.25 (t, *J* = 4.8 Hz, 4H), 3.92 (t, *J* = 4.8 Hz, 4H), 3.78–3.76 (m, 8H), 2.70 (t, *J* = 7.7 Hz, 4H), 1.69–1.59 (m, 4H), 1.38–1.28 (m, *J* = 4.9, 3.7 Hz, 12H), 0.89 (t, *J* = 6.7 Hz, 6H). $^{19}F\{^1H\}$ NMR (376 MHz, $CDCl_3$): δ -139.8 (d, *J* = 19.6 Hz), -156.1 (d, *J* = 19.4 Hz).$^{13}C\{^1H\}$ NMR (100 MHz, $CDCl_3$): δ 165.4, 150.7, 149.6, 149.0 (d, J_{F-C} = 241.7 Hz), 147.7 (q, J_{F-C} = 4.5 Hz), 142.1 (d, J_{F-C} = 248.0 Hz), 132.5, 130.4, 129.9 (d, J_{F-C} = 2.9 Hz), 128.8, 126.9, 123.8, 123.8, 122.8 (d, J_{F-C} = 10.9 Hz), 122.1, 110.2, 110.1, 71.1, 70.8, 69.7, 69.6, 36.2, 31.8, 31.3, 29.1, 22.7, 14.2. HRMS (ESI-TOF) *m/z*: $[M + Na]^+$ calcd for $C_{58}H_{62}F_4O_9$: 1001.4228, found: 1001.4188. Anal. Calcd for $C_{58}H_{62}F_4O_9$: C, 71.15; H, 6.38. Found: C, 71.09; H, 6.22.

General procedure for the synthesis of 2a[n] (n = 6, 9)

To a suspension of **2d[n]** (1.0 eq.) and 4-hexylbenzoic acid (2.2 eq.) in CH_2Cl_2 (15 mL), were added 1-ethyl-3-(3-dimethylaminopropyl)-carbodiimide hydrochloride (EDC·HCl, 3.2 eq.) and 4-dimethylaminopyridine (DMAP, 1 eq.). The reaction mixture was stirred overnight at room temperature. Progress in the reaction was monitored using TLC (SiO_2, CH_3CN/CH_2Cl_2, 1:4). After the reaction was complete, water (20 mL) was added in to the reaction mixture and CH_2Cl_2 layer was extracted (3 x 15 mL). The combined organic layer was dried over Na_2SO_4 and concentrated using a rotary evaporator to obtain the crude product. The target compound was isolated by column chromatography (SiO_2, CH_3CN/CH_2Cl_2, 1:4) to obtain the pure product **2a[n]**. The product was further purified by precipitation from a solution of ethyl acetate and hexane.

Preparation of 2a[6]

A suspension of **2d[6]** (351 mg, 0.51 mmol, 1.0 eq.) and 4-hexylbenzoic acid (231 mg, 1.12 mmol, 2.2 eq.) in CH_2Cl_2 (15 mL), when reacted in the presence of 1-ethyl-3-(3-dimethylaminopropyl)-carbodiimide hydrochloride (EDC·HCl, 311 mg, 1.63 mmol, 3.2 eq.) and 4-dimethylaminopyridine (DMAP, 62 mg, 0.51 mmol, 1 eq.) resulted in 360 mg (64% yield) of **2a[6]** as a white solid. ^{1}H NMR (400 MHz, $CDCl_3$): δ 8.12 (d, *J* = 8.3 Hz, 4H), 7.55 (d, *J* = 7.6 Hz, 4H), 7.38–7.26 (m, 8H), 7.12–7.08 (m, 2H), 6.86–6.81 (m, 2H), 4.25 (t, *J* = 4.8 Hz, 4H), 3.90 (t, *J* = 4.7 Hz, 4H), 3.81–3.73 (m, 4H), 3.72–3.61 (m, 12H), 2.70 (t, *J* = 7.7 Hz, 4H), 1.68–1.63 (m, 4H), 1.39–1.26 (m, 12H), 0.88 (t, *J* = 6.4 Hz, 6H). ^{19}F{^{1}H} NMR (376 MHz, $CDCl_3$): δ -139.7 (d, *J* = 19.9 Hz), -156.1 (d, *J* = 19.7 Hz). ^{13}C{^{1}H} NMR (100 MHz, $CDCl_3$): δ 165.4, 150.7, 149.7, 149.1 (d, $J_{F\text{-}C}$ = 237.3 Hz), 147.7 (q, $J_{F\text{-}C}$ = 7.0 Hz), 142.0 (d, $J_{F\text{-}C}$ = 262.7 Hz), 132.6, 130.4, 130.0 (d, $J_{F\text{-}C}$ = 3.0 Hz), 128.8, 126.9, 123.8, 122.8 (d, $J_{F\text{-}C}$ = 11.2 Hz), 122.1, 110.2, 71.1, 70.8, 70.7, 69.7, 69.6, 36.2, 31.8, 31.3, 29.1, 22.7, 14.2. HRMS (ESI-TOF) *m/z*: $[M + Na]^+$ calcd for $C_{62}H_{70}F_4O_{11}$: 1089.4752, found: 1089.4716. Anal. Calcd for $C_{62}H_{70}F_4O_{11}$: C, 69.78; H, 6.61. Found: C, 69.56; H, 6.55.

Preparation of 2a[9]

A suspension of **2d[9]** (319 mg, 0.39 mmol, 1.0 eq.) and 4-hexylbenzoic acid (175 mg, 0.85 mmol, 2.2 eq.) in CH_2Cl_2 (15 mL), when reacted in the presence of 1-ethyl-3-(3-dimethylaminopropyl)-carbodiimide hydrochloride (EDC·HCl, 178 mg, 0.93 mmol, 2.4 eq.) and 4-dimethylaminopyridine (DMAP, 20 mg, 0.16 mmol, 0.4 eq.) resulted in 297 mg (64% yield) of **2a[9]** as a white solid. ^{1}H NMR (400 MHz, $CDCl_3$): δ 8.12 (d, *J* = 8.3 Hz, 4H), 7.55 (d, *J* = 7.0 Hz, 4H), 7.32 (d, *J* = 8.3 Hz, 4H), 7.28 (d, *J* = 8.7 Hz, 4H), 7.10 (td, *J* = 8.5, 2.3 Hz, 2H), 6.86–6.81 (m, 2H), 4.25 (t, *J* = 4.8 Hz, 4H), 3.90 (t, *J* = 4.8 Hz, 4H), 2.70 (t, *J* = 7.7 Hz, 4H), 2.01 (s, 4H), 1.69–1.62 (m, 4H), 1.37–1.28 m, 12H), 0.91–0.87 (m, 6H). ^{19}F{^{1}H} NMR (376 MHz, $CDCl_3$): δ -

139.7 (d, J = 19.4 Hz), -156.1 (d, J = 19.8 Hz). $^{13}C\{^{1}H\}$ NMR (100 MHz, $CDCl_3$): δ 165.4, 150.7, 149.0 (d, $J_{F\text{-}C}$ = 242.3 Hz), 147.7 (q, $J_{F\text{-}C}$ = 5.0 Hz), 142.1 (d, $J_{F\text{-}C}$ = 264.1 Hz), 140.9, 132.6, 130.4, 130.00 (d, $J_{F\text{-}C}$ = 3.0 Hz), 128.8, 127.0, 123.8, 122.8 (d, $J_{F\text{-}C}$ = 10.8 Hz), 122.1, 110.2, 71.1, 70.8, 70.7, 69.7, 69.6, 36.2, 31.8, 31.3, 29.1, 22.7, 14.2, 2.0. HRMS (ESI-TOF) *m/z*: $[M + H]^+$ calcd for $C_{68}H_{82}F_4O_{14}$: 1199.5719, found: 1199.5742. Anal. Calcd for $C_{68}H_{82}F_4O_{14}$: C, 68.10; H, 6.89. Found: C, 68.03; H, 6.72.

General procedure for the synthesis of 2c[n]

To a solution of 4-bromo-2,3-difluorophenol (**1b**, 2.1 eq.) and *t*-BuOK (2.2 eq.) in EtOH (35 mL), $Ts(OCH_2CH_2)_nOTs$ (1.0 eq.) was added. The resulting solution was refluxed overnight, and EtOH was removed in a rotary evaporator upon completion of the reaction. Water was added to the resulting crude mixture and extraction was done in CH_2Cl_2 (3 × 25 mL). The combined organic layer was dried over Na_2SO_4 and the solvent was removed in a rotary evaporator to get the crude product. The target compound was isolated by column chromatography (SiO_2, CH_2Cl_2/EtOAc, 9:1).

Preparation of 2c[4]

Reaction of $Ts(OCH_2CH_2)_4OTs$ (3.98 g, 7.93 mmol, 1.0 eq.) with 4-bromo-2,3-difluorophenol (**1b**, 3.47 g, 16.64 mmol, 2.1 eq.) in EtOH (35 mL) in the presence of *t*-BuOK (1.96 g, 17.44 mmol, 2.2 eq.) gave 4.18 g (92% yield) of **2c[4]** as a colorless oily liquid. ^{1}H NMR (400 MHz, $CDCl_3$): δ 7.26–7.16 (m, 2H), 6.71–6.67 (m, 2H), 4.18 (t, J = 4.7 Hz, 4H), 3.92–3.86 (t, J = 4.7 Hz, 4H), 3.73–3.65 (m, 8H). $^{19}F\{^{1}H\}$ NMR (376 MHz, $CDCl_3$): δ -127.8 (d, J = 18.8 Hz), -152.9 (d, J = 18.8 Hz). $^{13}C\{^{1}H\}$ NMR (100 MHz, $CDCl_3$): δ 148.8 (d, $J_{F\text{-}C}$ = 260.1 Hz), 148.0 (q, $J_{F\text{-}C}$ = 3.8 Hz), 142.2 (d, $J_{F\text{-}C}$ = 262.7 Hz), 126.5(d, $J_{F\text{-}C}$ = 3.5 Hz), 110.9 (d, $J_{F\text{-}C}$ = 2.6 Hz), 101.2 (d, $J_{F\text{-}C}$ = 19.7 Hz), 71.1, 70.8, 69.8, 69.6. HRMS (ESI-TOF) *m/z*: $[M + H]^+$ calcd for

$C_{20}H_{20}Br_2F_4O_5$: 574.9692, found: 574.9713. Anal. Calcd for $C_{20}H_{20}Br_2F_4O_5$: C, 41.69; H, 3.50. Found: C, 41.70; H, 3.45.

Preparation of 2c[6]

Reaction of $Ts(OCH_2CH_2)_6OTs$ (4.40 g, 7.45 mmol, 1.0 eq.) with 4-bromo-2,3-difluorophenol (**1b**, 3.27 g, 15.65 mmol, 2.1 eq.) in EtOH (40 mL) in the presence of *t*-BuOK (1.84 g, 16.40 mmol, 2.2 eq.) resulted in 3.53 g (73% yield) of **2c[6]** as a colorless oily liquid. ^{1}H NMR (400 MHz, $CDCl_3$): δ 7.22–7.17 (m, 2H), 6.72–6.67 (m, 2H), 4.18 (t, J = 4.8 Hz, 4H), 3.86 (t, J = 4.8 Hz, 4H), 3.72–3.70 (m, 4H), 3.67–3.63 (m, 12H). ^{19}F{^{1}H} NMR (376 MHz, $CDCl_3$): δ -127.8 (d, J = 22.2 Hz), -152.9 (d, J = 18.8 Hz). ^{13}C NMR (100 MHz, $CDCl_3$): δ 148.8 (d, J_{F-C} = 257.4 Hz), 148.0 (q, J_{F-C} = 3.5 Hz), 142.2 (d, J_{F-C} = 265.2 Hz), 126.5 (d, J_{F-C} = 4.0 Hz), 111.0 (d, J_{F-C} = 2.9 Hz), 101.1 (d, J_{F-C} = 17.9 Hz), 71.1, 70.74, 70.70, 69.8, 69.6. HRMS (ESI-TOF) *m/z*: $[M + H]^+$ calcd for $C_{24}H_{28}Br_2F_4O_7$: 663.0216, found: 663.0223. Anal. Calcd for $C_{24}H_{28}Br_2F_4O_7$: C, 43.39; H, 4.29. Found: C, 43.60; H, 4.15.

Preparation of 2c[9]

Reaction of $Ts(OCH_2CH_2)_9OTs$ (3.03 g, 4.19 mmol, 1.0 eq.) and 4-bromo-2,3-difluorophenol (**1b**, 1.93 g, 9.22 mmol, 2.2 eq.) in EtOH (20 mL) in the presence of *t*-BuOK (1.22 g, 10.89 mmol, 2.6 eq.) gave 2.21 g (67% yield) of **2[9]** as a colorless oily liquid. Typical yield of the reaction is in the range 64-67%. ^{1}H NMR (400 MHz, $CDCl_3$): δ 7.21–7.17 (m, 2H), 6.72–6.68 (m, 2H), 4.18 (t, J = 4.8 Hz, 4H), 3.86 (t, J = 4.8 Hz, 4H), 3.75–3.68 (m, 4H), 3.67–3.61 (m, 24H). ^{19}F{^{1}H} NMR (376 MHz, $CDCl_3$): δ -127.1 (d, J = 18.8 Hz), -152.3 (d, J = 18.8 Hz). ^{13}C NMR (100 MHz, $CDCl_3$): δ 148.8 (d, J_{F-C} = 257.8 Hz), 148.0 (q, J_{F-C} = 3.5 Hz), 142.2 (d, J_{F-C} = 265.5 Hz), 126.5 (d, J_{F-C} = 4.3 Hz), 111.0 (d, J_{F-C} = 3.7 Hz), 101.1 (d, J_{F-C} = 17.8 Hz), 71.1,

70.74, 70.70, 69.8, 69.6. HRMS (ESI-TOF) *m/z*: $[M + H]^+$ calcd for $C_{30}H_{40}Br_2F_4O_{10}$: 795.1003, found: 795.0989. Anal. Calcd for $C_{30}H_{40}Br_2F_4O_{10}$: C, 45.24; H, 5.06. Found: C, 45.20; H, 5.01.

General procedure for the synthesis of 2d[n]

To a mixture of **2c[n]** (1.0 eq.), $Pd_2(dba)_3$ (4 mol%), $[HPCy_3][BF_4]$ (8 mol%), *t*-BuOK (8 mol%), and (4-hydroxyphenyl)boronic acid (2.0 eq.) in THF (25 mL), a solution of K_2CO_3 (2.1 eq.) in H_2O (25 mL) was added at room temperature. After refluxing the reaction mixture for 42 h, 10% HCl was added at room temperature until the solution becomes acidic. All the volatiles were removed *in vacuo* and the aqueous layer obtained was extracted in CH_2Cl_2 (3 × 20 mL). The target compound was isolated by column chromatography (SiO_2, CH_2Cl_2/EtOAc, 3:2).

Preparation of 2d[4]

Reaction of **2c[4]** (2.00 g, 3.47 mmol, 1.0 eq.) with 4-hydroxyphenylboronic acid (957 mg, 6.94 mmol, 2.0 eq.) in THF (25 mL) in the presence of Pd_2dba_3 (127 mg, 0.14 mmol, 4 mol%), $[HPCy_3][BF_4]$ (102 mg, 0.28 mmol, 8 mol%), *t*-BuOK (32 mg, 0.28 mmol, 8 mol%), and K_2CO_3 (1.01 g, 7.29 mmol, 2.1 eq.) dissolved in H_2O (25 mL) gave 1.51 g (72% yield) of **2d[4]** as a colourless, highly viscous oil. ^1H NMR (400 MHz, DMSO-d_6): δ 9.65 (s, 2H), 7.31 (d, J = 6.8 Hz, 4H), 7.16 (td, J = 8.7, 2.2 Hz, 2H), 7.04 (ddd, J = 9.2, 7.8, 1.8 Hz, 2H), 6.84 (d, J = 8.7 Hz, 4H), 4.21 (t, J = 4.4 Hz, 4H), 3.77 ((t, J = 4.5 Hz, 4H), 3.61–3.54 (m, 8H). $^{19}F\{^1H\}$ NMR (376 MHz, DMSO-d_6): δ -140.8 (d, J = 18.8 Hz), -157.1 (d, J = 18.8 Hz). $^{13}C\{^1H\}$ NMR (100 MHz, DMSO-d_6): δ 157.3, 147.8 (d, $J_{F\text{-}C}$ = 244.3 Hz), 146.4 (q, $J_{F\text{-}C}$ = 3.6 Hz), 140.7 (d, $J_{F\text{-}C}$ = 259.5 Hz), 129.7 (d, $J_{F\text{-}C}$ = 2.5 Hz), 124.7, 123.73, 123.68, 123.6, 122.3 (d, $J_{F\text{-}C}$ = 10.7 Hz), 115.5, 110.3, 110.2, 70.0, 69.9, 68.9, 68.8. HRMS (ESI-TOF) *m/z*: $[M + H]^+$ calcd for $C_{32}H_{30}F_4O_7$: 601.1849, found: 601.1866. Anal. Calcd for $C_{32}H_{30}F_4O_7$: C, 63.78; H, 5.02. Found: C, 63.84; H, 4.87.

Preparation of 2d[6]

Reaction of **2c[6]** (2.38 g, 3.58 mmol, 1.0 eq.) with (4-hydroxyphenyl)boronic acid (1.04 g, 7.67 mmol, 2.0 eq.) in THF (25 mL) in the presence of $Pd_2(dba)_3$ (132 mg, 0.14 mmol, 4 mol%), $[HPCy_3][BF_4]$ (106 mg, 0.28 mmol, 8 mol%), *t*-BuOK (32 mg, 0.28 mmol, 8 mol%), and K_2CO_3 (1.04 g, 7.52 mmol, 2.1 eq.) dissolved in H_2O (25 mL) gave 1.71 g (69% yield) of **2d[6]** as a yellow-orange colored, highly viscous oil. $^1H\{^{19}F\}$ NMR (400 MHz, DMSO-d_6): δ 9.68 (s, 2H), 7.32 (d, J = 8.1 Hz, 4H), 7.17 (d, J = 9.0 Hz, 2H), 7.04 (dd, J = 9.3, 4.6 Hz, 2H), 6.84 (d, J = 8.1 Hz, 4H), 4.21 (t, J = 4.4 Hz, 4H), 3.76 (t, J = 4.3 Hz, 4H), 3.63–3.49 (m, 16H). $^{19}F\{^1H\}$ NMR (376 MHz, DMSO-d_6): δ -141.5 (d, J = 21.0 Hz), -157.8 (d, J = 20.9 Hz). $^{13}C\{^1H\}$ NMR (100 MHz, DMSO-d_6): δ 170.4, 157.3, 147.8 (d, $J_{F\text{-}C}$ = 253.7 Hz), 146.4 (q, $J_{F\text{-}C}$ = 3.6 Hz), 140.7 (d, $J_{F\text{-}C}$ = 258.0 Hz), 129.7 (d, $J_{F\text{-}C}$ = 2.6 Hz), 124.71, 123.72, 123.68, 123.6, 122.3 (d, $J_{F\text{-}C}$ = 10.5 Hz), 115.5, 110.3, 110.2, 70.0, 69.82, 69.79, 68.9, 68.7, 59.8, 20.8, 14.1. HRMS (ESI-TOF) *m/z*: $[M + H]^+$ calcd for $C_{36}H_{38}F_4O_9$: 691.2530, found: 691.2540. Anal. Calcd for $C_{36}H_{38}F_4O_9$: C, 62.90; H, 5.55. Found: C, 62.84; H, 5.28.

Preparation of 2d[9]

Reaction of **2c[9]** (1.44 g, 1.99 mmol, 1 eq.) with 4-hydroxyphenylboronic acid (715 mg, 5.17 mmol, 2.6 eq.) in THF (25 mL) in the presence of Pd_2dba_3 (182 mg, 0.20 mmol, 10 mol%), $[HPCy_3][BF_4]$ (117 mg, 0.32 mmol, 16 mol%), *t*-BuOK (35 mg, 0.32 mmol, 8 mol%) and K_2CO_3 (715 mg, 5.17 mmol, 2.6 eq.) dissolved in H_2O (25 mL) gave 1.09 g (67% yield) of **2d[9]** as a yellow-orange colored waxy oil. $^1H\{^{19}F\}$ NMR (400 MHz, DMSO-d_6): δ 9.65 (s, 2H), 7.32 (d, J = 8.6 Hz, 4H), 7.16 (dd, J = 8.8, 2.8 Hz, 2H), 7.08–7.01 (m, 2H), 6.86 (d, J = 8.6 Hz, 4H), 4.24–4.19 (m, 4H), 3.79–3.74 (m, 4H), 3.62–3.58 (m, 4H), 3.55–3.48 (m, 24H). $^{19}F\{^1H\}$ NMR (376 MHz, $CDCl_3$): δ -140.3 (d, J = 18.8 Hz), -156.6 (d, J = 18.8 Hz). $^{13}C\{^1H\}$ NMR (100 MHz, $CDCl_3$): δ

156.2, 148.7 (d, J = 258.3 Hz), 147.0 (q, $J_{F\text{-}C}$ = 3.6 Hz) 141.9 (d, $J_{F\text{-}C}$ = 260.2 Hz), 129.9 (d, $J_{F\text{-}C}$ = 2.4 Hz), 126.6, 123.4, 123.3, 123.2, 115.8, 110.0 (d, $J_{F\text{-}C}$ = 2.7 Hz), 70.9, 70.7, 70.6, 70.5, 70.5, 69.7, 69.4. HRMS (ESI-TOF) *m/z*: $[M + H]^+$ calcd for $C_{42}H_{50}F_4O_{12}$: 823.3317, found: 823.3284. Anal. Calcd for $C_{42}H_{50}F_4O_{12}$: C, 61.31; H, 6.13. Found: C, 61.36; H, 6.08.

Preparation of 3e[NMe$_4$]:

To a solution of **3d[NMe$_4$]** (100 mg, 0.29 mmol, 1 eq.) and NaH (10 mg, 0.44 mmol, 1.5 eq.) in THF (5 mL), was added freshly prepared 4-(4-pentylcyclohexyl)benzoyl chloride (104 mg, 0.35 mmol, 1 eq.). The reaction mixture was stirred overnight and THF was removed in rotary evaporator. Water was added (5 mL) to the crude mixture and the white precipitate formed was collected by filtration. This was recrystallized from MeCN at ambient temperature gave 98 mg (56% yield) of pure **3e[NMe$_4$]** as a white microcrystalline powder. $^1H\{^{11}B\}$ NMR (400 MHz, CD_3CN): δ 8.05 (d, J = 8.3 Hz, 2H), 7.41 (d, J = 8.4 Hz, 2H), 7.18 (d, J = 8.5 Hz, 2H), 7.07 (d, J = 8.5 Hz, 2H), 3.06 (d, J = 1.0 Hz, 12H), 2.64–2.58 (m, 3H), 2.12–2.02 (m, 3H), 1.88 (d, J = 11.6 Hz, 5H), 1.55–1.46 (m, 4H), 1.36–1.21 (m, 12H), 1.12–1.03 (m, 3H), 0.90 (t, J = 6.9 Hz, 3H). ^{11}B NMR (128 MHz, CD_3CN): δ -1.5 (s, 1B), -9.7 (s, 1B), -12.8 – -13.9 (m, 8B). ^{13}C NMR (100 MHz, CD_3CN): δ 166.1, 155.3, 150.1, 140.8, 130.9, 130.1, 130.1, 128.2, 128.18, 122.6, 118.3, 70.8, 56.2, 56.13, 56.09, 45.4, 42.2, 38.0, 37.9, 36.6, 34.7, 34.1, 32.9, 27.3, 23.4, 14.3. HRMS (ESI-TOF) *m/z*: $[M]^-$ calcd for $C_{27}H_{44}B_{11}O_2$: 522.4443, found: 522.4420. Anal. Calcd for $C_{31}H_{56}B_{11}NO_2$: C, 62.71; H, 9.51; N, 2.36. Found: C, 62.15; H, 9.78; N, 2.47.

Preparation of 3a[Li]:

Li^+ salt **3a[Li]** was obtained by exchanging the $[NMe_4]^+$ cation in **3e[NMe$_4$]** with the Li^+ cation in a water/CH_2Cl_2 system, according to a known procedure [32].

$^1H\{^{11}B\}$ NMR (400 MHz, CD_3CN): δ 8.05 (d, J = 8.5 Hz, 2H), 7.41 (d, J = 8.5 Hz, 2H), 7.18 (d, J = 8.4 Hz, 2H), 7.07 (d, J = 8.5 Hz, 2H), 2.65–2.57 (m, 3H), 2.26–2.20 (m, 6H), 2.13–2.04 (m, 3H),

1.88 (d, *J* = 12.0 Hz, 4H), 1.51 (q, *J* = 12.3 Hz, 3H), 1.39–1.25 (m, 10H), 1.10 (q, *J* = 12.2 Hz, 2H), 0.90 (t, *J* = 6.9 Hz, 3H). ^{11}B NMR (128 MHz, CD_3CN): δ -1.5 (s, 1B), -9.7 (s, 1B), -12.8 – -13.9 (m, 8B). HRMS (ESI-TOF) *m/z*: $[M]^-$ calcd for $C_{27}H_{44}B_{11}O_2$: 522.4443, found: 522.4420. Anal. Calcd for $C_{27}H_{44}B_{11}O_2Li{\cdot}3H_2O$: C, 55.86; H, 8.68. Found: C, 55.85; H, 9.02.

5. AKNOWLEDGMENT

Financial support for this project is provided by the European Space Agency (NPI 542) grant. This work involves contributions from several people. Dr. Jannick Guschlbauer and Dr. Rafał Jakubowski contributed to the synthesis of derivatives **1a[3]** and **3d[NMe$_4$]**, respectively. Dr. Damian Pociecha from University of Warsaw contributed to the powder XRD measurements. Dr. Leszek Niedzicki of Technical University of Warsaw performed the EIS measurements.

6. REFERENCES

1. (a) Handbook of Liquid Crystals, 2nd ed. (Eds: J. W. Goodby, P. J. Collings, T. Kato, C. Tschierske, H. Gleeson, P. Raynes), Wiley-VCH, Weinheim, Germany, **2014**; (b) Handbook of Liquid Crystals (Eds: D. Demus, J. W. Goodby, G. W. Gray, H.-W. Spiess, V. Vill), Wiley-VCH, Weinheim, Germany, **1998**.
2. Sakuda, J., Hosono, E., Yoshio, M., Ichikawa, T., Matsumoto, T., Ohno, H., Zhou, H. and Kato, T., Liquid-crystalline electrolytes for lithium-ion batteries: Ordered assemblies of a mesogen-containing carbonate and a lithium salt, *Adv. Funct. Mater.*, **2015**, *25*, 1206–1212.
3. A. Kuwabara, M. Enomoto, E. Hosono, K. Hamaguchi, T. Onuma, S. Kajiyama, T. Kato, Nanostructured liquid-crystalline Li-ion conductors with high oxidation resistance:

Molecular design strategy towards safe and high-voltage-operation Li-ion batteries, *Chem. Sci.,* **2020**, *11*, 10631–10637.

4. H. Shimura, M.Yoshio, A. Hamasaki, T. Mukai, H. Ohno, T. Kato, Electric-field-responsive lithium-ion conductors of propylenecarbonate-based columnar liquid crystals, *Adv. Mater.*, **2009**, *21*, 1591–1594.
5. M. Yoshio, T. Mukai, H. Ohno, T. Kato, One-dimensional ion transport in self-organized columnar ionic liquids, *J. Am. Chem. Soc.*, **2004**, *126*, 994−995.
6. K. Kishimoto, T. Suzawa, T. Yokota, T. Mukai, H. Ohno, T. Kato, Nano-segregated polymeric film exhibiting high ionic conductivities, *J. Am. Chem. Soc.*, **2005**, *127*, 15618–15623.
7. Y. Iinuma, K. Kishimoto, Y. Sagara, M. Yoshio, T. Mukai, I. Kobayashi, H. Ohno, T. Kato, Uniaxially parallel alignment of a smectic A liquid-crystalline rod− coil molecule and Its lithium salt complexes using rubbed polyimides, *Macromolecules*, **2007**, *40*, 4874–4878.
8. [24] A. Eisele, K. Kyriakos, R. Bhandary, M. Schönhoff, C.M. Papadakis, B. Rieger, Structure and ionic conductivity of liquid crystals having propylene carbonate units. *J. Mater. Chem. A*, **2015**, *3*, 2942–2953.
9. 65. J. H. Lee, K. S. Han, J. S. Lee, A. S. Lee, A. S. K. Park, S. Y. Hong, J. C. Lee, K. T. Mueller, S. M. Hong, C. M. Koo, Facilitated ion transport in smectic ordered ionic liquid crystals, *Adv. Mater.*, **2016**, *28*, 9301−9307.
10. [26] T. Ichikawa, M. Yoshio, A. Hamasaki, J. Kagimoto, H. Ohno, T. Kato, 3D interconnected ionic nano-channels formed in polymer films: self-organization and polymerization of thermotropic bicontinuous cubic liquid crystals, *J. Am. Chem. Soc.*, **2011**, *133*, 2163–2169.

11. B. Soberats, M. Yoshio, T. Ichikawa, H. Ohno, T. Kato, Zwitterionic liquid crystals as 1D and 3D lithium-ion transport media, *J. Mater. Chem. A,* **2015**, *3*, 11232–11238.
12. T. Kobayashi, T. Ichikawa, T. Kato, H. Ohno, Development of Glassy Bicontinuous Cubic Liquid Crystals for Solid Proton-Conductive Materials, *Adv. Mater.,* **2017**, 29, 1604429.
13. J. Kalhoff, G.G. Eshetu, D. Bresser, S. Passerini, Safer electrolytes for lithium-ion batteries: state of the art and perspectives*, ChemSusChem*, **2015**, *8*, 2154–2175.
14. E. Quartarone, P. Mustarelli, Emerging trends in the design of electrolytes for lithium and post-lithium batteries, *J. Electrochem. Soc.,* **2020**, *167*, 050508.
15. K. Xu, Electrolytes and interphases in Li-ion batteries and beyond, *Chem. Rev.*, **2014**, *114*, 11503–11618.
16. T. Ohtake, M. Ogasawara, K. Ito-Akita, N. Nishina, S. Ujiie, H. Ohno, T. Kato, Liquid-crystalline complexes of mesogenic dimers containing oxyethylene moieties with $LiCF_3SO_3$: Self-organized ion conductive materials*, Chem. Mater.,* **2000**, *12,* 782–789.
17. K. Kishimoto, M. Yoshio, T. Mukai, M. Yoshizawa, H. Ohno, T. Kato, Nanostructured anisotropic ion-conductive films, *J. Am. Chem. Soc.*, **2003**, *125*, 3196–3197.
18. Y. Chen, Y. Kang, Y. Zhao, L. Wang, J. Liu, Y. Li, Z. Liang, X. He, X. Li, N. Tavajohi, B. Li, A review of lithium-ion battery safety concerns: The issues, strategies, and testing standards*, J. Energy Chem.,* **2021**, *59*, 83–99.
19. B. Soberats, E. Uchida, M. Yoshio, J. Kagimoto, H. Ohno, T. Kato, Macroscopic photocontrol of ion-transporting pathways of a nanostructured imidazolium-based photoresponsive liquid crystal, *J. Am. Chem. Soc.*, **2014**, *136*, 9552–9555.
20. (a) Z. Ahmad, Z. Hong, V. Vishwanathan, Design rules for liquid crystalline electrolytes for enabling dendrite-free lithium metal batteries, *Proc. Natl. Acad. Sci.,* **2020**, *117*, 26672–26680; (b) D. Gopalakrishnan, S. Alkatie, A. Cannon, S. Rajendran, N. K.

Thangavel, N. Bhagirath, E. M. Ryan, L. M. R. Arava, Anisotropic mass transport using ionic liquid crystalline electrolytes to suppress lithium dendrite growth, *Sustain. Energy & Fuels,* **2021**, *5,* 1488–1497.

21. T. Ohtake, M. Ogasawara, K. Ito-Akita, N. Nishina, S. Ujiie, H. Ohno, T. Kato, Liquid-crystalline complexes of mesogenic dimers containing oxyethylene moieties with $LiCF_3SO_3$: Self- organized ion conductive materials, *Chem. Mater.*, **2000**, *12*, 782−789.
22. A. Eisele, K. Kyriakos, R. Bhandary, M. Schönhoff, C. M. Papadakis, B. Rieger, Structure and ionic conductivity of liquid crystals having propylene carbonate units, *J. Mater. Chem. A*, **2015**, *3*, 2942−2953.
23. T. Ichikawa, M. Yoshio, A. Hamasaki, S. Taguchi, F. Liu, X. B. Zeng, G. Ungar, H. Ohno, T. Kato, Induction of thermotropic bicontinuous cubic phases in liquid crystalline ammonium and phosphonium salts, *J. Am. Chem. Soc*., **2012**, *134*, 2634−2643.
24. W. N. Lipscomb, Boron hydrides, New York: Benjamin; **1963**.
25. (a) R. N. Grimes, Boron clusters come of age, *J Chem Ed.,* **2004**, *81*, 658–672; (b) J. Poater, C. Vinas, I. Bennour, S. Escayola, M. Sola, F. Teixidor, Too persistent to give up: Aromaticity in boron clusters survives radical structural changes, *J. Am. Chem. Soc.*, **2020**, *142,* 9396–9407; (c) J. Aihara, Three-dimensional aromaticity of polyhedral boranes, *J. Am. Chem. Soc*., **1978**, *100*, 3339–3342.
26. (a) R. B. King, Three-dimensional aromaticity in polyhedral boranes and related molecules, *Chem. Rev*., **2001**, *101*, 1119–1152; (b) J. Poater, M. Sola, C. Vinas, F. Teixidor, π Aromaticity and three-dimensional aromaticity: Two sides of the same coin?, *Angew. Chem. Int. Ed.*, **2014**, *53,* 12191–12195; *Angew. Chem.*, **2014**, *126,* 12387–12391.

27. T. J. Udovic, M. Matsuo, W. S. Tang, H. Wu, V. Stavila, A. V. Soloninin, R. V. Skoryunov, O. A. Babanova, A. V. Skripov, J. J. Rush, A. Unemoto, H. Takamura, S. Orimo, Exceptional superionic conductivity in disordered sodium decahydro-closo-decaborate, *Adv. Mater.,* **2014**, *26*, 7622–7626.
28. W. S. Tang, A. Unemoto, W. Zhou, V. Stavila, M. Matsuo, H. Wu, S. I. Orimo, T. J. Udovic, Unparalleled lithium and sodium superionic conduction in solid electrolytes with large monovalent cage-like anions, *Energy Environ. Sci.,* **2015**, *8*, 3637–3645.
29. W. S. Tang, M. Matsuo, H. Wu, V. Stavila, W. Zhou, A. A. Talin, A. V. Soloninin, R. V. Skoryunov, O. A. Babanova, A. V. Skripov, Liquid-like ionic conduction in solid lithium and sodium monocarba-*closo*-decaborates near or at room temperature, *Adv. Energy Mater.,* **2016**, *6*, 1502237.
30. O. Tutusaus, R. Mohtadi, N. Singh, T. S. Arthur, F. Mizuno, Study of electrochemical phenomena observed at the Mg metal/electrolyte interface, *ACS Energy Lett.,* **2017**, *2*, 224−229.
31. R. Jakubowski, A. Pietrzak, A. C. Friedli, P. Kaszyński, C(1)-Phenethyl derivatives of [*closo*-1-$CB_{11}H_{12}$]$^-$ and [*closo*-1-CB_9H_{10}]$^-$ anions: Difunctional building blocks for molecular materials, *Chem. Eur. J.*, **2020**, *26*, 17481–17494.
32. J. Guschlbauer, L. Niedzicki, L. Jacob, E. Rzeszotarska, D. Pociecha, P. Kaszyński, Liquid crystalline electrolytes derived from the 1,12-disubstituted [*closo*-$CB_{11}H_{12}$]$^-$ anion, *J. Mol. Liq.*, **2023**, *377*, 121525.
33. G. R. Fulmer, A. J. M. Miller, N. H. Sherden, H. E. Gottlieb, A. Nudelman, B. M. Stoltz, J. E. Bercaw, K. I. Goldberg, NMR chemical shifts of trace impurities: common laboratory solvents, organics, and gases in deuterated solvents relevant to the organometallic chemist, *Organometallics*, **2010**, *29*, 2176–2179.

CHAPTER B4

Liquid crystalline polymer electrolytes based on [*closo*-$CB_{11}H_{12}]^-$ for Li-ion battery application

1. INTRODUCTION

The desire for a renewable energy source is at an all-time high, and Li-ion batteries (LIBs) are playing a significant role in the energy transition by providing emission-free energy. LIBs were commercially used for the first time in 1991, by a Japanese company SONY [1,2]. Currently, they are employed in many modern technologies including electric vehicles and portable electronic devices such as computers, smartphones etc. due to their high energy density, light weight, and improved lifespan [3-8].

Li-ion batteries based on conventional liquid electrolytes provides efficient room temperature ionic conductivity, decent capacity, and good charge-discharge property [9]. However, the decomposition products of thermally unstable Li^+ salts and volatility of the organic solvents and plasticizers used in these electrolytes rises many safety challenges in its commercial applications [10], especially during the battery operation that requires high voltage and temperature conditions. As a consequence, a new concept of whole solid-state batteries (SSEs) having high electrochemical stability, wide temperature range operation, high energy density, excellent safety, and easy processability has emerged.

Solid polymer electrolytes (SPE) are particularly interesting sub-class of SSEs because the additional flexibility they offer can leads to improved electrode/electrolyte contact [11-12]. In addition, they can function as both ion-conductor and electronically insulating separator in LIBs. An ideal SPE should have high mechanical strength, electrochemical stability, and high ionic

conductivity while maintaining the ion transference number close to unity [13]. Although several SPEs showed good mechanical properties and improved safety [14], their poor room temperature ionic conductivity and low transference number remains a challenge [12b, 15-16].

Liquid crystals (LCs) as an electrolyte material have gained significant attention in recent years due to their ability to self-organize and formation of channels for efficient Li-ion transport [17a-17d]. They are also found to have several advantages, such as improved electrochemical stability [18], ability to suppress the Li dendrite growth [19a], and high Li-ion transference number [19b]. Kato and co-workers in 2015 demonstrated the first Li-ion battery based on LC electrolytes [20]. Polymerization of LC electrolyte in its ordered LC phase results in nanostructured ion-conductive polymeric electrolyte films [21-24] with immobilized ion conducting channels. These LC polymer electrolytes offer good mechanical stability, a broad operating temperature range, and excellent electrode/electrolyte contact. Recently, Zhang and co-workers demonstrated a liquid crystalline solid polymer electrolyte film with a high ionic conductivity at room temperature (2.14×10^{-2} S cm^{-1}). This material was utilized in a $LiFePO_4$/Li cell which showed a discharge capacity of 150 $mAhg^{-1}$ [25].

The poor stability and environmental compatibility of conventionally used halogenated Li^+ salts are also a problem that must be resolved in order to improve the high temperature performance of the LIB. Utilizing Li^+ salts composed of anionic boron clusters is one way to accomplish this. Boron clusters are advantageous for use as lithium salts in electrolytes due to their excellent thermal and electrochemical stability and weekly coordinating nature [26-27]. Li^+ salts of boron clusters have already demonstrated high ionic conductivity and improved electrochemical stability [28-31].

Herein we present a new paradigm in solid polymer electrolytes by combining anisotropic ion transport of LC with derivatives of [*closo*-1-$CB_{11}H_{12}$]$^-$ as anions for Li-ions. The electrolyte system under investigation is a 10 mol% solution of Li^+ salt with anion which is a [*closo*-1-

$CB_{11}H_{12}]^-$ derivative structurally similar to or compatible with the liquid crystalline monomeric host containing an oligoethylene fragment. The polymeric electrolyte films obtained by the polymerization of the parallelly aligned LC electrolyte is expected to have improved ionic conductivity, thermal stability, and mechanical properties. This study involves several stages of development, including extensive synthesis and characterization of the LC electrolyte, its alignment using different surface treatment methods, photopolymerization of the aligned electrolyte, and finally testing of the polymer electrolyte film in CR-2032 type coin cell batteries. The progress made so far in the realization of such a LC polymer electrolyte is described in this Chapter.

2. RESULTS AND DISCUSSION

2.1 Synthesis

Monomeric LC host **1a[4]** was obtained in the sequence of reactions shown in Scheme 1. Thus, 4-hydroxybenzoic acid (**1b**) in reaction with $OH(CH_2)_6OTs$ [32] in the presence of *t*-BuOK gave 4-((6-hydroxyhexyl)oxy)benzoic acid (**1c)** in 66–70% yield. 4-(6-(Methacryloyloxy)hexyl)oxy)benzoic acid (**1d)** was prepared from **1c** in 35–45% according to a literature procedure [33]. Subsequently, Steglich-type esterification of benzoic acid derivative **1d** with biphenyl-4-ol derivative **1e** [34] in the presence of dicyclohexylcarbodiimide (DCC) and catalytic amounts of 4-dimethylaminopyridine (DMAP) resulted in the monomeric LC derivative **1a[4]** in 45–50% yield.

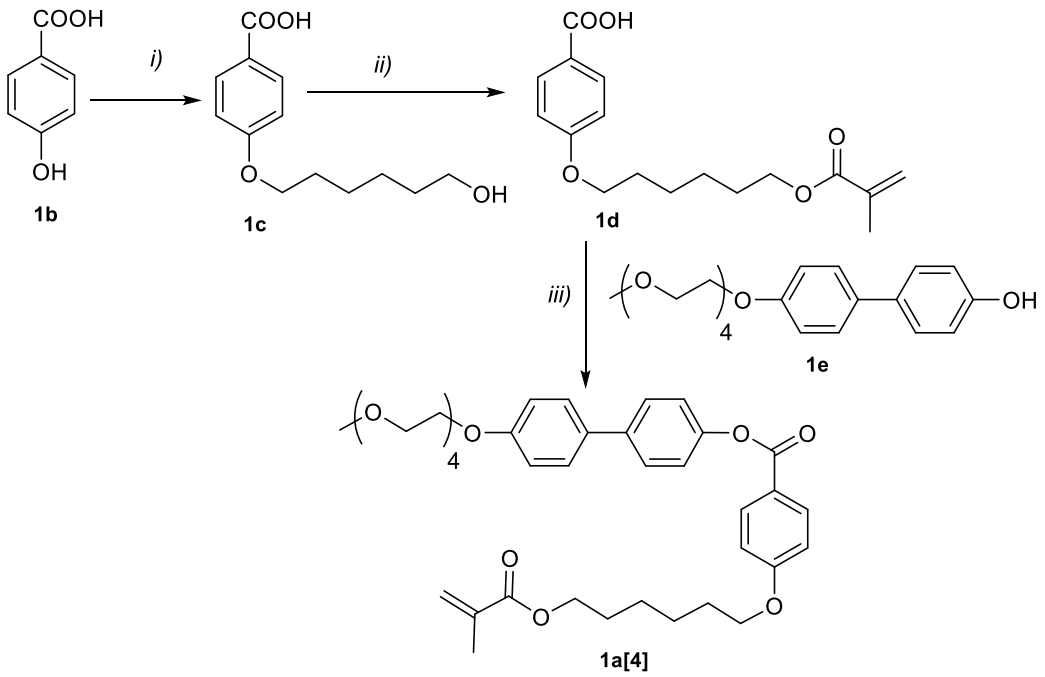

Scheme 1. Preparation of LC monomer matrix **1a[4]**. Reagents and conditions: (*i*) 1). $OH(CH_2)_6$-OTs, *t*-BuOK, EtOH, reflux, 12 h. 2). H^+, 65–70% yield; (*ii*) Methacryloyl chloride, NEt_3, THF, rt, 12 h, 35–40 % yield; (*iii*) **1e**, DMPA, DCC, CH_2Cl_2, rt, 18 h, 45–50% yield.

Synthesis of the monomeric derivative **2a** is shown in Scheme 2. Derivatives **2c** [35] and **2d** [36] were synthesized in 35% and 84% yields, respectively, according to the previously known procedures. The subsequent reaction of **2d** with ethyl 4-hydroxybenzoate in the presence of K_2CO_3, followed by deprotection of the benzoate ester in the product by refluxing with 20% KOH and acidification of the resulting solution, gave **2a** in 62–70% yield. A polymerization inhibitor, 3,5-di-tert-butylcatechol (0.01 wt%), was used during the preparation of these derivatives to prevent the polymerization of samples in light.

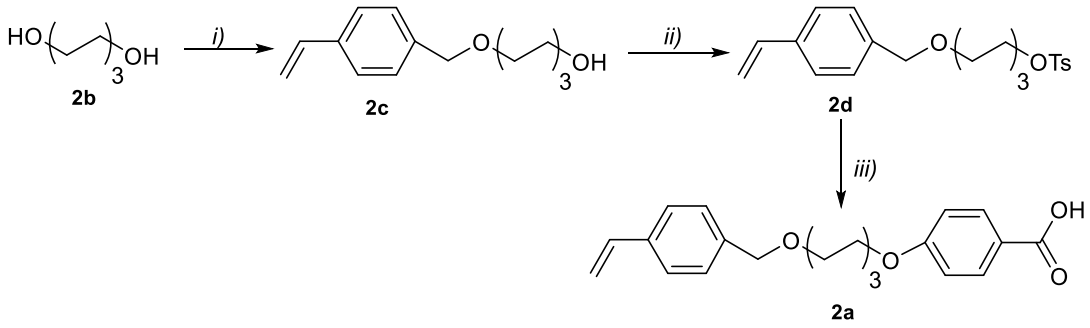

Scheme 2. Preparation of the monomer intermediate **2a**. Reagents and conditions: (*i*) NaOH, 4-vinylbenzyl chloride, 50 °C, 4 h, 35% yield; (*ii*) TsCl, NEt_3, CH_2Cl_2, rt, 84% yield; (*iii*) 1). Ethyl 4-hydroxybenzoate, K_2CO_3, reflux, 12 h, 2). 20% KOH, 3h, reflux, 3). 10% HCl, 62–70%.

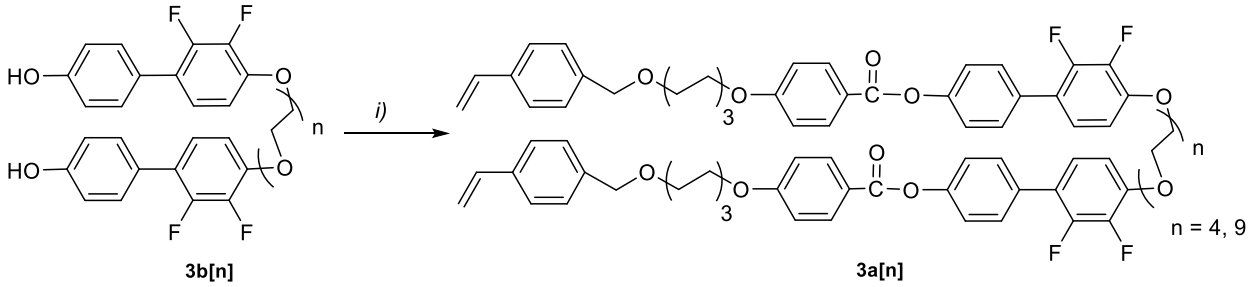

Scheme 3. Preparation of dimeric LC monomer **3a[n]**. Reagents and conditions: (*i*) **2a**, EDC·HCl or DCC, DMAP, CH_2Cl_2, rt, 12 h, 48–68% yield.

Synthesis of the monomeric LC matrix **3a[4]** and **3a[9]** is shown in Scheme 3. Hydroxyphenyl derivatives **3b[n]** were conveniently prepared according to the previously demonstrated procedure (Scheme 2, Chapter B3). Monomeric LC derivatives **3a[4]** and **3a[9]** were obtained through the Steglich type esterification of the corresponding **3b[n]** derivative with acid derivative **2a** in the presence of a carbodiimide dicyclohexylcarbodiimide (DCC) for the synthesis of **3a[4]** and *N*-(3-dimethylaminopropyl)-*N′*-ethylcarbodiimide hydrochloride (EDC·HCl), for the synthesis of **3a[9]**) and catalytic amounts of 4-dimethylaminopyridine (DMAP). Steglich-type

esterification using DCC for the synthesis of **3a[9]** was inefficient due to the difficulties in removing the urea biproduct formed during the reaction.

Electrolyte samples under investigation were prepared by dissolving Li^+ salt **4a[Li]** or **4b[Li]** (Figure 1) in appropriate LC matrix. Sample **1a[4]–4a[Li]** is a 10 mol% solution of **4a[Li]** in **1a[4]** and sample **3a[9]–5a[Li]** is a 10 mol% solution of **5a[Li]** in **3a[9]**.

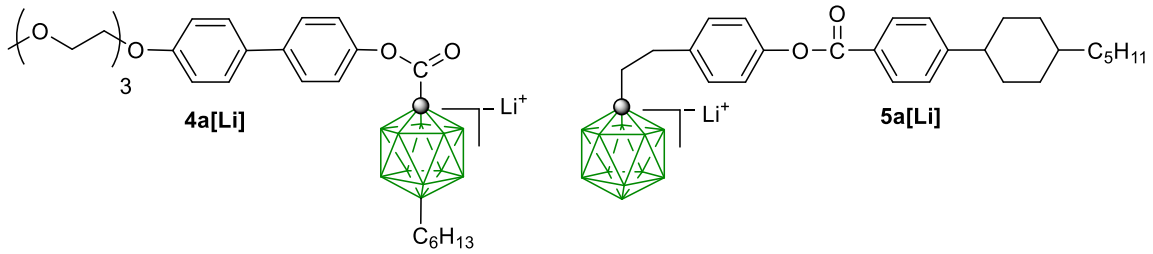

Figure 1. Molecular structures of the Li^+ salts **4a[Li]** and **5a[Li]** used in the preparation of the electrolyte samples **1a[4]–4a[Li]** and **3a[9]–5a[Li]**.

2.2 Liquid crystalline behavior

Thermal behavior of monomeric LC matrices and electrolyte samples was investigated using polarized optical microscopy (POM) and differential scanning calorimetry (DSC).

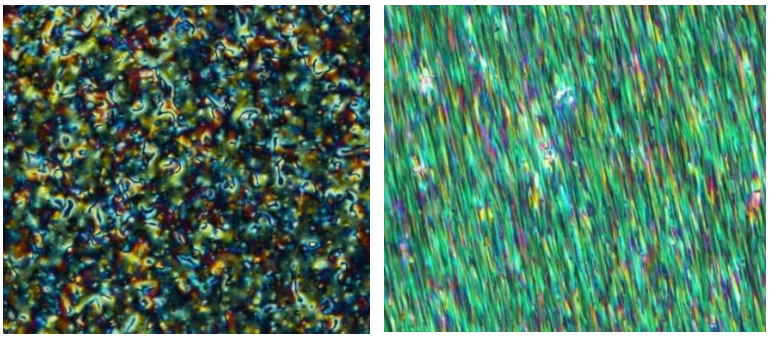

Figure 2. Optical textures for the monomer matrix **3a[9]** observed in the same region on cooling: N phase at 81 °C (left), Sm phase at 74 °C (right).

Analysis of the derivatives **1a[4]** and **3a[4]** was difficult due to the issue of partial polymerization of the sample before its clearing temperature of 77 °C and 170 °C, respectively. POM analysis of the derivative **3a[9]** showed characteristic textures of smectic (Sm) and nematic (N) phases (Figure 2). DSC thermograms for the monomer matrix **3a[9]** and electrolyte sample **3a[9]–5a[Li]** are shown in Figure 3. Matrix **3a[9]** exhibited an enantiotropic transition with Sm and N phases, with a clearing temperature of 81 °C. The transition from the Sm-Cr phase was not observed on cooling due to the supercooling effect. The addition of Li^+ salt **5a[Li]** to monomer **3a[9]** destabilized the N phase in favour of the Sm phase.

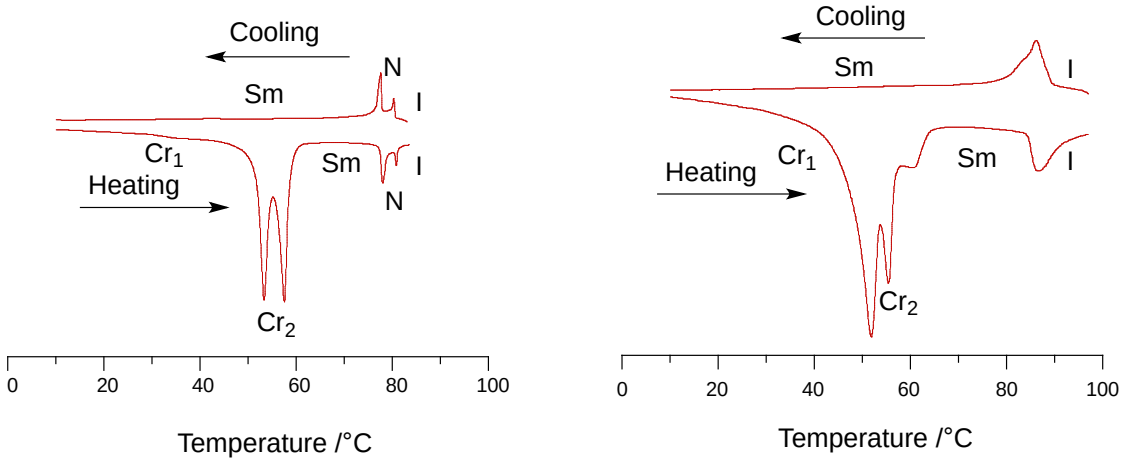

Figure 3. DSC trace for the monomer matrix **3a[9]** (left) and electrolyte sample **3a[9]–5a[Li]** (right). Heating and cooling rates are 10 K min^{-1}.

2.3 Powder XRD analysis

Powder XRD measurements were performed for the monomer LC matrix **3a[9]** and a representative diffractogram is shown in Figure 4. The presence of a sharp signal in the small angle region (*d*-spacing of 41.94 Å) and a diffuse peak in the wide angle region (*d*-spacing of 4.41 Å) confirmed a fluid Sm phase.

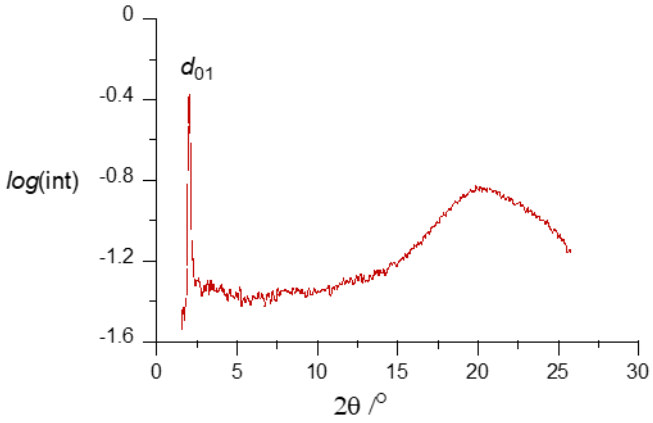

Figure 4. Powder XRD pattern of **3a[9]** in the smectic phase taken at 70 °C.

2.4 Alignment of electrolyte samples

The alignment of electrolyte samples was studied using ITO cells with varying thickness, cells coated with various alignment materials, including polyimides and nylons, and cells with cross-rubbed surfaces. The goal was to achieve a parallel alignment of the LC electrolyte sample in its smectic phase with ion conducting channels perpendicular to the plane of the cell (Figure 5).

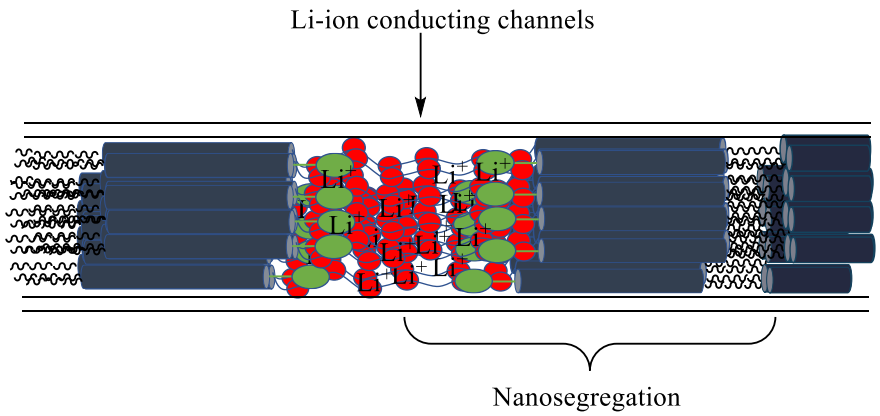

Figure 5. Schematic representation of a parallelly aligned electrolyte sample in the smectic phase with Li-ion conducting channels perpendicular to the plane of the cell.

Initial investigations were focused on electrolyte sample **1a[4]–4a[Li]**. However, only a partial alignment of this sample was achieved. The main challenges were the premature

polymerization of the electrolyte sample during cell filling (Figure 6) and the short circuit of the cell when an external electric field was applied to align the sample. Acrylates undergo radical and nucleophile-induced polymerization. Polymerization observed for sample **1a[4]–4a[Li]** could be base- or nucleophile-induced because the high electron density renders the faces of the [*closo*-1-$CB_{11}H_{12}]^-$ cluster Lewis basic. An attempt to avoid short circuit by using cells with a SiO_2 protective layer was not successful. To account for the issue of a short circuit, the cell components were investigated using the precision component analyzer-6425 before and after filling the electrolyte sample. It was found that the capacitance and resistance for the empty cell of thickness 15 μm were 115.9 pF and 2.2 GΩ respectively, whereas those of a cell filled with the electrolyte samples were 240 pF and 14 kΩ. This suggested high ionic conductivity between the electrodes of the filled cell, which led to a short-circuit in the cell when an external electric field was applied.

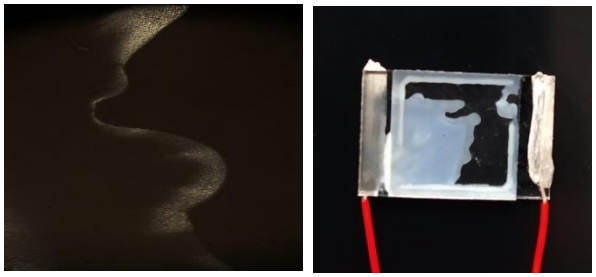

Figure 6. Premature polymerization of the electrolyte sample in an ITO cell.

In an attempt to improve the electrolyte system and resolve the issue of premature polymerization, a new electrolyte system was developed with modifications in the structure of both the LC matrix and Li^+ salt. Lateral fluorination in the modified host matrix **3a[n]** (Scheme 3) was to provide a transverse dipole in the monomer, which resulted in a negative dielectric anisotropy of the material. This was expected to facilitate a parallel alignment of the material when an external electric field is applied. Also, the polymerizable styrene group in the new design is stable towards

basic conditions, unlike the methyl acrylate in **1a[4]**. In the new design for the ionic additive, an alkyl chain is introduced at one of the apical positions of the [*closo*-$CB_{11}H_{12}]^{-1}$ anion, while the other apical boron atom remains unsubstituted. This design was expected to retain their function as ionic species and their ability to form dynamically ordered structures in the LC electrolyte system.

ITO cells with different alignment layers were tested initially for the modified electrolyte sample **3a[9]–5a[Li]** and the cells coated with nylon-11 and nylon-12 alignment layers provided a better parallel alignment. Further tests using nylon coated cells of different thicknesses revealed a decrease in the alignment of the sample with an increase in cell thickness. The best alignment was obtained in the cell with a thickness of 5 μm. Currently, investigations are going on to obtain parallelly aligned electrolyte samples with thickness up to 50 μm.

2.5 Polymerization of the aligned electrolyte sample

In an initial attempt to prepare the polymer electrolytes, we used the partially aligned electrolyte sample **1a[4]–4a[Li]**. Thus, a few minutes of UV irradiation (λ = 364 nm) of the electrolyte sample resulted in complete polymerization. Free-standing solid polymer electrolyte films were obtained by breaking the sample cell and peeling off the electrolyte film. The partially aligned electrolyte films obtained in this way had a thickness of approximately 70 μm and a size of approximately 1 cm (Figure 7).

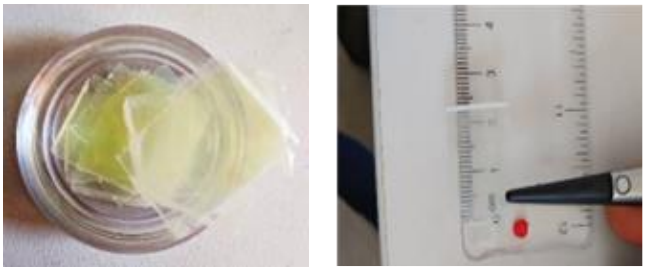

Figure 7. Solid polymer electrolyte obtained from electrolyte sample **1a[4]–4a[Li]**.

Subsequently, a fully aligned polymer electrolyte of thickness 5 μm was prepared by polymerizing a parallelly aligned electrolyte sample **3a[9]–5a[Li]** in its Sm phase. POM analysis of polymer electrolyte sample **3a[9]–5a[Li]** revealed that the Sm phase arrangement is maintained over a wide temperature range, with only thermal expansion observed upon heating. This is evident from the change in birefringence with increasing temperature (Figure 8). This polymer electrolyte was found to be stable after multiple heating and cooling cycles in the temperature range 0 to 130 °C. The preparation of aligned polymer electrolytes with a thickness up to 50 μm is in progress.

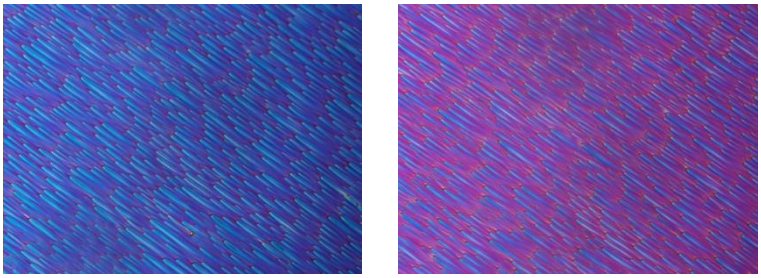

Figure 8. POM image of the aligned 5 μm thick polymer electrolyte sample **3a[9]–5a[Li]** taken in the same region at 30 °C (left) and 130 °C (right) in the cell.

2.6 Testing of the solid polymer electrolytes in Li-ion battery

So far, only a partially aligned polymer electrolyte sample **1a[4]–4a[Li]** was tested in Li-ion battery. Thus, several CR-2032 type coin cells were prepared (Figure 9). Nanostructured lithium iron phosphate ($LiFePO_4$) with particle sizes approximately 3 μm (80% particles in the 3.5 μm ±1 μm range) and conductive carbon coating were used as the cathode material, and lithium titanate ($Li_4Ti_5O_{12}$) was used as the anode material in the battery. The total nominal capacity for the battery was found to be 1.6 mAh, which is very low for a coin-cell battery.

Figure 9. CR2032 type coin cells made using the partially aligned solid polymer electrolyte sample **1a[4]–4a[Li]**.

2.6.1 Electrochemical impedance spectroscopy (EIS) measurements

Nyquist plots of the EIS measurements performed for the coin cells are shown below (Figure 10).

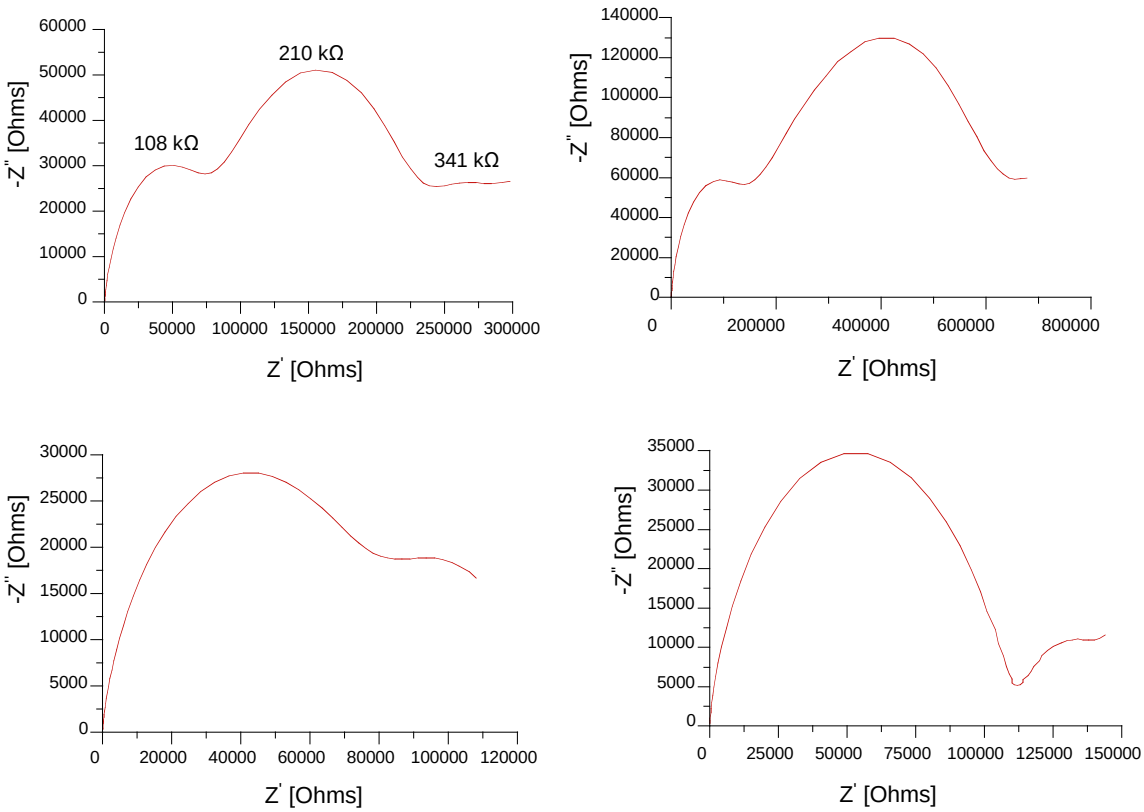

Figure 10. Clockwise: Nyquist plot for the coin cells 1, 2, 3, and 4 in the frequency range of 200 KHz to 10 MHz.

The overall internal resistance of the coin cells at 80 °C was measured using broadband dielectric spectroscopy (BDS), which revealed high internal resistance in the cells. For example, the internal resistance in cell-1 was estimated to be R (electrolyte) = 108 kΩ, R (passive layer) = 210 kΩ, and R (charge transfer) = 341 kΩ (Figure 10). The reason for the high internal resistance is presumed to be due to the wrong alignment of the molecules in the SPE or poor electrode-electrolyte contact.

2.6.2 Galvanostatic cycling

Charge-discharge cycles in the range of 2.0–3.9 V with the current C/1 for the first half cycle and 2C or C/1 for the second half cycle were performed in the Digatron BTS 600 battery test facility at the European Space Agency (ESA) to check the performance of the coin cells (Table 1).

Battery	**Test No.**	**No. of cycle**	**Voltage range (V)**	**Current Limit (mAh)**	
				Charging	**Discharging**
1	1	5	2.2-3.9	1.6	3.2
	2	100	2.2-3.9	1.6	1.6
	3	600	2.2-3.9	1.6	1.6
2	1	10	2.2-3.9	1.6	3.2
	2	100	2.2-3.9	1.6	1.6
3	1	100	2.2-3.9	1.6	3.2
	2	100	2.2-3.9	1.6	1.6

Table 1. Battery tests carried out in Digatron BTS 600 battery test facility.

During the charging cycle, the voltage of the battery reached its upper voltage limit (3.9 V) immediately (in a few seconds). However, when the charging was stopped, the voltage dropped to 0.5 V, which was below the lower voltage limit (2.0 V) of the battery. This behaviour was unexpected and the same result was observed for all three batteries tested. There was no

improvement, even for the test conducted with 600 cycles. To understand this issue, a test was performed by setting a one-hour time limit for charging, but the result was the same (Figure 11). This indicates that no energy was stored during the charging cycle and it can be attributed to the coin cell's high internal resistance. Currently, efforts are being made to address these issues.

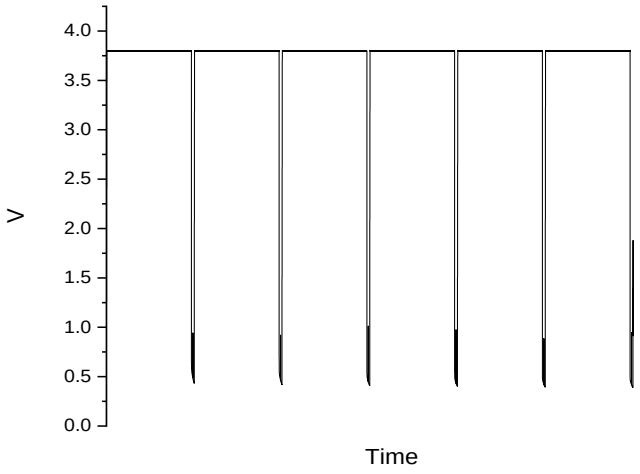

Figure 11. Battery cycling time curve with charging limit set to one hour.

3. SUMMARY AND CONCLUSIONS

We have synthesized and tested the first prototype of solid polymer electrolyte designed for Li-ion battery applications. The liquid-crystalline behavior of the samples was studied and confirmed using differential scanning calorimetry (DSC), polarized optical microscopy (POM), and powder XRD. Alignment of the electrolyte sample was achieved using ITO cells coated with different alignment layers, and polymerization was achieved by UV irradiation ($\lambda = 364$ nm).

Several CR2032 type coin cells were built using the partially aligned polymer electrolyte sample **1a[4]–4a[Li]**. EIS measurements conducted for these cells showed high internal resistance (kΩ range). This is assumed to be the result of improper alignment of the electrolyte and poor interfacial contact between the electrode and the electrolyte material. Also, the overall nominal

capacity of the cell was found to be 1.6 mAh and the battery test carried out clearly showed that no energy was stored in the cell during the charging process.

The development of a new batch of coin cell batteries using a modified polymer electrolyte sample **3a[9]–5a[Li]** is in progress. The new electrolyte design is expected to resolve the issues associated with the previous design by providing better alignment. So far, we have achieved the preparation of a fully aligned polymer electrolyte sample with a thickness of up to 5 μm, and currently efforts are being made to obtain sample with a thickness of up to 50 μm.

4. EXPERIMENTAL SECTION

General procedures

Reagents and solvents were obtained commercially. NMR spectra were obtained at 400 MHz (^{1}H), 100 MHz (^{13}C), 128 MHz (^{11}B), 376 MHz (^{19}F), in $CDCl_3$ and referenced to the solvent (δ = 7.26 ppm for ^{1}H and δ = 77.16 ppm for ^{13}C) or in DMSO-d_6 and referenced to the solvent (δ = 2.50 ppm for ^{1}H and δ = 39.52 ppm for ^{13}C) [33] or to an external sample of neat CF_3COOH in $CDCl_3$ and DMSO-d_6 (^{19}F NMR δ = 76.55 ppm). ^{19}F NMR chemical shifts were taken from the H–decoupled spectra.

Optical microscopy and phase identification were performed using a polarized microscope equipped with a hot stage. Thermal analysis was run on a TA Discovery DSC 2500 using samples of about 1.0 mg and a heating rate of 10 K min^{-1} under a flow of nitrogen gas. Melting points were determined on a Melt-Temp II apparatus in capillaries and they are uncorrected. High-resolution mass spectrometry was conducted with the TOF-MS ES method. Broad angle X-ray diffraction studies were performed for unaligned samples using a Bruker D8 GADDS instrument (Cu Kα radiation, λ=1.54 Å, incident beam formed by Göbel mirror monochromator and point collimator 0.5 mm, two-dimensional detector Vantec 2000).

Impedance spectroscopy

Electrochemical impedance spectroscopy measurements were performed using a Novocontrol BDS device at the ESTEC facility of the European Space Agency. The instrument consists of a spectrometer with sample cells, a temperature control system, and a computer with software for data acquisition and analysis. During the measurement, the sample cell is placed in a cryostat, which is connected to a liquid nitrogen dewar and allows for temperature cycling between -150 and 500 °C. The tests were conducted at 80 °C after stabilization, and the same temperature was maintained throughout the test. EIS measurements were performed in the range of 200 kHz to 10 MHz.

Galvanostatic cycling

The galvanostatic cycling test was performed using a Digatron BTS-600 battery test system. This is the third generation of a computer-controlled test system that allows testing the life cycle and capacity of a battery. The coin cells were thermostated at 80 °C in a thermal chamber for several hours prior to the test. The total nominal capacity for the battery was 1.6 mAh, and the minimum current limit at which the Digatron BTS 600 facility can operate is 1.6 mAh. So, the charge-discharge cycles were performed in the range of 2.2–3.9 V with the current C /1 for the first one and 2C or C/1 for the second half-cycles.

Preparation of the binary mixture

Electrolyte samples **1a[4]–4a[Li]** and **3a[9]–5a[Li]** were prepared by evaporating a solution of the corresponding monomer matrix (**1a[4]** or **3a[9])** and 10 mol% of Li^+ salt (**4a[Li]**$^+$ or **5a[Li]**$^+$) in CH_2Cl_2 using a rotary evaporator and drying it under high vacuum.

Preparation of 3a[4]

To a suspension of **3b[4]** (70 mg, 0.12 mmol, 1.0 eq.) and 4-hexylbenzoic acid (90 mg, 0.26 mmol, 2.2 eq.) in CH_2Cl_2 (4 mL), were added 1-ethyl-3-(3-dimethylaminopropyl)-carbodiimide hydrochloride (EDC·HCl, 71 mg, 0.37 mmol, 3.2 eq.) and 4-dimethylaminopyridine (DMAP, 9 mg, 0.069 mmol, 0.6 eq.). The reaction mixture was stirred overnight at room temperature. Aluminium foil was used to protect the reaction from light to avoid polymerization. Reaction progress was monitored using TLC (SiO_2, CH_2Cl_2/EtOAc, 9:1). After the reaction was complete, water (10 mL) was added in to the reaction mixture and CH_2Cl_2 layer was extracted (3 x 5 mL). The combined organic layer was dried over Na_2SO_4 and concentrated using a rotary evaporator to obtain the crude product. The target compound was isolated by column chromatography (SiO_2, CH_2Cl_2/EtOAc, 9:1) to give 72 mg (48% yield) of **3a[4]** as a white solid. ^{1}H NMR (400 MHz, $CDCl_3$): δ 8.15 (d, *J* = 8.9 Hz, 4H), 7.54 (d, *J* = 7.8 Hz, 4H), 7.40 (d, *J* = 8.0 Hz, 4H), 7.34–7.26 (m, 8H), 7.10 (td, *J* = 8.4, 2.3 Hz, 2H), 6.97 (d, *J* = 8.9 Hz, 4H), 6.86-6.81 (m, 2H), 6.72 (dd, *J* = 17.6, 10.9 Hz, 2H), 5.75 (d, *J* = 17.7 Hz, 2H), 5.24 (d, *J* = 10.9 Hz, 2H), 4.50 (s, 4H), 4.26 (t, *J* = 4.8 Hz, 4H), 4.04 (t, *J* = 6.5 Hz, 4H), 3.92 (t, *J* = 4.8 Hz, 4H), 3.8–3.69 (m, 8H), 3.49 (t, *J* = 6.5 Hz, 4H), 1.84 (quint, *J* = 6.7 Hz, 4H), 1.67 (quint, *J* = 6.7 Hz, 4H), 1.57–1.41 (m, 8H). ^{19}F{^{1}H} NMR (376 MHz, $CDCl_3$): δ -139.7 (d, *J* = 19.8 Hz), -156.2 (d, *J* = 19.7 Hz). ^{13}C{^{1}H} NMR (100 MHz, $CDCl_3$): δ 165.0, 163.7, 150.8, 149.0 (d, J_{F-C} = 243.1 Hz), 147.7 (q, J_{F-C} = 6.7 Hz), 142.0 (d, J_{F-C} = 261.2 Hz), 138.4, 137.0, 136.7, 132.5, 129.9 (d, J_{F-C} = 3.0 Hz), 128.0, 126.4, 123.8, 122.8 (d, J_{F-C} = 10.5 Hz), 122.1, 121.6, 114.4, 113.9, 110.1, 72.8, 71.1, 70.8, 70.3, 69.7, 69.6, 68.3, 29.8, 29.2, 26.1, 26.0. HRMS (ESI-TOF) *m/z*: $[M + Na]^+$ calcd for $C_{76}H_{78}F_4O_{13}$: 1297.5276, found: 1297.5198. Anal. Calcd for $C_{76}H_{78}F_4O_{13}$: C, 71.57; H, 6.16. Found: C, 71.46; H, 6.12.

Preparation of 3a[9]

To a suspension of **3b[9]** (488 mg, 0.59 mmol, 1.0 eq.) and 4-hexylbenzoic acid (462 mg, 1.30 mmol, 2.2 eq.) in CH_2Cl_2 (15 mL), were added 1-ethyl-3-(3-dimethylaminopropyl)-carbodiimide hydrochloride (EDC·HCl, 342 mg, 1.78 mmol, 3 eq.) and 4-dimethylaminopyridine (DMAP, 72 mg, 0.59 mmol, 1 eq.). The reaction mixture was stirred overnight at room temperature. Aluminium foil was used to protect the reaction from light to avoid polymerization. Reaction progress was monitored using TLC (SiO_2, CH_3CN/CH_2Cl_2, 1:4). After the reaction was complete, water (20 mL) was added in to the reaction mixture and CH_2Cl_2 layer was extracted (3 × 15 mL). The combined organic layer was dried over Na_2SO_4 and concentrated using a rotary evaporator to obtain the crude product. The target compound was isolated by column chromatography (SiO_2, CH_3CN/CH_2Cl_2, 2:3) to give 640 mg (72% yield) of **3a[9]** as a white solid. The typical yield of the reaction was in the range 56–72%. ^{1}H NMR (400 MHz, DMSO-d_6): δ 8.07 (d, J = 8.8 Hz, 4H), 7.59 (d, J = 8.1 Hz, 4H), 7.43 (d, J = 7.9 Hz, 4H), 7.35 (d, J = 8.4 Hz, 4H), 7.32–7.27 (m, 6H), 7.14–7.08 (m, 6H), 6.71 (dd, J = 17.7, 10.9 Hz, 2H), 5.80 (d, J = 17.6 Hz, 2H), 5.23 (d, J = 10.9 Hz, 2H), 4.42 (s, 4H), 4.25 (t, J = 4.3 Hz, 4H), 4.05 (t, J = 6.5 Hz, 4H), 3.78 (t, J = 4.4 Hz, 4H), 3.60 (t, J = 4.9 Hz, 4H), 3.55–3.46 (m, 24H), 3.41 (t, J = 6.4 Hz, 4H), 1.73 (quint, J = 6.7 Hz, 4H), 1.56 (quint, J = 6.7 Hz, 4H), 1.44–1.36 (m, 8H). ^{19}F{^{1}H} NMR (376 MHz, DMSO-d_6): δ -140.5 (d, J = 20.8 Hz), -156.9 (d, J = 20.8 Hz). ^{13}C{^{1}H} NMR (100 MHz, DMSO-d_6): δ 164.2, 163.3, 150.4, 147.9 (d, $J_{F\text{-}C}$ = 254.1 Hz), 147.2 (q, $J_{F\text{-}C}$ = 3.4 Hz), 140.6 (d, $J_{F\text{-}C}$ = 258.5 Hz), 138.5, 136.4, 136.2, 132.1, 131.6, 129.7 (d, $J_{F\text{-}C}$ = 2.7 Hz), 127.7, 126.0, 124.3, 124.2, 122.3, 121.3 (d, $J_{F\text{-}C}$ = 7.3 Hz), 120.7, 114.7, 114.0, 110.4, 71.5, 70.0, 69.8, 69.5, 69.0, 68.7, 68.0, 29.2, 28.5, 25.5, 25.3. HRMS (MALDI) *m/z*: $[M + Na]^+$ calcd for $C_{86}H_{98}F_4O_{18}$: 1518.67, found: 1519.00. Anal. Calcd for $C_{86}H_{98}F_4O_{18}$: C, 69.06; H, 6.60. Found: C, 69.21; H, 6.83.

Preparation of 2c

1,6-hexanediol (**2b**, 6.00 g, 50 mmol, 1.0 eq.) and NaOH (2.70 g, 67.5 mmol, 1.33 eq.) was heated at 50 °C for 2 h. To the waxy material formed, 4-vinyl chloride (4.66 mL, 33.5 mmol, 0.66 eq.) was added over a period of 15 minutes and allowed to stir at 50 °C for another 2 h. The reaction mixture was poured in to ice-cold water. Extraction was done in EtOAc (3 × 20 mL EtOA). The combined organic layer was dried over Na_2SO_4 and the solvent was removed in rotary evaporator to get the crude product. The target compound was isolated by column chromatography (SiO_2, EtOAc/Hexane, 1:4) to get 2.74 g (35% yield) of **2c** as a colorless oily liquid. ^{1}H NMR (400 MHz, $CDCl_3$): δ 7.39 (d, *J* = 8.2 Hz, 2H), 7.29 (d, *J* = 8.2 Hz, 2H), 6.71 (dd, *J* = 17.6, 10.9 Hz, 1H), 5.74 (d, *J* = 17.6 Hz, 1H), 5.23 (d, *J* = 10.9 Hz, 1H), 4.49 (s, 2H), 3.64–3.60 (m, 2H), 3.46 (t, *J* = 6.6 Hz, 2H), 1.67–1.51 (m, 4H), 1.43–1.32 (m, 4H). ^{13}C{^{1}H} NMR (100 MHz, $CDCl_3$): δ 138.3, 137.0, 136.9, 136.7, 128.0, 127.2, 126.3, 125.5, 114.1, 113.8, 63.0, 32.8, 29.8, 28.7, 26.1, 25.7. HRMS (ESI-TOF) *m/z*: $[M + Na]^+$ calcd for $C_{15}H_{22}O_2$: 257.1517, found: 257.1517.

Preparation of 2d

To an ice-cold solution of **2c** (5.00 g, 21.33 mmol, 1.0 eq.) and NEt_3 (9 mL, 64 mmol, 3 eq.) in CH_2Cl_2 (25 mL), was added TsCl (4.47 g, 23.47 mmol, 1.1 eq.). The clear solution formed was stirred at room temperature for 12 h. Extraction was done in CH_2Cl_2. The organic layer was collected and dried over Na_2SO_4. The crude product was obtained by evaporating the solvent in a rotary evaporator. Purification of the crude product was done using column chromatography (SiO_2, EtOAc/Hexane, 1:4) to give 7.41 g (89% yield) of **2d** as a white solid. The typical yield of the reaction was in the range 84-89%. ^{1}H NMR (400 MHz, $CDCl_3$): δ 7.78 (d, *J* = 8.4 Hz, 2H), 7.39 (d, *J* = 8.2 Hz, 2H), 7.33 (d, *J* = 8.0 Hz, 2H), 7.28 (d, *J* = 8.1 Hz, 2H), 6.71 (dd, *J* = 17.6, 10.9 Hz, 1H), 5.74 (d, *J* = 17.6 Hz, 1H), 5.23 (d, *J* = 10.4 Hz, 1H), 4.46 (s, 2H), 4.01 (t, *J* = 6.5 Hz, 2H),

3.41 (t, *J* = 6.5 Hz, 2H), 2.44 (s, 3H), 1.65 (quint, *J* = 6.9 Hz, 2H), 1.59–1.52 (m, 2H), 1.36–1.27 (m, 4H). $^{13}C\{^{1}H\}$ NMR (100 MHz, $CDCl_3$): δ 144.8, 138.3, 137.0, 136.7, 133.3, 129.9, 128.02, 127.96, 126.4, 113.9, 72.75, 70.71, 70.2, 29.7, 28.9, 25.7, 25.4, 21.8. HRMS (ESI-TOF) *m/z*: $[M + H]^+$ calcd for $C_{22}H_{29}O_4S$: 389.1787, found: 389.1805.

Preparation of 2a

A solution of 4-hydroxy ethyl benzoate (500 mg, 3.01 mmol, 1 eq.) and K_2CO_3 (1.25 g, 9.03 mmol, 3 eq.) in EtOH (20 mL) was heated for 30 minutes. **2d** (1.29 g, 3.31 mmol, 1.1 eq.) was added to the precipitate formed, and it was refluxed overnight. 20% aq. KOH (40 mL) was added in to the reaction mixture and it was refluxed for another 3 h. The clear solution formed was cooled to room temperature and it was acidified using 10% HCl to obtain a white precipitate. The precipitate was collected by filtration and dried under high vacuum to give 758 mg (71% yield) of pure **2a** as a white powder. The typical yield of the reaction was in the range of 62-71%. ^{1}H NMR (400 MHz, DMSO-d_6): δ 12.61 (s, 1H), 7.87 (d, *J* = 8.9 Hz, 2H), 7.43 (d, *J* = 8.2 Hz, 2H), 7.28 (d, *J* = 8.1 Hz, 2H), 6.99 (d, *J* = 8.9 Hz, 2H), 6.72 (dd, *J* = 17.7, 10.9 Hz, 1H), 5.81 (d, *J* = 17.2 Hz, 1H), 5.24 (d, *J* = 10.9 Hz, 1H), 4.43 (s, 2H), 4.02 (t, *J* = 6.5 Hz, 2H), 3.42 (t, *J* = 6.5 Hz, 2H), 1.72 (quint, *J* = 6.6 Hz, 2H), 1.56 (quint, *J* = 6.8 Hz, 2H), 1.45-1.37 (m, 4H). $^{13}C\{^{1}H\}$ NMR (100 MHz, DMSO-d_6): δ 167.0, 162.3, 138.5, 136.4, 136.2, 131.3, 127.7, 126.0, 122.9, 114.2, 114.1, 71.5, 69.5, 67.7, 29.1, 28.5, 25.5, 25.3. HRMS (ESI-TOF) *m/z*: $[M + Na]^+$ calcd for $C_{22}H_{26}O_4$: 377.1729, found: 377.1735. Anal. Calcd for $C_{22}H_{26}O_4$: C, 74.55; H, 7.39. Found: C, 74.43; H, 7.11.

Preparation of 1a[4]

To a suspension of **1d** (47 mg, 0.15 mmol, 1.0 eq.) and **1e** (64 mg, 0.17 mmol, 1.1 eq.) in CH_2Cl_2 (4 mL), were added dicyclohexylmethanediimine (DCC, 38 mg, 0.18 mmol, 1.2 eq.) and 4-dimethylaminopyridine (DMAP, 4 mg, 0.03 mmol, 0.2 eq.). The reaction mixture was stirred

overnight at room temperature. Progress in the reaction was monitored using TLC (SiO_2, MeCN/CH_2Cl_2, 1:4). After the reaction was complete, it was filtered and the collected filtrate was concentrated using a rotary evaporator to obtain the crude product. The target compound was isolated by column chromatography (SiO_2, MeCN/CH_2Cl_2, 1:4), followed by recrystallization in ethanol gave 53 mg (52% yield) of **1a[4]** as a white solid. ^{1}H NMR (400 MHz, $CDCl_3$): δ 8.16 (d, *J* = 8.9 Hz, 2H), 7.58 (d, *J* = 8.6 Hz, 2H), 7.51 (d, *J* = 8.8 Hz, 2H), 7.24 (d, *J* = 8.6 Hz, 2H), 7.00–6.96 (m, 4H), 6.10 (sext, *J* = 1.0 Hz, 1H), 5.56 (quint, *J* = 1.6 Hz, 1H), 4.18–4.15 (m, 4H), 4.05 (t, *J* = 6.4 Hz, 2H), 3.89 (t, *J* = 4.8 Hz, 2H), 3.76–3.72 (m, 2H), 3.70–3.64 (m, 8H), 3.59–3.51 (m, 2H), 3.38 (s, 3H), 1.95 (t, *J* = 1.3 Hz, 3H), 1.86 (quint, *J* = 6.5 Hz 2H), 1.73 (quint, *J* = 6.8 Hz, 2H), 1.56–1.47 (m, 4H). ^{13}C{^{1}H} NMR (100 MHz, $CDCl_3$): δ 165.2, 163.6, 158.4, 150.2, 138.5, 133.4, 132.4, 128.3, 127.8, 125.4, 122.1, 121.7, 115.1, 115.0, 114.4, 71.9, 70.9, 70.7, 70.6, 70.5, 69.9, 68.3, 68.2, 67.6, 64.7, 63.0, 59.2, 29.1, 28.7, 28.6, 26.0, 25.9, 25.8, 25.7, 18.5. HRMS (ESI-TOF) *m/z*: $[M + H]^+$ calcd for $C_{38}H_{48}O_{10}$: 665.3326, found: 665.3337. Anal. Calcd for $C_{38}H_{48}O_{10}$: C, 68.66; H, 7.28. Found: C, 67.92; H, 7.41.

5. AKNOWLEDGMENT

Financial support for this project is provided by European Space Agency (NPI 542) grant. This work involves contributions from several people. Dr. Rafał Jakubowski contributed to the synthesis of some of the intermediate compounds. Prof. Wiktor Piecek and Dr. Eva Oton of the Military University of Technology in Warsaw provided help in alignment of the electrolyte sample and preparation of the polymer electrolyte. Dr. Damian Pociecha from the University of Warsaw contributed to the powder XRD measurements. Dr. Leszek Niedzicki of the Technical University of Warsaw performed the EIS measurements and helped with the coin cell assembly. Help from Dr. Malgorzata Hołynska and Engr. Geraldine Palissat from the ESTEC facility of ESA is also

greatly acknowledged for their assistance in performing EIS measurements and battery tests, respectively.

6. REFERENCES

1. C. A. Vincent, Lithium batteries: A 50-year perspective, *Solid State Ion.*, **2000**, *134*, 159−167.
2. S. S. Shin, Y. K. Sun, K. Amine, Synthesis and electrochemical properties of $Li[Li_{(1-2x)/3}Ni_xMn_{(2-x)/3}]O_2$ as cathode materials for lithium secondary batteries, *J. Power Sources*, **2002**, *112*, 634−638.
3. A. R. Armstrong, P. G. Bruce, Synthesis of layered $LiMnO_2$ as an electrode for rechargeable lithium batteries, *Nature,* **1996**, *381*, 499−500.
4. J. M. Tarascon, J. Armand, Issues and challenges facing rechargeable lithium batteries, *Nature*, **2001**, *414*, 359−367.
5. F. Jiao, P. G. Bruce, Mesoporous crystalline β-MnO_2-a reversible positive electrode for rechargeable lithium batteries, *Adv. Mater.*, **2007**, *19*, 657−660.
6. P. G. Bruce, B. Scrosati, J. M. Tarascon, Nanomaterials for rechargeable lithium batteries, *Angew. Chem. Int. Ed*., **2008**, *47*, 2930−2946.
7. D. Mecerreyes, Polymeric ionic liquids: Broadening the properties and applications of polyelectrolytes, *Prog. Polym. Sci.*, **2011**, *36*, 1629−1648.
8. X. Xu, Z. F. Dou, E. L. Gu, L. Si, X. S. Zhou, J. C. Bao, Uniformly-distributed Sb nanoparticles in ionic liquid-derived nitrogen-enriched carbon for highly reversible sodium storage, *J. Mater. Chem. A*, **2017**, *5*, 13411−13420.
9. V. L. Martins, Advances on liquid electrolytes for Li-ion and Li metal batteries, *Curr.t Opin. Electrochem.*, **2023,** 101241.

10. M. Watanabe, M. L. Thomas, S. Zhang, K. Ueno, T. Yasuda, K. Dokko, Application of ionic liquids to energy storage and conversion materials and devices, *Chem. Rev.*, **2017**, *117*, 7190−7239.
11. Q. Zhao, S. Stalin, C. Z. Zhao, L. A. Archer, Designing solid-state electrolytes for safe, energy-dense batteries, *Nat. Rev. Mater.*, **2020**, *5*, 229−252.
12. (a) J. W. Fergus, Ceramic and polymeric solid electrolytes for lithium-ion batteries, *J. Power Sources*, **2010**, *195*, 4554−4569; (b) Z. Xue, D. He, X. Xie, Poly (ethylene oxide)-based electrolytes for lithium-ion batteries, *J. Mater. Chem. A*, **2015**, *3*, 19218−19253; (c) A. Manthiram, X. Yu, S. Wang, Lithium battery chemistries enabled by solid-state electrolytes, *Nat. Rev. Mater.*, **2017**, *2*, 1−16; (d) C. Sun, J. Liu, Y. Gong, D. P. Wilkinson, J. Zhang, Recent advances in all-solid-state rechargeable lithium batteries, *Nano Energy*, **2017**, *33*, 363−386.
13. H. Yang, N. Wu, Ionic conductivity and ion transport mechanisms of solid-state lithium-ion battery electrolytes: A review, *Energy Sci Eng.*, **2022**, *10*, 1643−1671.
14. R. Meziane, J. P. Bonnet, M. Courty, K. Djellab, M. Armand, Single-ion polymer electrolytes based on a delocalized polyanion for lithium batteries, *Electrochim. Acta*, **2011**, *57*, 14−19.
15. 86. F.M. Gray, Polymer Electrolytes, **1997**, (Royal Society of Chemistry, London)
16. J. B. Goodenough, Y. Kim, Challenges for rechargeable Li batteries, *Chem. Mater.*, **2010**, *22*, 587–603.
17. (a) B. Soberats, M. Yoshio, T. Ichikawa, H. Ohno, T. Kato, Zwitterionic liquid crystals as 1D and 3D lithium-ion transport media, *J. Mater. Chem. A*, **2015**, *3*, 11232−11238; (b) T. Onuma, E. Hosono, M. Takenouchi, J. Sakuda, S. Kajiyama, M. Yoshio, T. Kato, Noncovalent approach to liquid-crystalline ion conductors: high-rate performances and

room-temperature operation for Li-ion batteries, *ACS omega*, **2018**, *3*, 159−166; (c) Z**.** Liu, B. X. Dong, M. Misra, Y. Sun, J. Strzalka, S. N. Patel, F. A. Escobedo, P. F. Nealey, C. K. Ober, Self-assembly behavior of an oligothiophene-based conjugated liquid crystal and its implication for ionic conductivity characteristics, *Adv. Funct. Mater.*, **2019**, *29*, 1805220; (d) F. Yuan, S. Chi, S. Dong, X. Zou, S. Lv, L. Bao, J. Wang, Ionic liquid crystal with fast ion-conductive tunnels for potential application in solvent-free Li-ion batteries, *Electrochim. Acta*, **2019**, *294*, 249−259; (e) J. Uchida, B. Soberats, M. Gupta, T. Kato, Advanced functional liquid crystals, *Adv. Mater.*, **2022**, *34*, 2270171.

18. A. Kuwabara, M. Enomoto, E. Hosono, K. Hamaguchi, T. Onuma, S. Kajiyama, T. Kato, Nanostructured liquid-crystalline Li-ion conductors with high oxidation resistance: Molecular design strategy towards safe and high-voltage-operation Li-ion batteries, *Chem. Sci.*, **2020**, *11*, 10631−10637.
19. (a) D. Gopalakrishnan, S. Alkatie, A. Cannon, S. Rajendran, N. K. Thangavel, N. Bhagirath, E. M. Ryan, L. M. R. Arava, Anisotropic mass transport using ionic liquid crystalline electrolytes to suppress lithium dendrite growth, *Sustainable Energy Fuels*, **2021**, *5*, 1488−1497; (b) Y. Wang, C. J. Zanelotti, X. Wang, R. Kerr, L. Jin, W. H. Kan, T. J. Dingemans, M. Forsyth, L. A. Madsen, Solid-state rigid-rod polymer composite electrolytes with nanocrystalline lithium ion pathways, *Nat. Mater.*, **2021**, *20*, 1255−1263.
20. J. Sakuda, E. Hosono, M. Yoshio, T. Ichikawa, T. Matsumoto, H. Ohno, H. Zhou, T. Kato, Liquid-crystalline electrolytes for lithium-ion batteries: Ordered assemblies of a mesogen-containing carbonate and a lithium salt, *Adv. Funct. Mater.*, **2015**, *25*, 1206−1212.
21. D. Ndaya, R. Bosire, S. Vaidya, R. M. Kasi, Molecular engineering of stimuli-responsive, functional, side-chain liquid crystalline copolymers: Synthesis, properties and applications, *Polym. Chem.*, **2020**, *11*, 5937−5954.

22. X. L. Lyu, A. Q. Xiao, D. Shi, Y. J. Li, Z. H. Shen, E. Q. Chen, S. J. Zheng, X. H. Fan, Q. F. Zhou, Liquid crystalline polymers: Discovery, development, and the future, *Polymer*, **2020**, *202*, 122740.

23. A. Kuwabara, M. Enomoto, E. Hosono, K. Hamaguchi, T. Onuma, S. Kajiyama, T. Kato, Nanostructured liquid-crystalline Li-ion conductors with high oxidation resistance: Molecular design strategy towards safe and high-voltage-operation Li-ion batteries, *Chem. Sci.*, **2020**, *11*, 10631−10637.

24. K. Kishimoto, T. Suzawa, T. Yokota, T. Mukai, H. Ohno, T. Kato, Nano-segregated polymeric film exhibiting high ionic conductivities, *J. Am. Chem. Soc.*, **2005**, *127*, 15618−15623.

25. S. Wang, Q. Zeng, A. Wang, X. Liu, J. Chen, Z. Wang, L. Zhang, constructing stable ordered ion channels for a solid electrolyte membrane with high ionic conductivity by combining the advantages of liquid crystal and ionic liquid, *J. Mater. Chem. A*, **2019**, *7*, 1069−1075.

26. W. N. Lipscomb, Boron hydrides. New York: Benjamin;**1963**.

27. (a) R. N. Grimes, Boron clusters come of age, *J. Chem. Ed.*, **2004**, *81*, 658–672; (b) J. Poater, C. Vinas, I. Bennour, S. Escayola, M. Sola, F. Teixidor, Too persistent to give up: Aromaticity in boron clusters survives radical structural changes, *J. Am. Chem. Soc.*, **2020**, *142*, 9396–9407; (c) J. Aihara, Three-dimensional aromaticity of polyhedral boranes, *J. Am. Chem. Soc*., **1978,** *100*, 3339–3342; (d) R. B. King, Three-dimensional aromaticity in polyhedral boranes and related molecules, *Chem. Rev*., **2001**, *101*, 1119–1152; (d) J. Poater, M. Sola, C. Vinas, F. Teixidor, π Aromaticity and three-dimensional aromaticity: Two sides of the same coin?, *Angew. Chem. Int. Ed.*, **2014**, *53*, 12191–12195; *Angew. Chem.* **2014**, *126*, 12387–12391.

28. W. S. Tang, A. Unemoto, W. Zhou, V. Stavila, M. Matsuo, H. Wu, S. I. Orimo, T. J. Udovic, Unparalleled lithium and sodium superionic conduction in solid electrolytes with large monovalent cage-like anions, *Energy Environ. Sci.*, **2015**, 8, 3637–3645.

29. W. S. Tang, M. Matsuo, H. Wu, V. Stavila, W. Zhou, A. A. Talin, A. V. Soloninin, R. V. Skoryunov, O. A. Babanova, A. V. Skripov, Liquid-like ionic conduction in solid lithium and sodium monocarba-*closo*-decaborates near or at room temperature, *Adv. Energy Mater.*, **2016**, *6*, 1502237.

30. S. Kim, H. Oguchi, N. Toyama, T. Sato, S. Takagi, T. Otomo, D. Arunkumar, N. Kuwata, J. Kawamura, S. I. Orimo, A complex hydride lithium superionic conductor for high-energy-density all-solid-state lithium metal batteries, *Nat. Commun.*, **2019**, *10*, 1–9.

31. S. Kim, K. Kisu, S. I. Orimo, Stabilization of superionic-conducting high-temperature phase of $Li(CB_9H_{10})$ via solid solution formation with $Li_2(B_{12}H_{12})$, *Crystals*, **2021**, *11*, 330–340.

32. N. A. Clanton, T. E. Spiller, E. Ortiz, Z. Gao, J. M. Rodriguez-Poirier, A. J. DelMonte, D. E. Frantz, A metal-free reductive *N*-alkylation of indoles with aldehydes, *Org. Lett.*, **2021**, *23*, 3233–3236.

33. (a). M. P. Aldred, P. Vlachos, A. E. Contoret, S. R. Farrar, W. Chung-Tsoi, B. Mansoor, K. L. Woon, R. Hudson, S. M. Kelly, M. O'Neill, Linearly polarised organic light-emitting diodes (OLEDs): Synthesis and characterization of a novel hole-transporting photoalignment copolymer, *J. Mater. Chem.*, **2005**, *15*, 3208–3213; (b). R. M. Kumar, C. Saravanan, S. Senthil, P. Kannan, Synthesis, characterization and photolysis studies on liquid crystalline poly [4-(4′-x-biphenyl)yl-4″-(m-methacryloyloxyalkyloxy)-cinnamates], *Eur. Polym. J.*, **2007**, *43*, 2648–2659.

34. J. Guschlbauer, L. Niedzicki, L. Jacob, E. Rzeszotarska, D. Pociecha, P. Kaszyński, Liquid crystalline electrolytes derived from the 1,12-disubstituted [*closo*-$CB_{11}H_{12}]^-$ anion, *J. Mol. Liq.*, **2023**, *377*, 121525.

35. S. S. Shinde, B. S. Lee, D. Y. Chi, Polymer-supported protic functionalized ionic liquids for nucleophilic substitution reactions: Superior catalytic activity compared to other ionic resins, *Tetrahedron Lett.*, **2008**, *49*, 4245–4248.

36. S. I. Lee, K. H. Yoon, M. Song, H. Peng, K. A. Page, C. L. Soles, D. Y. Yoon, Structure and properties of polymer electrolyte membranes containing phosphonic acids for anhydrous fuel cells, *Chem. Mater.*, **2012**, *24*, 115–122.

37. R. Jakubowski, A. Pietrzak, A. C. Friedli, P. Kaszyński, C(1)-Phenethyl derivatives of [*closo*-1-$CB_{11}H_{12}]^-$ and [*closo*-1-$CB_9H_{10}]^-$ anions: Difunctional building blocks for molecular materials, *Chem. Eur. J.*, **2020**, *26*, 17481–17494.

Declaratory statement from co-authors of the published results

Prof. Piotr Kaszyński
Centre of Molecular and Macromolecular Studies,
Polish Academy of Sciences,
90-363 Łódź, Poland
E-mail: Piotr.Kaszynski@mtsu.edu

Łódź, 01.09.2023

Declaration

I hereby declare that in the preparation of publications:

1. L. Jacob, E. Rzeszotarska, A. Pietrzak, V. G. Young Jr., P. Kaszyński, Synthesis, structural analysis, and functional group interconversion in the [*closo*-$B_{10}H_8$-1,10-X_2]$^{2-}$ (X = CN, [$OCRNMe_2$]$^+$, OCOR, and [OH_2]$^+$) derivatives, Eur. J. Inorg. Chem., **2020**, 32, 3083–3093, DOI: 10.1002/ejic.202000456

2. L. Jacob, E. Rzeszotarska, M. Koyioni, R. Jakubowski, D. Pociecha, A. Pietrzak, P. Kaszyński, Tunable intermolecular charge transfer in ionic liquid crystalline derivatives of the [*closo*-$B_{10}H_{10}$]$^{2-}$ anion, *Chem. Mater.*, **2022**, 34, 6476–6491, DOI: 10.1021/acs.chemmater.2c01-165

3. J. Guschlbauer, L. Niedzicki, L. Jacob, E. Rzeszotarska, D. Pociecha, P. Kaszyński, Liquid crystalline electrolytes derived from the 1,12-disubstituted [*closo*-$CB_{11}H_{12}$]$^-$ anion, *J. Mol. Liq*., **2023**, 121525, DOI: 10.1016/j.molliq.2023.121525

My contribution was in performing quantum mechanical calculations, preparing the final draft, and submitting the manuscript for publication.

Piotr Kaszyński

Prof. Piotr Kaszyński

Ms. Edyta Rzeszotarska

E-mail:

Łódź, 30.08.2023

Declaration

I hereby declare that in the preparation of publications:

1. L. Jacob, E. Rzeszotarska, A. Pietrzak, V. G. Young Jr., P. Kaszyński, Synthesis, structural analysis, and functional group interconversion in the [*closo*-$B_{10}H_8$-1,10-X_2]$^{2-}$ (X = CN, [$OCRNMe_2$]$^+$, OCOR, and [OH_2]$^+$) derivatives, Eur. J. Inorg. Chem., **2020**, 32, 3083–3093, DOI: 10.1002/ejic.202000456

2. L. Jacob, E. Rzeszotarska, M. Koyioni, R. Jakubowski, D. Pociecha, A. Pietrzak, P. Kaszyński, Tunable intermolecular charge transfer in ionic liquid crystalline derivatives of the [*closo*-$B_{10}H_{10}$]$^{2-}$ anion, *Chem. Mater.*, **2022**, 34, 6476–6491, DOI: 10.1021/acs.chemmater.2c01-165

3. J. Guschlbauer, L. Niedzicki, L. Jacob, E. Rzeszotarska, D. Pociecha, P. Kaszyński, Liquid crystalline electrolytes derived from the 1,12-disubstituted [*closo*-$CB_{11}H_{12}$]$^-$ anion, *J. Mol. Liq.*, **2023**, 121525, DOI: 10.1016/j.molliq.2023.121525

My contribution was in the synthesis and characterization of some of the intermediate and final compounds.

Rzeszotarska Edyta

Ms. Edyta Rzeszotarska

Dr. Anna Pietrzak

Faculty of Chemistry, Łódź University of Technology,

Żeromskiego 114, 90-543 Łódź, Poland

E-mail: anna.pietrzak.1@p.lodz.pl

Łódź, 30.08.2023

Declaration

I hereby declare that in the preparation of publication:

1. L. Jacob, E. Rzeszotarska, A. Pietrzak, V. G. Young Jr., P. Kaszyński, Synthesis, structural analysis, and functional group interconversion in the [*closo*-$B_{10}H_8$-1,10-X_2]$^{2-}$ (X = CN, [$OCRNMe_2$]$^+$, OCOR, and [OH_2]$^+$) derivatives, Eur. J. Inorg. Chem., **2020**, 32, 3083–3093, DOI: 10.1002/ejic.202000456

2. L. Jacob, E. Rzeszotarska, M. Koyioni, R. Jakubowski, D. Pociecha, A. Pietrzak, P. Kaszyński, Tunable intermolecular charge transfer in ionic liquid crystalline derivatives of the [*closo*-$B_{10}H_{10}$]$^{2-}$ anion, *Chem. Mater.*, **2022**, 34, 6476–6491, DOI: 10.1021/acs.chemmater.2c01-165

My contribution was in the single crystal X-ray analysis of the compounds.

Anna Pietrzak

Dr. Anna Pietrzak

Dr. Damian Pociecha
Faculty of Chemistry,
University of Warsaw,
Żwirki i Wigury 101, 02-089 Warsaw, Poland
E-mail: pociu@chem.uw.edu.pl

Warsaw, 30.08.2023

Declaration

I hereby declare that my contribution in the preparation of publication listed below was performing and analyzing results of powder XRD measurements for the liquid crystalline samples.

1. L. Jacob, E. Rzeszotarska, M. Koyioni, R. Jakubowski, D. Pociecha, A. Pietrzak, P. Kaszyński, Tunable intermolecular charge transfer in ionic liquid crystalline derivatives of the [*closo*-$B_{10}H_{10}$]$^{2-}$ anion, *Chem. Mater.*, **2022**, 34, 6476–6491, DOI: 10.1021/acs.chemmater.2c01-165

2. J. Guschlbauer, L. Niedzicki, L. Jacob, E. Rzeszotarska, D. Pociecha, P. Kaszyński, Liquid crystalline electrolytes derived from the 1,12-disubstituted [*closo*-$CB_{11}H_{12}$]$^{-}$ anion, *J. Mol. Liq*., **2023**, 121525, DOI: 10.1016/j.molliq.2023.121525

Signature Not Verified
Dokument podpisany przez Damian Pociecha; UW
Data: 2023.08.30 10:08:56 CEST

Victor G. Young, Jr., Ph.D.

Director, X-Ray Crystallographic Laboratory

Department of Chemistry, University of Minnesota

192C Kolthoff Hall, 207 Pleasant St. SE, Minneapolis, MN 55455

email : vyoung@umn.edu

Minneapolis, 30.08.2023

Declaration

I hereby declare that in the preparation of publication:

L. Jacob, E. Rzeszotarska, A. Pietrzak, V. G. Young Jr., P. Kaszyński, Synthesis, structural analysis, and functional group interconversion in the [*closo*-$B_{10}H_8$-1,10-X_2]$^{2-}$ (X = CN, [OCRNMe$_2$]$^+$, OCOR, and [OH_2]$^+$) derivatives, *Eur. J. Inorg. Chem.*, **2020**, 32, 3083–3093, DOI: 10.1002/ejic.202000456

My contribution was in the single crystal X-ray analysis of some of the compounds.

Dr. Victor G. Young Jr.

Dr. Maria Koyioni
Department of Chemistry
University of Cyprus
P.O. Box 20537
1678 Nicosia, Cyprus
e-mail: mkogio01@ucy.ac.cy

Cyprus, 01.09.2023

Declaration

I hereby declare that in the preparation of publication:

L. Jacob, E. Rzeszotarska, M. Koyioni, R. Jakubowski, D. Pociecha, A. Pietrzak, P. Kaszyński, Tunable intermolecular charge transfer in ionic liquid crystalline derivatives of the [*closo*-$B_{10}H_{10}$]$^{2-}$ anion, *Chem. Mater.*, **2022**, *34*, 6476–6491, DOI: 10.1021/acs.chemmater.2c01-165

My contribution was in the synthesis and characterization of some of the intermediate compounds.

.....

Maria Koyioni

Dr. Rafał Jakubowski

Centre of Molecular and Macromolecular Studies,

Polish Academy of Sciences,

90-363 Łódź, Poland

E-mail: rrav@wp.pl

Łódź, 31.08.2023

Declaration

I hereby declare that in the preparation of publication:

L. Jacob, E. Rzeszotarska, M. Koyioni, R. Jakubowski D. Pociecha, A. Pietrzak, P. Kaszyński, Tunable intermolecular charge transfer in ionic liquid crystalline derivatives of the $[closo\text{-}B_{10}H_{10}]^{2-}$ anion, *Chem. Mater.*, **2022**, 34, 6476–6491, DOI: 10.1021/acs.chemmater.2c01-165

My contribution was in the synthesis and characterization of some of the intermediate compounds and in the preparation of the manuscript and supporting information.

Rafał Jakubowski

Dr. Rafał Jakubowski

Dr. Jannick Guschlbauer

(Langgasse 38, 65183 Wiesbaden, Germany)

E-mail: J.Guschlbauer@gmx.de

Wiesbaden, 29th August 2023

Declaration

I hereby declare that in the preparation of publication:

J. Guschlbauer, L. Niedzicki, L. Jacob, E. Rzeszotarska, D. Pociecha, P. Kaszyński,

Liquid crystalline electrolytes derived from the 1,12-disubstituted [*closo*-$CB_{11}H_{12}$]$^-$ anion,

J. Mol. Liq., **2023**, 121525, DOI: 10.1016/j.molliq.2023.121525

my contribution was in the synthesis and (thermo-)chemical characterization of the electrolyte materials comprising the liquid crystalline host matrix, the ionic liquid crystalline additive and the samples for electrochemical measurements. In addition, I prepared the first draft of the manuscript and compiled the data for submission.

Jannick Guschlbauer

Dr. Jannick Guschlbauer

dr. hab. inż. Leszek Niedzicki

Faculty of Chemistry,

Warsaw University of Technology,

Noakowskiego 3, 00-664 Warszawa, Poland

E-mail: leszek.niedzicki@pw.edu.pl

Warszawa, 30.08.2023

Declaration

I hereby declare that in the preparation of publication:

J. Guschlbauer, L. Niedzicki, L. Jacob, E. Rzeszotarska, D. Pociecha, P. Kaszyński, Liquid crystalline electrolytes derived from the 1,12-disubstituted [*closo*-$CB_{11}H_{12}$]$^-$ anion, *J. Mol. Liq.*, **2023**, 121525, DOI: 10.1016/j.molliq.2023.121525

My contribution was performing electrochemical impedance spectroscopy (EIS), linear sweep voltammetry (LSV) and analyzing their results.

Leszek Niedzicki

.....

dr. hab. inż. Leszek Niedzicki